FACULTAD DE CIENCIAS

Departamento de Física Aplicada. Área de Óptica.

Role of wavefront aberrations of amplified femtosecond pulses in nonlinear optics

VNiVERSiDAD D SALAMANCA

CAMPUS DE EXCELENCIA INTERNACIONAL

Tesis Doctoral

Rocío BorregoVarillas

Director: Javier Rodríguez Vázquez de Aldana

Salamanca, Octubre 2012

“Los grandes conocimientos engendran las grandes dudas”

Aristóteles

A mis padres.
A mi hermana.

Agradecimientos

Con el permiso de Javi y Luis, y saltándome por una vez todos los protocolos, las primeras personas a las que me gustaría dar las gracias son mis padres, simplemente porque os debo todo lo que soy. Habéis sido y seréis siempre mi mayor apoyo. Gracias papá, gracias mamá.

Ahora sí, gracias a mi familia profesional. En primer lugar, a mi "padre" Javi, por haber sabido supervisar mi trabajo dándome a la vez la libertad necesaria para poder comenzar una carrera investigadora. Gracias por tu infinita paciencia y por todo lo que me has enseñado: eres todo un ejemplo de profesionalidad.

Quizás uno de los agradecimientos más sencillos, y al mismo tiempo más sinceros, es para mi "abuelo" Luis, quien depositó una confianza ciega en mí desde el primer momento y me dio la oportunidad de formar parte de este gran equipo.

A mis "tíos", Íñigo y Julio, les quiero agradecer su desinteresada ayuda en todo momento, especialmente en el trabajo de los últimos meses, y a mis "tías" Isabel y Ana por introducirme, junto con Viqui, en el mundo de la Óptica y más tarde en el de la enseñanza. También a Chuspi, quien supo transmitir con creces el entusiasmo por lo que hace y su pasión por la Física.

A mis "hermanos", de forma muy especial a Carolina por hacer las horas de laboratorio más amenas; a Benja, mi compañero de fatiga en las medidas sistemáticas, y a mi "hermana" mayor, Cruz, que es el alma del laboratorio y que estuvo ahí desde el principio. Junto a ellos, al resto de "hermanitos" de doctorado (Alexis, Camilo G., Carlos, Fran, Jose, Jose Luis y Warein) por todos los buenos momentos compartidos, los detectores de germanio y haber ejercido incluso de directores de tesis.

A mis "tíos" Camilo, Enrique, Pablo, Plaja y Ricardo por su apoyo y orientación profesional en todo momento. A todo el equipo técnico (de forma especialmente cariñosa a Isa, Óscar, Javi Santa y Juan) por su ayuda en las cuestiones del laboratorio y, sobre todo, su paciencia en mis "un ratito más". Al personal de administración – con un guiño personal a Cristina, Javier y Yaiza – por tener siempre preparada una sonrisa con la que alegrar los días de trabajo más duros.

En general, os debo mucho a las personas que componéis el grupo de Óptica de la USAL y el CLPU, tanto a nivel profesional, como a nivel personal. Gracias a todos y cada uno de vosotros.

Ich danke der Gruppe von Prof. Krausz am MPQ, besonders Prof. Stefan Karsch und Dr. Zsuzsanna Major. Vielen Dank für eure Geduld und alles, was ihr mir beigebracht habt. Ich danke auch Dr. Jens Rauschenberger, der mir als Sommerstudentin beaufsichtigt hat. Danke auch zu Christoph Skrobol, der meine Arbeit in Deutschland versüßt hat, und Thomas Ganz, der mir geholfen hat einige wichtige Entscheidungen zu treffen. Ihr seid nicht nur (wunderbare) Kollegen, aber auch sehr gute Freunden.

Quedándonos en el terreno nacional, me gustaría dar también las gracias al Grupo de Óptica de la Universidad de Castellón (especialmente a Dr. Omel Mendoza-Yero y Dr. Gladys Mínguez-Vega)

y al Laboratorio de Óptica de la Universidad de Murcia (de forma muy especial a Dr. Juanma Bueno), por todo el entusiasmo que han puesto en los proyectos conjuntos.

Volviendo al plano personal, tengo que dar las gracias al resto de mi familia, de forma muy especial a mi tía Conchita y a Kika, quienes tantas tardes me han amenizado.

Se dice que los amigos son la familia que escogemos. A los míos solo les puedo decir: ¡gracias por formar parte de mi familia! A Ana, Ester, Julio, Fran, Raisa y Raúl por estar siempre dispuestos a escuchar y por sus insistentes "¿qué has descubierto hoy?". A Chisi y Juanmi, y a los molineros en general, por todos los momentos de risas y diversión.

Como para el final siempre se deja lo mejor, cierro los agradecimientos con la que, junto a aquellos con los que los empecé, es la persona más importante para mí: mi hermana Paloma (y su inseparable Piña), que en todo momento sabe cómo sacarme una sonrisa. Eres un ejemplo de superación del que todos deberíamos aprender.

Salamanca, a 20 de octubre de 2012

Acronyms List

CPA: Chirped Pulse Amplification

DFG: Difference Frequency Generation

DL: Diffractive Lens

FROG: Frequency Resolved Optical Gating

FWHM: Full Width Half Maximum

GDD: Group Delay Dispersion

GVD: Group Velocity Dispersion

GVM: Group Velocity Mismatch

HHG: High Harmonic Generation

NA: Numerical Aperture

OPA: Optical Parametric Amplification

OPCPA: Optical Parametric Chirped Pulse Amplification

OPG: Optical Parametric Generation

OPO: Optical Parametric Oscillator

PM: Phase Matching

PtV: Peak-to-Valley

RMS: Root Mean Squared

SC: Supercontinuum

SEA TADPOLE: Spatial Encoded Arrangement for Temporal Analysis by Dispersing a Pair of Light E-fields

SHG: Second Harmonic Generation

SPIDER: Spectral Phase Interferometry for Direct Electric field Reconstruction

SPM: Self Phase Modulation

STARFISH: Spatio-Temporal Amplitude and phase Reconstruction by Fourier-transform of Interference Spectra of High-complex-beams

SVEA: Slowly Varying Envelope amplitude Approximation

THG: Third Harmonic Generation

X-FROG: Cross- Frequency Resolved Optical Gating

WFS: Wavefront Sensor

Contents

1 Introduction

1.1. A brief history of intense ultrafast lasers

Since its first experimental demonstration by T. Maiman in 1960 [1], *laser* has revolutionized a variety of fields, from communications to medicine. Its development heralded an incredibly productive era of laser-based experimental physics that continues to this day. As a matter of fact, active laser-related scientific research has been awarded 10 Nobel prizes in the past decade [2]. Moreover, laser-related research is still a very active field and it is expected that recent advances in it, such as the development of petawatt and exawatt lasers [3-7] or the generation of coherent X rays [8], will lead to important scientific breakthroughs in the near future.

The *Q-switching* technique, which allows the generation of laser pulses, was demonstrated [9] shortly after the development of the ruby laser. Q-switching is based on the modification of cavity loss by external control. When radiation losses are applied in the laser cavity, the energy of the pump is stored in terms of population inversion. By contrast, when the losses are reduced the accumulated energy is delivered in a short pulse.

Q-switching allows for the production of pulses in the nanosecond regime. Since Q-switching is not valid to obtain shorter pulses (in the picosecond or femtosecond regime), the technique of *mode-locking* was developed in 1963 [10]. Mode-locking consists of fixing the relative phase of the longitudinal modes oscillating inside the cavity. This means that modes sum up coherently (constructively) and intra-cavity intensity increases. Therefore, by creating an intensity-dependent gain in the cavity, amplification will occur only in the modes that are in phase.

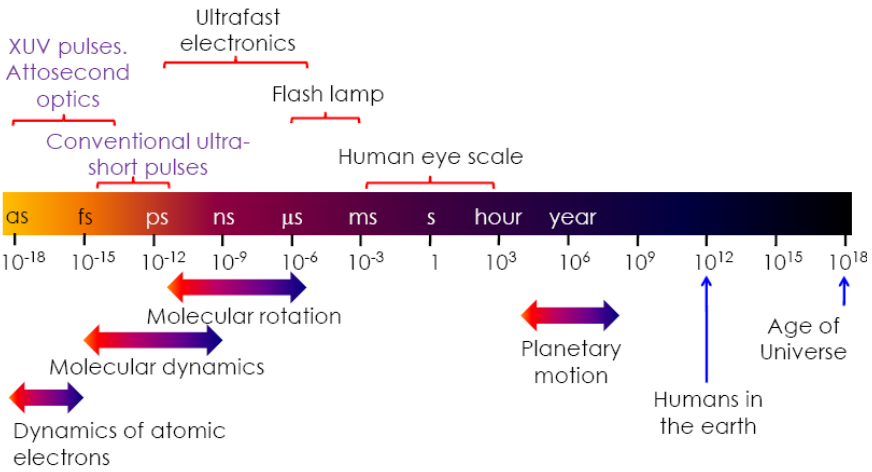

Fig 1. 1: Temporal scales. The lasers employed for the work presented in this thesis operated in the femtosecond (fs) regime.

A decade later, in 1974, E. P. Ippen and C. V. Shank demonstrated a sub-picosecond mode locked dye laser [11], this being considered the birth of ultrafast optics. Some years later, in 1982, a new laser material was discovered by P. F. Moulton, the Ti:Sapphire (Ti:Al_2O_3) [12]. Due to its very large gain bandwidth (650 – 1100 nm), this crystal allows the generation of very short pulses.

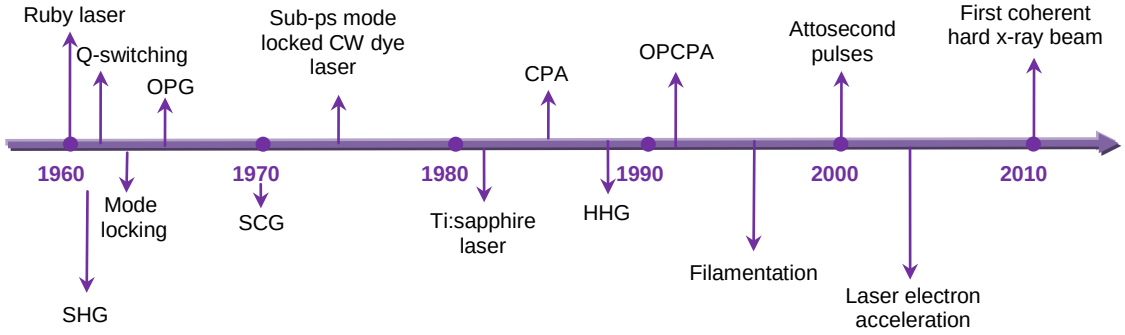

Fig 1. 2: Milestones in the history of ultrafast and ultraintense lasers (OPG: optical parametric generation; SHG: second-harmonic generation; SCG: supercontinuum generation; CPA: chirped pulse amplification; OPCPA: optical parametric chirped pulse amplification; HHG: high-harmonic generation)

1.1.1 The chirped pulse amplification technique

Although Ti:Sapphire lasers meant a revolution in the field of short pulsed lasers, peak intensity was limited by the optics and amplification crystal's damage threshold. For many applications, for example most femtochemistry experiments, femtosecond pulses lasting a few nanojoules (nJ) are sufficient. However, other applications require higher intensities that can only be accomplished by increasing the energy per pulse.

In this respect another breakthrough was developed in 1985 by Strickland and Mourou: *chirped pulse amplification* (CPA) technology [13], which enables the energy of femtosecond lasers to be increased by several orders of magnitude: from the millijoule (mJ) to the multi-Joule level.

A first approach to avoid the amplification crystal's damage was to increase the beam cross-section. However, at a certain point this presents a technological challenge since it involves the growth of crystals large enough to fit the beam.

CPA actually relies on this concept transferred to the temporal domain: the ultrashort pulses are stretched out in time, reducing peak power to a considerable extent (typically a 10,000 or higher factor), before amplification, thus avoiding crystal damage. Once the pulses are amplified, they are compressed back to the original duration achieving a high level of peak power.

The conceptual scheme of a CPA system is shown in Fig 1. 3. A first laser (*oscillator*) delivers ultrashort low-energy pulses at high repetition rates. The pulses then enter the *stretcher*, where temporal duration is increased to the nanosecond range. This is done by introducing *chirp*, or in other words, forcing the different frequencies that form the pulse to travel separately in time. In Fig 1. 3 this is accomplished by using a prism system, but it can also be achieved by means of diffraction gratings or by propagating the pulse through a transparent material in which it experiences a large chromatic dispersion.

The energy of the chirped pulses increases in one or more *amplification* stages. The crystals in the laser amplifiers are also Ti:sapphire, owing to the favourable thermal and mechanical properties of this crystal, which tolerates high power and intensities. For the pump, Q-switched frequency-doubled solid-state lasers based on Nd-doped crystals are used (~532 nm).

Multiple passes in the amplification crystals are needed to obtain the required gain factor. This can be achieved through different strategies. A common setup is a *regenerative* amplifier [14], where the Ti:sapphire crystal is placed in an optical resonator with two electro-optical switches. One of these switches allows the pulse to enter the resonator, thus reducing the repetition rate of the oscillator to the kHz level; and the other switch is activated to control the number of round trips in the cavity. The other approach is based on *multipass* amplifiers [15]. Unlike regenerative amplifiers, in a multipass there is no cavity and there is a fixed number of passes through the medium (which is determined by the beam path's geometry).

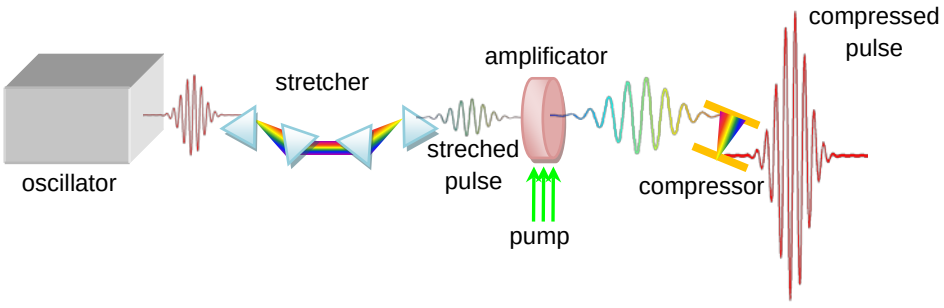

Fig 1. 3: CPA technology. The oscillator delivers short low-energy pulses which are stretched in the temporal domain by a prism based stretcher. The stretched pulses are amplified and incorporated into a grating compressor. Ultraintense ultrashort pulses are obtained at the laser chain's output.

Finally, the chirp introduced in the stretcher is eliminated through a *compressor*, made with reflective optics (usually gratings), since the damage threshold is higher than in refractive optics. Moreover the amount of material that the beam goes through is reduced, which is crucial for

ultrashort pulses. In this example, we have depicted a compressor made by a pair of gold gratings, a very common approach in high intensity lasers.

Once the chirp has been eliminated, the pulses return to their original temporal duration, generating high peak power.

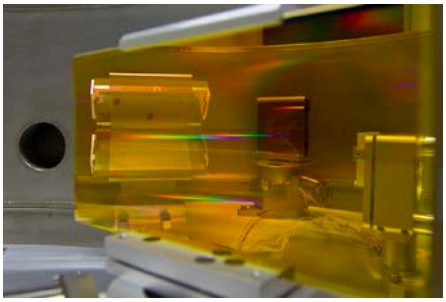

Fig 1. 4: Grating compressor of a high-intensity laser at the University of Salamanca.

1.1.2 A revolution in physics

The intensity scale-up in laser systems driven by CPA technology opened up completely new fields of research in physics, chemistry, biology and medicine.

In the fields of materials science and materials technology, femtosecond lasers enable the precise processing of any material, with minimal collateral damage and unprecedented reproducibility and precision. In this short pulse regime, only a very small fraction of the laser energy is transmitted as heat and transferred to the material surrounding the laser-irradiated area [16, 17]. The femtosecond pulses allow selective material removal in a process known as *ultrafast ablation*, with minimal thermal or mechanical damage to the surrounding material. Processed samples of very high quality can be obtained from almost any kind of material, including biological tissues. This permits, for example, microsurgery with minimal invasive effects [18].These particular features also allow the local modification of certain physical properties of any type of material.

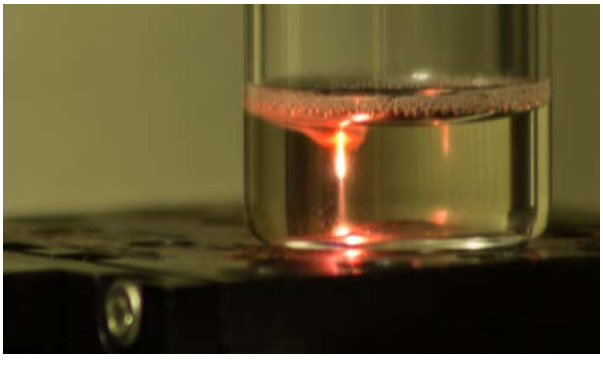

Fig 1. 5: a) Sample processed by a femtosecond laser: the pulses are focused into the sample by means of a microscope objective, which allows the modification of some of the material properties.

In physical chemistry, this kind of system has been extensively used in the study of molecular time-resolved dynamics, fostering a new discipline known as *femtochemistry*: the fact that the

stages in many molecular reactions and processes occur in the femtosecond timescale, makes it necessary to use pulses with comparable duration for their exploration. For instance, it allows the study of molecular photo-dissociation with unprecedent resolution.

Another relevant application is *laser electron acceleration* [19], which was originally suggested in underdense plasmas by Tajima and Dawson [20]. Two approaches have been effectively demonstrated to this end. In the first one, *laser wakefield acceleration*, the accelerating field is generated by relativistic plasma waves that can be excited when a high intensity laser propagates through a plasma [21, 22]. The second type is *direct laser acceleration* by means of the interaction between the laser field and the electrons in the plasma [23, 24]. Recently the first real-time observation of the accelerated electron pulse and the accelerating plasma wave was reported [25].

Laser-plasma accelerators are considered to be the next generation of accelerators because of their compactness and the huge electric fields they can sustain. Recent developments have shown peak energies reaching GeV [26].

When the intensity exceeds 10^{20} W/cm^2, it is also possible to accelerate protons [27]. *Proton laser acceleration* can lead to effective use of proton beams for medical applications [28] for example in cancer treatment since, unlike photons, protons penetrate tissue leaving most energy in the Bragg peak.

Another important application is *high-harmonic generation* (HHG) and the generation of *attosecond pulses* [29]. HHG is a process in which atoms excited by an intense laser field emit radiation of higher frequencies that are multiples of the driven pulse's frequency. HH radiation can span from the optical into the extreme ultraviolet (XUV) range. We will return to this topic in section 1.2.

1.1.3 Towards a promising future

Advances in laser physics experiments are intimately linked to technological advances in laser development, since developments in laser technology have opened up new regions in the exploration of light-matter interaction.

Far from being at a standstill, research in ultrafast science is now more alive than ever. In addition to the applications described in the previous section, new fields and investigations are currently emerging [3, 5, 6, 30, 31]. Among others, the generation of very dense plasmas at high temperatures has paved the way to study stars (astrophysics in the lab). Multi-petawatt lasers are also expected to allow for the study of nonlinear quantum vacuum effects [32] (photon scattering, pair creation processes, pseudoscalar modifications of the standard model…) and the possible detection of Hawking-Unruh radiation [33, 34] (the thermal spectrum emitted by black holes in quantum field theory).

Moreover, further innovations in short pulse laser technology will exploit the full potential of attosecond technology, with sources exhibiting much higher levels of efficiency. This will eventually allow for the imaging of the position of nuclei and electrons with sub-atomic resolution simultaneously in space and time in any transient state of matter [35].

1.1.4 Laser systems at the University of Salamanca

The ultrafast ultraintense lasers laboratory in Salamanca began operating in 2003 when the first CPA based Ti:sapphire laser system was installed. This system remains fully operational to this day and has been used to conduct most of the experiments of the work presented in this thesis.

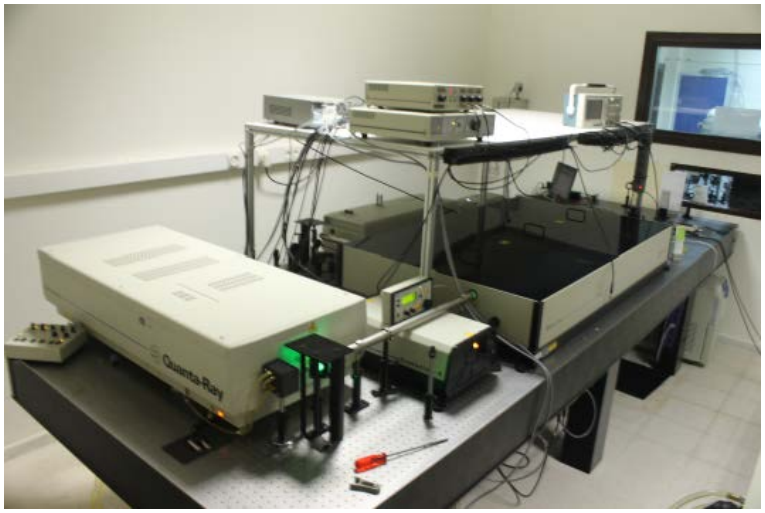

Fig 1. 6: Photograph of the Spectra Physics laser system at the University of Salamanca.

This laser produces 120 fs pulses at a central wavelength of 795 nm and has two outputs: the first one delivers pulses of ~1 mJ at 1 kHz repetition rate (peak power ~9 GW) and the other with a repetition rate of 10 Hz and a pulse energy of 50 mJ has a peak power of 0.5 TW. This is illustrated in Fig 1. 7. A mode locked oscillator (Tsunami, Spectra Physics) delivers 120 fs pulses at nJ level, which enter the first amplification stage. Only one regenerative amplifier (Spitfire, Spectra Physics) pumped by a Nd:YLF laser is used at this stage. The compressed pulses from this stage constitute the first output. One of 100 pulses is further amplified in a multipass amplifier pumped by a Nd:YAG laser, reaching a peak power of 0.5 TW. This was the most intense laser in Spain until a new system arrived in Salamanca in 2008.

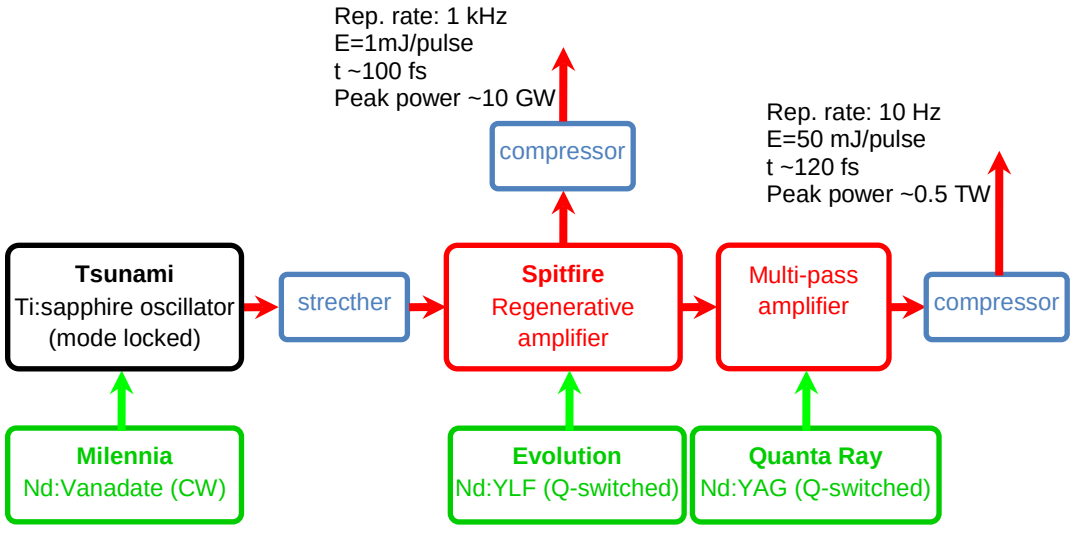

Fig 1. 7: Scheme of Spectra Physics laser system at the University of Salamanca.

The new laser system was also a CPA commercial system from Amplitude Technologies. It had a peak power of 20 TW, with a pulse energy of 500 mJ and a pulse duration of 25 fs, at a repetition rate of 10 Hz. Currently, this laser is being integrated within a more powerful one that will deliver pulses of 200 TW peak power, with an energy per pulse of 5 J. This new laser system corresponds to the secondary phase of the *Centro de Láseres Pulsados* (CLPU) [36, 37]. The CLPU is expected to be a leading scientific facility, with laser systems with peak powers of GW, TW and PW, that will be open to the international scientific community.

1.2. Nonlinear optics: a vibrant field

Just one year after the experimental demonstration of laser, Franken et al. obtained experimental evidence of *second-harmonic generation* (SHG) (i.e., the frequency doubling of light) from a ruby laser using a quartz crystal [38]. This was the beginning of what is called *nonlinear optics*, which could be described in a simple way as the light-matter interactions that take place at high intensities. In spite of being discovered more than fifty years ago, this process is still crucial for many of the latest advancements. For example, it is used to generate the radiation that pumps the amplification stages in petawatt lasers.

In the mid 1960s there was a great interest, which still persists today, in obtaining *tunable laser sources*. The laser's wavelength is determined by the amplification crystal's band structure, which in the case of Ti:sapphire is centred around 800 nm, so the wavelength tunability is limited to a certain range around that wavelength. However, many applications require laser pulses centred at other wavelengths (in the visible, UV, or mid-IR parts of the spectrum). To name some examples, biological tissues absorb in visible-UV range and proteins in the deep UV. In general, most spectroscopic experiments require pulses at differing wavelengths dictated by the absorption features of the sample, in order to excite a given transition. In material processing, for instance, the pulses are usually focused into the sample to be processed; since the focal spot scales up with the wavelength, shorter wavelengths allow more precision. A third example is found in HHG: the cut-off frequency in high-harmonics, which is related to the resulting attosecond pulse durations, increases with the wavelength [39-41]. For this reason, the scientific community is interested in developing lasers that emit in the mid-infrared [42-45].

Although SHG provided access to shorter wavelengths, these were restricted to the doubled frequencies of the existing laser sources. This bottleneck was sorted out by *optical parametric amplification* (OPA) [46].

The first mixing experiment involving three optical frequencies was conducted in 1965 [47]. Almost at the same time, Giordmaine and Miller described a $LiNbO_2$ *optical parametric oscillator* [48] for the first time. Some years later, in 1970, Alfano and Saphiro were the first to report supercontinuum (SC) generation [49] after exciting a borosilicate glass under high-power picoseconds pulses.

Parallel to the developments in laser technology has been the discovery of novel nonlinear optical crystals such as BBO (β-BaB_2O_4) and LBO (LiB_3O_5), combining improved optical characteristics (high nonlinear optical coefficients, low group-velocity dispersion, and broad transparency ranges,) with high damage thresholds.

The demonstration of the first high-energy femtosecond *optical parametric amplifiers* (OPAs) of the travelling-wave type, pumped by amplified Ti:sapphire laser systems, took place in the early

1990s. In the OPA process, the signal beam (the one to be amplified) propagates through the nonlinear medium together with a pump beam of shorter wavelength. The photons of the pump wave are converted into signal photons and the same number of idler photons (photons with energy equal to the difference between the energies of the pump and signal waves). Fig 1. 8 illustrates the OPA concept.

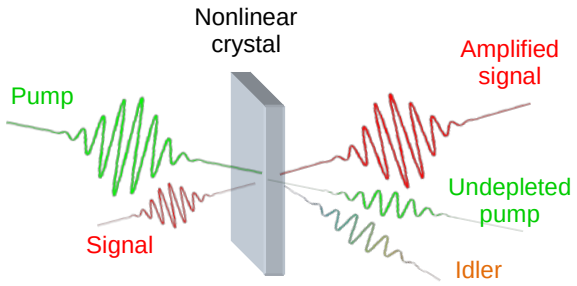

Fig 1. 8: Concept of optical parametric amplification (OPA) in a noncollinear geometry

Nowadays, OPAs are routinely used in optics laboratories since many modern studies of light-matter interaction require optical pulses with short duration as well as broad frequency tunability. OPAs have become, for example, workhorses in the field of ultrafast spectroscopy [50]. At present, some OPA designs have become standard and are even commercially available. In particular, near-IR OPAs pumped by the fundamental wave of a Ti:sapphire laser offer tunability from 1.1 to 2.5 µm with several tens of microjoule energy , while visible OPAs pumped by the SH of a Ti:sapphire laser are tunable from 0.45 to 2.5 µm with somewhat lower energies. Additionally, upconversion techniques allow for the extension of tunability from the UV [51] to the mid-IR, in the range of 5 to 9 µm [42-45]. In addition, they have the capacity to generate significantly shorter pulse than those of the pump, thus exploiting the broad gain bandwidths available in parametric interaction. If proper phase matching conditions are achieved, OPAs can generate widely tunable few-cycle laser pulses [52].

The advances in the development of OPAs were the first step towards *optical parametric chirped pulse amplification* (OPCPA) technology in 1992 [53] , though this has not been fully exploited until the last decade. Nevertheless, as we have already seen, CPA is crucial to obtain high-intensity ultrashort pulses, the pulse duration is typically limited by the amplification crystal's bandwidth to a few tens of femtoseconds. OPCPA bears some similarities with CPA, but the amplification is based on OPA, thus presenting a high single pass gain and negligible thermal load together with a huge amplification bandwidth [54]. This approach allows for the generation of few-cycle pulses at very high intensities [55] and has been successfully implemented in multi-terawatt and petawatt class lasers [56-61].An example worth mentioning is the Petawatt Field Synthetizer at the Max Planck Institute of Quantum Optics, which will deliver sub 8 fs at a petawatt scale [62, 63].

A few years earlier, in 1987, advances in technology and progressively more intense laser systems, led to the discovery of HHG in gases [64], though the first experimental observation of this phenomenon had been described in 1977 in the interaction of intense CO_2 laser pulses with plasma generated from solid targets [65]. In the presence of strong laser fields, the electrons from the gas may be ionized and accelerated by the electric field. As the electric field changes its direction half an optical cycle later so does the electron, returning to the parent nucleus. During the

recombination process with the atom, it can emit bremsstrahlung-like radiation with a frequency that is multiple of that of the laser [66]. In the case of Ti:sapphire laser, it provides trains of pulses in the extreme ultraviolet (XUV) range [67], opening a door to the generation of coherent X-rays [68]. The generation of such pulses is not only important in physics and chemistry, but in also many other disciplines: compact, brilliant monoenergetic X-ray sources could revolutionize medical and biological imaging. The recent demonstration of bright coherent ultrahigh harmonics in the keV X-regime from femtosecond lasers [69] paves the way to many of these applications.

The spectrum of high-harmonics corresponds to a train of *attosecond pulses* (1 as= 10^{-18} s) in the temporal domain [70]. The use of few cycle laser pulses together with a proper geometry makes it possible to obtain isolated attosecond pulses [71]. Such pulses provide time-domain access to a wide range of electron dynamics in the atomic shells [72-77] and the precise study of molecular dynamics [78-80]. Two complete reviews about attoscience are referenced [77, 81].

The last nonlinear process we will review is femtosecond laser *filamentation*, which was first observed in 1995 by Braun et al [82]. It had been long believed that, due to diffraction and group velocity dispersion, a laser pulse would spread after a long propagation in air. However, the experiment of Braun and his co-workers showed that the trend of intense femtosecond pulses was, in fact, the opposite.

Filamentation is a self-guiding process arising from a balance between the Kerr effect and the ionization defocusing. A nice review about filamentation can be found in reference [83]. As a consequence of this phenomenon, the spectral bandwidth is increased (Fig 1. 9b) yielding very short pulses if properly compressed [84]. Nowadays, filamentation, together with hollow core fibre, is one of the most widespread techniques to achieve spectral broadening (white light generation).

Filamentation has not only been applied in the field of ultrashort pulse generation, but has also been exploited for remote atmospheric diagnostics [85, 86], lighting protection [87] and laser induced breakdown spectroscopy (LIBS) [88], among others.

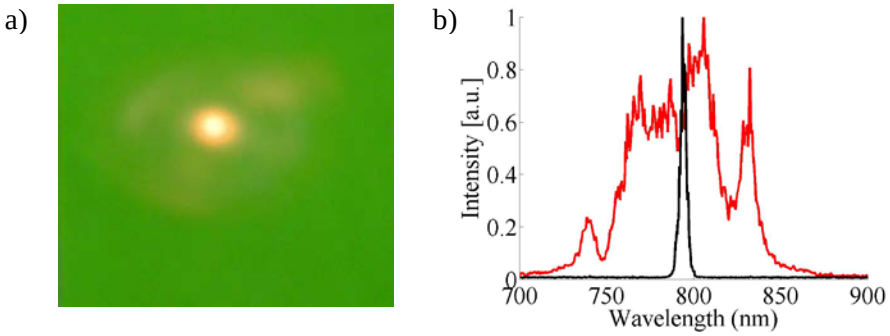

Fig 1. 9: a) Projection of a filament onto a fluorescence card. The filament corresponds to the inner core. b) Comparison between the spectra of the original laser pulse (black) and the filament (red).

1.3. Motivation

Researchers are now interested in implementing the applications of ultrafast femtosecond lasers, as well as in further developing their technology [3, 8]. Current efforts are focused, on the one hand, on obtaining more energetic pulses and, on the other, on reducing their temporal duration. In addition, scientific advances in laser development involve technological challenges related to pulse measurement in both the spatial and the temporal domains, as well as to the better control of certain properties such as wavelength and beam quality.

In the previous section we have reviewed some of the most important nonlinear processes and discussed their relevance for obtaining ultraintense ultrashort pulses. This is the main reason why the optimization of the previously described phenomena remains a constant concern in the community.

The aim of this thesis is, on the one hand, the *improvement of ultrafast nonlinear processes* by means of wavefront control and, on the other, the development of *spatial diagnostic tools* suitable for this kind of system. Moreover, there was no previous experience on wavefront sensing and spatial control in our group, and, therefore, acquiring a reasonable "know-how" was also necessary to *take full advantage of our laser systems*.

The most significant example to illustrate this is probably the paper by Bahk et al [89], where one of the highest laser peak intensities (10^{22} W/cm^2) was reported. In 2008 an upgrade of this system achieved the world record in laser intensity ($2x10^{22}$ W/cm^2) [90]. In spite of the current existence of petawatt-class lasers, this world record was achieved with a 300 TW laser (the results reported in [89] were accomplished with 45 TW). Bahk and his colleagues demonstrated that it was possible to focus the beam near diffraction limit (thus increasing peak intensity) by wavefront correction (*adaptive optics, AO*). AO has also played an important role in parametric processes. To name some examples, the shortest pulses from an OPA have been obtained from a noncollinear blue-pumped system with the help of an adaptive pulse compressor [91], and a focused intensity above 10^{19} W/cm^2 with 10^9:1 contrast ratio was obtained by combining SHG and wavefront correction of a terawatt laser chain [92].

Although progress concerning the study and optimization of nonlinear processes has been made over the last decade, certain issues still need to be addressed. In this respect, the enhancement of SHG is interesting, since it offers a better contrast ratio than the fundamental pulse, making it attractive for laser-matter interaction experiments involving solid targets [92]. Unfortunately, the nonlinear effect involved in *SHG leads to significant wavefront distortions* that limit the focusability of the laser beam. The study of these phase effects is therefore crucial for the applications of frequency doubled pulses.

SH pulses also serve as pumps in visible OPAs. The study of their spatial properties is crucial to determine the beam quality of the amplified signal from an OPCPA chain [93].

Another important aspect is the optimization and flexibility in the design of tunable pulses for spectroscopic applications. In femtosecond pump-probe spectroscopy, the system under study is resonantly excited by a pump pulse and its subsequent evolution is monitored by measuring the pump-induced transmission change of a delayed probe pulse [94]. The need to excite a system on resonance and probe optical transitions occurring at different photon energies requires broad frequency tunability of both the pump and the probe pulses [95]. Although current visible OPAs

can deliver pulses from 0.45 to 2.5 μm, many experiments, such as the tracking of ultrafast energy flow in biomolecules [96], require pulses in the near and deep UV. These can be obtained by upconversion techniques, but the accomplishment of setups with the characteristics of stability and reliability sufficient for systematic studies is still a very challenging task. In addition, for some of these experiments it is interesting to have *pulses with tailored spectra*. The generation of pulses with tailored spectra to seed OPAs is also one of the issues addressed in this thesis.

With respect to filamentation, the *energy scaling up of pulse postcompression* is still an open issue. The main constraint of these schemes originates from the upper limit for input and, consequently, output energies, which are not high enough for the requirements of currently available high power lasers. Many efforts are now focused on the development of strategies to overcome this limitation [97, 98]. In this dissertation we will propose a scheme based on astigmatic focusing.

The particular features of intense femtosecond pulses need measurement devices adapted to them. In the case of wavefront sensing, traditional methods, such as Hartmann-Shack, present some drawbacks due to the broad bandwidth of these pulses [99]. Specifically, they are not able to resolve frequency dependent wavefronts, their resolution being limited by the camera's pixel size.

Finally, many laser-matter interaction experiments can benefit from knowledge in wavefront sensing and spatial control. Now that the fundamental mechanism for electron laser acceleration is well-established, more energetic and stable beams are pursued. In particular, the gas jet employed in the setups for particle acceleration can be characterized by the use of a wavefront sensor. This allows for the optimization of the jet in terms of pressure, geometry... etc. [100]

1.4. Thesis outline

The main goal of this thesis is the study and manipulation of wavefront aberrations and their applications in ultrafast nonlinear optics. The work has been divided into four main blocks. The first one (Chapter 2) is devoted to the fundamentals of wavefront sensing and its further exploitation for the optimization of particle acceleration and filamentation. On the one hand, the complete spatial characterization of our laser was used as input to simulate pulse propagation and its interaction with matter for the generation of electrons from solids. Wavefront analysis was also applied to optimize the experimental setup for electron acceleration in gases, allowing accurate control of the density of the gas and its dynamics under different experimental conditions. On the other hand, astigmatic lenses are used to focus femtosecond pulses in a gas cell. We have demonstrated an increase in the multifilamentation threshold, which allows for the input energy to be increased, consequently favouring postcompression.

The second part (Chapters 3 and 4) presents a characterization of SHG of aberrated femtosecond pulses. We first applied numerical simulations assuming a flat wavefront to study the spatial and temporal characteristics of second-harmonic pulses. The second step was to study the phase effects in SHG of both aberrated and non-aberrated femtosecond pulses. The purpose of this is twofold. On the one hand, it allows us to determine how the spatial profile affects the characteristics of the frequency doubled pulses, which is interesting for the optimization of the auxiliary beams in the laboratory of *Microprocesado de materiales con laser*, since these beams are obtained through second- and third- harmonic generation in crystals. On the other hand, it helps to set the limitations and validity of the technique presented in Chapter 5.

The third block (Chapter 5) is devoted to the development of a novel wavefront sensing technique whose aim is to overcome some of the bottlenecks present in traditional methods when dealing with intense short pulses. This method is based on the phase dependence of the SHG process. Additionally, we also demonstrate the capability of the spatiotemporal characterization technique STARFISH for frequency-resolved wavefront sensing (Chapter 6).

Finally, the fourth section (Chapters 6 and 7) deals with the generation and optimization of SC generation in bulk media by means of diffractive optics. The aim was to improve the SC generation stage to be later implemented in an OPA with special attention to the ultraviolet (UV) range. As we mentioned in the previous section, this is of great interest in spectroscopy since the tracking of many ultrafast processes requires shaped UV pulses.

Below is a more detailed description of the different issues addressed in each chapter of this thesis.

Chapter 2 – Spatial characterization of intense short pulses: applications. This section is devoted to a revision of the fundamentals of wavefront sensing and beam spatial characterization. The second part of it is focused on its applications in nonlinear optics. We first provide a description of its use for the optimization of the experimental setups involved in particle generation and acceleration (in solids and gases). Secondly, we apply this knowledge for filamentation enhancement by means of astigmatic focusing.

Chapter 3 – Basic concepts of nonlinear optics. In this chapter we describe all the processes discussed in this thesis and revise the physical mechanisms behind them.

Chapter 4 – Second-harmonic generation of aberrated femtosecond beams. In this chapter we revise the theoretical framework of SHG in nonlinear crystals from the simple approach of monochromatic plane waves. However, the application of this theory to femtosecond pulses requires certain modifications. To this end, the wave equations for SHG are numerically solved, which allows us to study the temporal and spatial characteristics and compare them to the experimental results. The wavefront dependence of the process and its consequences in terms of beam quality, focusability and spatio-spectral dynamics are also discussed.

Chapter 5 – Wavefront retrieval of femtosecond pulses by second-harmonic generation. A wavefront sensing technique based on the phase dependence of the SHG process is presented in this chapter. The validity and limitations of the method are studied in different crystals and wavefront aberrations. Simulations to support the experimental results are also dealt with in this chapter.

Chapter 6 – Chromatic aberration for spectral shaping of pulses generated via nonlinear processes. A brief introduction to diffractive optical elements (DOE's) is provided in this chapter. We present the applications of DOE's for the spectral control of second-harmonic, third-harmonic and SC generation. The latter is further explained in Chapter 7.

Chapter 7– Supercontinuum generation in solids with diffractive lenses. A kinoform diffractive lens is used to achieve spectral shaping in SC generation, reaching a larger cut-off frequency than that reached with an achromatic lens under similar conditions. We also demonstrate that it is possible to obtain spectral tunability. A detailed study of the phenomenology and a characterization of the so-generated pulses are also included in this chapter.

1.5. Publications

G. Mínguez-Vega, C. Romero, O. Mendoza-Yero, J. R. Vázquez de Aldana, R. Borrego-Varillas, C. Méndez, P. Andrés, J. Lancis, V. Climent, and L. Roso
Wavelength tuning femtosecond pulses generated in nonlinear crystals by using diffractive lenses
Optics Letters **35**, 3694-3696 (2010)

C. Romero, R. Borrego-Varillas, A. Camino, G. Mínguez-Vega, O. Mendoza-Yero, J. Hernández-Toro, and J. R. Vázquez de Aldana
Diffractive optics for spectral control of the supercontinuum generated in sapphire with femtosecond pulses
Optics Express **19**, 4977-4984 (2011)

B. Alonso, R. Borrego-Varillas, I. J. Sola, O. Varela, A. Villamarín, M. V. Collados, J. San Román, J. M. Bueno and L. Roso
Enhancement of filamentation postcompression by astigmatic focusing
Optics Letters **36**, 3867-3870 (2011)

R. Borrego-Varillas, C. Romero, J. R. Vázquez de Aldana, J. M. Bueno, and L. Roso
Wavefront retrieval of amplified femtosecond beams by second-harmonic generation
Optics Express **19**, 22851-22862 (2011)

B. Alonso, R. Borrego-Varillas, O. Mendoza-Yero, I. J. Sola, J. San Román, G. Mínguez-Vega and L. Roso
Frequency resolved wavefront retrieval and dynamics of diffractive focused ultrashort pulses
J. Opt. Soc. Am. B **29**, 1993-2000 (2012)

R. Borrego-Varillas, C. Romero, O. Mendoza-Yero, G. Mínguez-Vega, and J. R. Vázquez de Aldana
Supercontinuum visible femtosecond pulses generated in sapphire with diffractive lenses
Submitted, 2012

C. Romero, R. Borrego-Varillas, O. Mendoza-Yero, G. Mínguez-Vega, C. Méndez, and J. R. Vázquez de Aldana
Second-harmonic generation of femtosecond pulses focused on BBO with a diffractive lens
In preparation

2 Spatial characterization of intense short pulses: applications

2.1. Introduction: importance of spatial quality

Most laser-matter interaction experiments, such as high-harmonic generation (HHG) or particle acceleration, require high peak intensities. To achieve this, a good temporal profile, free of pre- and post- pulses, is desirable. In this regard, many efforts have been made to characterize the contrast and clean the pulses [101-105]. Moreover, there is also interest in achieving the shortest temporal duration provided by the laser. In other words, the phase acquired by the pulses as they propagate through different media needs to be compensated in order to become as flat as possible. In this sense, and during the last decades, several temporal diagnostic tools have developed [106]. Among them, the most widespread methods are frequency- resolved optical gating (FROG) [107] and spectral phase interferometry for direct electric-field reconstruction of ultrashort optical pulses (SPIDER) [108]. Compensation of the spectral phase can be carried out using different strategies such as prisms or gratings [109], a combination of both (grisms) [110] or double chirped mirrors [111, 112].

Besides pulse duration, intensity distribution is the other key parameter to achieve the highest possible peak intensity. In fact, in spite of existing petawatt-class lasers, the highest intensity has been achieved with a terawatt system by correcting its aberrations with a deformable mirror [89]. A brief look at the theoretical definition of peak intensity of a Gaussian beam shows the importance of spatial quality [113]:

$$I_{peak} = \frac{E}{1.69\omega^2\tau} \tag{1}$$

where E is the energy, ω the radius at $1/e^2$ of the maximum intensity and τ the pulse duration at FWHM. The intensity has a quadratic dependence with the beam radius compared to a linear dependence with the energy and the pulse duration.

As in the temporal domain, the beam is spatially characterized by its amplitude and phase (wavefront). In femtosecond lasers thermal instabilities, clipping by optical components, cavity misalignment and crystal inhomogeneities distort the beam profile and the wavefront. Therefore, it is necessary to correct both of them in order to obtain a near diffraction limit focal spot. The first can be improved by using spatial filters, at the expense of a loss of energy. The latter can be corrected with adaptive optics (AO), i.e. deformable mirrors or spatial light modulators. As an example, Fig 2. 1 shows the focal spot obtained for beams with different amplitudes and phases.

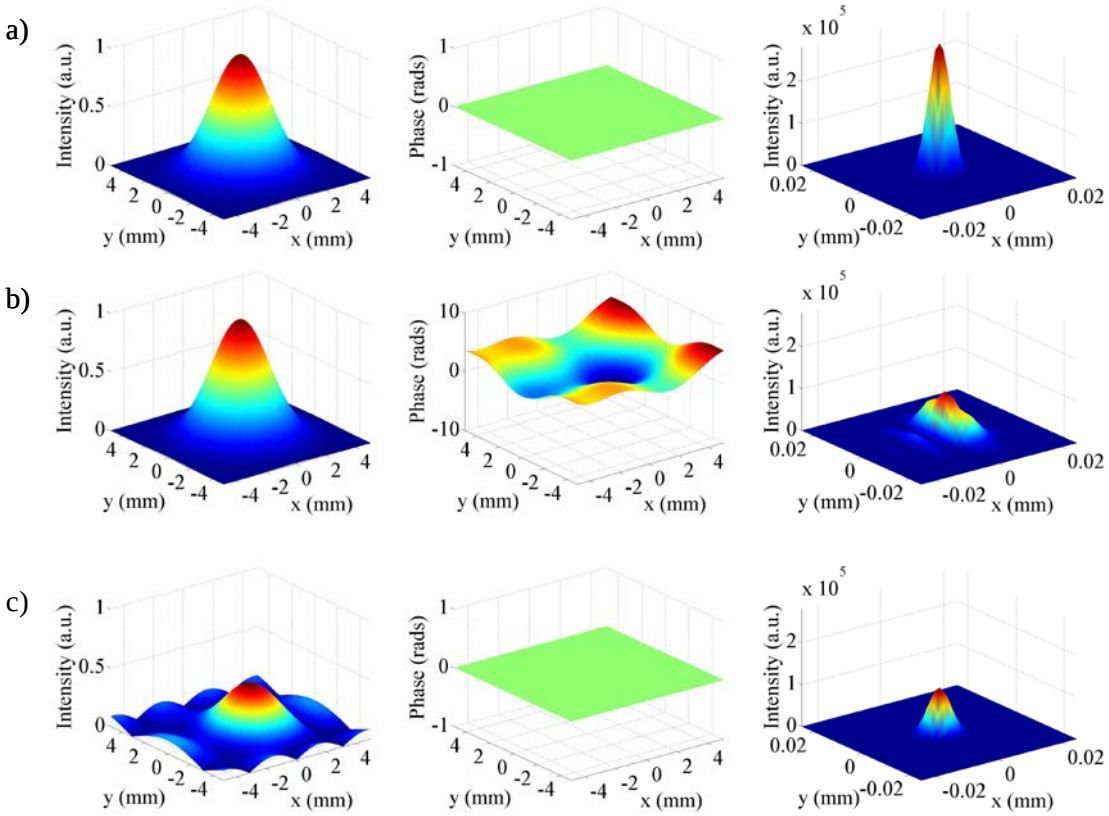

Fig 2. 1: Different beam profiles (first column) and wavefronts (second column) and corresponding focal spot (third column). a) Gaussian beam profile and flat wavefront, b) Gaussian beam profile and distorted phase and c) modulated amplitude and flat phase.

This chapter is focused on wavefront aberrations and their measurement (sections 2.2 to 2.4), concluding in sections 2.5 and 2.6 with a review of some of the applications we have developed in our laboratory, mainly characterization techniques for laser acceleration experiments.

2.2. Quantitative criterions

2.2.1 Strehl ratio

On the basis of the preceding sections, one can easily deduce that the ratio to the diffraction limit size is an indicator of beam quality. The *Strehl ratio* is usually chosen as a quantitative factor. The Strehl ratio [114] is defined as the ratio of the experimental peak intensity at the focus, I_{peak}, as compared to the theoretical maximum peak intensity when the wavefront is flat, I_{peak}^{flat}.

$$S = \frac{I_{peak}}{I_{peak}^{flat}} \tag{2}$$

For diffraction-limited beams the Strehl factor reaches 1. Therefore, the smaller S, the worse quality the beam has. As an example, in Fig 2. 1b the Strehl factor is obtained by dividing the peak intensity (as given in the third column) by that in Fig 2. 1a, yielding S=0.35. Since this number is far from the unit, it indicates poor quality.

2.2.2 M^2 factor

The *M^2 parameter*, also known as beam quality factor or beam propagation factor, was suggested by Siegman in 1990 [115] and is now widely used to characterize laser beam quality. It is determined by

$$M^2 = \frac{\pi\theta\omega_0}{\lambda} \tag{3}$$

where ω_0 is the radius at the beam waist, λ is the wavelength and θ the half-angle divergence. A perfect Gaussian beam has an M^2 factor of 1. Smaller values of M^2 are physically impossible.

It must be noticed that extensions of the theory should bare needed in the case of strongly aberrated beams or when the paraxial regime cannot be applied [116].

Experimentally, the M^2 factor of a given beam can be found by monitoring the beam size along the Rayleigh length [117].

2.3. Wavefront aberrations

As is stated in the introduction, the electromagnetic field is fully characterized in the spatial domain by its phase and amplitude. The spatial dependence of the electric field can be generally formulated as:

$$\vec{E}(\vec{r}) = \vec{A}(\vec{r})\exp[-i\psi(\vec{r})] \tag{4}$$

where A is the amplitude and ψ the wavefront (phase). This section provides a review of some of the basic concepts concerning wavefront measurement, such as commonly used units and the polynomial basis. A complete review can be found in [118].

2.3.1 Units

In the international system of units (SI units) phases are measured in *radians*. However, here it is important to remark other commonly used units such as *wavelengths* (λ) and *microns* (μm).

First we shall first recall the equation for plane waves:

$$\vec{E}(\vec{r}) = \vec{A}\exp\left(-i\vec{k}\cdot\vec{r}\right) = \vec{A}\exp\left(-i\frac{2\pi}{\lambda}\vec{u_k}\cdot\vec{r}\right) \tag{5}$$

where k is the wave vector and u_k is a unit vector that points in the direction of the wave vector. In this case, $\psi_{rads} = \vec{k}.\vec{r}$ and $\psi_{\lambda} = \frac{1}{\lambda}\vec{u}_k.\vec{r}$. Using these expressions as a basis, we can deduce the conversion between the three unit systems:

$$\begin{aligned} \psi_{rads} &= 2\pi\psi_{\lambda} \\ \psi_{\mu m} &= \lambda\psi_{\lambda} \end{aligned} \tag{6}$$

2.3.2 Pupil definition

Another issue to take into account is the *pupil*. Real imaging systems have a limited size that is termed exit pupil. In some cases, we set a pupil (either by placing a diaphragm just at the entrance of the sensor or by software) to select the part of the beam we are interested in. Since the magnitude of the aberrations depends on the pupil size, it is important to mention this datum when giving a wavefront aberration value.

2.3.3 Peak-to-valley and RMS

The wavefront is usually expressed in two different ways: the *peak-to-valley* (PtV) or the *root mean squared* (RMS) error. The first simply states the difference between the maximum and the minimum values taken by the wavefront surface. The latter tells us how much the "height" varies across the entire wavefront. The RMS wavefront error is defined as

$$RMS = \sqrt{\frac{1}{N}\sum_{\rho,\theta}\left(\psi(\rho,\theta) - \bar{\psi}\right)^2} \tag{7}$$

where N stands for the number of sample points and $\bar{\psi}$ for the averaged wavefront. The above equation is the ordinary statistical formula for the standard deviation of N sample points taken over the pupil of the wave aberration function, $\psi(\rho,\theta)$.

For small values of the RMS, it can be related to the Strehl factor through the following equation:

$$S = 1 - 4\pi^2 RMS^2 \tag{8}$$

2.3.4 Zernike polynomials

The *Zernike polynomials* are a set of orthogonal polynomials on the unit disk that constitute a proper basis to express the wavefront, since they allow us to interpret the measurement and

determine the origin of beam aberrations [119]. The Zernike functions are defined over a disk pupil, which is suitable for most laser shapes.

In polar coordinates they are defined as the product of a radial function and an azimuthal function:

$$\begin{aligned} {}^{e}Z_n^m &= R_n^m(\rho)\cos(m\theta) \\ {}^{o}Z_n^m &= R_n^m(\rho)\sin(m\theta) \end{aligned} \tag{9}$$

Since Zernike polynomials are orthogonal, the phase projection is unique and can be expressed as follows:

$$\psi(\rho,\theta) = \sum_{n,m} {}^{e}c_n^m \, {}^{e}Z_n^m(\rho,\theta) + {}^{o}c_n^m \, {}^{o}Z_n^m(\rho,\theta) \tag{10}$$

In order to follow a criterion, we have chosen the RMS mode, which uses an orthonormalized version of the Zernike polynomials [120]:

$$\begin{aligned} {}^{e}Z_n^m &= \sqrt{2(n+1)}R_n^m(\rho)\cos(m\theta) \\ {}^{o}Z_n^m &= \sqrt{2(n+1)}R_n^m(\rho)\sin(m\theta) \end{aligned} \tag{11}$$

A table with the Zernike polynomials up to the fourth order is presented in Appendix C.

One of the useful features of the Zernike projection is that the aberration coefficient is also the RMS value for any given Zernike mode. Furthermore, the total RMS error in a wavefront is the square-root of the sum of the squared Zernike coefficients:

$$RMS = \sqrt{\sum_{n,m} \left(c_n^m\right)^2} \tag{12}$$

2.3.5 Point spread function (PSF)

Linear systems theory shows how an image is composed of an object convolved with the *point spread function* (PSF) of the imaging system, which is the image of a point source of light. Adding aberrations to the optical system results in a broadening of the PSF and increased blurring (see the example presented in Fig 2. 2).

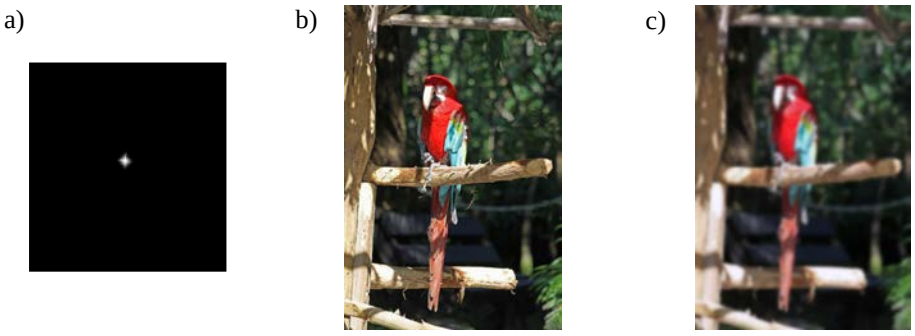

Fig 2. 2: a) PSF function of an optical system, b) object and c) image by the optical system. The image is the convolution of the object and the PSF function.

2.4. Wavefront sensing

2.4.1 Wavefront sensors

Nowadays there is a wide variety of well-developed wavefront sensors (WFS): Hartmann-Shack [121], lateral shearing interferometers [122], Foucault knife-edge test [123], Ronchi test [124]... Moreover, wavefront sensing is a very active research field and recent approaches include pyramid WFS [125], axicons [126] and computer-generated holograms [127-129].In this section we will briefly review the most common ones in the field of ultrafast optics, the Hartmann-Shack sensor and the multiwave lateral shearing interferometers.

2.4.1.1 Hartmann-Shack

One of the most popular WFS is the Hartmann-Shack (HS) [130-132]. An HS sensor consists of a microlens array and a camera placed on its focus. The array splits the beams in subdivisions, each of them focused on the detector. Since the wavefront curve can be locally considered as a tilted segment, the focal spot corresponding to each beam subdivision will be displaced in a quantity proportional to the local tilt (see Fig 2. 3). This displacement is therefore directly connected to the local phase slope, i.e., the derivative of the wavefront.

The validity of the HS sensor has been discussed in relation to ultrashort pulses: since these pulses have a broad spectral bandwidth, there might be chromatic aberration in the lenset-array based imaging. In [99], Hauri and co-workers demonstrated the validity of the HS for ultrashort pulses. In their experiment, they analysed the wavelength dependence of the wavefront by using interferential filters. They concluded that, although the wavefront was frequency dependent, the result given by the HS was equal to the sum of wavefronts for each wavelength.

More recently, Aleksandrov et al report the applicability of the HS for measuring the wavefront of high-power lasers, concluding that it is a suitable device to study the dynamics of the aberrations of intense lasers [133].

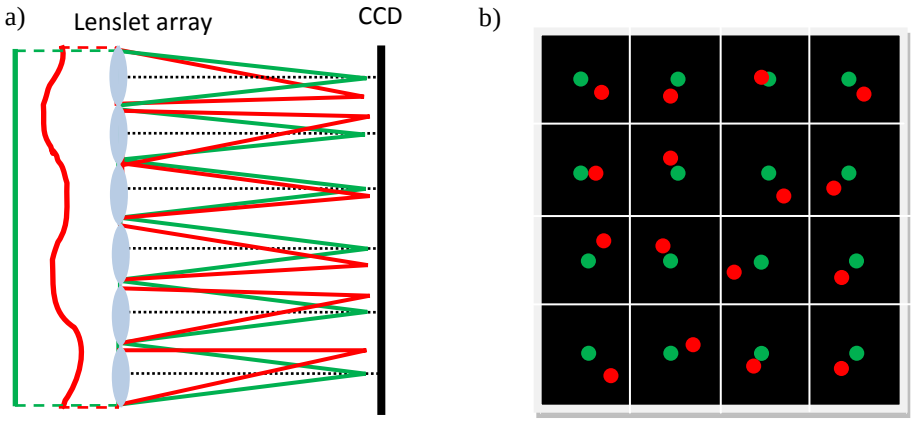

Fig 2. 3: Hartmann-Shack sensor. a) The incident beam (a flat wavefront – in green – or an aberrated phase front – in red) is focused onto the CCD by the array of microlenses. b) The spot deviation from a perfectly flat phase is proportional to the local angle.

2.4.1.2 Multiwave lateral shearing interferometry

A *shear plate* is a device consisting of high quality optical wedge. When a beam is incident at an angle of 45º it is reflected two times. The sum of both reflections yields an interference pattern that can be used to test the beam collimation. This concept can be extended to wavefront retrieval since the interference pattern is related to the phase gradient in the direction of the translation. However, these setups need to be spatially or temporally split to yield the two orthogonal gradients required for wavefront retrieval.

In the 90's Primot generalized this concept to *three-wave lateral shearing interferometer* [134]. Since the replicas are generated in three noncollinear directions, the phase gradients are obtained in those directions. From them, it is possible to retrieve the two orthogonal phase gradients needed for phase reconstruction. An achromatic version of the device was proposed in 1995 [135]. Due to their high dynamic range, achromaticity and self-reference, this kind of sensors are particularly interesting in relation to broadband lasers [136, 137]. Moreover, in the past decade, the concept was extended to four waves, which allows for an increase in measurement precision [138].

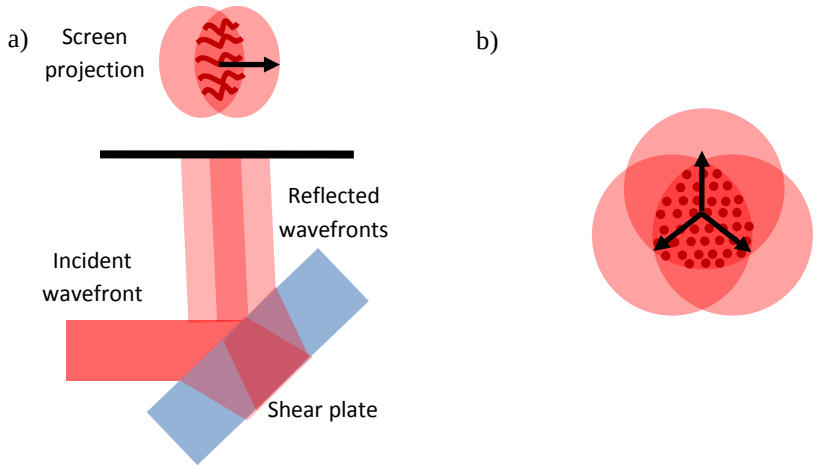

Fig 2. 4: a) Working principle of a shear plate and b) basis of three-wave interferometry. The arrows indicate the shearing directions.

Fig 2. 5 presents the sketch of a home-made achromatic three-wave lateral shearing interferometer [139]. A 2D grating is placed in the measurement plane, which is at an f distance (f being the focal length) from the first lens. The pattern at the focal plane consists of a hexagonal array of spots. A spatial mask allows for the selection of three first-order harmonics that are deconvoluted by means of a second lens. Therefore, interference between the three waves, which is registered with a CCD sensor, is achieved in the focal plane of the second lens.

By taking two interferograms (at distances of f and f+z from the second lens – z being a small displacement) it is possible to retrieve the phase gradients, and thus the wavefront, by applying the transport equation. The complete mathematical development, accompanied by experimental examples, can be found in [140].

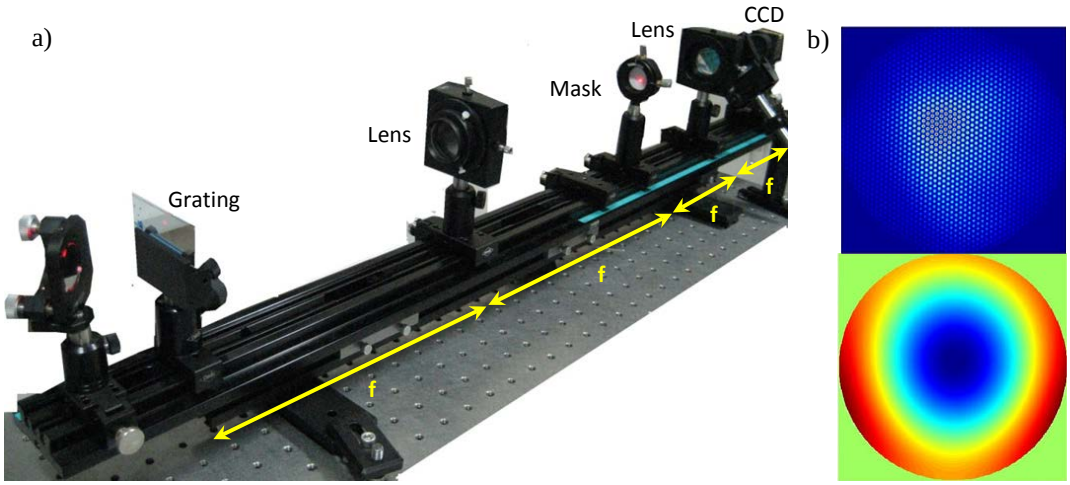

Fig 2. 5: a) Home-made achromatic three-wave lateral shearing interferometer (see detailed description in the text). b) Experimental interferogram and corresponding retrieved wavefront.

2.4.2 Phase conjugation

In many situations it is not possible to access the plane where we want to measure the wavefront. In those cases, it is necessary to set up a system that images the beam onto the WFS. Such a system is usually a *4f telescope*, formed by two identical lenses separated by a distance 2f (f being the focal length). The plane situated at a distance f from the first lens is then imaged onto the WFS, which is placed at the focal plane of the second lens. If magnification is needed, the second lens may have a different focal length. The most common representation for this case is in Fig 2. 6.

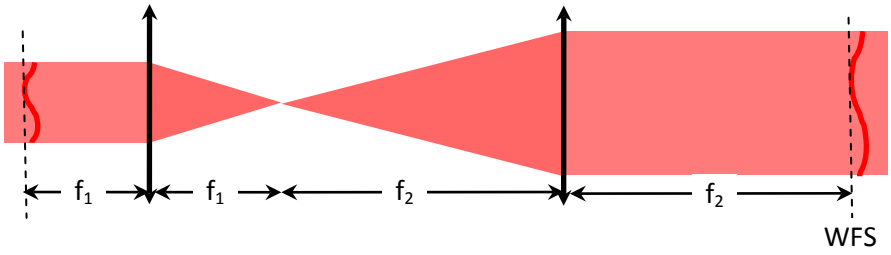

Fig 2. 6: Imaging system for phase conjugation

2.5. Characterization of our laser

2.5.1 Aberrations in terawatt class lasers

Wavefront aberrations are difficult to avoid in terawatt class lasers for several reasons: thermal lensing due to a high average power operation, relatively low optical quality of the large diameter crystals used in the amplifiers, defects in the gratings used in the compressor... In this section, we will briefly report on the sources of aberrations in high-power lasers.

Ranc et al., tracked the wavefront along the different stages of a multiterawatt 10 Hz CPA chain [113]. The authors concluded that the stretcher is almost aberration free (phase distortions below $\lambda/20$ for a 2 mm pupil size and Strehl ratio above than 90%). According to them, the amplifiers added some distortions due to thermal effects and doping inhomogeneities in the crystals. To clean

the pulses, spatial filters were used after each amplification stage. With this setup, following the first amplification stage, the energy was 5 mJ, the phase distortions below λ/25 and the Strehl ratio 93%.

The more the pulses are amplified, the more difficult it becomes to mainain a good spatial quality. The spatial filters must be placed in vacuum in order to avoid air ionization. Furthermore, the laser pointing becomes less stable so the spatial filters must be less sensitive to the beam positioning. A conical pinhole can be used in these cases. Following this sketch, the Strehl ratio was improved from 68% to 95%, and the remaining phase distortions were below λ/30. Due to the damage threshold of the material used for the pinhole, it was not possible to implement it in the third amplification stage. At this level, high thermal effects appear in the amplifiers, this being known as *thermal lensing*. Thermal lensing affects the wavefront mainly in the form of defocus and astigmatism aberrations. A possible solution to avoid thermal lensing and high order distortions is crystal cooling below -150 ºC [141] or the use of adjustable curvature mirrors [142].

Finally, compressor misalignments and local changes in the groove spacing lead to spatiotemporal distortions of the compressed pulses. Moreover, one has to be very careful concerning the material used for the gratings, since thermal effects also take place at this stage.

Another example is given by C. Hernández-Gómez and co-workers, who fully characterized the behaviour of the Vulcan CPA chain. In their study [143] they determined the origin of wavefront aberrations and identified correction methods. Aberrations were divided into static (optics), dynamic (thermal) or transient (short related). For this purpose, the authors recorded the wavefront during a set period of time. In their case, the aberrations were mainly astigmatism and coma. The first one was found to be static and could be corrected by introducing a fixed amount of astigmatism, whereas the latter had a dynamic nature. While static aberrations could be compensated by means of fixed optics [144], dynamic phase distortion required to be corrected with adaptive optics (AO), such as deformable mirrors [145] or spatial light modulators [146]. Nowadays most ultraintense lasers are equipped with AO systems [147-156].

2.5.2 Description of our sensor

The Laboratory for Ultraintense Lasers of the Universidad de Salamanca is equipped with several diagnostics tools. For spatial characterization, apart from CMOS sensors, we have a commercial WFS.

The model is a Phasics SID4-HR [157] based on quadri-wave lateral shearing interferometry. It presents several features that make it attractive for its use with intense short pulses:

- High dynamic range
- Achromaticity
- Self-reference (the measurement is insensitive to environment vibration)
- High resolution of phase map
- Capability of measuring high diverging beams directly (up to 0.75 NA)

Software is provided for beam analysis. It consists of the following modules [120]:

- *Beam profiler*: it provides parameters for a complete description of the electromagnetic field, such as the intensity centroid, ellipticity and Gaussian fits.

- *Zernike polynomials projection*: the phase decomposition in Zernike (or Legendre) polynomials is given. It also enables to remove certain low order aberrations.
- *Far-field analysis*: this window displays simulations of the far-field corresponding to the measured intensity and phase maps. Usual beam characterization figures (Strehl ratio, M^2, encircled energy) are deduced from these simulations.
- *Line-out*: generation of horizontal and vertical line-outs corresponding to the phase and intensity.
- *Beam alignment*: this module provides a further interpretation of the defocus and astigmatism coefficients, transforming them into beam propagation characteristics, such as Rayleigh length, beam waist... etc.

In Appendix B there is a detailed description of the features of the sensor, together with a calibration.

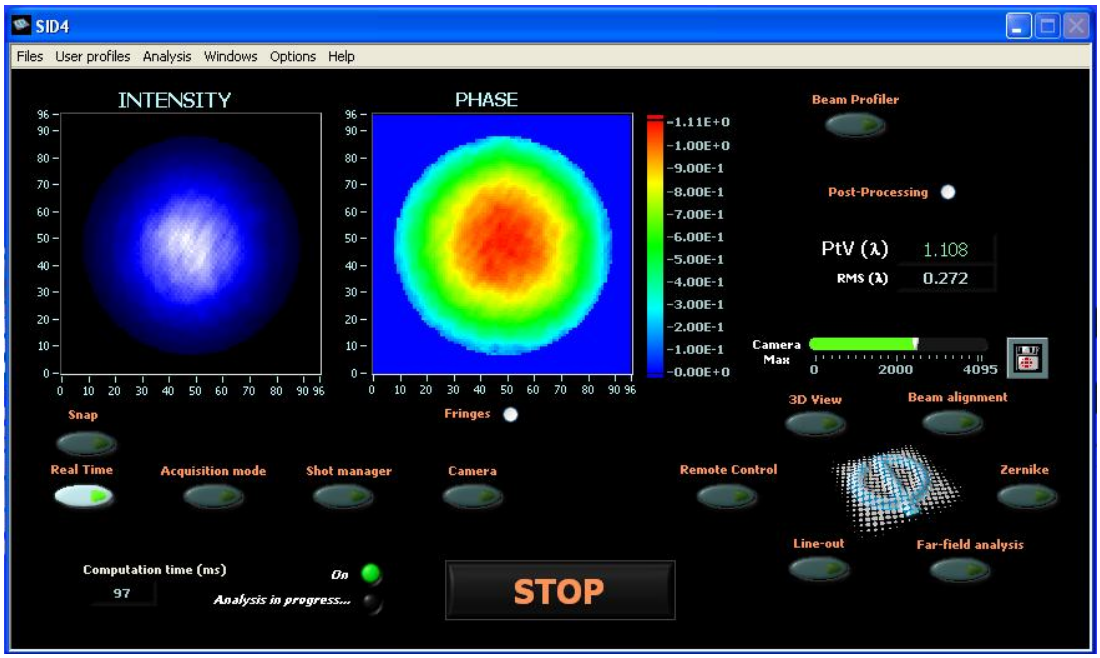

Fig 2. 7: Main window of the SID4 software

2.5.3 Wavefront

The measurements presented in this section were performed after seven hours of laser operation. This ensures that the system is stable enough. Due to the time response of the sensor (see Appendix B) it was not possible to perform a measurement of the transient aberrations (i.e., when the laser system starts to operate until it is completely warmed up). Such a measurement would be very useful in order to determine which aberrations are due to thermal effects.

The first to be presented is the time stability measurement (Fig 2. 8): the wavefront was recorded each 30 seconds during a period of 90 minutes. The pupil was fixed to 6.4 mm and all the data are given in RMS mode and λ units.

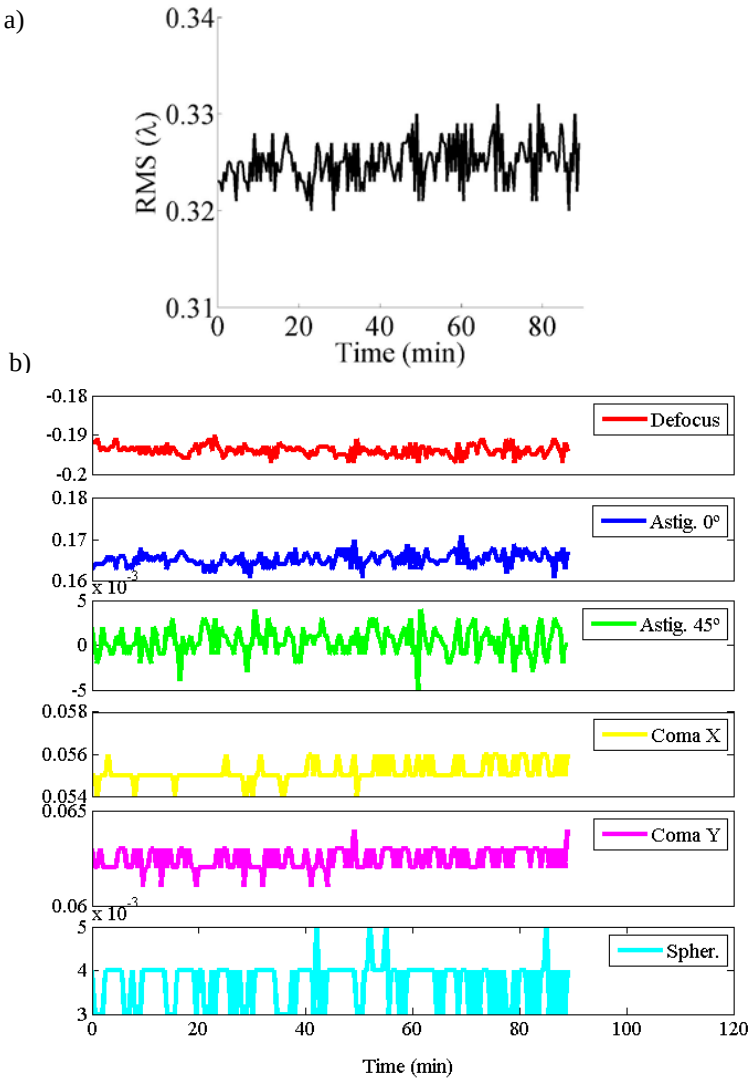

Fig 2. 8: Time stability of a) global RMS and b) low order aberrations. The values are given in RMS mode and λ units.

The average value (Fig 2. 9) of the RMS was 0.323λ with a standard deviation of 0.002λ, which is compatible with the laser shot-to-shot fluctuations. The main contributions come from low order aberrations. In particular, defocus, (-0.193±0.001)λ, and astigmatism at 0º, (0.165±0.001)λ play a major role. The third dominant term is trefoil at 30º, (-0.102±0.001)λ.

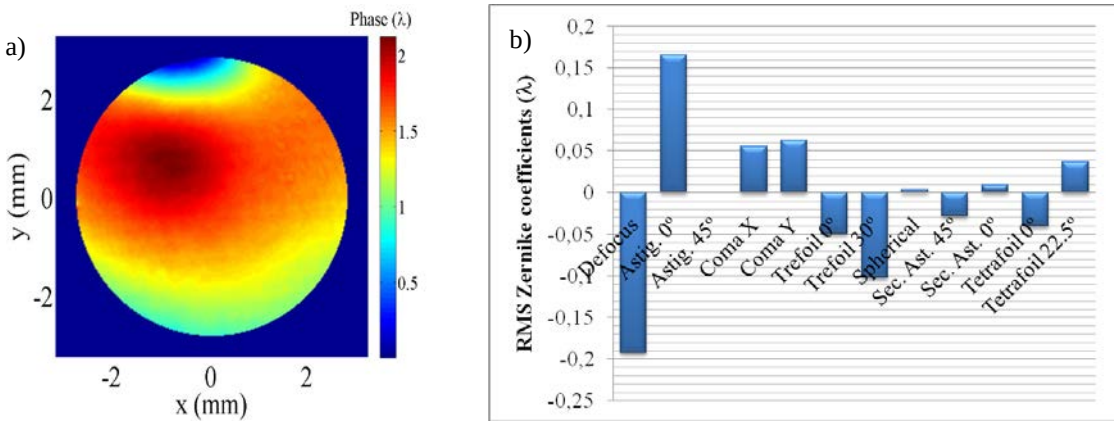

Fig 2. 9: a) Wavefront registered by the sensor. The result was averaged over 180 measurements. The color bar indicates the PtV in λ units. b) Phase decomposition in Zernike polynomials.

A measurement before the amplification stages was also performed. To this end, a beam sample was taken at the output of the stretcher (Fig 2. 10). At this level, the beam is smaller and presents an elliptical shape. For this reason, the analysis mask (pupil) was adapted in size and shape: we chose an elliptical mask (1.231 mm x1.908 mm) for the wavefront retrieval. For the decomposition in Zernike polynomials, the program applies the weighted average of the ellipse axis for the pupil size which in this case was 1.354 mm. The main contributions come from low order aberrations, in particular defocus (0.010±0.001)λ, astigmatism 0º, (0.016±0.001)λ, and astigmatism 45º, (-0.016±0.001)λ.

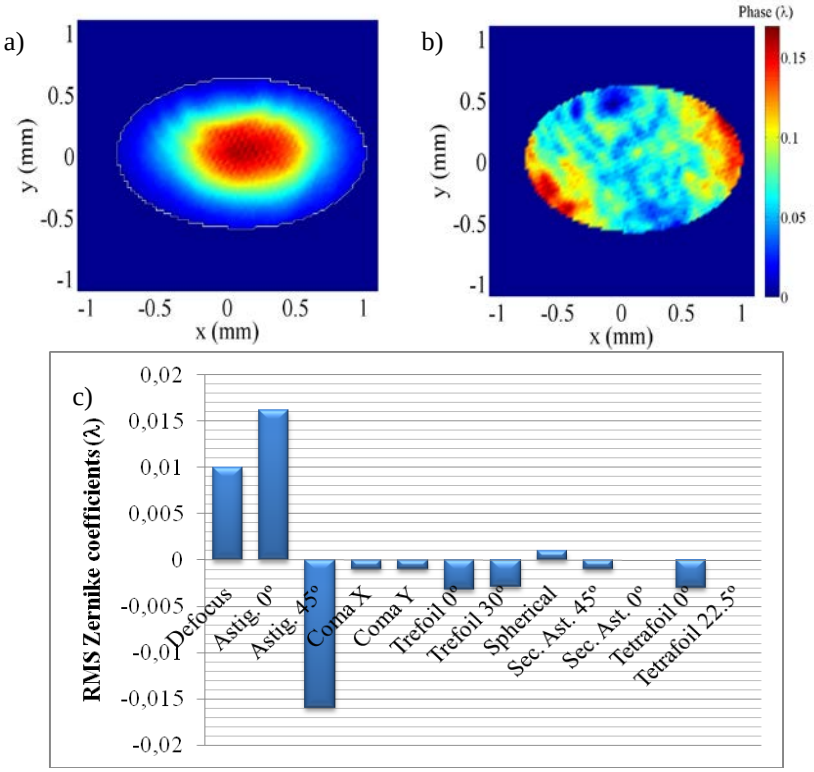

Fig 2. 10: Characterization of the output beam from the stretcher: a) Beam profile, b) wavefront and c) phase decomposition in Zernike polynomials.

Although it is not possible to make a quantitative comparison (we would need the same pupil), we can still make a qualitative one between the unamplified stretched beam and the compressed pulses. We first observe that the defocus is of opposite sign, which indicates that after the amplification stage the defocus is not inherited from the stretcher, which might be due to thermal lensing. The focal length of a thermal lens is given by:

$$f = \left(\frac{1}{2\kappa A} \frac{\partial n}{\partial T} P_{heat} \right)^{-1} \tag{13}$$

where P_{heat} is the dissipated power, A is the pumped area, κ is the thermal conductivity, n the refractive index and T the temperature.

We should remark that this equation is valid for uniform pump intensities and purely radial heat flow. For a non-homogeneous distribution of the dissipated power, the thermal lens will generally exhibit aberrations [158]. The focal length is usually negative and this negative lens causes beam divergence, which is consistent with the negative defocus term of the amplified compressed pulses.

In contrast, the astigmatism 0º shows the same trend in both cases, which suggests that it could be introduced by the system optics.

2.5.4 Beam profile

The beam profile was registered with a CCD (WinCam, DataRay) and is shown in Fig 2. 11. The data in the picture must be multiplied by 1.6, the taper factor used to take the shot.

The laser presents a fairly good Gaussian profile with an ellipticity 0.9. The beam diameter os 5.72 mm at FWHM and 8.58 mm at $1/e^2$, which conforms to the specifications of the manufacturer.

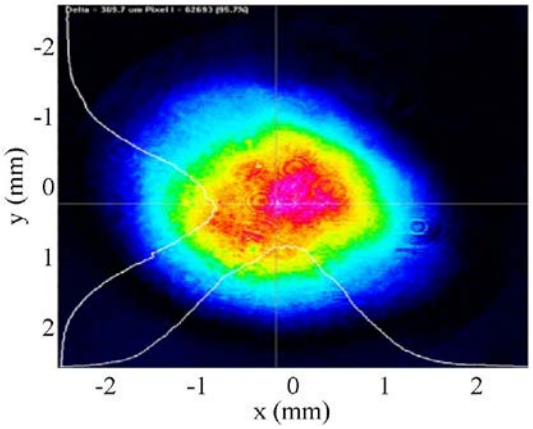

Fig 2. 11: CCD image of the beam profile

2.6. Applications

Apart from the experiments that will be extensively reviewed in this thesis, there is another set of experiments where wavefront characterization has played a major role. In this section we will describe some of the most important applications of wavefront sensing that have supported other experiments conducted in our laboratory following different research lines.

2.6.1 Characterization of a gas jet for laser acceleration in the λ^3 regime

Laser acceleration is currently one of the most promising schemes for particle acceleration [20, 22]. In a few years, ultraintense lasers are expected to be able to generate electrons at similar energies to those achieved with the existing linear accelerators.

The study of *laser acceleration in the λ^3 regime*, which refers to the limit where the pulse is shortened as much as possible and focused near the diffraction limit, is particularly interesting. This regime makes it possible to reach intensities above the electron bound energy. Once the electrons have been released from their parent ions, they are accelerated in the laser electric field. In this sense, one of the most common targets for electron generation and acceleration is a gas jet.

That the laser characterization is not enough for this kind of experiments is obvious; nevertheless it is also mandatory to adequately characterize the target. Among other possibilities, wavefront sensing is a suitable tool for the characterization of the gas jet [100].

In this project, the dynamics of the gas jet used for electron acceleration has been studied by means of interferometry and wavefront sensing. This makes it possible to correlate the gas jet to the electron generation as a function of different parameters (e.g., piston position, gas density). Here we strictly provide a brief summary of the measurements performed by means of the WFS; nevertheless the complete study can be found in F. Valle's MSc thesis [159].

In order to achieve a good stability level and reduce the noise and fluctuations as much as possible, a HeNe laser was used. The beam was expanded by means of an x10 telescope and directed onto the gas jet (nitrogen). The modification of the refractive index due to the presence of the gas results in a change of the wavefront. This change was analysed with our commercial sensor (SID4-HR, Phasics).

The gas jet was characterized according to different pressures. For pressures above 4 bar (Fig 2. 12) a sequence of high density knots was observed. These "knots" are known as *shock diamonds* or Mach disks and are caused by the formation of standing waves when a supersonic gas jet propagates in the atmosphere.

Finally, the focusing of the pulses (120 fs, 2.4 mJ) with a 10x microscope objective (theoretically this would yield a focal spot of 1 μm) could results in a peak intensity of $6x10^{17}$ W/cm^2 for electron acceleration. To this end, the pressure was set to 6 bar (the ionization potential of the nitrogen is in the order of 10^{16} W/cm^2). With this setup, 50 keV electrons were generated.

Moreover, the number of counts registered by a Geiger counter was studied as a function of the gas pressure. A saturation regime, which could be explained by means of the gas characterization in terms of shock diamonds, was found for high pressures. As the pressure increases, the shock diamonds are displaced. In spite of the fact that the gas density increases with pressure, the shock diamond moves away from the focal point. For this reason, the beam goes through an area with a similar gas density to that present at lower pressures, and the number of ejected electrons does not change.

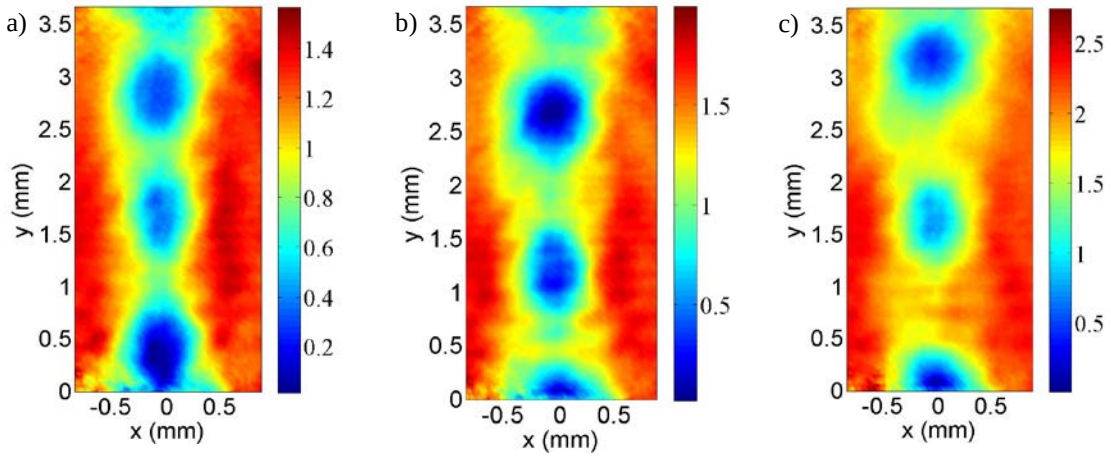

Fig 2. 12: Phase acquired by a HeNe laser as it propagates through the gas jet at different pressures: a) 4 bar, b) 5 bar and c) 6 bar. The reference for the y axis is the exit of the piston. The scale of color bar is given in radians.

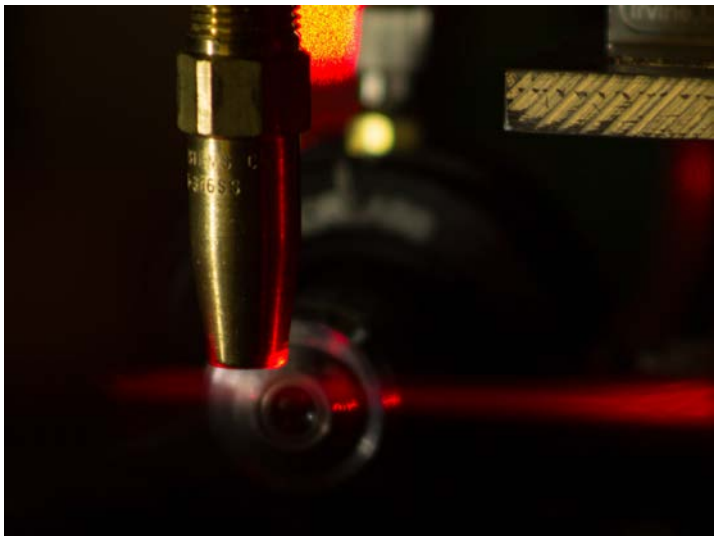

Fig 2. 13: The beam from a HeNe laser goes through the gas jet provided by a nozzle. The aperture of the piston is 890 μm.

2.6.2 Electron acceleration and X ray emission in plasmas

When a short (~100 fs) intense (>10^{16} W/cm^2) laser pulse interacts with an overdense plasma, the energy of the pulse can be coupled to generate plasma waves which can in turn generate longitudinal fields to accelerate electrons from the plasma [160]. On their way out, these hot electrons can generate X rays by bremsstrahlung or K_α emission.

In this project our group conducts experimental research into the production of electron and X rays in the λ^3 regime by focusing short pulses with modest energy (E~0.8 mJ) onto solid targets [161]. When the pulses are focused close to the diffraction limit (i.e., a focal spot of approximately 2 μm), large intensities (>5x10^{16} W/cm^2) are achieved.

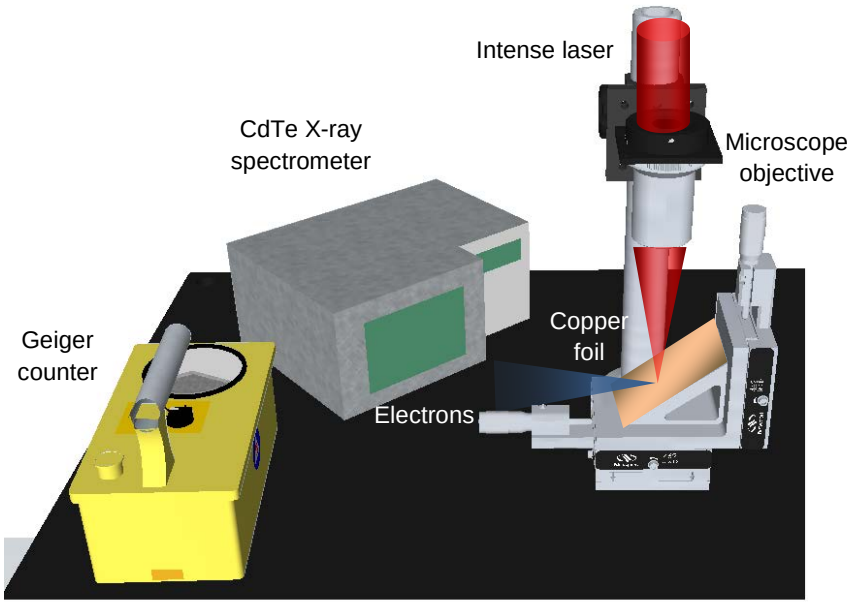

Fig 2. 14: Setup for electron generation at kHz repetition rates: the laser pulses are focused with a microscope objective onto a solid target (aluminum). A Geiger counter registers the radiation.

The experimental setup is depicted in Fig 2. 14: the pulses are incident at a 45º angle with respect to the target (copper, aluminium or lead foils). In this interaction the laser induces a plasma wave by means of the resonance absorption mechanism so that hot electrons (13 keV) that eventually generate X rays are emitted. A Geiger-Müller counter makes it possible to register the amount of generated electrons, which is used to optimize the focusing. Finally, an X ray CdTe spectrometer measures the spectra of the X rays produced by bremsstrahlung.

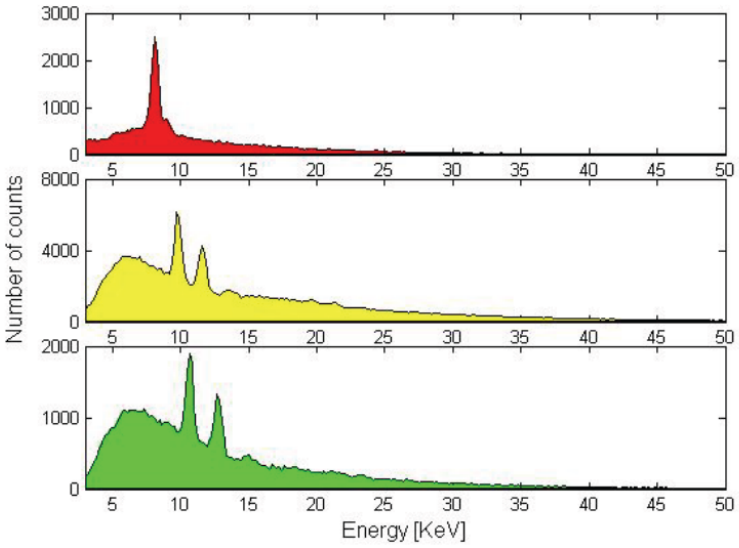

Fig 2. 15: X ray spectra which show the bremsstrahlung and Kα peaks for different materials: copper (red), aluminium (yellow) and lead (green).

Since the experiment is conducted in air, nonlinear effects will take place as the pulse approaches the focal region and increases its intensity. At some point, the intensity will become high enough to ionize the air and generate a plasma, the pulse being thus distorted in space and time. Furthermore, it is well known that plasmas absorb radiation and, therefore, we could expect a decrease in peak intensity.

The capability of predicting such behavior is crucial for acceleration experiments, since it will allow us to correlate the laser pulses with the generated X ray spectra. To this end, our group has developed a propagation code BALAS [162], which provides the pulse at the target.

Pulse characterization plays an important role in this experiment. On the one hand, a complete spatial and temporal characterization is required in order to consider the experimental phase and amplitude as inputs for the simulation. On the other hand, by implementing an optical system with a magnification factor (*Fig 2. 6*,) it is possible to image the focal spot, which is crucial to validate the propagation code. Due to the short focal length of the microscope objective, f_m, a different setup has to be used in each case. In the first one, we set up a 4f telescope with $f_1=f_2>2f_m$. In this way, the first lens is far enough from the focus, thus avoiding damage. Moreover, the beam is collimated at the output of the first lens ensuring that the beam does not clip at the second lens. In the second case, we need $f_1>f_m$ to obtain a near-collimated beam after the first lens and avoid beam clipping. The second lens will determine the magnification factor, f_2/f_1.

In particular the setup (Fig 2. 14) uses a 20 mm focal length microscope objective (Edmund Optics). For the beam characterization we first measured the spatial phase and intensity at the microscope input plane, obtaining similar results to those presented in Fig 2. 9. Additionally, a 4f imaging system ($f_1=f_2=45$ mm) was mounted to measure the wavefront at the objective output plane in order to check the microscope aberrations (Fig 2. 16a). To this end, we first measured the phase distortions introduced by the imaging system and subtracted them to obtain the change in the wavefront produced by the microscope. The PtV wavefront aberration resulted to be 120λ measured over a 3.56 mm pupil.

In order to check the results predicted by the simulation, a telescope with a magnification power of 10 ($f_1=30$ mm and $f_2=300$ mm) was used to track the beam profile in the vicinity of the focus of the microscope (Fig 2. 16b).

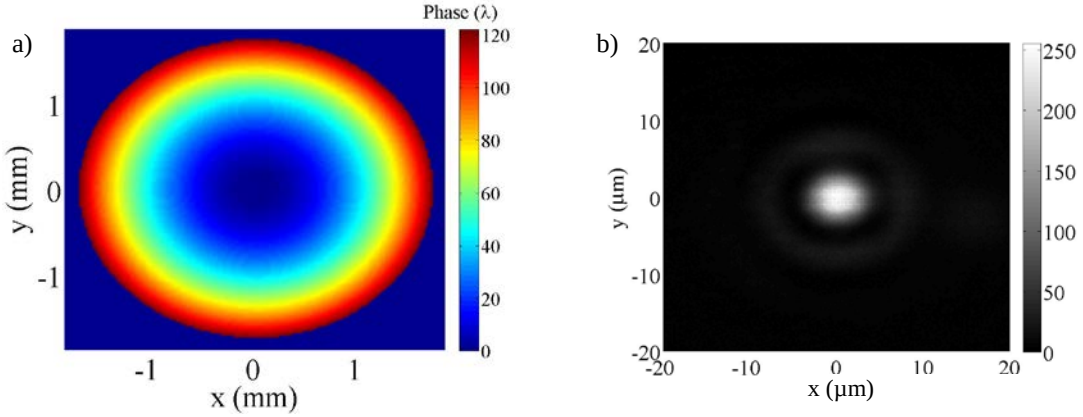

Fig 2. 16: a) Wavefront registered at the microscope output plane. A 4f telescope was used to this end (see details in the text). b) Image of the beam at the focal plane of the microscope: the spot is close to the diffraction limit (6 μm diameter).

The simulation code [162] solves either time-dependent Schrödinger equation, TDSE, to track the evolution of an electronic wave function under a strong field or the nonlinear Schrödinger equation, NLSE, to simulate the nonlinear propagation of a short pulse, using the Crank Nicholson and the split operator methods. The code assumes cylindrical symmetry and uses a base of plane waves and Bessel functions. To this end, Bessel and Fourier transforms are used to decompose the pulse in the function's base. The program calculates the moment distribution in the TDSE context, and the generalized spectrum (frequency, wave-vectors for each frequency) in the context of the nonlinear propagation.

According to the results of the simulation, the pulse presents the so called *X wave* structure in the spectral domain. X waves are responsible for the pulse splitting that is observed in the temporal domain. During pulse splitting, the pulse develops short spikes (~25 fs), which are responsible for high intensities at the focus, compensating in this way the absorption by the plasma.

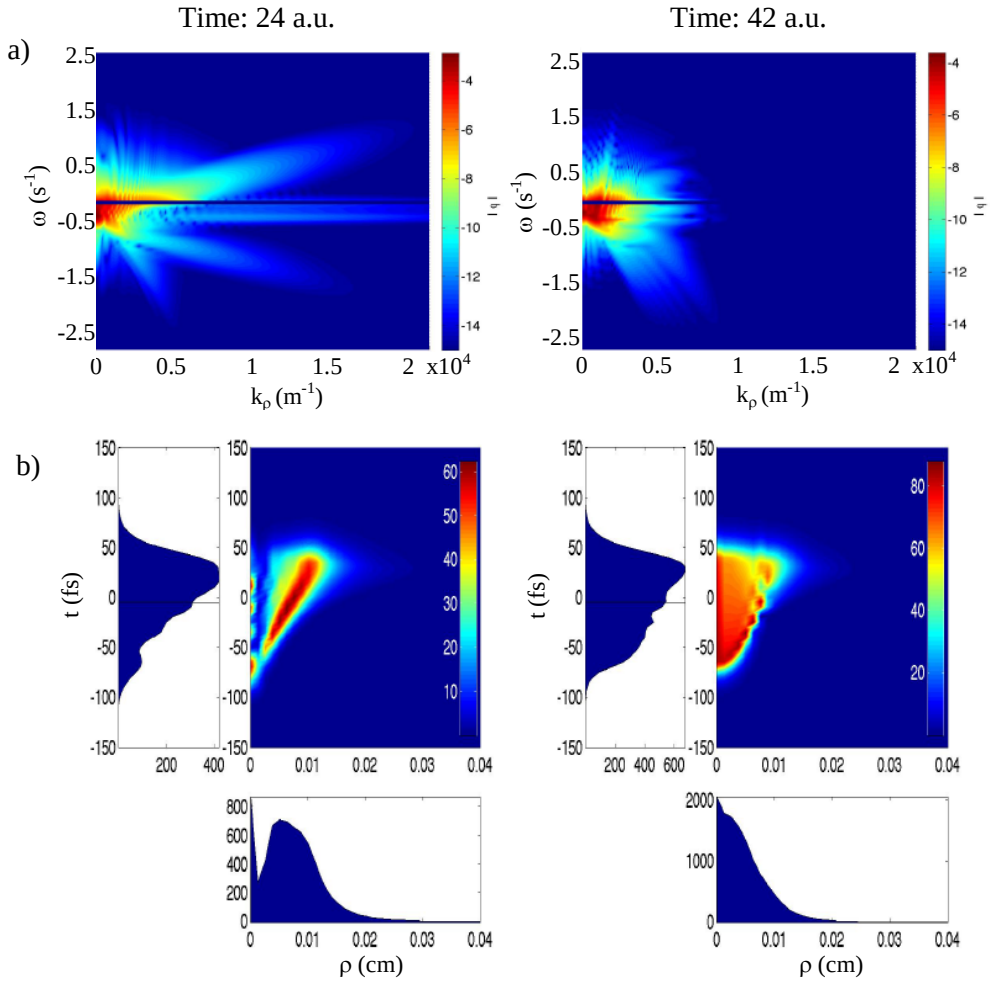

Fig 2. 17: Results provided by the simulation code at two propagation distances: a) pulse in the spectral domain and b) corresponding spatiotemporal structure.

2.6.3 Characterization of a gas jet for HHG

High-harmonic generation (HHG) is a phenomenon by which very high harmonics of an intense input laser beam are generated [64]. It is usually achieved by focusing very intense pulses in gases, in such a way that strong nonlinear interactions can lead to an extreme form of nonlinear frequency conversion [66].

The same procedure described in the previous case was used for the characterization of a gas jet for HHG. The main difference with respect to the previously mentioned experiment is that in this case the system is installed within a vacuum chamber (<10 mbar). Therefore, the jet dynamics are expected to be different.

The vacuum chamber imposes an additional condition on the experimental setup for wavefront sensing: since diffraction would affect the beam as it propagates and it is not possible to place the sensor near the gas jet, an imaging system is required (*Fig 2. 6*). We took advantage of the system to introduce a magnification factor of 2 (f_1=500 mm, f_2=1000 mm) that would allow us to perform a more accurate measurement.

The valve had a diameter of 500 µm and the gas employed for the experiment was argon. In Fig 2. 18 we show the average of 100 measurements for a gas pressure of 7.5 bar.

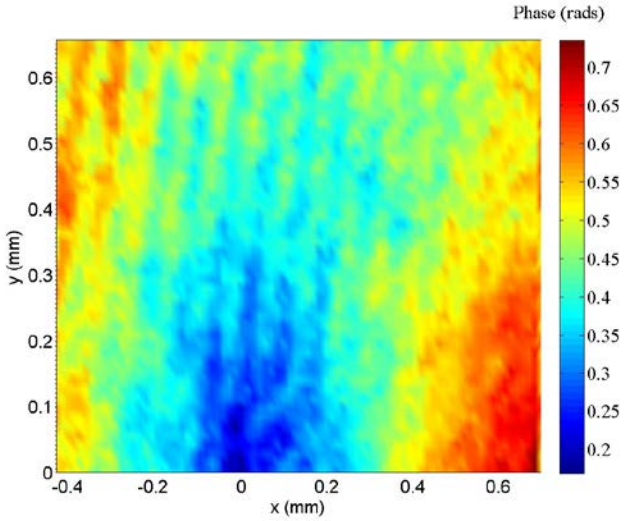

Fig 2. 18: Wavefront measurement of a HeNe laser propagating through a gas jet (argon, 7.5 bar) in a vacuum chamber. The piston is placed at y=0 and therefore the gas expands from bottom to top (the bluer the phase is, the denser the gas)

2.6.4 Filamentation enhancement

As we shall see in Chapter 3, *filamentation* [82] is a light self-guiding process that is achieved through the balance between self-focusing by Kerr effect and ionization defocusing, and allows for pulse shortening for different applications. The main drawback of this technique is the existence of an upper energy limit: above a certain energy threshold, the single filament regime becomes unstable and multiple filaments appear. The development of new strategies to overcome this limit [97, 98] is of great interest in the field.

In this study we have shown an enhancement of filamentation post-compression by focusing with an astigmatic lens [163]. The experimental setup (Fig 2. 19) does not differ from that of traditional filamentation schemes, except for the fact that we employed an astigmatic lens as the

focusing element. Two different astigmatic lenses were used: the first one (labeled Astig1) had focal lengths of 0.8 and 1.0 m, whereas the second one (Astig2) had focal lengths of 1.0 and 1.33 m. A third spherical lens (Spher), f= 1.0 m, was used for comparison purposes. The lenses focused the pulses (16 nm FWHM) into a nitrogen gas cell at a pressure of 2100 mbar. The diameter of the input iris was fixed at 5.6 mm diameter, whereas the output iris allowed for the selection of the inner core.

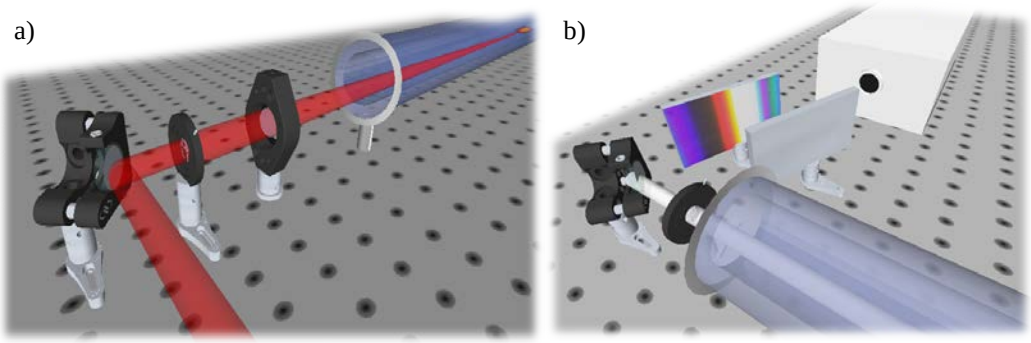

Fig 2. 19: Experimental setup for filamentation with astigmatic focusing: a) Input: the beam is focused with an astigmatic or a spherical lens in a gas cell. An iris is used to control the aperture. b) Output: an iris is used to select the filament which is compressed by means of a grating compressor, and it is then spatially and temporally characterized.

The results obtained from the use of each of the three lenses have been summarized in Table 2. 1. For the spherical lens the input energy had to be considerably reduced to avoid unstable filamentation, as expected according to our proposal for post-compression optimization. Since the astigmatic lenses tolerated higher input energies, the spectral broadening obtained with them was considerably larger than the one obtained for the spherical lens, which allows shorter compressed pulses. Moreover, no residual astigmatic phase or distortion of the filament profile was observed when astigmatic focusing is employed.

Lens	**Input energy (mJ)**	**Output energy (mJ)**	**FWHM (nm)**	**τ (fs)**
Spher	1.37	0.30	198	6.4
Astig1	1.71	0.55	300	4.3
Astig2	1.66	0.68	280	4.4

Table 2. 1: Experimental values obtained for filamentation with different lenses: input and output energies, spectral bandwidth and estimated Fourier transform temporal duration.

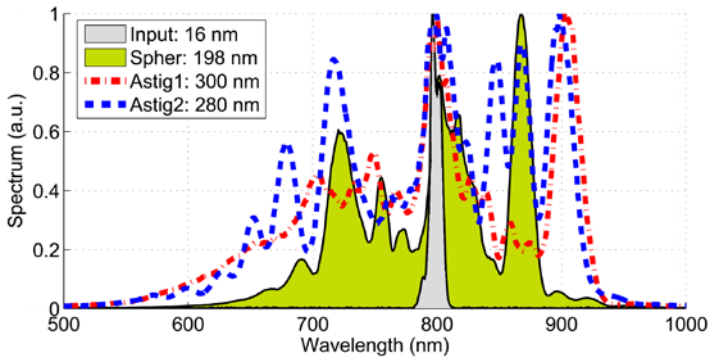

Fig 2. 20: Input and output spectra after filamentation with different lenses.

These results may be explained by the astigmatic beam propagation and the nonlinear nature of the filament. Increased Rayleigh length in astigmatic propagation due to two foci at different distances contributes to the spectral broadening due to SPM induced by Kerr effect during self-guiding. As reported in [164], longer focusing depths also lead to longer plasma channels. Moreover, non-circular beams and non-symmetric focusing [165] increase the critical power for self-focusing. This lengthening in the Rayleigh distance makes it possible to increase increasing the multi-filamentation threshold and therefore it is possible to improve the stability and levels of energy post-compression.

Finally, we analyzed the process under optimal conditions in order to demonstrate that the pulses could be compressed for further applications. In our case, temporal measurements were limited by the range of SPIDER (≥10 fs). We used 100 fs input pulses (10 nm FWHM) focused with the Astig1 lens, and the pressure was increased to 2570 mbar. Positive output spectral phase was compensated with a holographic-grating pair compressor before entering the SPIDER. A broadband spectrum (142 nm FWHM) was produced (see Fig 2. 21). The Fourier transform limit of the spectrum was 10 fs and the experimental pulse duration was 13 fs.

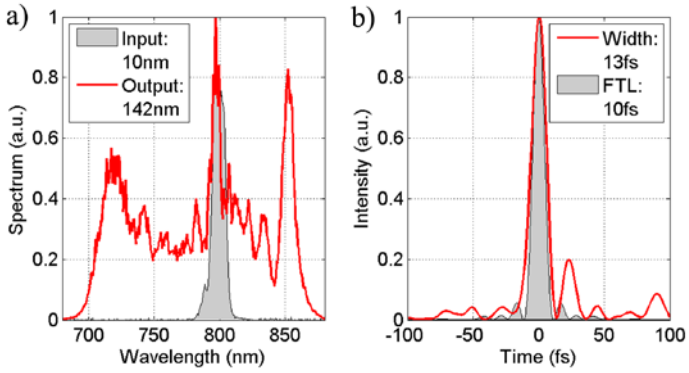

Fig 2. 21: Input and output pulses in a) the spectral domain and b) the temporal domain.

2.7. Summary and conclusions

In this chapter we have briefly reviewed the fundamentals of wavefront sensing and described two of the most commonly used wavefront sensors: Hartmann-Shack and lateral shearing interferometers. Our commercial sensor (SID4-HR, Phasics) is actually based on the latter.

We have provided the complete spatial characterization of our laser. Although the beam profile is fairly good, the wavefront presents an RMS aberration of 0.323λ over a 6.4 mm pupil mainly coming from low order aberrations (defocus and astigmatism). This suggests the need for an adaptive optics system for applications requiring flat wavefronts (e.g. focusing to diffraction limit for electron laser acceleration). It would also be possible to correct the spatial phase by means of diffractive optics (DOEs), since the aberrations have been shown to remain stable over time. However this approach presents two difficulties. On the one hand, the DOE must exhibit a high damage threshold in order to support the high intensity pulses delivered by the laser. On the other hand, beam shaping by a DOE would be at the expense of a loss of energy since the transmission efficiency is typically around 0.8.

We have also reported four experiments involving a wavefront sensor as a diagnostic tool. In a first block, we have revised the characterization of gas jets for electron acceleration and HHG.

Since the gas jet produces a change in the refraction index, a beam going through it will acquire a phase related to the gas density. By measuring these induced wavefront variations, we have been able to study the gas dynamics. This investigation is very helpful to find the suitable position of the piston in order to enhance the HHG/laser acceleration. Moreover, we are currently using a similar setup for determining the electron density in a plasma created by laser [166-168].

In a second block, spatial characterization has been used for numerical simulations. The study had a dual purpose: on the one hand, the wavefront and beam profile were used as inputs for a nonlinear propagation code (BALAS); on the other hand, the study helps to determine the validity of the code by comparing, for example, the results from BALAS with the experimental characterization in the focal plane.

Third, astigmatic lenses have been employed for filamentation post-compression. The particular focusing of astigmatic lenses leads to considerably larger effective Rayleigh lengths than with spherical lenses (around twice). This implies, on the one hand, that nonlinear effects accumulate longer and, on the other, an increase of the input energy without reaching the multi-filamentation regime. As a result, a particular broader spectrum compatible with shorter pulses is obtained. In particular, we have demonstrated post-compression from 100 fs, 10 nm, 3 mJ input pulses to 13 fs, 142 nm, near 1 mJ pulses. This technique is simple and does not require any non-conventional optical elements. Therefore, it is a suitable approach to enhance the shortening of the output pulse duration.

3 Basic concepts of nonlinear optics

3.1. Introduction

As defined by Boyd in [169], "*nonlinear optics is the study of phenomena that occur as a consequence of the modification of the optical properties of a material system by the presence of light*". Contrary to conventional (i.e., linear) optics, these effects depend in a nonlinear manner on the intensity of the incident light.

When subjected to very intense laser irradiation, any medium can, in principle, exhibit a nonlinear optical response. However, as we shall see later, there are materials that possess certain characteristics that make them adequate for the generation of nonlinear effects, even with moderate intensities.

The aim of this chapter is to provide a framework common to all the nonlinear processes that will be addressed in this thesis. These have been divided them into two main blocks, according to the main processes that will be studied throughout this thesis.

Section 3.2 is devoted to a brief description of the most important nonlinear optical parametric processes such as second-harmonic generation, sum frequency, optical parametric amplification… In contrast, in section 3.3 we will review some non-parametric processes involved in the supercontinuum generation.

3.2. Frequency mixing processes

If we concentrate on a very simple microscopic model of the atom, we will perceive an interaction between the electric field and the electrons in the medium via the Lorentz force. On the one hand, it tends to displace the electron from the atom by a quantity x. On the other hand, the Coulomb potential acts against this displacement by a quantity qx, q representing the charge of the electron.

The term qx is known as the dipole moment, and the dipole moment per unit volume is known as the polarization density P(t). Since the electric field of the light oscillates in time, so too will the dipole moment. The polarization density thus represents an ensemble of oscillating dipoles. In this section we show that this acts as a source of radiation, generating new fields with different phases and frequencies from those of the driving field.

The general expression for polarization is as follows:

$$P(t) = \int \varepsilon_0 \chi(t') E(t - t') dt' \tag{14}$$

where ε_0 is the permittivity of free space and χ is the susceptibility.

Assuming a dispersionless and lossless medium and an intensity of the incident radiation low enough for the displacement of the electrons to be small, Eq. (14) can be rewritten as:

$$P(t) = \varepsilon_0 \chi E(t) \tag{15}$$

In this case, induced polarization depends linearly on the electric field as and χ is a constant known as linear susceptibility.

When dealing with intense light sources (i.e. in nonlinear optics regime), the atomic potential can no longer be approached as a quadratic function, making it necessary to include higher-order terms. In such cases, the optical response can often be described by expressing the polarization P(t) as a power series expansion of the electric field E(t) under a perturbation treatment. This means that the electric force due to the laser field is small compared to the bonding atomic force or, in other words, that such expansion loses its validity in the case of extreme laser fields and therefore requires an exact treatment.

$$P(t) = \varepsilon_0 \left[\chi^{(1)} E(t) + \chi^{(2)} E^2(t) + \chi^{(3)} E^3(t) + ... \right] \tag{16}$$

The quantities $\chi^{(2)}$ and $\chi^{(3)}$ are known as second and third-order nonlinear optical susceptibilities.

It must be noticed that this equation has been written for simplicity for monochromatic scalar fields, E(t) and P(t). In the most general case, both E and P present time and space variations and are described by vectors. Therefore, $\chi^{(1)}$, $\chi^{(2)}$ and $\chi^{(3)}$ are no longer scalars, but second, third and fourth-rank tensors [169]. Additionally, Eq. (16) is valid under the assumption of a lossless and dispersionless medium, since it implies an instantaneous response to the electric field. In a real medium, these conditions are not satisfied, so there will be phase differences between E(t) and P(t) and the susceptibilities will depend on the frequency.

The relationship between the electric field and polarization is established through the wave equation, which is derived from Maxwell's equations. In the next chapter we will derive the coupled wave equations for the particular case of the second-harmonic generation. For the moment, we can establish that for a nonlinear medium the wave equation often takes the form of:

$$\nabla^2 E - \frac{n^2}{c^2} \frac{\partial^2 E}{\partial t^2} = \frac{1}{\varepsilon_0 c^2} \frac{\partial^2 P^{NL}}{\partial t^2} \tag{17}$$

where n is the refractive index, c is the speed of light in vacuum and P^{NL} refers to nonlinear polarization:

$$P^{NL}(t) = \varepsilon_0 \left[\chi^{(2)} E^2(t) + \chi^{(3)} E^3(t) + ... \right] \tag{18}$$

Therefore it is clear that a time-varying nonlinear polarization can generate new components of the electric field oscillating at different frequencies.

However, second-order nonlinear interactions only occur in non-centrosymmetric media, i.e., media without inversion symmetry. Liquids, gases and amorphous solids present, macroscopically, inversion symmetry, the second-order susceptibility in this kind of media being zero. As a result, these materials cannot produce second-order optical nonlinearities. By contrast, certain crystals [170], such as Beta Barium Borate (BBO), Lithium Triborate (LBO) or Potassium Titanyl Phosphate (KTP), exhibit large second-order susceptibility and can efficiently generate these processes.

On the other hand, the third-order nonlinear interactions, i.e., those described by $\chi^{(3)}$, can occur in both centrosymmetric and non-centrosymmetric media.

In the following subsections we will focus on dispersionless media with second-order nonlinear susceptibility, proving that this term gives rise to the simplest nonlinear optical phenomena, which will be described in detail

3.2.1 Second-harmonic generation

Second-harmonic generation (SHG) refers to the nonlinear optical interaction where the incident light is frequency doubled [171].

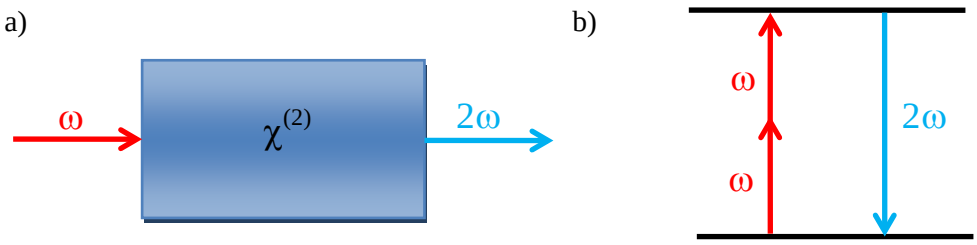

Fig 3. 1: a) Scheme of second-harmonic generation. b) Energy level diagram.

Considering monochromatic waves and disregarding the spatial dependence, it is possible to express the electric field as:

$$E(t) = Ae^{-i\omega t} + c.c \tag{19}$$

where c.c is the complex conjugate. Let us now substitute this expression in Eq.(16) and set $\chi^{(3)}$=0:

$$P(t) = \left[\varepsilon_0 \chi^{(1)} Ae^{-i\omega t} + c.c \right] + 2\varepsilon_0 \chi^{(2)} AA^* + \left(\varepsilon_0 \chi^{(2)} A^2 e^{-2i\omega t} + c.c \right) \tag{20}$$

The first term corresponds to linear interaction, while the second and third correspond to second-order nonlinearity. We can see that this term contains a zero frequency component

($2\varepsilon_0\chi^{(2)}AA^*$), called optical rectification, and a contribution oscillating at 2ω ($\varepsilon_0\chi^{(2)}A^2e^{-2i\omega t}$). According to Eq. (17), this latter term can lead to the generation of radiation at the second-harmonic frequency.

This process can be explained in terms of photons absorption and emission, as it is shown in Fig 3. 1.: two photons of energy hω are absorbed by the medium to be re-emitted as one photon of energy 2hω.

3.2.2 Sum frequency generation

Let us now consider an electric field containing two frequency components, ω_1 and ω_2:

$$E(t) = A_1 e^{-i\omega_1 t} + A_2 e^{-i\omega_2 t} + c.c \tag{21}$$

For simplicity, we will use the expression in Eq.(18) instead of the one in Eq. (16) (i.e., we are not taking the linear part into account):

$$P^{NL}(t) = 2\varepsilon_0\chi^{(2)}\left(A_1A_1^* + A_2A_2^*\right) + \varepsilon_0\chi^{(2)}\left(A_1^2e^{-2i\omega_1 t} + A_2^2e^{-2i\omega_2 t} + 2A_1A_2e^{-i(\omega_1+\omega_2)t} + 2A_1A_2^*e^{-i(\omega_1-\omega_2)t}c.c\right) \tag{22}$$

For convenience, we will split polarization into $P(\omega_n)$ components, each oscillating at the same frequency ω_n:

$$P^{NL}(t) = \sum_n P(\omega_n)e^{-i\omega_n t} \tag{23}$$

where the summation extends over positive and negative frequencies.

If we compare expressions (22) and (18) we can identify the complex amplitudes of various frequency components of nonlinear polarization, each of which has an equivalent expression at the corresponding negative frequency. The latter will not be taken into account, since they are simply the complex conjugates of the expressions given below.

$$\begin{aligned}
&P(2\omega_1) = \varepsilon_0\chi^{(2)}A_1^2 && (SHG\ at\ \omega_1)\\
&P(2\omega_2) = \varepsilon_0\chi^{(2)}A_2^2 && (SHG\ at\ \omega_2)\\
&P(\omega_1+\omega_2) = 2\varepsilon_0\chi^{(2)}A_1A_2 && (SFG)\\
&P(\omega_1-\omega_2) = 2\varepsilon_0\chi^{(2)}A_1A_2^* && (DFG)\\
&P(0) = 2\varepsilon_0\chi^{(2)}(A_1A_1^* + A_2A_2^*) && (OR)
\end{aligned} \tag{24}$$

In Eq. (24) SFG stands for sum-frequency generation, DFG for difference-frequency generation and OR for optical rectification. Although all these processes appear in the equation above, in practice only one of these frequency components will be efficiently generated simultaneously, due to phase-matching conditions.

In terms of photon exchange, SFG can be interpreted in a similar way to the SHG visualization that appears in the previous section. Indeed, SHG can be considered to be a particular case of SFG

where the frequencies of the input fields are the same. The energy level scheme for SFG is given in the figure below.

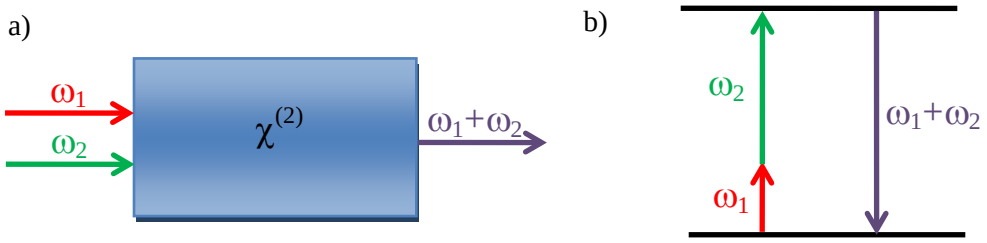

Fig 3. 2: a) Scheme of sum-frequency generation. b) Energy level diagram.

SFG has been widely applied to produce tunable radiation in the ultraviolet region and for cross correlation temporal measurements.

3.2.3 Optical parametric amplification

In the process of DFG the frequency of the generated wave is the difference of those of the applied fields. The description in terms of photons exchange is presented in Fig 3. 3. From it, we can see that a photon at ω_1 is destroyed by interacting with the medium and a photon at ω_2. This creates a new photon ω_1-ω_2, but also, by energy conservation, another at ω_2. Thus, the electric field at the lower frequency is amplified by the process of DFG. For this reason, the DFG is also known as optical parametric amplification (OPA). In an OPA, the fields at ω_1, ω_2 and ω_1-ω_2 are usually termed as pump, signal and idler, respectively. Nowadays, OPA's are commonly used to achieve tunable laser sources [46].

Additionally, if the crystal is placed inside a resonator the ω_2 and/or ω_1-ω_2 fields can build up to large values. Such a device is known as optical parametric oscillator (OPO).

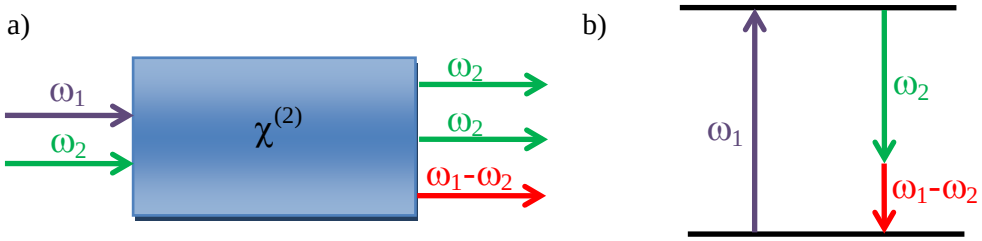

Fig 3. 3: a) Scheme of optical parametric amplification (or difference frequency generation). b) Energy level diagram.

Although a photon at ω_1 is absorbed and the photon at ω_2 stimulates the two-photon emission, the process can occur even if the photon at ω_2 is not present, but in that case the generated field will be much weaker, since it is created by spontaneous emission. This process is known as parametric fluorescence.

3.2.4 Third-order interactions

Let us now consider the contribution of the third-order nonlinear susceptibility to the polarization:

$$P^{NL}(t) = \varepsilon_0 \chi^{(3)} E(t)^3 \tag{25}$$

In the general case where the electric field consists of three different frequencies

$$E(t) = A_1 e^{-i\omega_1 t} + A_2 e^{-i\omega_2 t} + A_3 e^{-i\omega_3 t} + c.c \tag{26}$$

the resulting expression contains 44 different frequency components (considering negative and positive frequencies to be distinct).

Upon splitting the polarization in a power series of the frequency components as in (23), we find that:

$$P(\omega_i) = \varepsilon_0 \chi^{(3)} \left(3E_i E_i^* + 6E_j E_j^* + 6E_k E_k^*\right) E_i \qquad (i \neq j \neq k) \tag{27}$$

$$P(3\omega_i) = \varepsilon_0 \chi^{(3)} E_i^3 \tag{28}$$

$$P(\omega_i + \omega_j + \omega_k) = 6\varepsilon_0 \chi^{(3)} E_i E_j E_k \qquad (i = j \neq k) \tag{29}$$

$$P(\omega_i + \omega_j - \omega_k) = 6\varepsilon_0 \chi^{(3)} E_i E_j E_k^* \qquad (i = j \neq k) \, or \, (i \neq j \neq k) \tag{30}$$

where i, j and k take integer values from 1 to 3.

The energy level diagrams corresponding to the polarization terms given by Eq. (29) and (30) are depicted in Fig 3. 4.

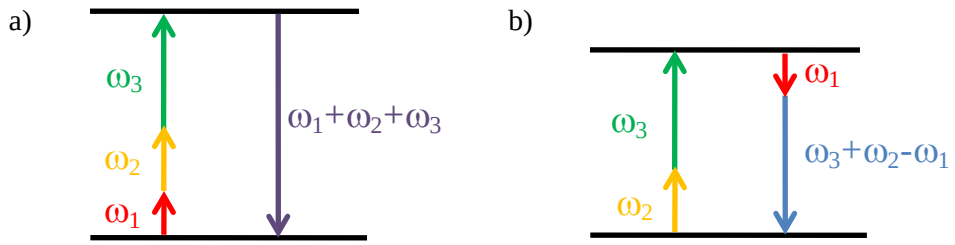

Fig 3. 4: Energy level diagrams for the third-order nonlinear interactions corresponding to a) Eq. (29) and b) Eq. (30)

To clarify the physical meaning of the processes described by Eqs. (27)-(30), let us consider the case where the applied field is a monochromatic wave given by Eq. (19). By substituting it in Eq. (25) and taking into account the identity $\cos^3(\omega t) = \frac{1}{4}\cos(3\omega t) + \frac{3}{4}\cos(\omega t)$ we deduce that:

$$P^{NL}(t) = \frac{1}{4}\varepsilon_0 \chi^{(3)} A^3 \cos(3\omega t) + \frac{3}{4}\varepsilon_0 \chi^{(3)} A^3 \cos(\omega t) \tag{31}$$

The first term of Eq. (31) describes a response at a frequency of 3ω, which is why it is called third-harmonic generation (THG). In the energy level diagram (Fig 3. 5,) three photons at frequency ω are absorbed to be re-emitted as a photon at a frequency of 3ω.

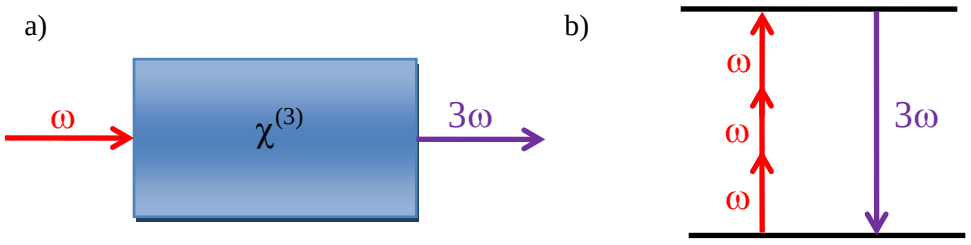

Fig 3. 5: a) Scheme of THG in a nonlinear medium with third-order susceptibility. b) Energy level diagram.

The second term of Eq.(31) corresponds to a two-photon absorption (2PA) process [172]. It results in an intensity dependent contribution to the polarization of the fundamental field:

$$P^{NL}(\omega) = 3\varepsilon_0 \chi^{(3)}(\omega + \omega - \omega)\left|E(\omega)\right|^2 E(\omega) \tag{32}$$

We now recall the expression of the polarization in a linear medium:

$$P(t) = \varepsilon_0 \chi^{(1)} E(t) \tag{33}$$

and the definition of the refractive index:

$$n_0 = \sqrt{1+\chi^{(1)}} \tag{34}$$

If Eq.(32) and (33) are compared, it is clear that the nonlinear contribution to the polarization at ω leads to an intensity dependent refractive index. We hence introduce an effective susceptibility χ_{eff}:

$$\chi_{eff} = \chi^{(1)} + 3\chi^{(3)}\left|E(\omega)\right|^2 \tag{35}$$

The refractive index will be now given by:

$$n = \sqrt{1+\chi_{eff}} \tag{36}$$

Assuming that the nonlinear terms in (35) are small compared to the linear terms ($\chi^{(3)} << \chi^{(1)}$), we use the binomial expansion in (36):

$$n \simeq \sqrt{1+\chi^{(1)}} + \frac{3\chi^{(3)}}{2\sqrt{1+\chi^{(1)}}}\left|E(\omega)\right|^2 \tag{37}$$

Since the intensity of the incident wave is given by

$$I = 2n_0\varepsilon_0 c\left|E(\omega)\right|^2 \tag{38}$$

we can rewrite Eq.(37) as

$$n = n_0 + n_2 I \tag{39}$$

where n_0 is the usual linear index of refraction and n_2 is known as Kerr nonlinear index:

$$n_2 = \frac{3\chi^{(3)}}{4n_0^2\varepsilon_0 c} \tag{40}$$

As in the linear case, the real and imaginary parts of n_2 are associated with the nonlinear refraction (NLR) and nonlinear absorption (NLA). The propagation of the electromagnetic field will be now governed by the following irradiance, I, and phase, ϕ equations:

$$\frac{dI}{dz} = -\mathrm{Im}(n_0)I - \mathrm{Im}(n_2)I^2 \tag{41}$$

$$\frac{d\phi}{dz} = \frac{\omega}{c}\left[\mathrm{Re}(n_0) + \mathrm{Re}(n_2)I\right] \tag{42}$$

3.2.5 Cascaded $\chi^{(2)}$:$\chi^{(2)}$ processes

In the previous section we have described third-order processes taking place in media with nonzero third order susceptibility. Some of them can also be achieved by cascading two second-order nonlinear processes in media having nonzero $\chi^{(2)}$.

A very well-known example is THG. In this interaction, the fundamental beam at ω is frequency doubled via the second-order susceptibility $\chi^{(2)}(\omega+\omega)$. The SH and the fundamental then mix by SFG $\chi^{(2)}(2\omega+\omega)$ to produce the third-harmonic. The process is represented in Fig 3. 6.

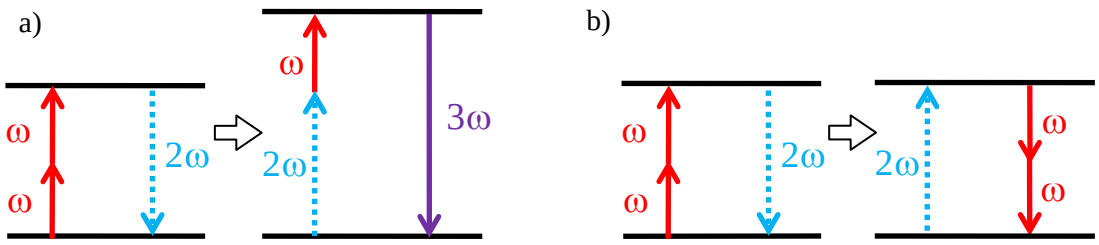

Fig 3. 6: Schemes of a) THG by means of SFG and b) two-photon absorption.

Cascaded $\chi^{(2)}$ effects can also be used for 2PA, as depicted in Fig 3. 6 where the SHG process is followed by a DFG.

As in the case of media with third-order susceptibility, this nonlinearity has two consequences: the depletion of the pump beam (equivalent to NLA) and phase distortion (equivalent to NLR). NLR occurs only off phase matching where a part of the SH is downconverted with a shifted phase. For this reason, the net phase of the fundamental will be changed proportionally to its irradiance.

This effect has received considerable attention during the last decades. Using the Z-scan technique [173] DeSalvo et al. measured the induced phase change in KTP [174] and Caumes and co-workers monitored the phase distortion in BBO by directly measuring the wavefront with a Hartmann-Shack sensor [175]. Several studies have also focused on the theoretical description of the process, such as those presented in [176, 177].

In Chapter 4, second-order cascaded processes and their implications in wavefront distortion during SHG process will be discussed in depth.

3.3. Supercontinuum generation in bulk media

When an intense pulse propagates in a medium in which the dominant lowest order of the nonlinear susceptibility is $\chi^{(3)}$, it suffers a spectral broadening termed as supercontinuum (SC) (or white light) generation. A typical SC signal covers the visible region of the electromagnetic spectrum from the near infrared to the near UV. The generation of these new extra frequencies is the result of the interplay of different phenomena [178], which we will briefly describe in the following subsections.

SC generation with femtosecond pulses has been observed in a variety of transparent media ranging from gases and liquids, to solids [179]. In bulk materials it was first described in 1970 by Alfano and Saphiro [180] and since then it has been the subject of intensive investigations [181-184], with applications in spectroscopy [185], spectral interferometry [186] or in optical parametric amplifiers [46].

3.3.1 Diffraction

As it is well-known, diffraction tends to spatially spread the Gaussian pulse as it propagates in a medium. Although peak intensity decreases (the energy is distributed in a larger transverse area), the pulse maintains the same shape.

The "strength" of diffraction is typically characterized by the Rayleigh length, defined as the distance where a beam with a flat spatial phase increases its size by a factor of $\sqrt{2}$:

$$L_{DF} = \frac{\pi n(\lambda_0) w_0^2}{\lambda_0} \tag{43}$$

where w_0 is the beam waist.

3.3.2 Dispersion

Along with diffraction, dispersion is the other linear effect that we have to consider to explain supercontinuum generation. Since the refractive index depends on the wavelength, the frequencies that compose the pulse will propagate at different speeds. This effect is known as *group velocity dispersion* (GVD).

If a Taylor expansion is made in the wave-vector around the central frequency of the pulse, ω_0, one finds that:

$$k(\omega) \cong k(\omega_0) + \left|\frac{\partial k}{\partial \omega}\right|_{\omega=\omega_0} (\omega - \omega_0) + \frac{1}{2}\left|\frac{\partial^2 k}{\partial \omega^2}\right|_{\omega=\omega_0} (\omega - \omega_0)^2 + \ldots \tag{44}$$

The different terms in (44) represent the different parameters that characterize the propagation of ultrashort pulses. The first term is related to the *phase velocity*:

$$k(\omega_0) = n(\omega_0)\frac{\omega_0}{c} = \frac{\omega_0}{v_{ph}(\omega_0)} \tag{45}$$

The next term is the inverse of the *group velocity*:

$$v_g(\omega_0)^{-1} = \left|\frac{\partial k}{\partial \omega}\right|_{\omega=\omega_0} \tag{46}$$

The GVD is identified as the second-order dispersion in (44). The strength of the GVD is accounted through the parameter:

$$\beta_2 = \left|\frac{\partial^2 k}{\partial \omega^2}\right|_{\omega=\omega_0} = \left|\frac{1}{v_g^2}\frac{\partial v_g}{\partial \omega}\right|_{\omega=\omega_0} \tag{47}$$

In materials exhibiting normal dispersion ($\beta_2>0$) the red wavelengths travel faster than the blue ones, while in anomalous dispersion ($\beta_2<0$) the situation is the opposite. In the absence of other physical effects, GVD causes a stretching (anomalous dispersion) or compression (normal dispersion) of the pulse.

Additionally, GVD may cause pulse splitting in extreme short pulses, which would eventually give rise to spectral broadening [187]. Certain theories [188, 189] consider pulse splitting and conical emission to be responsible for SC generation.

3.3.3 Self-focusing

What is usually referred to as a Kerr medium is one in which the dominant lowest order of the nonlinear susceptibility is $\chi^{(3)}$. As it has already been described in Sect. 3.2.4., in such cases the refraction index is dependent on the intensity of the input beam as follows:

$$n = n_0 + n_2 I(r,t) \tag{48}$$

Self-focusing of light [190, 191] is the process in which a powerful beam propagating in a Kerr medium modifies its optical properties in such a manner that the beam is caused to come to a focus within the material. It is actually the spatial manifestation of the third-order nonlinearity.

According to Eq.(48), if a Gaussian beam enters a Kerr medium, the refractive index will increase in those points where the beam intensity is higher. Since a Gaussian beam is more intense at the axis, the refractive index will decrease from the centre to the borders. The direct consequence of this index modulation is an induced convergent phase that leads to the focusing of the beam:

$$\phi_{NL} \simeq \frac{2\pi}{\lambda} n_2 I(r,t) L \tag{49}$$

L being the sample thickness. The effect is represented in the diagram in Fig 3. 7.

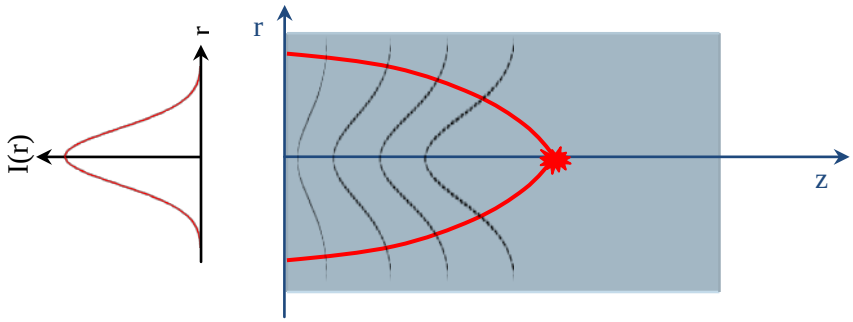

Fig 3. 7: Sketch representing the process of self-focusing. The dotted black lines represent the wavefronts, while the red line stands for the radius at $1/e^2$ of the peak intensity.

A widely used parameter to quantify the nonlinear phase shift is the B-integral, which represents the total on-axis nonlinear phase shift accumulated in a passage through the material.

$$B = \int_0^L \frac{2\pi}{\lambda} n_2 I(z) dz \tag{50}$$

As an example, let us consider a Gaussian beam with a 30 GW/cm^2 peak intensity propagating in a 2 mm thick fused silica sample (n_2=3.49x10^{-16} cm^2/W). The change in the refractive index due to the Gaussian intensity beam profile (Fig 3. 8) induces in the latter a nonlinear phase given by Eq. (49). In this case, it leads to a focusing wavefront of 0.2 rads (PtV).

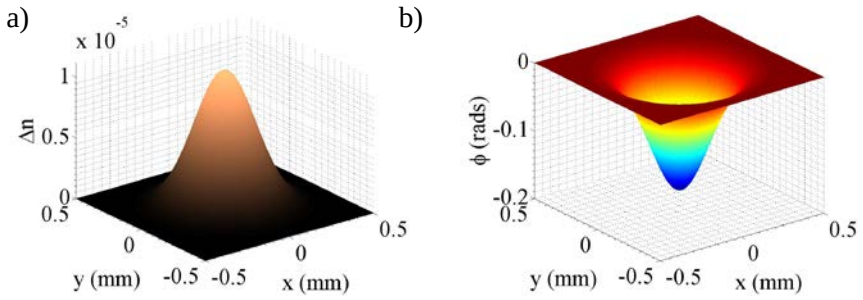

Fig 3. 8: a) Induced refractive index change and b) phase when a 30 GW/cm^2 peak intensity Gaussian beam propagates in a 2 mm thick fused silica sample.

Self-focusing occurs when the beam power exceeds the so-called *critical power*, which for a cw Gaussian beam is:

$$P_{cr} = \frac{3.77\lambda_0^2}{8\pi n_0 n_2} \tag{51}$$

When the input power is less than the critical power, $P<P_{cr}$, the beam will diverge due to diffraction effects. In contrast, when $P>P_{cr}$ the effect of self-focusing will be stronger than that of diffraction, and the beam will undergo catastrophic collapse. Finally, if $P=P_{cr}$, the intensity will maintain the input shape, in a process known as *self-trapping*.

Eq.(51) implies that with only 1 μJ energy and with a laser pulse of 100 fs we can achieve self-focusing in a solid.

After entering the medium, the Gaussian beam collapses to a singularity at a distance known as the self-focusing distance, which can be approximated fairly well by a semi-empirical formula [191]:

$$z_f = \frac{0.367 k \rho_0^2}{\left[\left(\sqrt{P/P_{cr}} - 0.852\right)^2 - 0.0219\right]^{1/2}} \tag{52}$$

where P is the beam power, k is the wave number and ρ_0 is the input beam's radius at the $1/e^2$ level of intensity.

3.3.4 Space-time focusing

Space-time focusing is a geometrical effect that becomes important in the presence of strong self-focusing. Pulses travelling along the rays that keep an angle with the optical axis take longer to propagate over fixed distances than those travelling along the optical axis. In a similar way, the projection of the group velocity onto the optical axis will vary depending on the tilt of the light rays. This causes a coupled time-space focusing that yields a dramatic shift of energy towards the back of the pulse in time, which can eventually lead to asymmetric pulse splitting and shock front formation on the trailing edge of the pulse [192, 193].

3.3.5 Self-phase modulation

Self-phase modulation (SPM) is the change in the phase of an optical pulse that arises from the nonlinearity of the refractive index (it is indeed the temporal manifestation of the optical Kerr effect).

A laser pulse with on-axis intensity distribution I(z,t) that propagates over a distance L in a Kerr medium will accumulate a nonlinear phase given by Eq.(49). As a result of the time-varying phase, the spectrum of the transmitted pulse will be modified, becoming typically broader than that of the incident pulse.

To understand this effect, let us consider the electric field of an optical pulse as

$$E(z,t) = A(z,t) e^{i[n(t)kz - \omega_0 t]} \tag{53}$$

propagating in a medium characterized by a nonlinear refractive index of the sort of Eq.(48).

By introducing Eq.(48) in Eq.(53) we obtain:

$$E(z,t) = A(z,t) \exp\left\{ i \left[\frac{2\pi}{\lambda_0} n_0 z + \frac{2\pi}{\lambda_0} n_2 z I(z,t) - \omega_0 t \right] \right\} \tag{54}$$

Note that we are assuming that the medium is able to instantaneously respond to the pulse intensity and that the length of the nonlinear medium is short enough to neglect reshaping of the pulse within the medium.

As the central frequency is the derivative of the phase with respect to the time, the concept of instantaneous frequency ω(t) of the pulse can be introduced in the same way:

$$\omega(t) = \omega_0 + \delta\omega(t) \tag{55}$$

where

$$\delta\omega(t) = \frac{\partial}{\partial t}\phi_{NL}(r,t) \tag{56}$$

At this point it should be noted that Eq.(55) is valid under the assumption of slowly varying envelope approximation (SVEA).

The spectrum extension is therefore given by the maximum rate of increase (decrease) in the nonlinear phase along the pulse. Therefore it depends on the slope of the pulse $\partial I(z,t)/\partial t$, the propagation distance z in the Kerr medium and its nonlinear index coefficient n_2. In a purely Kerr medium, the front part of the pulse generates redder frequencies, i.e. lower frequencies, than the central wavelength of the pulse (positive slope), and the back part generates bluer frequencies (negative slope). The redder frequencies are usually termed as Stokes components, while the blue-shifted frequencies are called anti-Stokes components.

To better clarify this effect, let us consider the example of an initial beam with the following on-axis temporal distribution:

$$I(t) = I_0 \exp\left[-2\ln(2)\left(\frac{t}{\tau}\right)^2\right] \tag{57}$$

where I_0=30 GW/cm^2 peak intensity and τ=120 fs centred at λ_0=795 nm enter a 20 mm thick fused silica sample. After propagation over a distance L, the spectrum can be calculated using the Fourier transform Eq.(54).

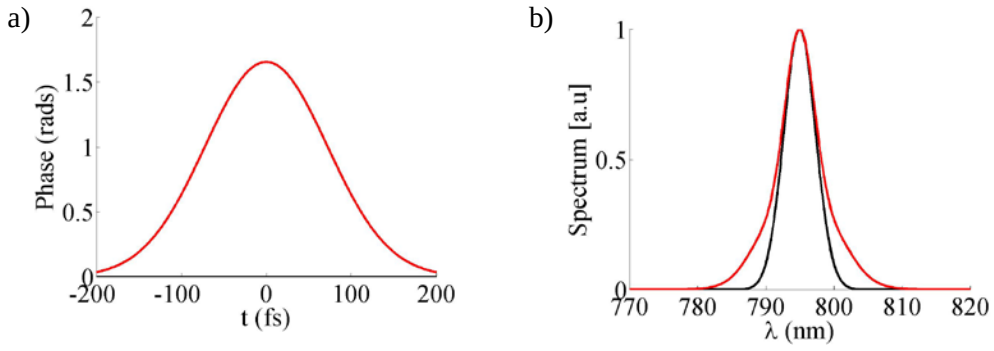

Fig 3. 9: a) Temporal phase (the term $\omega_0 t$ has been subtracted) and b) spectrum of the input pulse (black) and spectrum after propagating through a 20 mm fused silica plate (red).

Since the input pulse shape was symmetric in the temporal domain, the spectrum has become symmetrically broadened after undergoing SPM. It must be remarked that if a rigorous interpretation of SPM theory were to be adopted [194], the resulting broadening would be asymmetrical.

The SPM theory discussed so far arises from the Kerr nonlinearity. We shall later see that the free-electron mechanism also yields an index change and can therefore contribute to SPM.

3.3.6 Self-steepening

The last n_2 process that should be discussed is *self-steepening*. This effect arises from the intensity dependent group velocity of the pulse.

The group velocity is given by:

$$v_g = \left(\frac{\partial k}{\partial \omega}\right)^{-1} = \frac{c}{\omega \frac{\partial n}{\partial \omega} + n} \tag{58}$$

Since in a Kerr medium the refractive index depends on the intensity distribution, so will the group velocity. When dealing with a Gaussian pulse, the peak slows down with respect to the pulse group velocity, while the trailing part catches up with the peak. In Fig 3. 10 we have plotted the group velocity for a Gaussian pulse (120 fs FWHM, 795 nm central wavelength, 30 GW/cm^2 peak intensity) propagating in a fused silica sample.

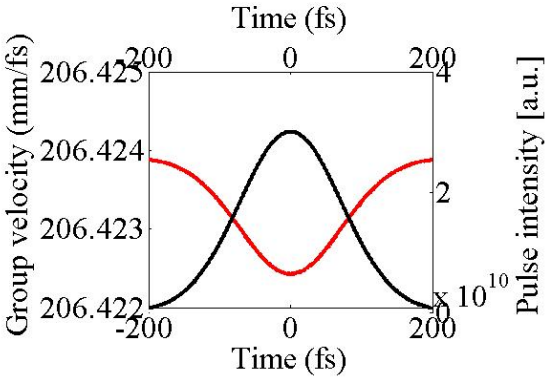

Fig 3. 10: Group velocity for a Gaussian pulse propagating in a Kerr medium (see details in the text). The black line corresponds to pulse intensity, whereas group velocity has been represented in red.

This implies that the magnitude of $\frac{\partial I}{\partial t}$ will become much larger in the back side of the pulse than in the leading edge. As it was discussed in Eq.(56), the blue-shifted frequencies are created on the trailing edge of the pulse (where $\frac{\partial I}{\partial t} < 0$). Thus, self-steepening will result in an increase in the production of blue-shifted frequencies.

According to some authors, shock formation due to space-time focusing and self-steepening are the main mechanisms governing SC generation [195].

3.3.7 Raman response

The processes we have reviewed so far are due to the instantaneous Kerr effect, caused by a fast (< 1 fs) electronic response of the medium. In addition to this response, many materials also exhibit a delayed third order response that yields an asymmetric extension of the Stokes side.

The non-instantaneous Kerr response is the consequence of a delayed rotational Raman molecular response [196]. A comprehensive semi-classical model of the *stimulated Raman scattering* in terms of nonlinear polarization can be found in Chapter 10 of [169]. The key assumption of this theory is that the optical polarizability of the molecule (which is typically predominant in origin) is not constant, but depends on the internuclear separation. Therefore, when the molecule is set into oscillation its polarizability will be periodically modulated in time, and so will the refractive index.

In such case, the change in the refractive index is no longer $n_2 I$, but is instead given by [179]:

$$\Delta n(z,t) = \int_{-\infty}^{t} n_2(z, t-t') \left| E(z,t') \right|^2 dt' \tag{59}$$

This delayed response causes SPM to become asymmetric even in the case of symmetric pulses and leads to a red-shift. This can be understood in terms of Raman Stokes scattering, and illustrated in Fig 3. 11. A photon of energy $\hbar\omega$ is absorbed by the medium, whereas a photon at the Stokes frequency $\hbar\omega_s$ is created, therefore leaving the molecule in an excited state of energy $\hbar\omega_v$.

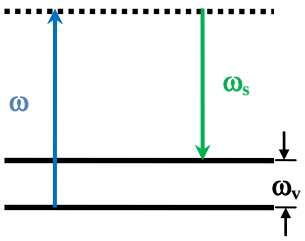

Fig 3. 11: Stimulated Raman scattering.

3.3.8 Ionization

The last essential process that might produce changes in the refractive index is *ionization* (or plasma generation) [197], which consists of the generation of free electrons that are released from the bounding potentials that keep them linked to their "parent" ions.

In the case of wide bandgap dielectrics under intense femtosecond laser irradiation, several mechanisms (depending on the laser parameters) may take place and contribute to plasma generation and development [178]. The most relevant are multiphoton ionization, tunnel ionization, free carrier absorption and avalanche ionization, which are illustrated in Fig 3. 12.

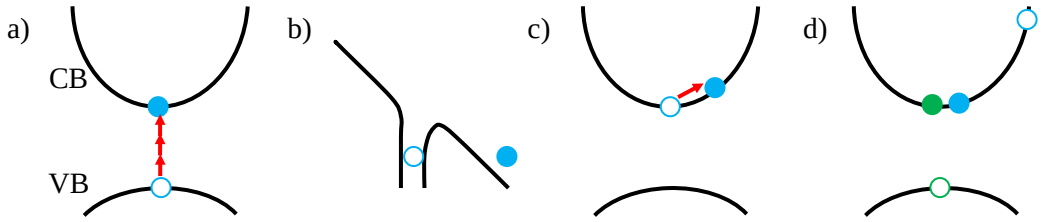

Fig 3. 12: Main ionization mechanisms: a) multiphoton ionization, b) tunnel ionization, c) free carrier absorption and d) avalanche ionization. The red arrows represent the absorption of photons, and the circles represent electrons in their initial (open dots) and final (coloured dots) states. CB and VB are the conduction and valence bands, respectively.

Multiphoton ionization (MPI) refers to the simultaneous absorption of multiple photons to excite a valence band electron. In this process the photoionization rate strongly depends on the laser intensity. A second photoionization process is *tunnel ionization*, where the electrons are forced to a Coulomb potential by the application of a strong laser field. This potential becomes an oscillating barrier through which bound electrons can tunnel. The transition from MPI to tunnel ionization is characterized by the Keldysh parameter, $\gamma = \frac{\omega\sqrt{2m^* E_g}}{eE}$, where m^* and e are the effective mass and charge of the electron, E_g is the band gap energy and E is the amplitude of the laser field oscillating at frequency ω. When the electron density generated by photoionization reaches high levels, the excited electrons can sequentially absorb several laser photons, moving to higher energy states in a process termed as *free carrier absorption*. When an electron in the conduction band has gained enough energy (exceeding the conduction band minimum by more than E_g) by free carrier absorption, it can ionize another electron from the valence band in a process known as *avalanche ionization*, resulting in two excited electrons.

The free electron density, ρ, is governed by the following the equation [183]:

$$\frac{\partial \rho}{\partial t} = \frac{\sigma}{n_b^2 E_g}\rho I + \frac{\beta^{(K)}}{K\hbar\omega_0} I^K - a\rho^2 \tag{60}$$

K being the order of the MPI, σ the cross-section, β the MPI coefficient, n_b the background refractive index and a the recombination parameter. The first term describes avalanche ionization, the second accounts for electron generation via MPI and the third term represents recombination.

Once ionization begins, the free electrons form a plasma inside the material, reducing the refractive index as follows

$$n = \sqrt{n_0^2 - \frac{\rho(r,t)}{\rho_{cr}}} \tag{61}$$

where $\rho_{cr} = \varepsilon_0 m_e \omega_0^2 / e^2$ is the critical plasma density, and m_e and e the mass and charge of the electron, respectively. In the low density plasma regime ($\rho << \rho_{cr}$) the change in the refractive index induced by the plasma can be approximated by:

$$\Delta n \simeq -\frac{\rho(r,t)}{2\rho_{cr}} \tag{62}$$

Thus, Eq.(62) involves a decrease in the refractive index. Since the plasma density is larger at the centre of the beam than at the borders, it will act as a divergent lens. This effect is the opposite of that created by the Kerr effect and tends to defocus the beam.

The role of plasma defocusing in determining the spectral features of SC is still under discussion. Some authors believe that a second effect of the plasma would be frequency shift [197], which is given by:

$$\delta\omega(t) \approx \frac{\omega_0 z}{2cn_0\rho_{cr}} \frac{\partial\rho(t)}{\partial t} \tag{63}$$

Since the electron density is growing during pulse propagation (and relaxation of the electrons is slow), this frequency shift is positive, indicating that the plasma shifts the laser towards blue frequencies. However, years later this theory was questioned by Gaeta in relation to the case of solids. According to [195] multiphoton absorption and plasma formation simply halt the collapse at power levels significantly above the threshold for collapse. This assertion is supported by numerical simulations which show that the simulated SC spectrum in the absence of plasma closely conforms to the experimental results.

3.3.9 Filamentation

Filamentation or self-guided propagation [83] is the creation of a light channel (filament) with negligible divergence over a distance much larger than that expected by the limits of diffraction. It is the result of a balance between the Kerr effect (which tends to focus the beam) and diffraction and ionization (which defocus the beam). Along with other effects (saturation of the nonlinear index by a higher order defocusing nonlinearity, nonlocal effects and nonlinear absorption) plasma defocusing certainly contributes to the *arrest of collapse*.

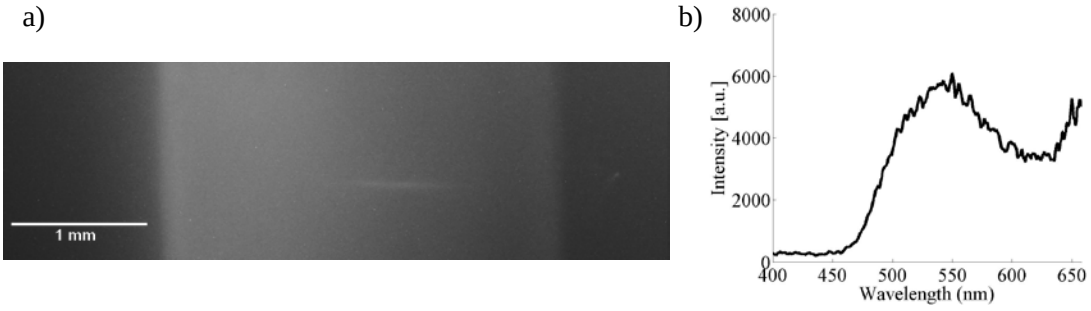

Fig 3. 13: a) Filament inside a 3 mm thick sapphire sample. The pulses (120 fs FWHM, 795 nm central wavelength) were focused into the crystal with a 100 mm focal length lens. b) Corresponding spectrum in the visible. A band-pass filter (FG37S, Thorlabs) was used to remove the non-converted infrared radiation.

It must also be mentioned that GVD in solids is also an efficient mechanism to arrest collapse. This is relevant for pulses of sufficiently low peak power, since the critical power threshold for collapse in dispersive media increases with dispersion.

3.3.10 Four-wave mixing

Four-wave mixing is a phenomenon arising from the third-order nonlinear susceptibility, $\chi^{(3)}$. In the media where it predominates, three wavelengths interact to give rise to a fourth one, as presented in Eqs. (29) and (30). Four-wave mixing is thought to be responsible for *conical emission* [198].

The spectral broadening obtained during filamentation gives rise to new bluer and redder frequencies that interact with the laser central frequency, producing new wavelengths with different wave-vectors. The generated white light beam generally consists of a white central part surrounded by a rainbow-like conical emission.

3.3.11 Supercontinuum generation (SCG)

Supercontinuum generation (SCG) results from an intense ultrashort pulse subjected to the nonlinear processes described above. The role of the different mechanisms in the spectral shaping of SC is still under discussion. Nevertheless, most authors agree that self-focusing is the triggering process that gives rise to SC. It is believed that the onset of catastrophic self-focusing leads to a drastic increase in intensity, which further enhances SPM. Collapse is arrested by plasma defocusing, which, along with stimulated Raman scattering, contributes to wavelength generation in the anti-Stokes side.

The dynamics of the pulses subjected to all these processes is rather complicated, but recent results [199] suggest that laser radiation propagates under conditions of competition between alternating focusing and defocusing phases that give rise to pulse splitting.

As a result, the spectrum of a pulse initially centred in the near infrared will broaden until it covers the entire visible range. In Fig 3. 13b, we show the spectrum in the visible range of SC pulses generated by focusing 795 nm (central wavelength), 120 fs (FWHM) pulses in a 3 mm thick sapphire plate.

In Chapter 7 we will provide further insight into the physical factors conditioning the process of SCG, as well as into the spatial and spectral characteristics of SC pulses.

4

Second-harmonic generation of aberrated femtosecond beams

4.1. Introduction

In the previous chapter, the different frequency-mixing processes were described. Among them, second-harmonic generation (SHG) [171] has proved to be an effective method for obtaining short-wavelength laser sources. As mentioned in Chapter 3, the second harmonic (SH) of a beam is obtained in noncentrosymmetric crystals. This is the case of β-barium-borate (BBO) or potassium dihydrogen phosphate (KDP), which are widely used for SHG.

It is clear that for further applications of these pulses not only the temporal profile, but also beam quality are crucial. In this respect, the enhancement of SHG is interesting for the fact that it provides better contrast ratios than the fundamental pulse, making it attractive for laser-matter interaction experiments involving solid targets [200]. Unfortunately, in many cases the nonlinear effect involved in SHG leads to significant wavefront distortions that limit the focusability of the laser beam. The study of these phase effects is therefore essential for the applications of frequency doubled pulses. SH pulses are also employed as pumps in visible OPAs. The study of their spatial properties is crucial to determine the beam quality of the amplified signal of an OPA [201] or an OPCPA chain [202].

Many efforts have been made to establish a theory of SHG including transverse effects [203-207]. Nevertheless, most of these studies are based on the assumption of plane waves, which in practice is seldom true, since aberrations must also be taken into account when dealing with real beams.

In [208], Hou et al. present a complete model, including walk-off and diffraction, of the transverse effects in SHG with aberrated beams. Although their model is based on continuous waves, their conclusions show the importance of the role played by the wavefront in SHG. When the aberrations of the fundamental pulse are small and diffraction and walk-off effects can be neglected, the transverse distribution of the SH beam remains almost undisturbed. In addition, the wavefront of the SH in such cases is approximately linear to the aberrations of the fundamental beam, i.e.,

$$\psi_{SH}(x,y) \approx 2\psi_{F}(x,y) \tag{64}$$

where ψ_{SH} and ψ_{F} are the wavefront (expressed in terms of wavelengths) of the SH and the fundamental beams respectively, and (x,y) are the transverse coordinates.

On the contrary, if the aberrations are large, they can influence the fundamental beam and the intensity-dependent phase distortion effect cannot be neglected. In such cases, the linear relationship (64) no longer holds.

The purpose of this chapter is to present an experimental study of the SHG of aberrated femtosecond beams. The results from this investigation will allow us to optimize SHG for its further application, in particular as a secondary source in microprocessing and as pump in an OPA.

In order to achieve this goal, we will first review the theoretical background of SHG (Sections 4.2 and 4.3). Then, we will revise the spatial effects that take place during the process of SHG for plane waves at low and high intensities. Finally, a similar study will be performed for aberrated femtosecond pulses. In particular, we will investigate the phase effects for focusing and astigmatic beams.

4.2. Second-harmonic generation with monochromatic waves

4.2.1 The coupled wave equations

In this section we provide a mathematical description of SHG for monochromatic waves [209]. To ease the derivation process we will consider monochromatic, continuous wave, plane waves travelling in a lossless medium.

The total electric field in the medium is obtained by the sum of both the fundamental and the SH beams. Thus we can write:

$$\vec{E}(z,t) = \vec{E}_1(z,t) + \vec{E}_2(z,t) \tag{65}$$

Each of the components must obey the wave equation

$$\nabla^2\vec{E}(\vec{r},t) - \frac{\varepsilon(\omega)}{c^2}\frac{\partial^2\vec{E}(\vec{r},t)}{\partial t^2} = \frac{1}{\varepsilon_0 c^2}\frac{\partial^2\vec{P}(\vec{r},t)}{\partial t^2} \tag{66}$$

where c is the speed of light in vacuum, n the refractive index of the medium, ε the permittivity, E the electric field and P the polarization.

In the absence of a nonlinear source term, Eq. (66) has the following solution for a plane wave propagating in the +z direction at frequency ω:

$$E(z,t) = Ae^{-i(\omega t - kz)} + c.c \tag{67}$$

where $k = n\frac{\omega}{c}$, $n = \sqrt{\varepsilon(\omega)}$ and amplitude A is constant.

When the nonlinear term is not too large, the solution to Eq. (66) is still expected to take the form of (67), although with a slowly varying z-dependent amplitude. For this reason, in the presence of nonlinearity the solution assumes the following form:

$$E(z,t) = A(z)e^{-i(\omega t - kz)} + c.c \tag{68}$$

In particular, Eq. (68) will be valid for each of the components. Therefore:

$$E_j(z,t) = A_j(z)e^{-i(\omega_j t - k_j z)} + c.c \qquad (j = 1,2) \tag{69}$$

The nonlinear polarization is represented as

$$P^{NL}(z,t) = P_1(z,t) + P_2(z,t) \tag{70}$$

with

$$P_j(z,t) = P_j(z)e^{-i\omega_j t} \qquad (j = 1,2) \tag{71}$$

The expressions of the polarization amplitudes, $P_j(z)$, are given by [169]:

$$P_1(z) = 2\varepsilon_0 \chi^{(2)} A_2 A_1^* e^{i(k_2 - k_1)z} \tag{72}$$

$$P_2(z) = 2\varepsilon_0 \chi^{(2)} A_1^2 e^{i2k_1 z} \tag{73}$$

Eq. (69) and (71) are now substituted in the wave equation (66) for the SH and the fundamental in order to obtain the wave equation for each component. Since the fields depend only on the longitudinal coordinate z, it is possible to replace ∇^2 by $\frac{d^2}{dz^2}$.

$$\omega \rightarrow \quad \left(\frac{d^2 A_1}{dz^2} + 2ik_1 \frac{dA_1}{dz}\right) e^{ik_1 z} = -\frac{4d_{eff}\omega^2}{c^2} A_1^* A_2 e^{i(k_2 - k_1)z} \tag{74}$$

$$2\omega \rightarrow \quad \left(\frac{d^2 A_2}{dz^2} + 2ik_2 \frac{dA_2}{dz}\right) e^{ik_2 z} = -\frac{16d_{eff}\omega^2}{c^2} A_1^2 e^{i2k_1 z} \tag{75}$$

where $d_{eff} = \frac{1}{2}\chi^{(2)}$.

Eq. (74) and (75) are known as coupled-amplitude equations, since they show the amplitude dependence of the SH with respect to the fundamental wave and vice versa.

4.2.2 Strong coupling regime

In general Eq. (74) and (75) do not have an analytical solution and must be solved numerically. For simplicity, and being of interest in many practical situations, we will invoke the slowly varying envelope approximation (SVEA):

$$\left|\frac{d^2A_2}{dz^2}\right| \ll \left|k_2\frac{dA_2}{dz}\right| \tag{76}$$

This allows us to write Eq. (74) and (75) as

$$\frac{dA_1}{dz} = \frac{i2d_{eff}\omega^2}{k_1c^2}A_2A_1^*e^{-i\Delta kz} \tag{77}$$

$$\frac{dA_2}{dz} = \frac{i8d_{eff}\omega^2}{k_2c^2}A_1^2e^{i\Delta kz} \tag{78}$$

where we have introduced the quantity

$$\Delta k = (2k_1 - k_2) \tag{79}$$

known as wave-vector mismatch.

4.2.3 Weak coupling regime

The weak coupling regime approximation consists of assuming that the amplitude variation of A_1 can be neglected, or in other words, A_1 is constant.

Under this assumption, Eq. (78) can be easily solved to obtain the amplitude of the SH signal at the exit of a nonlinear crystal with length L:

$$A_2 = \int_0^L \frac{i8d_{eff}\omega^2}{k_2c^2}A_1^2e^{i\Delta kz}dz = \frac{8d_{eff}\omega^2}{k_2c^2}A_1^2\left(\frac{e^{i\Delta kL}-1}{\Delta k}\right) \tag{80}$$

The intensity of the SH is obtained through the time-averaged magnitude of the Poynting vector, which is given by:

$$I_2 = 2n_2\varepsilon_0c\left|A_2\right|^2 \tag{81}$$

We thus obtain:

$$I_2 = 2n_2\varepsilon_0c\left(\frac{8d_{eff}\omega^2}{k_2c^2}A_1^2\right)^2\left|\frac{e^{i\Delta kL}-1}{\Delta k}\right|^2 \tag{82}$$

Or its equivalent:

$$I_2 = \frac{32L^2 d_{eff}^2 \omega^2}{n_1^2 n_2 \varepsilon_0 c^2} I_1^2 \mathrm{sinc}^2\left(\frac{\Delta kL}{2}\right) \tag{83}$$

According to Eq. (83) the intensity of the SH is proportional to the square of that of the fundamental beam. Conversion efficiency is then defined by:

$$\eta = \frac{32L^2 d_{eff}^2 \omega^2}{n_1^2 n_2 \varepsilon_0 c^2} I_1 \mathrm{sinc}^2\left(\frac{\Delta kL}{2}\right) \tag{84}$$

where I_1 is the intensity of the input beam. Note that the efficiency takes values from 0 to $\frac{32L^2 d_{eff}^2 \omega^2}{n_1^2 n_2 \varepsilon_0 c^2} I_1$.

4.2.4 Phase matching

The factor $\mathrm{sinc}^2\left(\frac{\Delta kL}{2}\right)$ is known as phase mismatch (PM). It accounts for the phase relationship with the nonlinear polarization.

In Fig 4. 1 the intensity variation I_2 is depicted as a function of $\Delta kL/2$. When Δk=0, the condition of perfect phase-matching is fulfilled. In such case, the generated wave is able to extract energy most efficiently from the fundamental wave. From a microscopic point of view, when the perfect phase-matching condition is satisfied, the individual atomic dipoles are properly phased, so that the field emitted by each of them adds coherently in the forward direction.

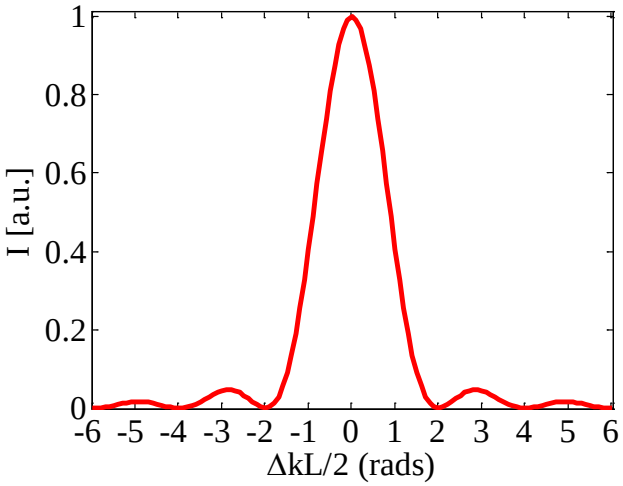

Fig 4. 1: Intensity of the SH as a function of the wave-vector mismatch.

In general, since Δk depends on the refractive indices, the phase-matching curve will be different for different crystals. In Fig 4. 2, the intensity of the phase-matching curve is depicted as a function of the wavelength for different crystals, all of them 0.5 mm thick.

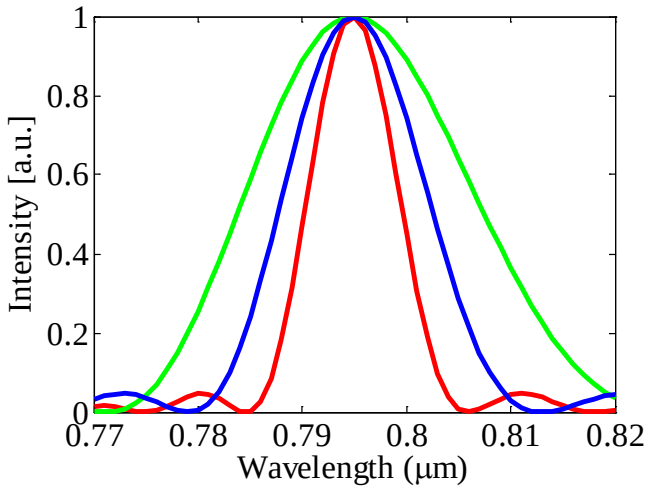

Fig 4. 2: Intensity as a function of the wavelength for different crystals (0.5 mm thick): BBO (red), LBO (blue) and KDP (green).

It should be noted that the efficiency of the SHG process decreases as $|\Delta kL|/2$ increases, presenting some oscillations. According to Eq. (84), when $L = 2/\Delta k$ the conversion efficiency decays to 70% of its maximum value. This quantity is known as coherence length of interaction.

$$L_c = 2/\Delta k \tag{85}$$

Physically, when $L>L_c$ the SH can get out of phase with its driving polarization, and power can flow from the SH to the fundamental.

The perfect phase-matching condition requires, according to Eq. (79) that

$$n(\omega) = n(2\omega) \tag{86}$$

It is obviously not possible to achieve the condition (86) in materials where the refractive index increases monotonically with ω. This is achieved by making use of birefringent crystals, where the refractive index depends on the direction of polarization. Depending on the value of the extraordinary index with respect to the ordinary index, we will classify them into positive ($n_e>n_o$) and negative ($n_e<n_o$) uniaxial crystals.

The extraordinary refractive index depends on the angle between the propagation direction and the optical axis, θ. It is then possible to orientate the crystal in such a way that the SH is polarized in the direction that gives it the lowest refractive index. In the case of positive uniaxial crystals, this is the ordinary index, while in the case of negative uniaxial ones it is the extraordinary index.

In Fig 4. 1 the ordinary and extraordinary indices for BBO are plotted for θ=29.4º. Under this angle, the extraordinary index at 400 nm has the same value as the ordinary index at 800 nm.

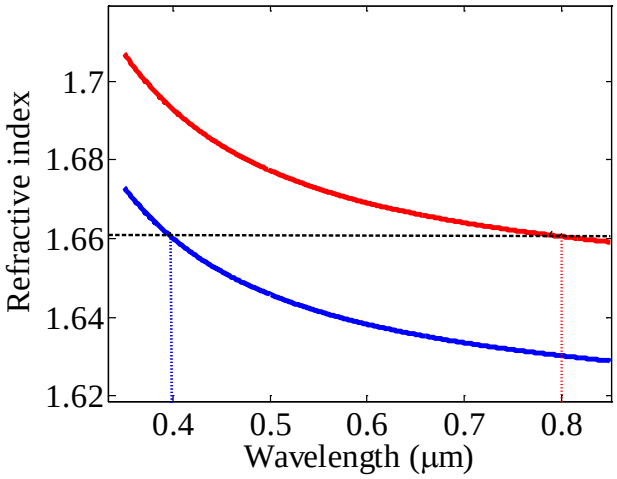

Fig 4. 3: Ordinary (red) and extraordinary (blue) indices for BBO for θ=29.4º.

It must be noted though that for a fixed value of θ the band of frequencies that can be efficiently doubled depends on the thickness of the crystal, as is deduced from Eq. (84). In Fig 4. 4 the phase-matching curve of a BBO crystal is represented for different degrees thickness. It is clear that the thicker the crystal is, the narrower the band of frequencies that can be doubled.

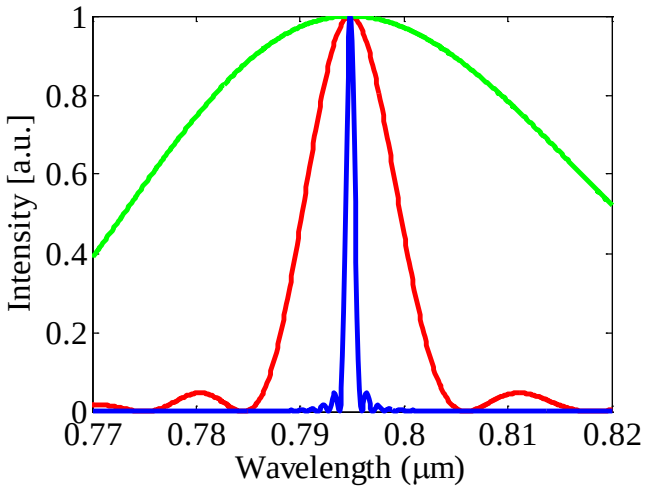

Fig 4. 4: Phase-matching curves for 5 mm (blue), 0.5 mm (red) and 0.1 mm (green) thick BBO crystals.

As regards the fundamental beam, there are two types of polarizations: in Type I phase-matching the polarizations of both fundamental photons are the same, whereas in Type II they are orthogonal. A summary of the phase-matching possibilities is presented in Table 4. 1.

	Positive uniaxial ($n_e>n_o$)	Negative uniaxial ($n_e<n_o$)
Type I	$n_o(2\omega)=n_e(\omega,\theta)$ ee→o	$n_e(2\omega,\theta)=n_o(\omega)$ oo→e
Type II	$2n_o(2\omega)=n_e(\omega,\theta)+n_o(\omega)$ oe→o	$2n_e(2\omega,\theta)=n_e(\omega,\theta)+n_o(\omega)$ oe→e

Table 4. 1: Phase-matching methods for uniaxial crystals

Up to this point we have only considered collinear geometries, i.e. there is only one direction of propagation of the fundamental beam and the SH is generated in that direction. In a non-collinear scheme, two fundamental beams propagate in different directions. The resulting SH propagates in a different direction that depends on the angle between both fundamental beams. An example is shown in Fig 4. 5.

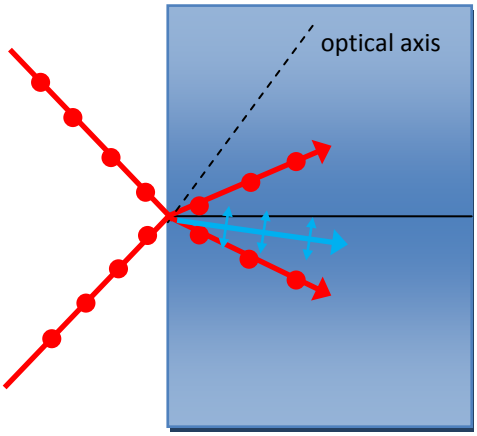

Fig 4. 5: Non-collinear Type I second-harmonic generation in a negative uniaxial crystal.

The phase-matching condition will be different in this case. We can deduce it by taking into account the law of momentum conservation:

$$\vec{k_1} + \vec{k_1}' = \vec{k_2} \tag{87}$$

If we define α, α' and β as the angles between the z-axis (perpendicular to the crystal's surface) and the first and second fundamental beams and the SH, respectively, we can rewrite Eq. (87) as:

$$\begin{aligned} n_1 \cos(\alpha) + n_1' \cos(\alpha') &= n_2 \cos(\beta) \\ n_1 \sin(\alpha) + n_1' \sin(\alpha') &= n_2 \sin(\beta) \end{aligned} \tag{88}$$

4.2.5 Spatial walk-off effect

When a beam propagates in an isotropic medium, the transverse intensity distribution propagates along the beam axis as defined by the medium k-vector. However, in anisotropic crystals there are two refractive indices (ordinary and extraordinary) and it can occur that the intensity distribution drifts away from the direction defined by the k-vector. In other words, unless θ has the value 0 or 90 degrees (which is usually not the case), the Poynting vector S and the propagation vector k are not parallel in the case of extraordinary rays. As a result, ordinary and extraordinary rays with parallel propagation vectors quickly diverge from one another as they propagate through the crystal. This phenomenon, known as walk-off effect, limits the spatial overlap of the two waves, thus decreasing the efficiency of any nonlinear mixing process involving such waves and degrading the beam's spatial quality.

To account for these effects the *walk-off angle*, ρ, is defined as the angle between the wave-vector (normal to the wavefront surface) and the Poynting vector (which defines the direction of energy transport):

$$\rho = -\frac{1}{n_e}\frac{\partial n_e}{\partial \theta} \tag{89}$$

n_e being the extraordinary index and θ the angle between the k-vector and the optical axis.

4.3. Description of second-harmonic generation with femtosecond pulses

4.3.1 Coupled-amplitude equations

The equations that govern SHG with femtosecond pulses can be derived from Maxwell's equations by following a similar procedure to that employed in the previous section. We will consider media with nonzero second and third order susceptibilities.

In the case of short pulses, the electric field will no longer be a plane wave and we need to include a time-dependent amplitude:

$$\vec{E}_j(\vec{r},t) = A_j(\vec{r},t)e^{i(\omega_j t - k_j \vec{r})} + c.c \qquad (j = 1,2) \tag{90}$$

For the nonlinear polarization expression, we will include the contribution up to the third order, since it plays an important role in the case of intense femtosecond pulses. By substituting Eq. (90) in the expression of the nonlinear polarization we find that

$$\begin{aligned} P_1^{(NL)}(\vec{r},t) &= \left[2\chi^{(2)} A_1 A_2^* + 12\chi^{(3)} \left|A_1\right|^2 A_1 + 24\chi^{(3)} \left|A_2\right|^2 A_1 \right] e^{i(\vec{k}_1\vec{r} - \omega_1 t)} \\ P_2^{(NL)}(\vec{r},t) &= \left[2\chi^{(2)} A_1 A_2^* + 12\chi^{(3)} \left|A_2\right|^2 A_2 + 24\chi^{(3)} \left|A_1\right|^2 A_2 \right] e^{i(\vec{k}_2\vec{r} - \omega_2 t)} \end{aligned} \tag{91}$$

Please note that for the sake of simplicity we have abbreviated the notation in Eq. (91) and omitted the (r,t) dependence in the amplitude.

If we now substitute Eq. (90) and (91) in the wave equation and use the SVEA, we obtain the following pair of coupled-amplitude equations:

$$\begin{aligned} &\frac{\partial A_1}{\partial z} - \frac{1}{2k_1}\left(\frac{\partial^2 A_1}{\partial x^2} + \frac{\partial^2 A_1}{\partial y^2} \right) + v_{12g}\frac{\partial A_1}{\partial t} + id_1 \frac{\partial^2 A_1}{\partial t^2} = \\ &= i\frac{\omega_1 \chi^{(2)}}{n_1 c} A_2 A_1^* e^{-i\Delta k z} + i\frac{3\omega_1 \chi^{(3)}}{n_1 c} A_1 \left|A_1\right|^2 + i\frac{6\omega_1 \chi^{(3)}}{n_1 c} A_1 \left|A_2\right|^2 \end{aligned} \tag{92}$$

$$\begin{aligned} &\frac{\partial A_2}{\partial z} - \frac{1}{2k_2}\left(\frac{\partial^2 A_2}{\partial x^2} + \frac{\partial^2 A_2}{\partial y^2} \right) + id_2 \frac{\partial^2 A_2}{\partial t^2} = \\ &= i\frac{\omega_2 \chi^{(2)}}{n_2 c} A_1^2 e^{i\Delta k z} + i\frac{3\omega_2 \chi^{(3)}}{n_2 c} A_2 \left|A_2\right|^2 + i\frac{6\omega_1 \chi^{(3)}}{n_1 c} A_2 \left|A_1\right|^2 \end{aligned} \tag{93}$$

where $\Delta\vec{k} = \vec{k}_2 - 2\vec{k}_1$ is the wave-vector mismatch, $d_j = \frac{1}{2}\frac{\partial^2 k_j(\omega)}{\partial\omega^2}\Big|_{j=1,2}$ $(j=1,2)$ is the group-velocity dispersion (GVD) coefficient and $\frac{1}{v_{12g}} = \left[\frac{\partial k_1(\omega)}{\partial\omega}\right]^{-1} - \left[\frac{\partial k_2(\omega)}{\partial\omega}\right]^{-1}$ is the group velocity mismatch (GVM) of the SH with respect to the fundamental. It must be remarked that in equations (92) and (93) we have neglected spatial walk-off, absorption by the medium and higher order dispersion effects.

The equation system (92)-(93) needs to be solved numerically. It has been studied in depth by several groups and applied in the comparison with experiments [208, 210-214].

Before introducing the numerical solutions for Eq. (92)-(93) , we will examine the physical meaning of coupled-amplitude wave equations. For the sake of simplicity, we will neglect the spatial dependence of the amplitudes, so that the equation system becomes reduced to:

$$\frac{\partial A_1}{\partial z} + v_{12g}\frac{\partial A_1}{\partial t} + id_1\frac{\partial^2 A_1}{\partial t^2} = i\frac{\omega_1\chi^{(2)}}{n_1 c}A_2 A_1^* e^{-i\Delta kz} + i\frac{3\omega_1\chi^{(3)}}{n_1 c}A_1\left|A_1\right|^2 + i\frac{6\omega_1\chi^{(3)}}{n_1 c}A_1\left|A_2\right|^2 \tag{94}$$

$$\frac{\partial A_2}{\partial z} + id_2\frac{\partial^2 A_2}{\partial t^2} = i\frac{\omega_2\chi^{(2)}}{n_2 c}A_1^2 e^{i\Delta kz} + i\frac{3\omega_2\chi^{(3)}}{n_2 c}A_2\left|A_2\right|^2 + i\frac{6\omega_1\chi^{(3)}}{n_1 c}A_2\left|A_1\right|^2 \tag{95}$$

By looking at Eq. (94) and (95), we can deduce the physical implications of $\chi^{(2)}$ and $\chi^{(3)}$. The terms where $\chi^{(2)}$ nonlinearity is present correspond to those containing the product $A_2 A_1^*$. The $\chi^{(2)}$ nonlinearity gives rise to the parametric gain of the fundamental and SH pulses, whereas the $\chi^{(3)}$ is responsible for the self-phase modulation (SPM) and cross-phase modulation (XPM) effects.

Since nonlinear crystals are dispersive media, dispersion will cause the pulse to suffer phase distortion:

$$\varphi(\omega) = \frac{\omega}{c}n(\omega)L = k(\omega)L \tag{96}$$

where L is the thickness of the medium. A Taylor expansion in k(ω) allows us to express Eq. (96) as:

$$\varphi(\omega) \cong \varphi(\omega_0) + \frac{1}{v_g(\omega_0)}(\omega-\omega_0)L + d(\omega_0)(\omega-\omega_0)^2 L + \ldots \tag{97}$$

where ω_0 is the pulse central frequency.

The coefficient of the second term in Eq. (97) is the inverse of the group velocity, whereas d is the GVD coefficient. Physically, this term accounts for the different velocities that form the pulse and is responsible for a stretching (d>0) or a compression (d<0) in time of the initially Fourier transformed pulses when propagating through a dispersive medium.

A parameter that accounts for the effect of the GVD is the *pulse-spreading distance*, defined as [211]:

$$l_{d,j} = \frac{\tau_0^2}{4GVD} \quad (j = 1,2) \tag{98}$$

Although this effect cannot be avoided, in the case of nonlinear crystals it becomes important only when the pulses are very short (close to few-cycle regime) which is not the case in the studies presented here. For example, 120 fs Fourier-transform limited pulses centred at 800 nm or 400 nm will become increased by less than 1 fs when travelling through 2 mm of BBO.

GVM accounts for the velocity difference between the SH and the fundamental pulse, tending to lengthen the SH pulse.

In spectral regions of normal dispersion, the group velocity of the fundamental is greater than the group velocity of the SH. This difference in the group velocity of the interacting pulses makes them separate as they propagate in the medium, introducing distortions in the temporal shape of the pulses. The parameter that relates the difference in group velocities of two interacting pulses is called *group velocity mismatch* (GVM), defined as:

$$GVM = \left| v_g(2\omega)^{-1} - v_g(\omega)^{-1} \right| \tag{99}$$

A parameter related to GVM is *pulse walk-off distance*:

$$d_w = \frac{\tau_0}{GVM} \tag{100}$$

where τ_0 is the pulse duration.

Finally, let us define two other parameters that will be used throughout this chapter to quantify the cumulative nonlinear phase resulting from the Kerr effect.

The first one is the break-up integral (or B integral), which is defined as:

$$B = \frac{2\pi}{\lambda} \int_0^L n_2 I(z) dz \tag{101}$$

Since $n_2 I$ is the nonlinear change in the refractive index, it can be easily perceived that the B integral is the total on-axis nonlinear phase shift accumulated in a medium of thickness L.

The second parameter is self-phase modulation length:

$$L_{SPM} = \frac{2c}{\omega_0 n_2 I} \tag{102}$$

defined as the thickness where the B-integral equals unity in the undepleted pump approximation.

In the following subsections, we will solve Eq. (92) and (93) by making use of SNLO software, and the results obtained from the simulations will be compared with the experiments performed in the laboratory.

4.3.2 Temporal and spectral characteristics

Although the aim of this chapter is to present a study of spatial effects in SHG, it is worthy to first provide a brief overview of the temporal characteristics of SHG with femtosecond pulses. A complete description of the temporal and spectral characteristics of SHG can be found in references [210, 211, 215-217].

To solve the coupled-amplitude equations that govern the process of type I SHG we will make use of SNLO [218, 219]. This software accounts for diffraction, self-modulation, walk-off, absorption and group-velocity mismatch, and allows us to consider non-uniform transverse profiles. It calculates intensity and phase in the temporal and spectral domains for both the SH, and the non-converted fundamental pulse, using the crystal parameters and the fundamental pulse at the entrance as inputs. It also returns information about the spatial profile and phase distortions (in terms of M^2, tilt and curvature), although we will leave the study of spatial characteristics for the next section. A description of the code can be found in [220].

The spatial characteristics of the input fundamental beam will remain the same in all the simulations of this subsection: we will consider a Gaussian intensity profile with a diameter of 2.5 mm at full-width half maximum (FWHM). We will restrict our study to Type I SHG of 120 fs transform limited pulses centred at 795 nm. As nonlinear medium we have chosen a 2 mm thick BBO crystal. The perfect phase-matching condition is always satisfied for the central wavelength (θ=29.4º). In Table 4.2, we have summarized the most important parameters of several non-linear crystals cut for type I phase matching.

		BBO	KDP	LBO
Walk-off (mrad)		68.04	29.55	16.48
Phase velocity	800 nm	c/1.660	c/1.502	c/1.611
	400 nm	c/1.660	c/1.502	c/1.611
Group velocity	800 nm	c/1.684	c/1.526	c/1.632
	400 nm	c/1.742	c/1.550	c/1.668
GDD (fs^2/mm)	800 nm	75.1	27.3	46.6
	400 nm	195.9	106.8	128.1
θ_{PM} (º)		29.4	44.9	90
φ (º)				31.6
d_{eff} (pm/V)		2.00	0.30	0.75
n_2 (cm^2/GW)		3.49×10^{-16}	4.35×10^{-16}	

Table 4. 2: Parameters for commonly used frequency doubling crystals

We have chosen two different input energies, 5 and 320 μJ corresponding to 0.5 and 34 GW/cm^2 peak intensities. The results are summarized in Fig 4. 6.

First of all, we observe that conversion efficiency is higher for the most intense fundamental pulse, which is in line with the trend described by Eq. (84).

As to the spectrum, thickness of the crystal limits the spectral bandwidth. However, when high intensities are reached (Fig 4. 6c) the spectral wings that appear (mainly due to SPM, XPM and higher order nonlinear effects) broaden the spectrum.

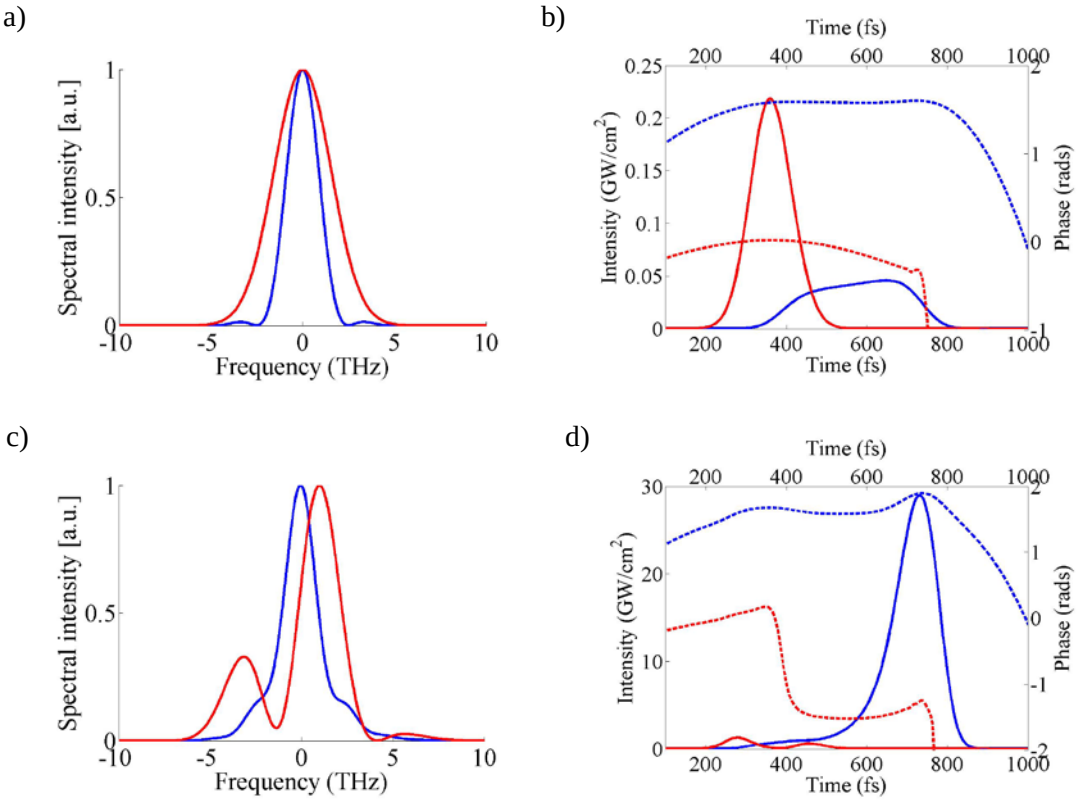

Fig 4. 6: Time and spectral characteristics of the fundamental (red) and the SH (blue). Spectrum for (a) 5 and (c) 320 µJ input energy pulses (0.5 and 34 GW/cm^2 peak intensity, respectively). Intensity (solid line) and phase (dotted line) for (b) 5 and (d) 320 µJ input energy pulses.

For transform-limited pulses the effects of GVD must be taken into account if the pulse-spreading distance is shorter than the thickness of the crystal. In this case, the walk-off distance is 0.5 mm and the pulse-spreading distance for the SH is 19 mm. Since the crystal length is 2 mm, we can conclude that pulse broadening due to GVD can be neglected.

On the other hand, if the pulse walk-off distance is shorter than the crystal length, once the fundamental pulse begins to separate from the generated SH pulse, the more intense part of the fundamental pulse will be spatially overlapped with the leading part of the blue pulses, making the conversion into SH more efficient in this zone and thus elongating the SH pulse (Fig 4. 6b).

As to phase, when the energy is low we observe that the fundamental pulse presents a quadratic phase (linear chirp). This is mainly due to GVM, since longer wavelengths travel faster than shorter ones. The phase of the SH is more complex and can be seen as the combined action of GVM and the phase mismatch.

For BBO, the Kerr nonlinear index of refraction is $n_2=3.49\text{x}10^{-16}$ cm^2/GW and, therefore, in low-intensity cases the effects of SPM and XPM are clearly negligible. However, as intensity

increases, the Kerr nonlinearity starts to play a role and thus, apart from the previous effects, SPM, XPM and other higher order nonlinear effects must be considered. This is the reason why, for example, at 34 GW/cm^2 input intensity the frequency chirp becomes much more complex (for both the fundamental and the SH).

For comparison purposes, in Fig 4. 7 we illustrate the simulation with a peak intensity of 0.5 GW/cm^2 and a crystal thickness of 10 μm (all other parameters are kept the same), where GVD and walk-off effects can be neglected. In the frequency domain, the spectrum is broader than in the previous case. This is explained by the fact that crystal thickness in this case does not limit the range of wavelengths to be frequency doubled.

Three main differences are observed in the temporal domain: the pulse is shorter, it maintains a Gaussian profile and it presents a purely quadratic phase (linear chirp). The first feature is related to the broader spectrum. In addition, the time delay of just 2 fs in 10 μm between the SH and the fundamental caused by GVM, together with the absence of chirp in the fundamental beam and the low energy that prevents higher order nonlinear effects (mainly SPM and XPM), is what maintains the Gaussian profile. The purely linear chirp is associated with the intrapulse group-velocity dispersion, IGVD (i.e., the different velocities among the spectral components that form the pulse). The effect of the IGVD results in a slight broadening of the pulse in the temporal domain.

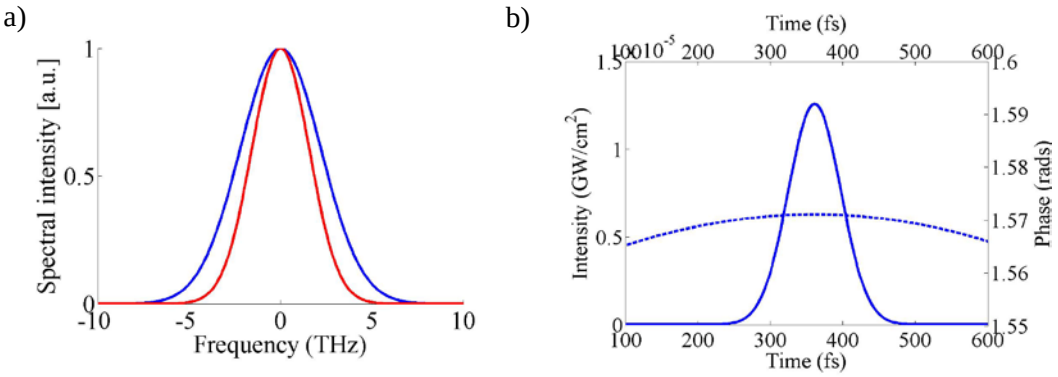

Fig 4. 7: a) Comparison between the spectral intensity of the fundamental (red) and the SH (blue) and b) time characteristics of the SH when using a 10 μm thick BBO and 0.5 GW/cm^2 peak intensity pulses. In panel b) the dotted line represents the phase and the solid line the intensity.

4.4. Spatial effects in the absence of aberrations (plane waves)

4.4.1 Numerical model and experimental setup

As in the previous section, we will solve the coupled-amplitude equations by making use of SNLO. Although the software allows us to vary many parameters, for comparative purposes we have chosen conditions similar to those in the laboratory.

To carry out the experimental study, we used the setup sketched in Fig 4. 8. A half-wave plate and a polarizer allow us to control the energy that can be increased up to 1 mJ. A telescope

composed of two achromatic lenses collimates the beam and reduces its size by one half. The beam is frequency doubled in a 2 mm thick BBO crystal (θ= 29.2º, φ= 90º, Ekspla), cut for type I perfect phase matching at 795 nm working at normal incidence. The crystal is mounted on a rotating stage, which allows us to tune the angle. The reflection, from a wedge, is filtered through a band-pass filter (FG37S or FGL610S, both from Thorlabs) and directed towards a SID4-HR wavefront sensor from Phasics S.A. [157]. Note that we decided to use a wedge to attenuate the beam instead of neutral filters to avoid phase distortions (e.g. Kerr effect in the filters) that could affect the results. The transmitted second-harmonic is used to control the wavelength by spectrum monitoring with a high resolution spectrometer (Ocean Optics, HR4000).

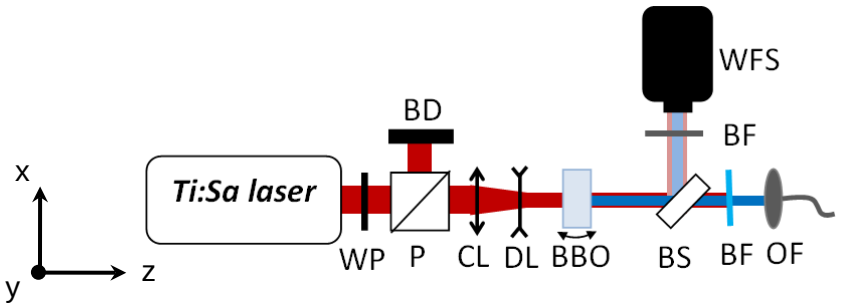

Fig 4. 8: Experimental setup (WP: half-wave plate; P: polarizer; BD: beam dumper; CL: convergent lens; DL: divergent lens; BS: beam sampler; BF: band-pass filter; OF: optical fibre coupler; WFS: wavefront sensor).

A good spatial characterization of the input fundamental beam is crucial to predict the intensity distribution and focusability of the SH. First of all, the beam profile and wavefront were characterized (Fig 4. 9). All the measurements have been averaged over 10 shots.

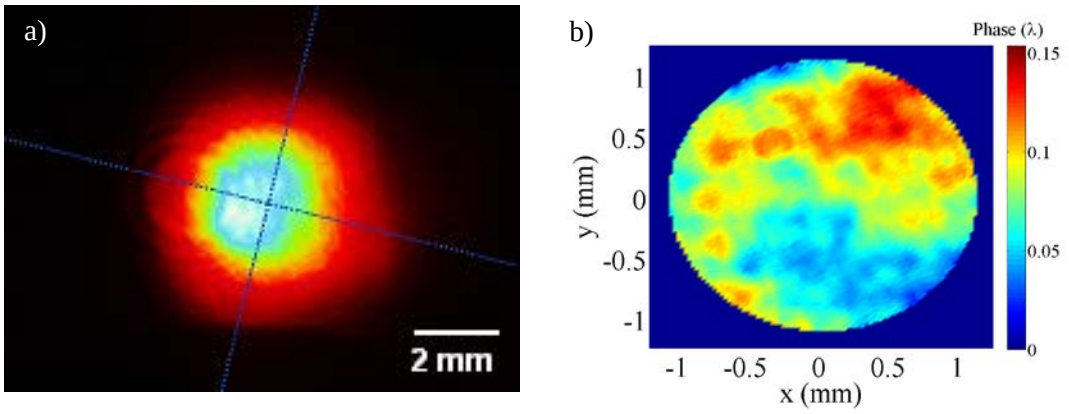

Fig 4. 9: Characterization of the collimated input fundamental beam : a) beam profile and b) spatial phase (PtV in λ units).

A closer look at the results reveals a phase distortion of (0.153±0.003)λ (PtV) over a 2.5 mm pupil. Since there are currently no adaptive mirrors available in our laboratory, it was not possible to further correct the remaining aberrations from the optical systems and the laser itself.

Although the intensity profile can be termed as Gaussian, there are certain hot spots that have a clear influence on the SH distribution. A beam profile analysis shows an ellipticity of 0.99 and a beam diameter of 4.2 mm at $1/e^2$.

4.4.2 Low-intensity regime

First, we will focus on beams with almost flat wavefronts at intensities low enough to neglect high-order nonlinear effects inside the crystal. For the simulation we will consider Gaussian time and spatial profiles that fit within the laser parameters.

We have studied type I SHG in a 2 mm BBO for the case of transform limited 120 fs pulses centred at 795 nm. The energy was set to 5 μJ (corresponding to 0.5 GW/cm^2 peak intensity), satisfying the perfect phase-matching condition for the central wavelength (θ=29.4º). The nonlinear refractive index is also included in the simulation (n_2=3.49x10^{-16} cm^2/W). The detector was situated 100 mm away from the crystal exit face. The pupil diameter for the wavefront characterization was set at 2.5 mm for all cases.

Results from the simulation with SNLO (2D-mix-SP module) are presented in Fig 4. 10. As it can be observed, the SH retains the Gaussian distribution of the fundamental, although with a smaller radius, which is explained by the fact that the intensity of the SH scales up, in a first approximation, in quadratic proportion to that of the fundamental.

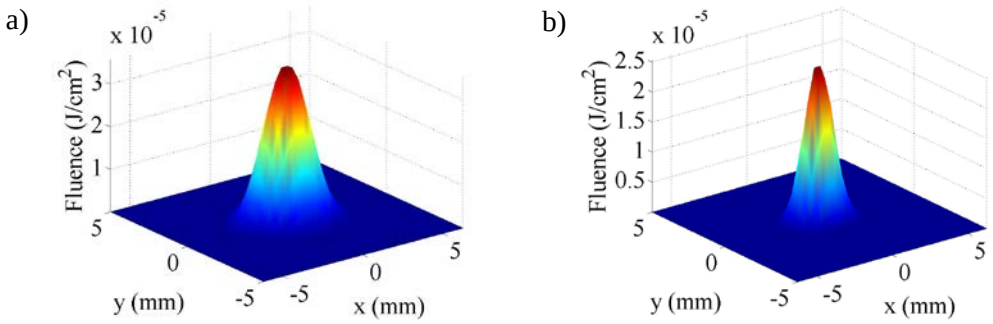

Fig 4. 10: Simulated fluence a) the non-converted fundamental beam and b) the SH for an incident fundamental pulse (flat wavefront) of 120 fs with 5 μJ input energy (0.5 GW/cm^2 peak intensity). The condition of perfect phase matching is satisfied for the central wavelength.

The experimental results for this case are presented in Fig 4. 11. The intensity profiles are very much in accordance with the theory. The calculated walk-off angle in this case is ρ=68.36 mrad. For a crystal thickness of 2 mm this leads to a separation between the ordinary (fundamental) and extraordinary (SH) waves of 137 μm. Since the beam size is much larger than this value it is possible to conclude that the SH beam quality is not degraded by walk-off effect, which is shown in Fig 4. 11.

The intensity distribution of the fundamental beam plays a role in shaping the wavefront of the SH. In this case the Gaussian distribution of the fundamental beam, together with diffraction, is expected to yield a slight curvature in the SH phase [208]. However, the magnitude of the aberrations produced by these effects is small and can therefore be considered negligible when compared to the aberrations “inherited” from the fundamental wave.

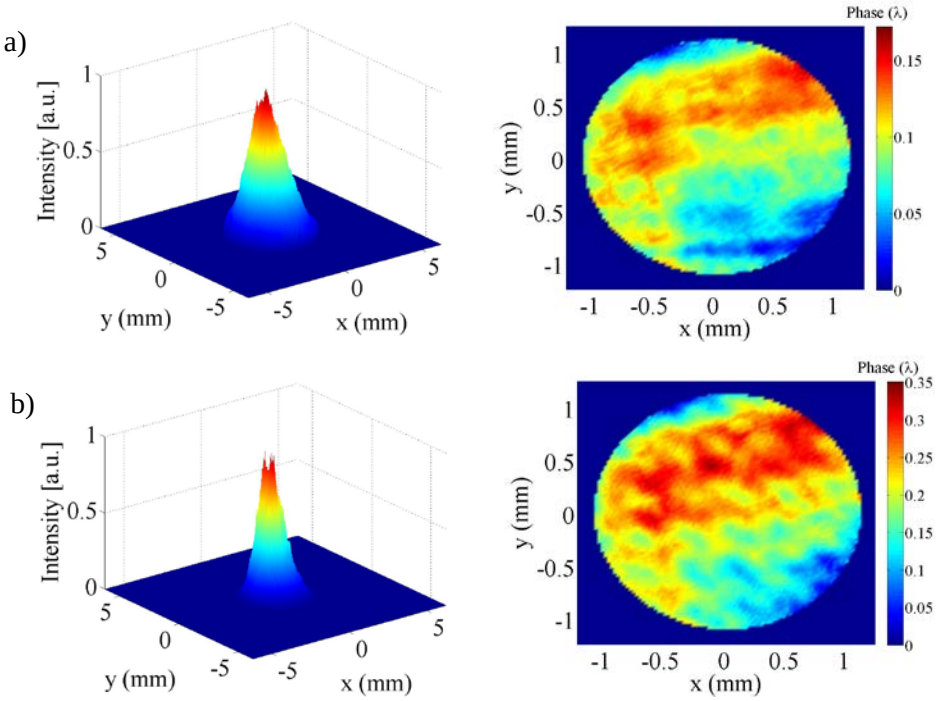

Fig 4. 11: Experimental intensity profile and wavefront for a) the non-converted fundamental beam and b) the second-harmonic of 120 fs pulses with 5 μJ input energy. The condition of perfect phase matching is satisfied for the central wavelength. The beam is collimated, although it was not possible to remove high order aberrations.

The magnitude of (0.171±0.009) λ PtV for the fundamental beam in Fig 4. 11a corresponds to the absolute measurement 100 mm away from the exit face of the crystal. In order to elucidate the wavefront distortions resulting from SHG, these results must be referred to the initial phase (i.e., without the BBO) measured in the same detection plane. In Fig 4. 12 we show the wavefront of the non-converted fundamental beam once the initial phase has been subtracted resulting in a PtV aberration of (0.091±0.005)λ. These remaining distortions can be explained in terms of laser fluctuations and phase distribution of the input beam. On the one hand, we must take refraction in the crystal into account, since it will cause phase distortion in non-perfect plane waves. On the other hand, the initial aberrations of the fundamental beam induce a non-uniform phase mismatching factor across the beam, affecting conversion efficiency and distorting the SH beam profile [208, 210]. We will return to this topic in the next section, where beams with different aberrations will be examined.

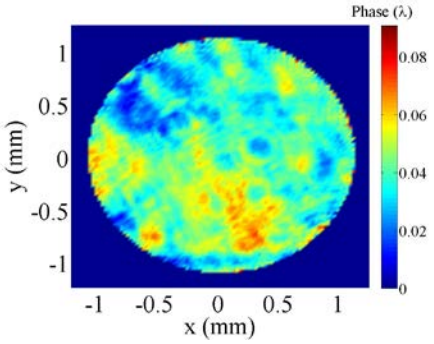

Fig 4. 12: Wavefront aberrations of the non-converted light referred to the initial phase of a collimated input fundamental beam.

We also computed the difference $2\psi(\omega)-\psi(2\omega)$ (Fig 4. 12). Under perfect phase matching conditions, it is found to be $(-0.011\pm0.037)\lambda$. This value is comparable to the error (such a large error comes from laser shot-to-shot fluctuations), indicating that no substantial phase distortion has been induced in the SH beam.

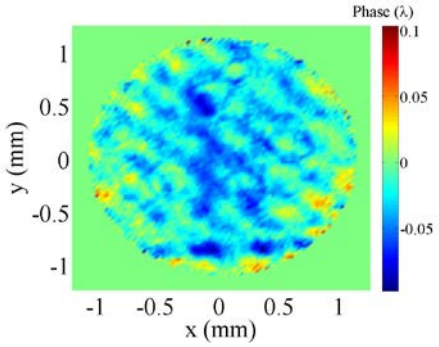

Fig 4. 13: Computed difference $2\psi(\omega)-\psi(2\omega)$ for a collimated input pulse.

Finally, we studied the spatio-spectral distribution of the SH beam by monitoring the spectrum along the transversal axis (x axis, see definition of the axes in Fig 4. 8). The optical axis is contained in the XZ plane, keeping a 29.4º angle with respect to the y axis. We can conclude that spatial chirp is negligible, since no spectral dependence is found with respect to the transversal coordinate. The corresponding on-axis spectrum was also numerically computed with SNLO and is shown in Fig 4. 6.

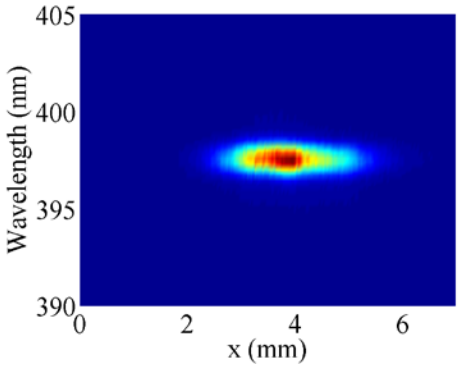

Fig 4. 14:Spectrum along the x-axis for the SH . The fundamental pulse has an almost flat wavefront and the input intensity was 0.5 GW/cm^2.

4.4.3 High-intensity regime

We will now proceed to examine the results when the energy is increased to 320 μJ (corresponding to 34 GW/cm^2 peak intensity), keeping all other parameters the same. The calculated value of the B-integral is 0.20, indicating that in this case high-order effects are small but not negligible.

Fig 4. 15 illustrates the experimental results (as in the previous case, for a proper comparison, the experimental results must be referred to the initial phase).

When compared to the low-intensity case, it is observed that the non-converted fundamental beam exhibits a modulated profile together with the appearance of a pedestal. These spatial features indicate that downconversion is taking place at a larger rate at those points where the incident

pump intensity was maximal. In spite of this change in pump beam spatial quality when the energy is increased, no significant changes are found in the SH beam profile.

The wavefront is found to be (0.206±0.010)λ PtV for the non-converted fundamental beam and (0.421±0.019)λ PtV for the SH. This wavefront aberration is mainly a defocus due to cascaded second-order effects. Additionally, the effects of the third-order susceptibility cannot be fully neglected and will therefore yield small phase distortions following the intensity pattern of the fundamental beam.

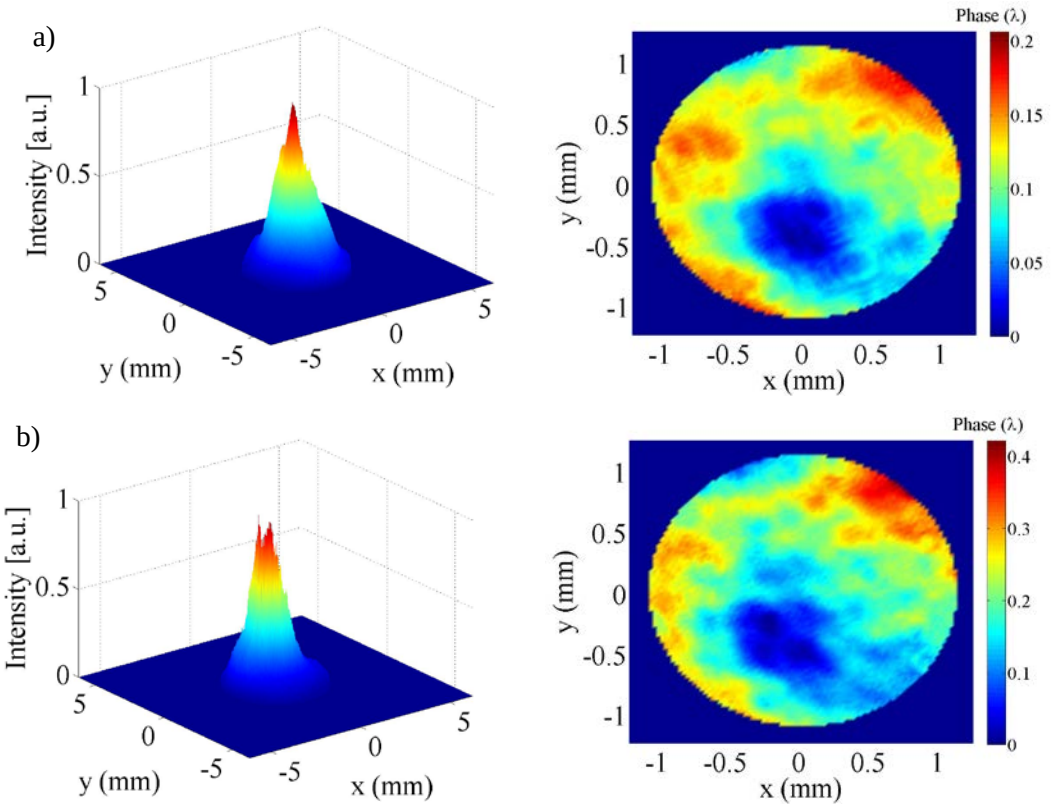

Fig 4. 15:Experimental intensity profile and wavefront for a) the non-converted fundamental beam and b) the second-harmonic of 120 fs pulses with 320 μJ input energy. The condition of perfect phase matching is satisfied for the central wavelength.

It is interesting to study the focusability of the generated SH, which will be strongly affected by the aberrations. Although the size of the focal spot makes it difficult to perform the experimental measurements, we have computed the intensity of the SH in the focal plane of a 100 mm focal length lens in the Fresnel approximation [221] assuming monochromatic waves (λ=397.5 nm):

$$I(x_2, y_2) = \left| -i \exp\left[i \frac{k}{2f} \left(x_2^2 + y_2^2 \right) \right] \int\int U_0(x_1, y_1) P(x_1, y_1) \exp\left[-i \frac{k}{f} \left(x_1 x_2 + y_1 y_2 \right) \right] dx_1 dy_1 \right|^2 \quad (103)$$

where (x_1,y_1) and (x_2,y_2) are the spatial coordinates at the input of the lens and in the focal plane respectively, U_0 is the electric field against the lens, P is the pupil function of the lens (1 inside the lens and 0 outside) and f is the focal length of the lens. In Fig 4. 16 we represent the focal spot

using the measured SH intensity as input amplitude for U_0 and assuming a flat wavefront (left column) or the actual wavefront aberrations (right column).

To estimate peak intensity in the focal spot, I_0, we have assumed a SH Gaussian temporal profile in Fig 4. 16:

$$I(x_2, y_2, t) = I_0 I(x_2, y_2) \exp\left(-4 \ln 2 \frac{t^2}{\tau^2}\right) \tag{104}$$

with τ being the temporal duration at FWHM calculated by SNLO software (335 fs for 0.5 GW/cm^2 and 123 fs for 34 GW/cm^2 input pulses, respectively). The SH energy, E, has been estimated by taking into account the conversion efficiency, η. Moreover, in the case of aberrated beams, we corrected this factor including the phase matching condition, PM:

$$E = PM . \eta . E_{IR} \tag{105}$$

where E_{IR} is the input energy of the fundamental beam.

In the case of a flat wavefront, PM takes a value of 1. For aberrated beams we compute phase matching at each point of the input beam by finding the wave vectors k (perpendicular to the wavefront surface). This value is normalized as:

$$PM = \frac{\sum_{i=1}^{N_x} \sum_{j=1}^{N_y} PM(x_i, y_j)}{N_x N_y} \tag{106}$$

where N_x and N_y are the number of points on the grid along the x and y directions, and $PM(x_i,y_j)$ the phase matching condition evaluated at each point.

The beam is then spatially integrated and peak intensity is calculated as:

$$I_0 = \frac{E}{\iint I(x_2, y_2) dx dy} \sqrt{\frac{4 \ln 2}{\pi \tau^2}} \tag{107}$$

The conversion efficiency η has been experimentally found for the case of real collimated beams, obtaining η=37.5% at 34 GW/cm^2 and η=3.3% at 0.5 GW/cm^2. Since aberrations are still present, we estimated conversion efficiency for a perfect plane wave by taking into account the PM factor:

$$\eta_{PW} = \frac{\eta_{RB}}{PM} \tag{108}$$

where η_{RB} is the efficiency of the real beam and η_{PW} is that of the perfect plane wave.

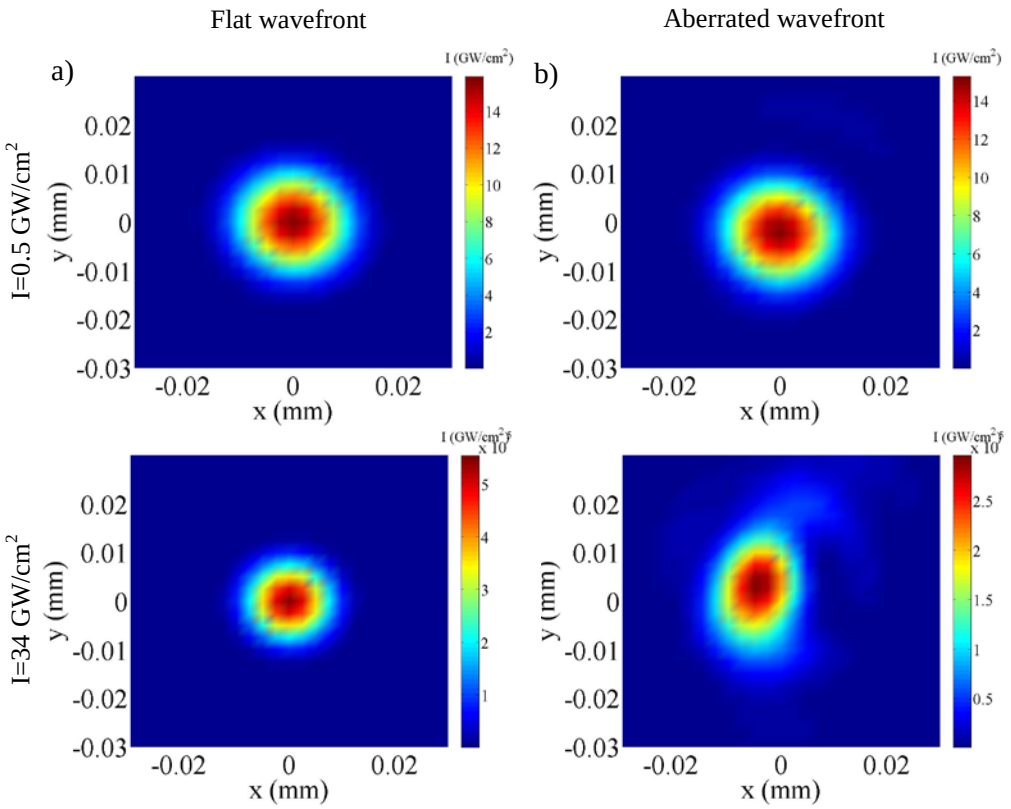

Fig 4. 16:Comparison of the calculated focal spot a) without aberrations and b) with aberrations in the low-intensity (top) and high-intensity (bottom) cases.

When compared to the low-intensity case, it is observed that when assuming a field with the experimental intensity profile but a perfect flat wavefront, the focal spot is smaller (0.025 mm at $1/e^2$ criterion for 0.5 GW/cm^2 peak intensity, opposed to 0.018 mm for 34 GW/cm^2). This fact is easily explained by simply looking at the SH beam profile: in the high-intensity case we are operating in the saturation regime and therefore the contrast ratio is reduced, which makes the beam diameter larger. Since the focal spot scales inversely to the size of the input beam, it is expected to become smaller as the energy is increased. This, together with a higher input energy and additional conversion efficiency yields a much higher peak intensity in the second case (I_0=2.95x10^5 GW/cm^2 for 34 GW/cm^2 in contrast to I_0=15.24 GW/cm^2 for 0.5 GW/cm^2).

It is worth pointing out that, despite its size, the beam profile is very similar in both cases, indicating that further modulations in the focal intensity can be attributed to wavefront aberrations.

When the aberrations are taken into account, the degradation of the focal spot is significant in the high-intensity case, leading to a dramatic drop of peak intensity to I_0=2.95x10^5 GW/cm^2 (nearly half of that for a perfect plane wave, which was found to be I_0= 5.53x10^5 GW/cm^2). Moreover, contrary to what happens in the case of aberrated free pulses, the beam size in the focal plane of the lens becomes larger as the intensity increases. This is a direct consequence of wavefront distortion due to high-order nonlinear phenomena: in particular, induced defocus forces the beam in the low intensity case to focus later.

Finally, we recorded the spectrum along the transverse axis. The spectrum of the SH is broader than in the low-intensity case due to the spectral wings generated by SPM. This allows us to

achieve a spectral bandwidth similar to that of thin crystals at the cost of degrading the temporal profile. In panel b) we have plotted the graph for the fundamental beam. In this case, we observe certain modulations in the spectrum of the fundamental beam that indicate that SPM has started to play a role.

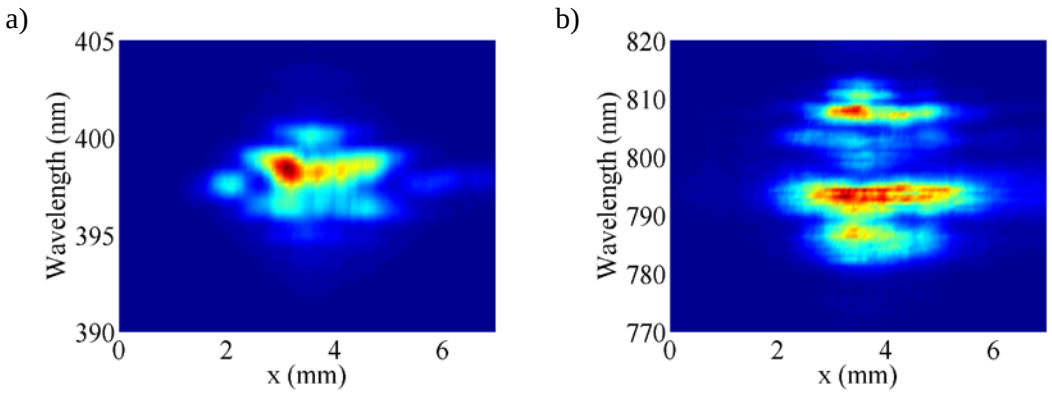

Fig 4. 17: Normalized spectra along the x-axis for a) the SH and b) the non-converted fundamental beam. Input peak intensity was 34 GW/cm^2 and the beam presented a nearly flat spatial phase.

4.4.4 Phase distortions by cascaded second-order effects

Additionally, we have monitored induced defocus in both the SH and the non-converted fundamental beam, as a function of the phase mismatch condition. For this purpose, we mounted the BBO crystal on a rotational stage that allowed us to accurately control the angle.

The results are presented in Fig 4. 18. The experimental dots are obtained by averaging 10 pulses. For the 5 μJ case, no trend is observed (the oscillations in the plot appear in the order of the wavefront sensor precision).

The situation is completely different when the energy is increased to 320 μJ. Due to the Gaussian beam profile, the Kerr effect will yield a small wavefront distortion in terms of focusing. However, this phenomenon alone cannot explain the trend observed in the defocus as the phase mismatch condition is tuned.

The key is the nonlinear refraction (NLR) produced by cascaded second-order effects $\chi^{(2)}(2\omega=\omega+\omega):\chi^{(2)}(\omega=2\omega-\omega)$. As mentioned in the previous chapter, in this process a 2ω photon produced by SHG interacts with a photon of the fundamental beam through DFG to generate a photon at ω. Therefore, part of the frequency-doubled light is downconverted with a shifted phase in proportion to the irradiance of the fundamental. This effect has been exploited, for example, for direct B-integral compensation [175] or for self-compression in visible femtosecond optical parametric oscillators [222].

According to the theory and previous studies [174, 175], we should observe a change in the defocus (from positive to negative) around $\Delta k=0$. We believe there could be two reasons that might explain why our results are not in agreement with those previously reported. On the one hand, there might be a spatial tilt of the beam. On the other, we believe that the broad bandwidth of our pulses

could give rise to mixing effects and high-order nonlinear processes that could also contribute to the induced phase.

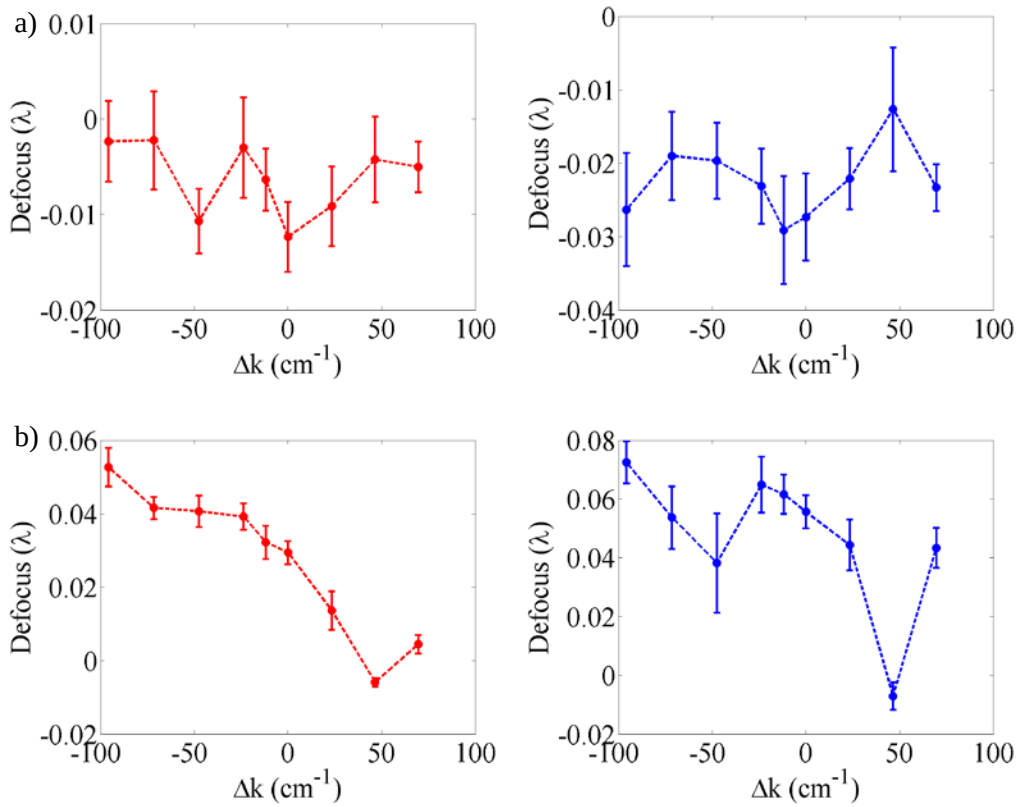

Fig 4. 18: Graphics showing defocus (RMS) as a function of the phase mismatch for the non-converted fundamental (red) and the SH (blue) with a) 5 μJ and b) 320 μJ input pulses.

4.5. Wavefront dependence of second-harmonic generation

4.5.1 Overview

Although Eq. (84) was deduced for plane waves, we can still extract certain conclusions for the case of aberrated beams. For the sake of simplicity, we will restrict our study to two dimensions. At each point, the wave-vector will be perpendicular to the wavefront curvature (see Fig 4. 19).

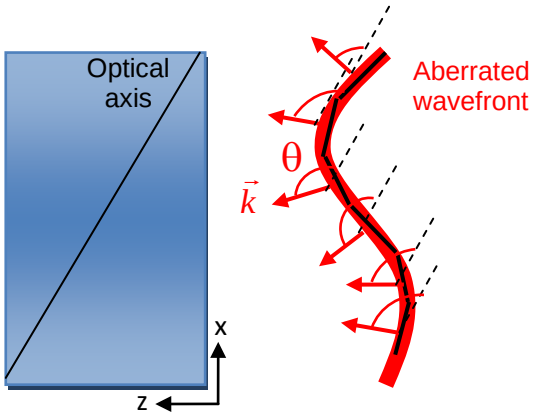

Fig 4. 19: Sketch of an aberrated beam inciding on a uniaxial crystal and corresponding wave-vectors

It is obvious that the angle between the wave-vector and optical axis θ will be different at each point. Therefore, while the ordinary index remains the same in all positions (it only depends on wavelength), the extraordinary index does not. Consequently, the conversion efficiency for a given wavelength will be different depending on the point under analysis. In Chapter 5 we will take advantage of this fact to build a wavefront sensor.

Following this reasoning we can conclude that for a flat wavefront (i.e., plane waves) the phase mismatch factor will remain the same throughout the whole beam. Thus, conversion efficiency will change from one point to another exclusively according to intensity variations, and the intensity of the SH will maintain the shape of that of the fundamental beam. On the contrary, in the case of aberrated wavefronts, conversion efficiency will also depend on the aberrations, and the SH intensity shape will be distorted.

When the aberrations are small (below 0.2λ PtV over an 8 mm pupil size), the intensity distribution remains nearly undisturbed. The SH wavefront aberrations are very similar to those of the fundamental beam and satisfy relationship expressed in (64). Differences arise from phase mismatching induced by the aberrations, which affects the whole process of SHG coupling. In these cases, the effects of diffraction and intensity dependent aberrations are very small compared to the aberrations of the fundamental waves, and can therefore be neglected. However, walk-off still plays a significant role: it affects the intensity distribution of the SH and induces a tilt in the wavefront that will compete with the aberrations [208].

When the aberrations are more severe (for example, 0.2λ PtV over a 0.25 mm pupil size), relationship (64) does not hold. Moreover, conversion efficiency across the aperture will not be uniform due to phase mismatching and changes in the transverse intensity distribution. Although it will be the most significant source, it is important to remark that the final SH intensity distribution will not only depend on phase mismatching, but also on other processes (diffraction, walk-off…).

Up to this point, we have assumed that the main propagation direction maintained perfect phase matching conditions. When this is not the case, total efficiency decreases and the effects of the aberrations become more evident. At some points, aberrations may compensate for a small part of the mismatch, thus increasing conversion efficiency in those points.

In the following sections, we will provide a description of SHG of aberrated femtosecond beams.

4.5.2 Experimental setup

The experimental setup, which is shown in Fig 4. 20 below, is very similar to that presented in Fig 4. 8. In this case, the telescope has been removed and substituted by lenses in order to introduce an aberrated wavefront. We will restrict our study to low-order aberrations: defocus and astigmatism. For the study of defocus, we placed a 1 m focal length lens 55 cm away from the crystal, while an astigmatic oftalmologic lens (1.50+0.25 Dp) was used in the case of astigmatism.

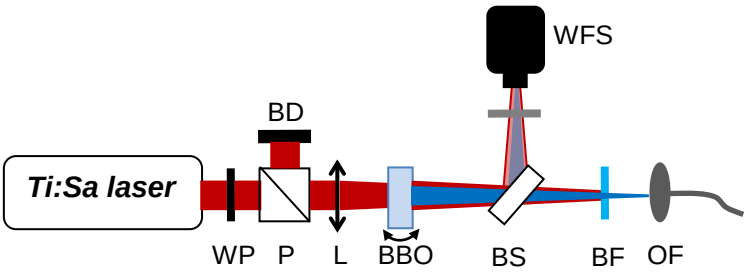

Fig 4. 20: Experimental setup (WP: half-wave plate; P: polarizer; BD: beam dumper; L: lens (either spherical or astigmatic); BS: beam sampler; BF: band-pass filter; OF: optical fibre coupler; WFS: wavefront sensor).

4.5.3 Defocus

The beam profile and wavefront were averaged over 10 shots (Fig 4. 21), resulting in an induced phase distortion of (1.760±0.003)λ (PtV) over a 2.5 mm pupil. An analysis of the beam profile shows an ellipticity of 0.96 and a beam diameter of 5 mm at $1/e^2$. In order to compare the results with those of the plane wave presented in the previous section, we adjusted the energy to obtain the same peak intensity in the crystal's plane. For this reason, the energy was increased to 7 µJ in the low-intensity case (0.5 GW/cm^2 peak intensity) and to 460 µJ for high-intensity measurements (34 GW/cm^2 peak intensity).

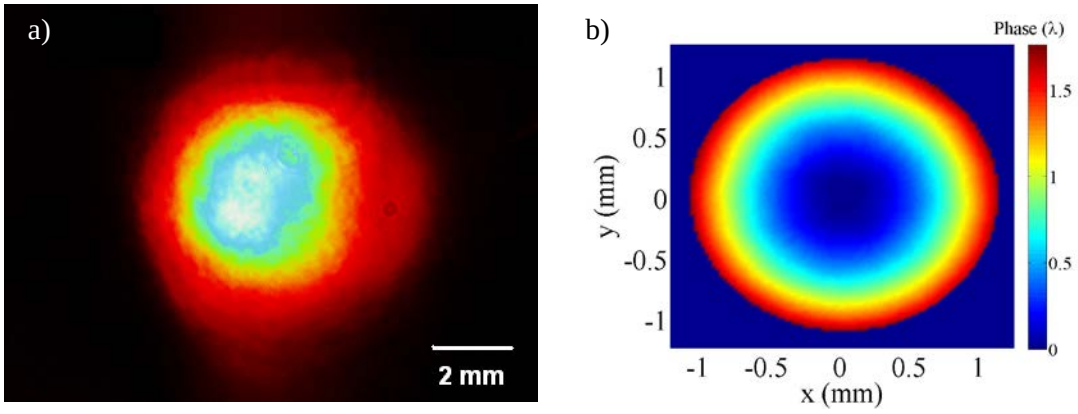

Fig 4. 21: Characterization of the input fundamental beam: a) beam profile and b) spatial phase.

4.5.3.1 Low-intensity regime

The non-converted fundamental beam exhibits a wavefront aberration of (2.141±0.014)λ (PtV) (Fig 4. 22a). The difference with respect to the input phase simply comes from the fact that the measurement is done 90 mm away from the crystal output face. For the SH (Fig 4. 22b) the resulting PtV phase is (4.323 ±0.015)λ.

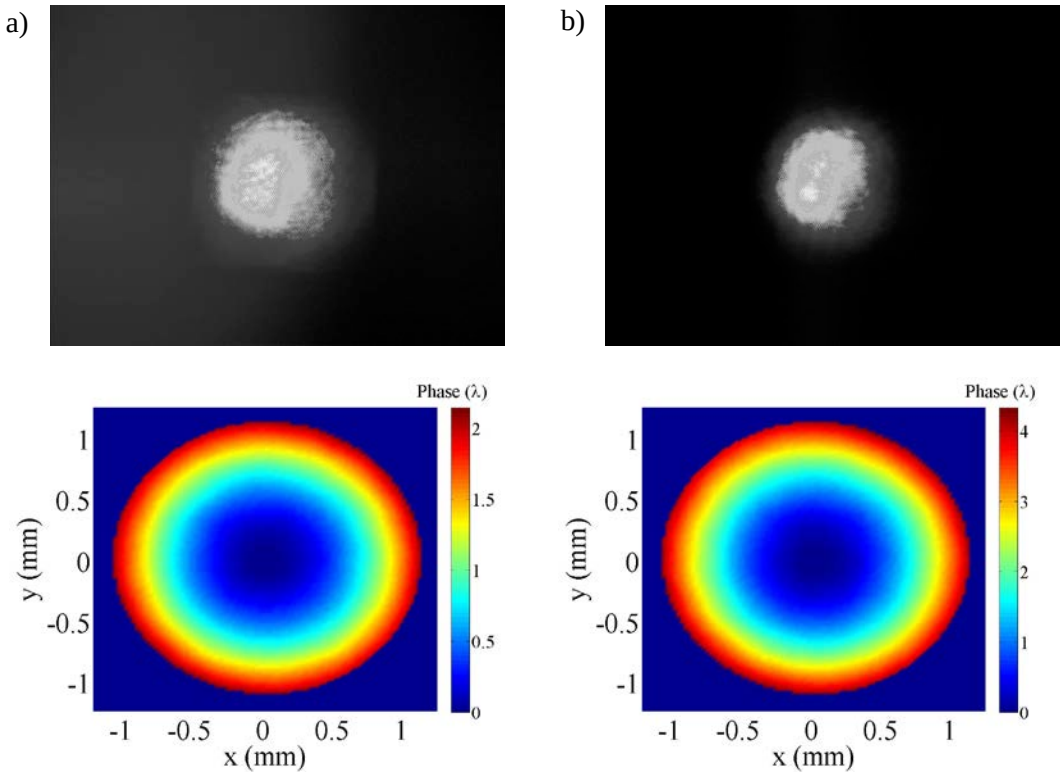

Fig 4. 22: Beam profile (top) and wavefront (bottom) for a) the non-converted fundamental beam and b) the SH.

In order to obtain different phase mismatches, the crystal was rotated around the axis that is perpendicular to the plane within which the optical axis is contained. In Fig 4. 23 we show the SH beam profile for different phase mismatches (Δk=-70 cm^{-1}, Δk=0 cm^{-1} and Δk=+70 cm^{-1}). If we focus on the intensity (Fig 4. 23b) under perfect phase matching conditions for the central wavelength, the first difference we notice with respect to the plane wave is that there is a change in ellipticity (0.88 as opposed to the 0.95 of the plane wave).

This feature can be easily understood in terms of phase mismatch due to the dependence of conversion efficiency for a given wavelength on it. When the wavefront is aberrated the phase mismatch condition is different at each point: the wave-vectors are perpendicular to the wavefront surface, presenting different angles with respect to the optical axis. As a direct consequence, the intensity profile of the SH will not only depend on the beam profile of the fundamental beam, but also on the wavefront (see Fig 4. 24).

When the angle is tuned to achieve phase mismatches of Δk=-70cm^{-1} and Δk=+70cm^{-1}, the condition of perfect phase matching is no longer satisfied for the central frequency (see Fig 4. 24), although it is satisfied for other wavelengths (789 nm and 801 nm, respectively). This produces a redistribution of the SH intensity: on the one hand, the Gaussian shape yields higher conversion efficiency at the beam centroid; on the other hand, the phase matching condition imposes higher conversion efficiency for the central wavelength in the periphery. This effect can be clearly seen in Fig 4. 23, where we appreciate a flatter beam profile in those cases where $\Delta k \neq 0$.

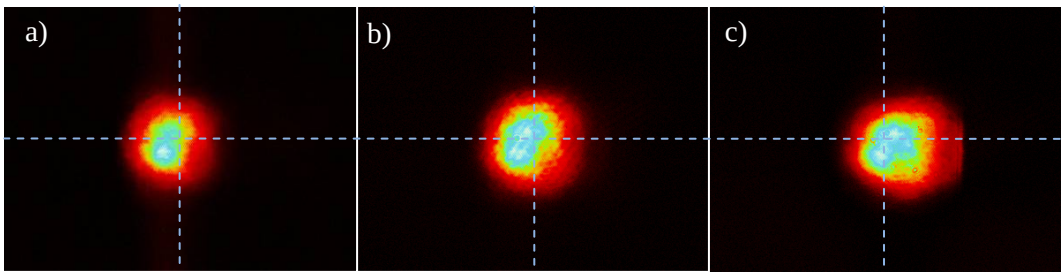

Fig 4. 23: SH beam profile for different phase mismatches: a) Δk=-95 cm^{-1},b) Δk=0 cm^{-1} and c) Δk=+70 cm^{-1}

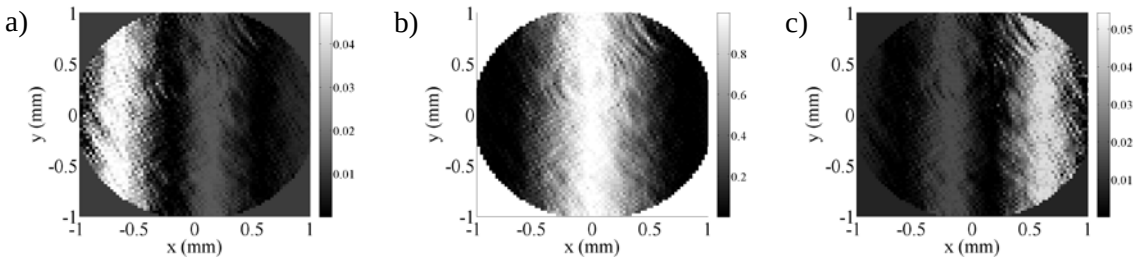

Fig 4. 24: Computed phase mismatch factor $\left(\frac{\sin\left(\Delta kL/2\right)}{\left(\Delta kL/2\right)}\right)^2$ *maps corresponding to the beams shown in Fig 4. 23 for the central wavelength.*

The spatial chirp was also monitored (Fig 4. 25). The spectral traces present a tilt that is a direct consequence of phase matching dependence on the wavelength and on the spatial phase. For Δk=0, the doubled wavelength is 795 nm just at the beam centre, where the wave-vector travels perpendicularly to the crystal surface. For other points in the x-axis the wave-vectors are at different angles with the optic axis and maximal efficiency is achieved for other wavelengths contained in the pulse.

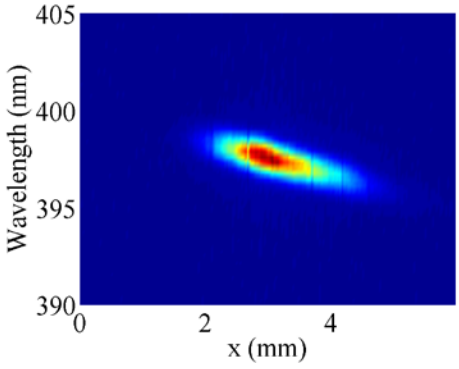

Fig 4. 25: Spatial chirp of the SH for a defocusing beam (I=0.5 GW/cm^2)

4.5.3.2 High-intensity regime

We will now increase the energy to achieve a peak intensity of 34 GW/cm^2 (maintaining all other conditions the same, as in the previous case) and repeat similar measurements. We will first study the wavefront for the non-converted fundamental and SH beams.

To discern defocus induced by an increase in peak intensity, we have subtracted the wavefront registered in the low-intensity regime (see Fig 4. 26) for the SH and the fundamental beams. For comparison purposes, in the left side of the picture we show the induced phase when the fundamental pulse presents a flat wavefront. It must be remembered that in the first case the beam is slightly larger in the detection plane.

For better understanding we have decomposed the SH phase in terms of Zernike polynomials. The analysis reveals an RMS defocus term of (0.076±0.006)λ when dealing with a plane wave and (0.047±0.004)λ for focusing pulses. Another important difference is in astigmatism at 0º, which is found to be of opposite sign: in the first case it is (0.033±0.008)λ, whereas for the focusing beam it is (-0.033±0.004)λ. To further explain these features, we have also analysed variations in the non-converted fundamental beam. As peak intensity is increased from 0.5 to 34 GW/cm^2, the original flat wavefront suffers a distortion of (0.032±0.005)λ RMS defocus and (-0.014±0.002) x-comma, any other Zernike terms being almost negligible. For the focusing beam, the change in the defocus term is comparable to that of the previous case, (0.033±0.002)λ, although in this case a 45º astigmatism of (0.014±0.005)λ appears.

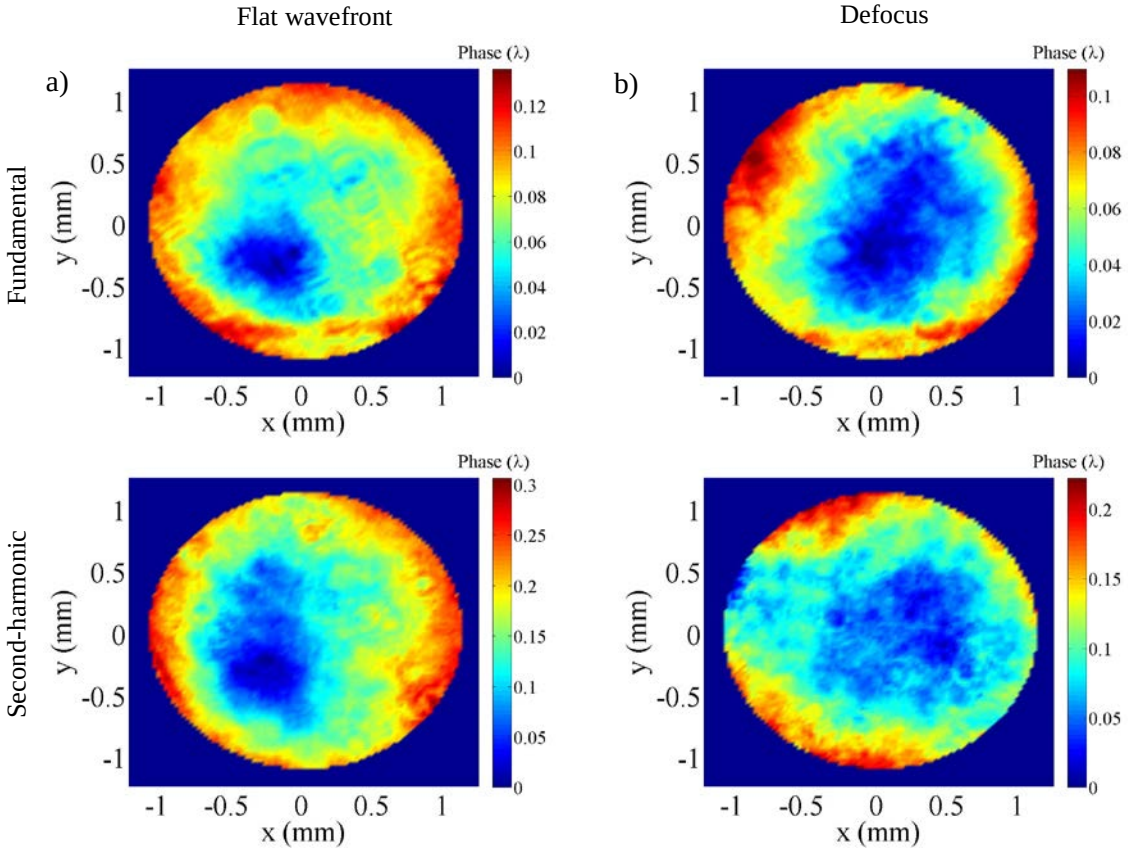

Fig 4. 26: Induced defocus in the SH (bottom) as peak intensity is increased from 0.5 to 34 GW/cm^2 under perfect phase-matching conditions when the incident fundamental pulse (top) presents a) a flat wavefront or b) a focusing wavefront.

On the one hand, these variations can be attributed to differences in the input pulse beam profile, since the nonlinear phase shifts are directly connected to the intensity of the incident fundamental beam. On the other hand, the phase shift depends not only on the intensity, but also on the phase mismatch condition which in the case of focusing beams varies across the aperture.

These phase distortions have an impact on the focusability of the SH pulses (Fig 4. 27): the degradation of the focal spot is considerable and it is enlarged by a factor 40, leading to a dramatic drop in peak intensity. In particular, for an input fundamental intensity of 0.5 GW/cm^2, the SH peak intensity at the focus of the lens is 0.035 GW/cm^2, in contrast to the resulting 20.33 GW/cm^2 when aberrations were not present. This fact is even more pronounced when the input intensity of the fundamental pulse is increased to 34 GW/cm^2, obtaining a SH peak intensity that is several orders of magnitude lower (454 GW/cm^2 as opposed to the 6.28 x10^5 GW/cm^2 that could be achieved for a plane wave).

Similar to the case presented in Fig 4. 16, the focal spot for non-aberrated beams becomes larger as the energy decreases (0.021 mm FWHM for 0.5 GW/cm^2 peak intensity, as opposed to 0.017 mm FWHM for 34 GW/cm^2). The situation is the opposite when the wavefront aberrations are included in the calculation: in such case, the Kerr effect induced defocus moves the focus forward with respect to the low-intensity case and, therefore, the beam size in the focal plane of the lens grows as the intensity is increased.

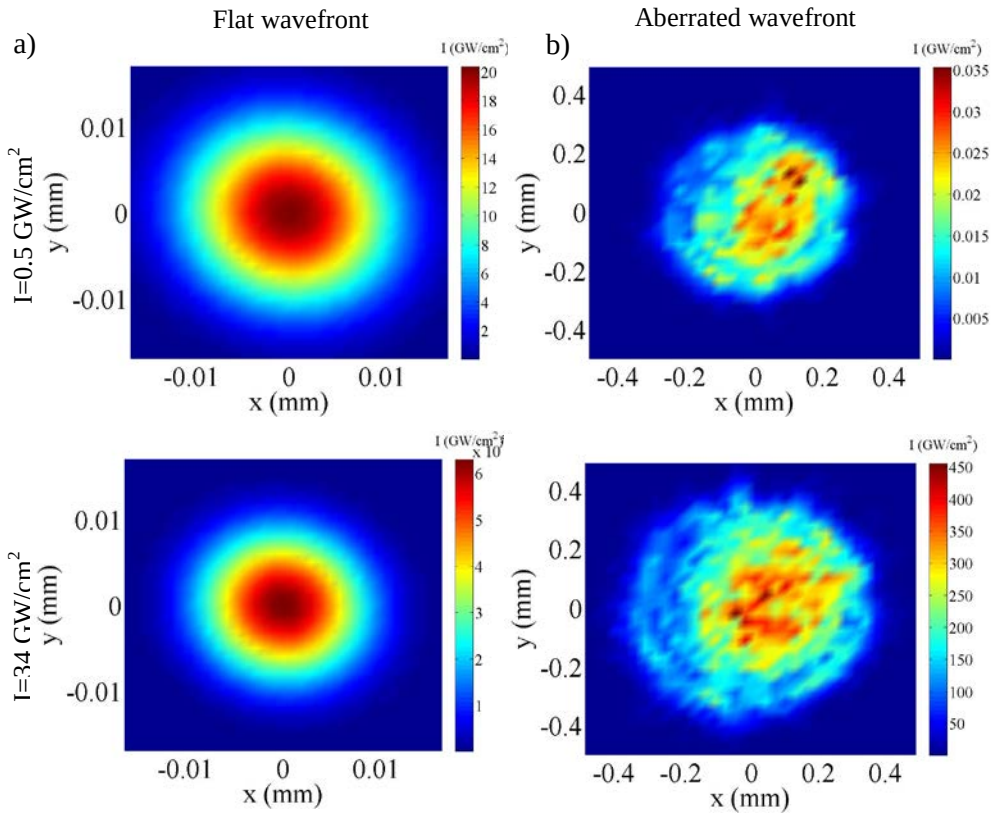

Fig 4. 27: Comparison of the numerically calculated focal spot a) without aberrations and b) with aberrations for the low-intensity (up) and high-intensity (bottom) cases. Note that the x and y dimensions are different in a) and b).

Spatio-spectral behavior was also studied in this case (Fig 4. 28): the tilt of the trace is similar to that in Fig 4. 25, although in this case it is spectrally broadened due to SPM. The trace is slightly distorted at the edges, where the spectrum shifted towards the central wavelength. We must remember that, according to the phase map, it is precisely at those points where the maximal phase

mismatch becomes larger. Outside phase matching, there are crossing effects between GVM, GVD and SPM, and the spectrum is distorted.

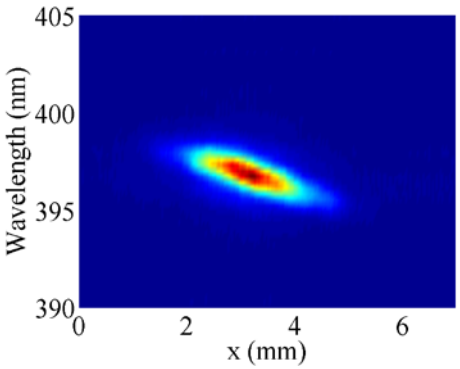

Fig 4. 28: Spatial chirp of the SH from a focusing fundamental beam (I=34 GW/cm^2)

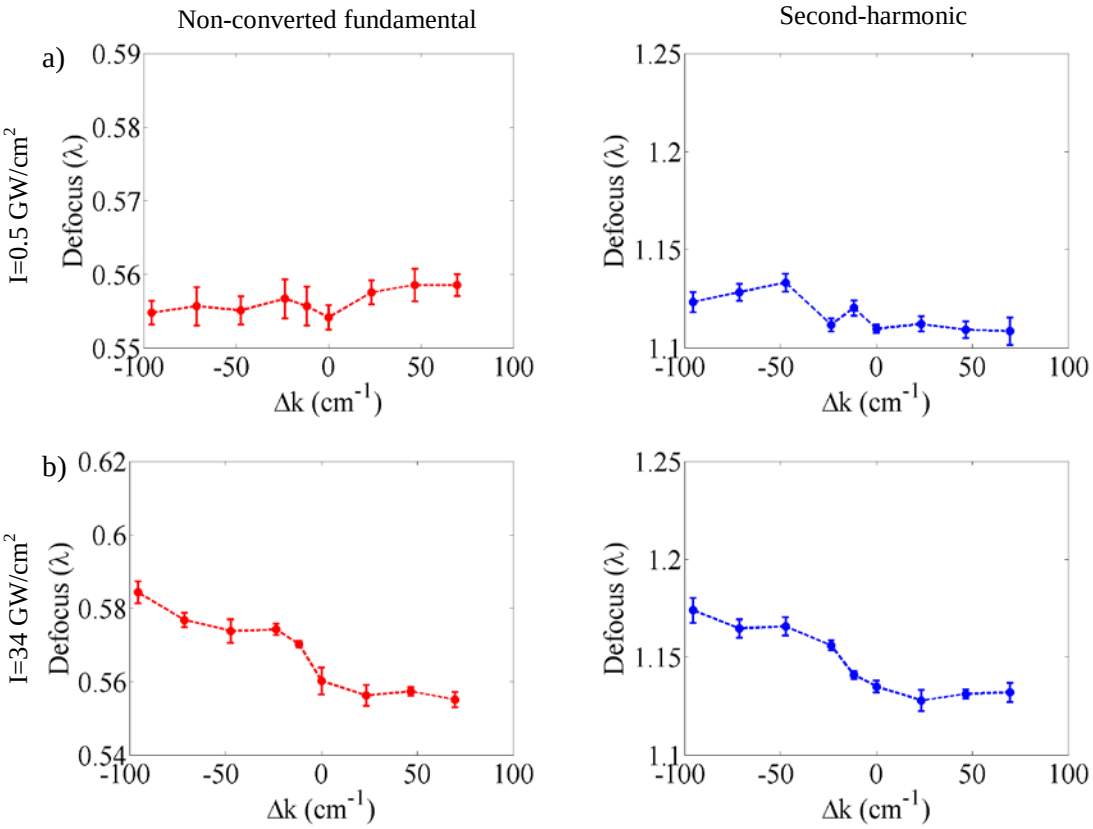

Fig 4. 29: Graphics showing the defocus (RMS) as a function of the phase mismatch for the non-converted fundamental (red) and the SH (blue) with a) 7 μJ and b) 460 μJ input pulses.

Phase distortions by cascaded second-order effects were also examined in this case. As in Fig 4. 18, when the peak intensity is of just 0.5 GW/cm^2 no trend is observed as the phase mismatch is changed, but there is a decrease in the defocus when intensity reaches 34 GW/cm^2. However, the amount of phase shift of the non-converted fundamental beam as the mismatch is shifted from Δk=-95 cm^{-1} to Δk=+70 cm^{-1} is noticeably larger in the case of flat wavefronts ($\Delta\Phi_{def}$=0.029λ RMS for focusing beams, compared to $\Delta\Phi_{def}$=0.052λ RMS for nearly plane waves). Similar results are found for the SH, where the phase shifts are $\Delta\Phi_{def}$=0.042λ RMS for focusing beams, compared to $\Delta\Phi_{def}$=0.072λ RMS for nearly plane waves.

4.5.4 Astigmatism

Unlike conventional (spherical) lenses, astigmatic lenses present two foci. For our study, we have chosen a 1.50 + 0.25 Dp lens (i.e., with nominal foci at 57.1 cm and 66.7 cm). The spatial characterization at the entrance of the crystal of the pulses focused by the astigmatic lens is presented in Fig 4. 30. The beam exhibits an ellipticity of 0.34: the width along the major axis is 4.63 mm, whereas for the minor axis it is 1.37 mm (FWHM).

The phase measurement was averaged over 10 shots over a 2.5 mm pupil, as illustrated in Fig 4. 30b. Wavefront aberration is (3.265±0.009)λ PtV. Upon decomposition in terms of Zernike polynomials, the results are mainly astigmatism at 45º, (0.617±0.002)λ RMS, and defocus, (-0.226±0.001)λ RMS.

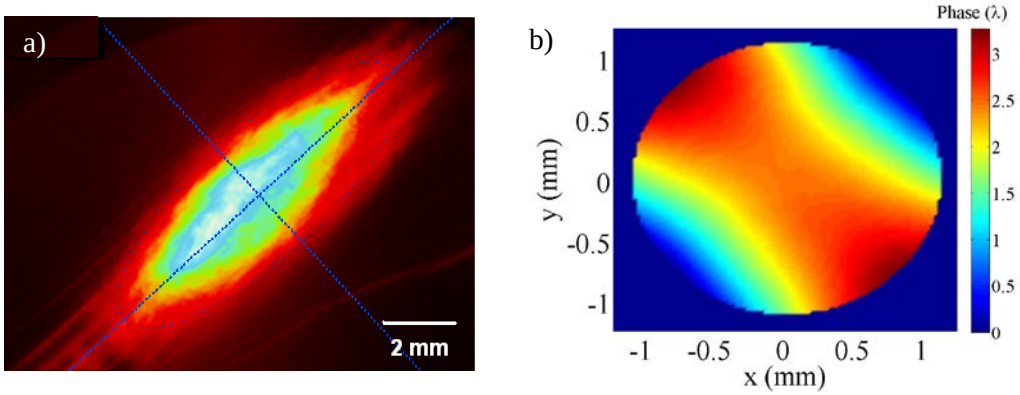

Fig 4. 30: Characterization of the input fundamental beam: a) beam profile and b) spatial phase.

4.5.4.1 Low-intensity regime

In order to distinguish the effects arising from the SHG process from those coming from the fact that the detection plane is situated 90 mm away from the crystal exit, we decided to first register the phase in the detection plane without the BBO crystal (Fig 4. 31). When compared to the reference, it is observed that defocus maintains similar, (-0.233±0.002)λ RMS, however, the 45º astigmatism increases to (1.403±0.003)λ RMS. As in the case of focusing beams, these differences arise simply from the fact that the measurements are registered in different planes.

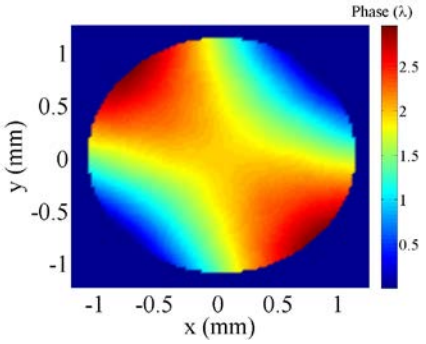

Fig 4. 31: Wavefront of the fundamental pulses measured in the detection plane without the BBO crystal

The phase fronts and spatial profiles for the non-converted fundamental and the SH beams are presented in Fig 4. 32. Wavefront aberration is found to be (3.053±0.018)λ PtV for the non-converted fundamental beam and (6.030±0.156)λ PtV for the SH. When decomposed in Zernike polynomials, it follows that the main contributions come from defocus and 45º astigmatism. In the

case of the SH, defocus is found to be (-0.436±0.008)λ RMS and the 45º astigmatism (2.757±0.017)λ RMS, whereas for the non-converted fundamental light these values are (-0.213±0.005)λ RMS and (1.414±0.009)λ respectively. These values are reasonably in line with those resulting from measuring the input fundamental pulses in the detection plane, thus indicating that at this intensity SHG does not produce any significant phase shifts.

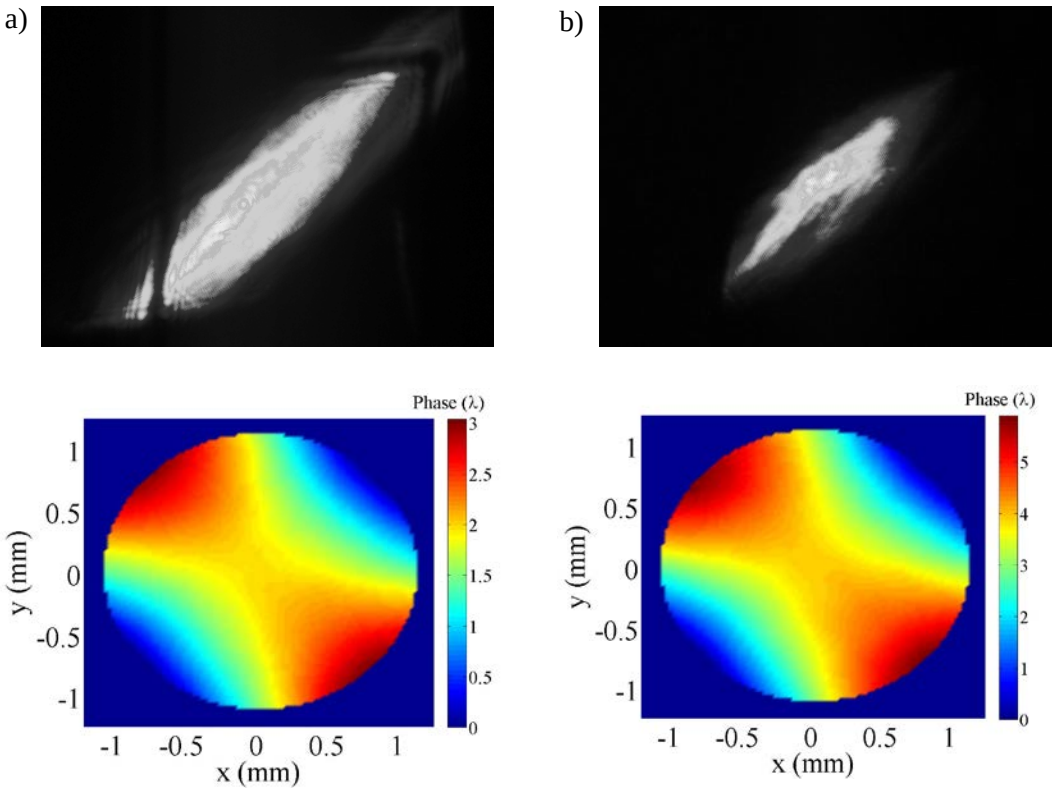

Fig 4. 32: a) Non-converted fundamental and b) SH spatial profiles and wavefronts when the intensity is set at 0.5 GW/cm^2

Under perfect phase matching conditions for the central wavelength, the SH beam profile (Fig 4. 33b) presents 3.62 and 0.70 mm major and minor axes respectively, thus exhibiting a larger degree of ellipticity (0.32) than that of the fundamental pulse without the crystal (0.23). This can be explained in terms of phase mismatching: in Fig 4. 34b, phase mismatching limits conversion efficiency along the major axis, thus increasing ellipticity. Moreover, refraction also plays a significant role, since the beam grows along the axis where it experiences a defocus (minor axis according to the spatial phase map), whereas it narrows along the focusing axis (major axis).

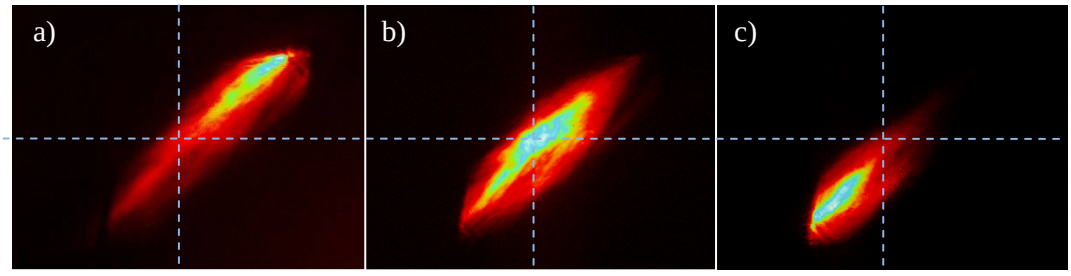

Fig 4. 33: SH beam profile for different phase mismatches: a) Δk=-95 cm^{-1},b) Δk=0 cm^{-1} and c) Δk=+70 cm^{-1}

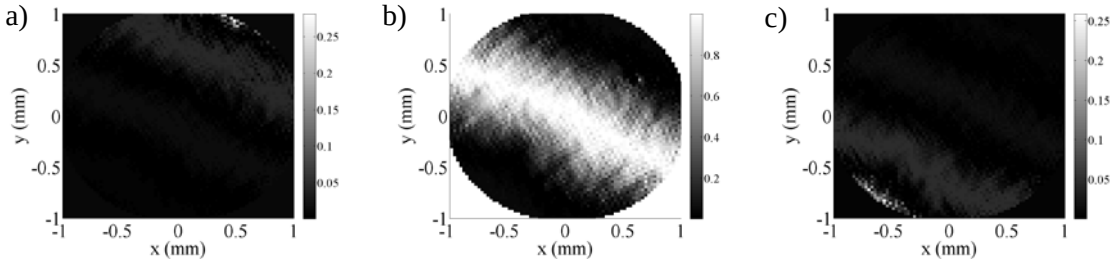

Fig 4. 34: Computed phase mismatch factor maps corresponding to the beams shown in Fig 4. 33 for the central wavelength.

Out of phase matching (Δk=-70 cm^{-1} and Δk=+70 cm^{-1}), the condition of perfect phase matching is no longer satisfied for the central frequency (see Fig 4. 34); however, it is satisfied for other wavelengths (789 nm and 801 nm, respectively), yielding a redistribution of SH intensity (Fig 4. 33). On the one hand, conversion efficiency is higher in the centre of the beam, where it is more intense. On the other hand, phase matching imposes a higher degree of conversion efficiency in the periphery for those wavelengths whose spectrum weight is greater (i.e., the central wavelength). Unfortunately, it is not possible to further analyse this effect, since the crystal's width restricts the observation window.

As to the spatio-spectral characterization, no tilt was observed in the trace, which is in line with the almost flat phase profile along the x-axis. The asymmetry that can be observed in the trace is due to intensity distribution along the x-axis (see Fig 4. 32b).

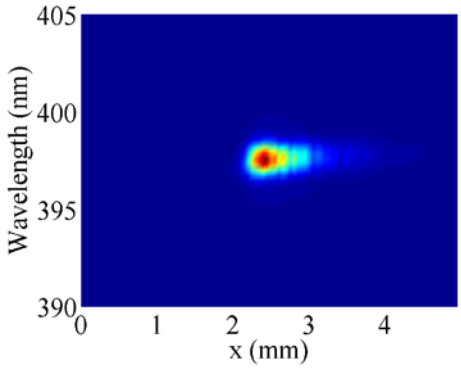

Fig 4. 35: SH spatial chirp for an astigmatic beam (I=0.5 GW/cm^2)

4.5.4.2 High-intensity regime

A phase shift is expected when intensity is increased from 0.5 to 34 GW/cm^2. In order to quantify this effect, we have subtracted the wavefront measured at low-intensity from that registered at high-intensity. Results are summarized in Fig 4. 36: the phase shift is mainly astigmatism at 45º, (0.068±0.007)λ RMS, and defocus, (0.055±0.005)λ RMS. This is in accordance to the intensity pattern (see Fig 4. 37b), suggesting that beam profile is playing a key role in the shaping of the wavefront through second-order cascading processes and the Kerr effect. Additionally, as it was previously commented in the analysis of focusing beams, phase mismatch generated across the aperture must also be taken into account in second-order cascading processes.

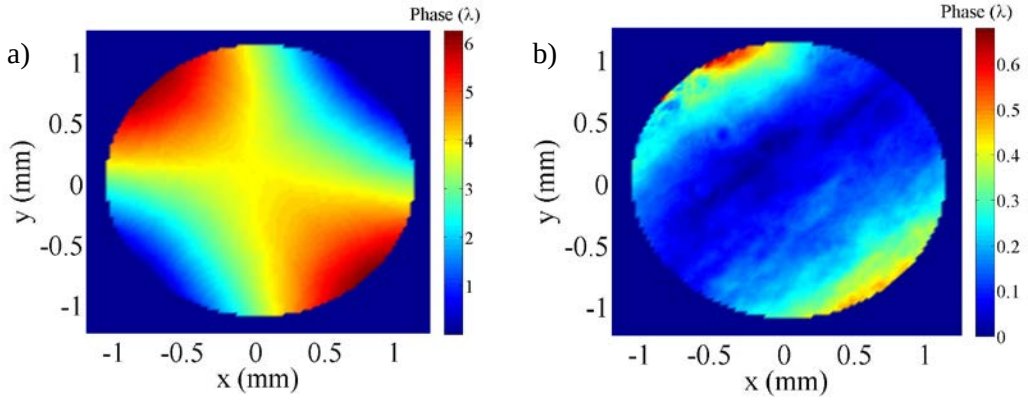

Fig 4. 36: a) SH wavefront at 34 GW/cm^2 and b) phase shift when the intensity is increased from 0.5 GW/cm^2 to 34 GW/cm^2

The saturation regime is entered when intensity reaches 34 GW/cm^2. For this reason, the beam surroundings tend to be enhanced, presenting a flatter and broader profile. In contrast, the wavefront presents a more pronounced focusing along the 45º axis compared to the low-intensity case, leading to a narrowing in this direction.

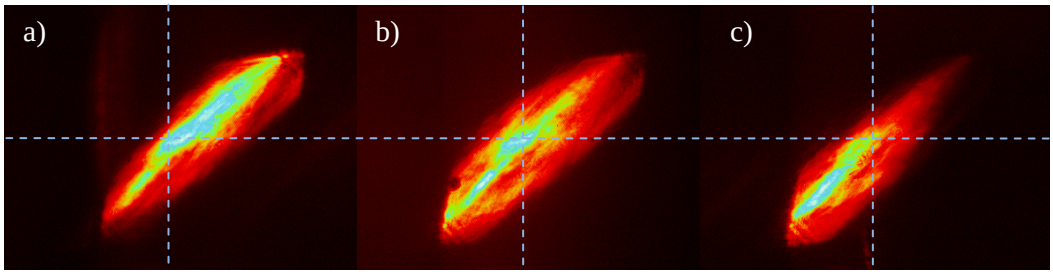

Fig 4. 37: SH beam profile for different phase mismatches: a) Δk=-95 cm^{-1},b) Δk=0 cm^{-1} and c) Δk=+70 cm^{-1}

The intensity distribution at the focal plane of a 100 mm focal length lens is presented in Fig 4. 38. In panel a), the SH beam shape leads to an elliptical focus for plane waves, with 0.0393 mm and 0.0115 major and minor axes, respectively, in the low-intensity regime. This implies an ellipticity of 0.30, which is in good agreement with experimental SH ellipticity before using the focusing lens.

The results obtained when the wavefront aberrations are included in the propagation code are presented in Fig 4. 38b. We first notice an inversion of the beam. If we plot the wavefront profiles along the -45º and 45º axes, we find focusing of the beam along the 45º direction and defocusing along the -45º axis. This implies that the beam will be narrowed in the first direction and broaden along the second axis, which yields inversion of the ellipse with respect to the original beam shape. As in previous examples, the aberrations deteriorate beam quality, leading to a drop in peak intensity. In particular, for an input fundamental intensity of 0.5 GW/cm^2, SH peak intensity varies from 10.31 GW/cm^2 for a flat wavefront, to 0.052 GW/cm^2 for the aberrated beams. When input intensity is increased to 34 GW/cm^2, the results are different by several orders of magnitude: 3.74x10^5 GW/cm^2 for plane waves in contrast to 698 GW/cm^2 for the astigmatic phase.

If the outcomes for the high-intensity regime are compared to those of the low-intensity one, when there is an absence of aberrations the pattern is similar, although a decrease in spot size can be observed in relation to larger input beam sizes. In contrast, when the actual wavefront is computed, the focal spot becomes larger, this being directly connected to phase shift along the 45º axis.

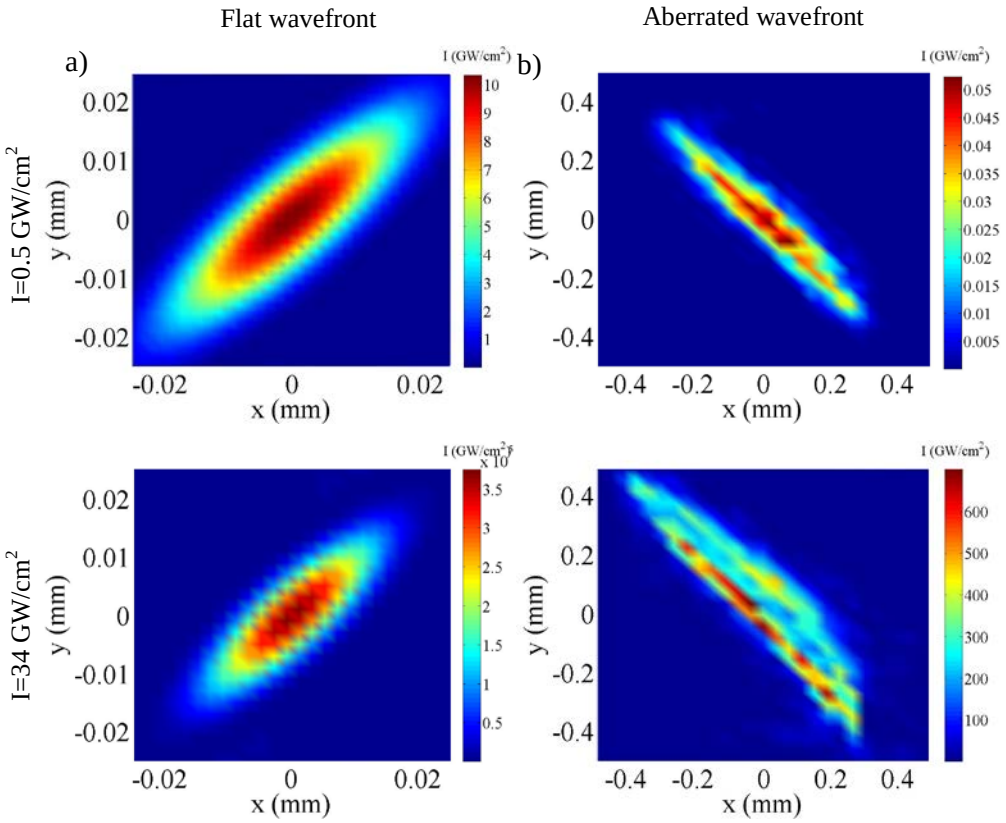

Fig 4. 38: Focused SH astigmatic beams by a 100 mm lens: a) assuming a flat wavefront and b) taking into account the aberrations. Note that the scale along the x and y directions is different in a) and b).

4.6. Summary and conclusions

In this chapter we have reviewed the fundamentals of SHG with femtosecond pulses. An experimental study of the phase effects arising from the process has been presented for both plane waves, and aberrated beams.

At low intensities, the wavefront of the SH verifies the relationship (64) for all the cases presented in this study. Diffraction and walk-off effect did not play a significant role under these experimental conditions. At high intensities cascaded second-order and Kerr effects induce phase distortions in the non-converted fundamental beam, as well as in the SH. These aberrations mainly manifest as defocus due to the Gaussian intensity distribution of input pulses.

The intensity distribution of the SH is closely connected to the wavefront of the fundamental pulses. This is easily explained in terms of phase mismatch: SHG is optimized for an angle between the optical axis and the propagation direction. Since the wave vectors are perpendicular to

the wavefront surface, when the latter is not flat, the wave vector is at a different angle and conversion efficiency is reduced.

A numerical model has been solved to find the far field distribution. The presence of aberrations degrades the quality of the focal spot, yielding a considerable drop in peak intensity. The focusing of pulses on a nonlinear crystal to increase the efficiency of the SHG process is a common approach. From the results obtained we can conclude that it is advisable to correct the wavefront of the SH, especially if it is going to be focused for its use in further experiments.

The spatio-spectral features of the SH have also been examined. To this end, the SH spectrum has been studied along the transverse axis. The traces found have revealed spatial chirp in cases of non-uniform wavefront profiles along this axis.

5 Wavefront retrieval of femtosecond pulses by second-harmonic generation

5.1. Introduction

In Chapter 2 we discussed the importance of an accurate characterization and appropriate control of the spatial phase. As we already mentioned, wavefront measurement of intense femtosecond pulses meets, however, certain difficulties due to broad spectra and high intensity.

So far, different methods have been used for this purpose. Hauri et al. demonstrated the validity of the Hartmann-Shack (HS) sensor to measure the phase of this kind of laser systems [99]. Wavefront sensors based on multi-wave lateral shearing interferometry have also been widely used in this field [134, 136, 138]. Their main advantages are achromaticity and their high dynamic range. In particular, in the work presented in [136], Chanteloup et al. used this technique for the first time to measure the wavefront of a high-intensity femtosecond laser carrying a strong B integral.

More recently, a remarkable effort has been made to fully characterize these pulses (both in the temporal and spatial domains), resulting in new techniques to measure both the wavefront and the temporal structure [223-225]. In [223], Grunwald et al. demonstrated simultaneous spatial and angular resolution in pulse characterization by combining an HS sensor and autocorrelation. In the approach presented in [224], a grating images the beam into an HS sensor, which enables the retrieval of the wavefront for each wavelength. This is combined with a frequency-resolved-optical-gating (FROG) measurement at a single spatial position, enabling the retrieval of the full

spatiotemporal structure of the pulses. Finally, Bowlan et al. measured the spatiotemporal field of pulses with SEA-TADPOLE and retrieved the spatial phase by using a Gerchberg-Saxton algorithm [225]. More recently, STARFISH [226], a spatiotemporal characterization technique developed in our laboratory, has demonstrated its capability for frequency resolved wavefront retrieval [227]. The details of this method will be provided in Chapter 6.

In this Chapter we present a technique for the retrieval of the spatial phase of intense short laser pulses through second-harmonic generation (SHG) in non-linear crystals [228]. To our knowledge, this is the first attempt to measure the wavefront of a laser beam by means of nonlinear processes. As we already discussed in Chapters 3 and 4, the efficiency and spectral properties of the frequency conversion process strongly depend on the angle between the wave vector and the orientation of the crystal. Our approach takes advantage of such dependence: by measuring the spectrum of the generated second harmonic (SH) beam along the transversal direction, it is possible to recover the wavefront of the incident femtosecond beam.

This chapter is organized as follows. In section 5.2 we present a summary of some theoretical considerations of SHG that are used throughout this paper, as well as the fundamentals of the proposed technique. In section 5.3 the retrieval algorithm is described. Simulations concerning the measurement process and the accuracy of the algorithm are presented in section 5.4. The experimental setup arranged and used in our work is described in section 5.5. Results of wavefront measurements for different aberrated femtosecond beams are shown in section 5.6. Section 5.7 is devoted to the conclusions drawn, and it is where the goals and limitations of the proposed technique are discussed.

5.2. Theoretical background

In Chapter 4 we demonstrated that an efficient SHG process can only be achieved in media characterized by a large value of the second-order susceptibility, and that certain conditions regarding the wave vectors of the interacting waves had to be fulfilled (phase-matching) [169].

Let us consider a monochromatic plane wave. For the particular case of type-I phase matching in a collinear configuration (both the fundamental and the SH propagating in the same direction θ) and under slowly varying envelope and undepleted pump wave approximations, the intensity of the second harmonic beam $I_{2\omega}$ can be expressed in terms of the intensity of the fundamental wave I_{ω} [169] as:

$$I_{2\omega} = \frac{8 d_{eff}^2 L^2 \pi^2}{n_e\left(\lambda/2, \theta\right) n_o^2(\lambda) \varepsilon_0 c} \frac{1}{\lambda^2} PM(\lambda, \theta) I_{\omega}^2 \tag{109}$$

where d_{eff} is the effective non-linear coefficient of the crystal, L is the crystal length, c is the speed of light in vacuum, ε_0 is the vacuum permittivity and θ is the angle between the wave vectors of the interacting waves and the optic axis of the crystal. λ is the wavelength of the fundamental wave. The phase mismatch factor PM is defined as:

$$PM(\lambda, \theta) = \left[\frac{\sin\left(\Delta k(\lambda, \theta) L/2\right)}{\Delta k(\lambda, \theta) L/2} \right]^2 \tag{110}$$

$\Delta k(\lambda, \theta)$ being the phase mismatch for type-I SHG (ie., oo→e), which can be expressed as:

$$\Delta k(\lambda,\theta) = \frac{4\pi}{\lambda}\left[n_e\left(\lambda/2, \theta\right) - n_o(\lambda)\right] \tag{111}$$

where n_o and n_e are the ordinary and extraordinary indices respectively. The dependence of these indices with respect to the wavelength is given by the Sellmeier equations [170]. For the particular case of a β-Ba_3BO_4 (BBO) crystal, the Sellmeier equations are formulated as:

$$n_0^2(\lambda) = 2.7359 + \frac{0.01878}{\lambda^2 - 0.01822} - 0.01354\lambda^2 \tag{112}$$

$$n_e(\lambda,\theta) = \frac{n_z n_o}{\sqrt{n_0^2 sen^2(\theta) + n_z^2 \cos^2(\theta)}} \tag{113}$$

$$n_z^2(\lambda) = 2.3753 + \frac{0.01224}{\lambda^2 - 0.01667} - 0.01516\lambda^2 \tag{114}$$

From Eq.(109) we can deduce that the strongest dependence of $I_{2\omega}$ on both the wavelength and the propagation direction comes from phase mismatch factor PM(λ, θ), peaked at the so-called perfect phase-matching curve Δk(λ,θ)=0 (Fig 5. 1a). Eq.(111) requires $n_e\left(\lambda/2, \theta\right) = n_o(\lambda)$: for a given wavelength λ_0 there is a single phase-matching angle θ_0 that satisfies this condition and thus maximizes SH conversion efficiency.

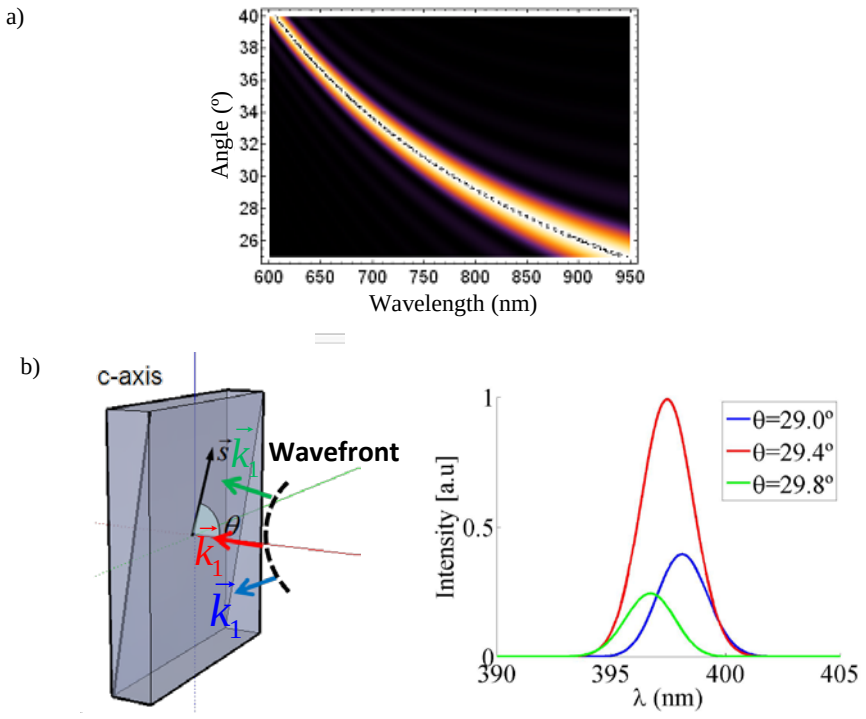

Fig 5. 1: a) Density plot of phase mismatch factor PM(λ, θ) for a BBO crystal of 100 µm thick BBO crystal. The wavelength values that satisfy the perfect phase-matching condition are marked with the dashed line. θ is the angle between the wave-vector and the optic axis of the uniaxial crystal. b) An aberrated wavefront reaches the surface of a 300 µm thick BBO crystal cut at θ=29.4° (s is a unitary vector following the direction of the optical axis). The wave vectors k hold different angles with the optical axis and the corresponding spectral intensities are depicted on the right side of the figure.

Therefore, the wavelength that generates the maximum degree of spectral intensity is unequivocally related to the angle between the wave-vector and the optical axis (Fig 5. 1b). The fact that the wave-vectors are perpendicular to the wavefront surface enables us to determine phase curvature.

So far we have only focused on monochromatic waves. Now it is time to examine the validity of this method for short pulses.

In the case of ultrashort pulses, the accurate study of the spectral characteristics of the SH beam requires the solution of the wave equations that govern the process (see Chapter 4). However, although Eq.(109) was obtained for monochromatic plane waves, it can also be applied in first order approximation for the estimation of the spectral intensity of the SH signal generated by a femtosecond laser pulse under the assumptions set out in the following.

First, it could be reasonably used in the case of moderate intensities, in order to neglect higher order nonlinear effects (SPM, XPM, Kerr effect....) that distort the pulse, as discussed in the previous chapter. Within the framework of this model, we are also neglecting nonlinear phase distortions induced by cascaded processes in non-centrosymmetric crystals [174, 175], which could play a role in wavefront retrieval for very high intensities of the fundamental. In addition to pulse deformations induced by these effects, one has to prevent pulse distortions due to dispersion by using crystals short enough to neglect dispersion of both the fundamental and SH pulses.

Second, we need to analyse the effect of the temporal phase in the SHG process to test the validity in the case of chirped pulses. In general, when quadratic or higher order spectral phases are present in the fundamental pulse, both spectral intensity and the pulse envelope of the second harmonic can become strongly distorted. These effects are particularly relevant for ultra-high intensities (typically tens of GW/cm^2 or above) [211] due to the contribution of other frequency mixing processes (SPM, XPM…), and in the case of long crystals due to complicated dispersion effects (note that in [211] there is no spectral shaping for crystals that are shorter than 1 mm and f intensities below 10 GW/cm^2 for 120 fs pulses chirped with a quadratic phase to 150 fs).

Therefore we can expect Eq.(109) to be of no use when dealing with intense pulses that are far from the transform limit, since in this case spectral phase effects cannot be properly accounted for, at least for arbitrarily long crystals.

To verify this, we tested an analogous case to that presented in [211], which allowed us to check the validity of near (but not perfectly) transform limited pulses. For the experiment, we arranged the setup presented in the sketch below, where the chirp of the fundamental pulse was modified by controlling the grating distance in the compressor.

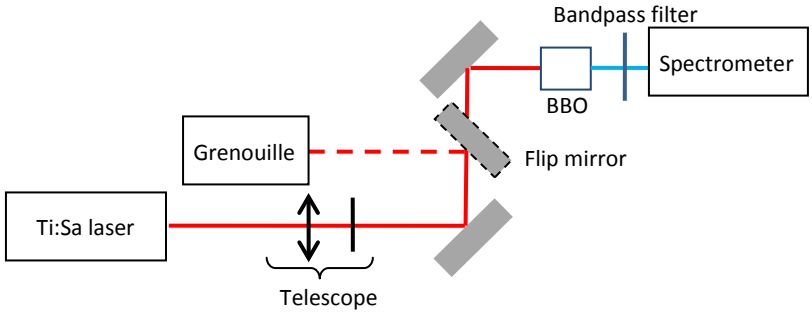

Fig 5. 2: Experimental setup for the study of SHG with chirped pulses

The intensity and phase of the fundamental pulse were measured with a Grenouille (Swamp Optics) and averaged over 10 measurements. The SH spectra were recorded with a spectrometer (HR4000, Ocean Optics). The exposure time was set at 5 ms and the measurements were averaged over 100 shots.

We have analysed three cases, whose results are summarized in Fig 5. 3: in the left-hand column, the plot corresponding to the temporal profile of the fundamental pulse can be observed, whereas the right-hand column illustrates the SH spectrum.

Up to a certain amount of positive chirp, we observed a drop in SH intensity, although no spectral shaping can be observed. This is easily explained by the temporal broadening of the fundamental beam due to the chirp, which translates into lower peak intensity. If we increase the chirp further, a limit where the spectrum gets distorted is reached and, therefore, the approximation (109) would lose its validity. The experiments conducted in our study will focus on near Fourier transform limited pulses at moderate intensities.

In such cases, I_ω is taken as the spectral intensity of the fundamental for each wavelength. Note that this expression (Eq.(109)) is a simplified version of the equation given in [229], where only SHG is considered, that is, other frequency mixing processes that could take place among the different wavelengths of the fundamental pulse (i.e. sum-frequency generation) are not accounted for. Neglecting sum-frequency generation is expected to become less reasonable when dealing with much shorter pulses.

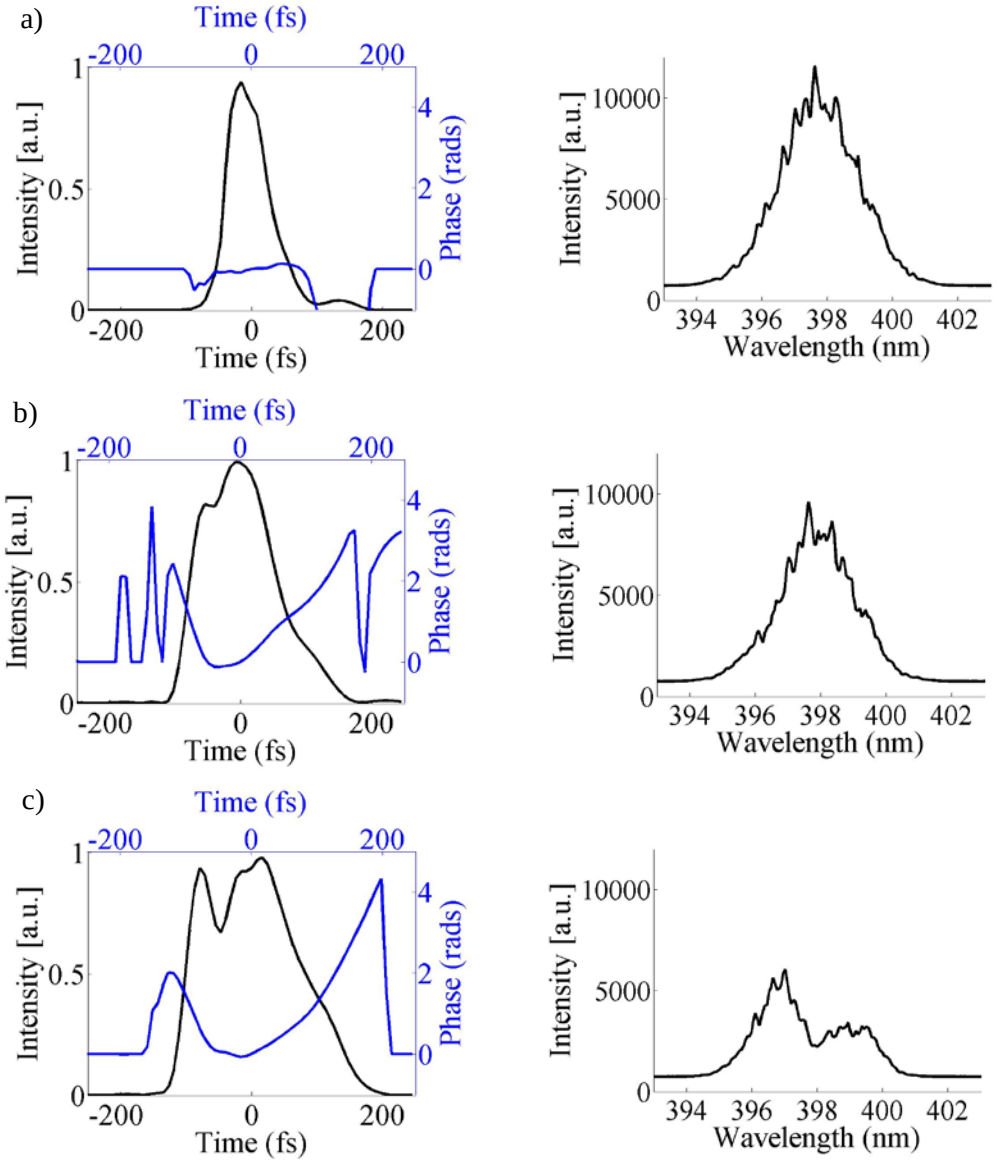

Fig 5. 3: Temporal characterization of the fundamental pulses and corresponding SH spectra: a)under the best compression achievable under our experimental conditions; b) moderate positive chirp; c) large positive chirp.

The accuracy of this monochromatic-wave approach has been tested along the different sections of this work under different experimental conditions. In particular, for a fundamental 120 fs pulse with a central wavelength of 795 nm and a 1 mm thick BBO crystal (typical parameters employed in our study) Fig 5. 4 compares the measured spectrum of the generated SH pulse with that obtained from Eq. (1). We found a reasonably good agreement, which justifies the use of such a simple expression in the experimental conditions described in our study.

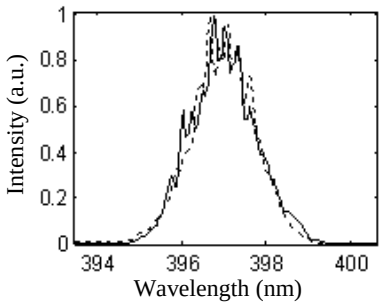

Fig 5. 4: Comparison between the measured SH signal (solid line) and the estimation (dashed line) for the fundamental spectrum applying Eq. (109).

In general, in the case of non-plane waves, for each point of the transverse plane of the beam, I_ω would be the corresponding spectral intensity. In this case θ represents the angle between the wave vector (always perpendicular to the wavefront surface) and the optic axis of the crystal at that point. This approximation is significant in case of very thin crystals, in which propagation effects (i.e. diffraction) can be neglected. Under such conditions, Eq.(109) can be applied to estimate conversion efficiency for each wavelength of the fundamental beam at any point of its profile provided the wavefront is known. The algorithm used to retrieve the wavefront is based on the solution of the inverse problem, so that in this case the spectral intensities of both the fundamental and the SH (and therefore the conversion efficiency for each wavelength) in a set of points along one axis ("scanning" axis) are known. From this, the wavefront along such axis can be computed by using a retrieval algorithm.

5.3. Wavefront retrieval algorithm

The retrieval algorithm to compute the wavefront in this general case is summarized in Fig 5. 5.

$$I_{2\omega}(\lambda,\theta) \propto PM(\lambda,\theta) I_\omega^2$$

$$PM(\lambda,\theta) = \left[\frac{\sin\left(\frac{\Delta k(\lambda,\theta) L}{2} \right)}{\left(\frac{\Delta k(\lambda,\theta) L}{2} \right)} \right]^2$$

$$\Delta k(\lambda,\theta) = \frac{4\pi}{\lambda} \left[n_e\left(\lambda/2, \theta \right) - n_o(\lambda) \right]^2$$

$$n_e(\lambda,\theta) = \frac{n_z n_o}{\sqrt{n_o^2 \sin^2(\theta) + n_z^2 \cos^2(\theta)}}$$

$$\Psi(x) = \Psi(x - \Delta x) - \frac{\Delta x tg(\alpha)}{\lambda}$$

Fig 5. 5: Summary of the retrieval algorithm to compute the wavefront. The quantities calculated in each step are marked in red.

First, the phase mismatch factor PM(λ, θ) of Eq.(109) is calculated by using the experimental measurements of the spectral intensity of the SH, $I_{2\omega}$, and the fundamental, I_{ω}. At this point, provided that the main angular dependence of the efficiency comes from the phase mismatch factor, $n_e\left(\lambda/2,\theta\right)\approx n_o\left(\lambda\right)$ can be assumed in the denominator of Eq.(109). Once PM(λ, θ) is known, Δk is computed from Eq.(110). Finally, angle θ can be obtained by equalling Δk with Eq. (111) and using Sellmeier expressions for the refractive indices [170]. θ is the angle between the wave vector, k, and the optic axis (see caption of Fig 5. 6a for a detailed description of the corresponding geometry).

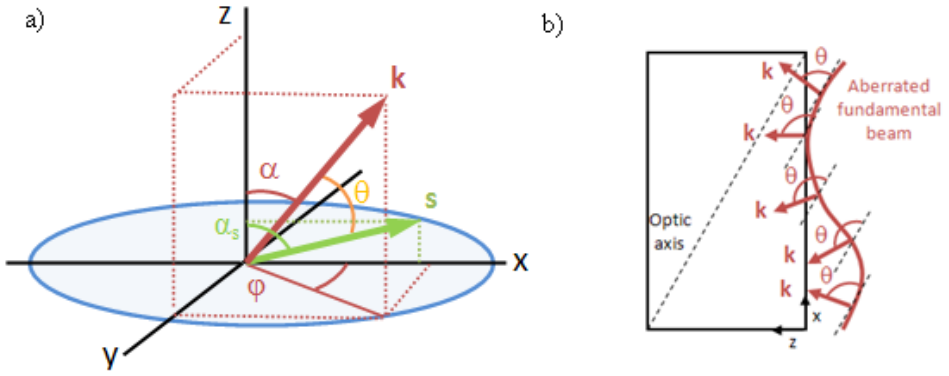

Fig 5. 6: a) General diagram for the distribution of axes and angles. The beam is assumed to propagate along the z axis. k represents the wave vector at a given point of the beam wavefront; s is the unitary vector along the optic axis. The section of the beam is showed in blue. b) Geometry in the particular case where measurements are restricted to the plane containing the optic axis.

However, for phase retrieval it is necessary to obtain angle α between the wave vector and the reference axis (z in Fig. 2). If the scanning is made in a plane containing the optic axis (i.e., φ = 0º according to Fig. 2a), once θ is known two possible solutions for α are possible:

$$\alpha = \alpha_s \pm \theta \tag{115}$$

α_s being the angle between the optic axis and the propagation axis (in this case, the z-axis).

When dealing with a BBO crystal as non-linear medium, one of the two values for α can be discarded based on the following argument: α_s is around 29.4º (phase matching angle for a 795 nm wavelength), and the two values for α are 29.4º+θ and 29.4º-θ. However, the critical angle (namely α_c) for a wavelength of 795 nm is 37.0º, which renders the first solution unsustainable, since it would only be feasible for values where α is between 29.4º and 37.0º, i.e. far from the typical values. Note that this angle corresponds to the one inside the crystal. Thus, it is necessary to take refraction into account by applying the Snell law:

$$\alpha_0 = \arcsin\left[n_o\left(\lambda\right)\sin\left(\alpha\right)\right] \tag{116}$$

At each scanned point x, the wavefront is finally reconstructed in terms of wavelength λ as:

$$\psi(x) = \psi(x - \Delta x) - \frac{\Delta x tg(\alpha_0)}{\lambda} \tag{117}$$

where Δx is the increase between two consecutives values of x.

As an example, Fig 5. 7 shows a typical sequence of the wavefront retrieval algorithm above described, from the measured spectral map of the SH beam (Fig 5. 7a) to the final estimation of the wavefront (Fig 5. 7d). Phase mismatch factor PM(λ,θ) is obtained from the spectral map (Fig 5. 7b), which allows us to calculate the extraordinary index. At this point, a Gaussian fitting for the spectrum of the fundamental beam was used to minimize noise in the wavefront retrieval process. Then, Sellmeier equations (for the BBO crystal) are numerically solved in order to compute the distribution of angles θ (Fig 5. 7c). Finally, the wavefront (or phase) for a given wavelength is retrieved by applying Eq.(117) (Fig 5. 7d).

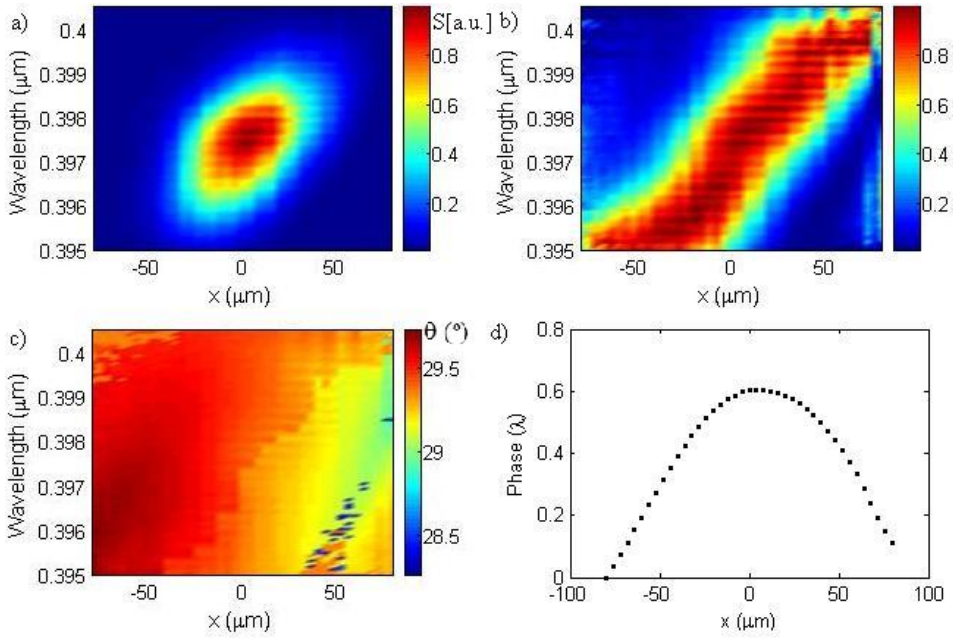

Fig 5. 7: Example of phase retrieval for a diverging beam using a BBO crystal (αs = 29.4º, 500 μm thick): a) measured spectral map; b) phase mismatch factor PM; c) map of angles with respect to the optic axis (θ, in degrees); d) retrieved wavefront for the central wavelength (795 nm) of the incident beam (in λ units).

In addition, this algorithm allows us to explore dependence between wavefront and wavelength. This might be useful when using ultra-broadband laser pulses, however, under the experimental conditions here reported, no difference between the wavefront recovered for each wavelength was found.

In cases where phase frequency dependence can be overlooked, an alternative algorithm based on the deviation of the maximum of the phase-matching curve at each point can be applied. By obtaining the wavelength corresponding to the maximum of the phase-matching curve, it is possible to attain the extraordinary index of refraction for this wavelength and, therefore, the angle.

5.4. Simulations

5.4.1 Proof of concept

To validate the proposed method, we developed a mathematical model of the wavefront sensor that included the reconstruction algorithm and simulated the whole phase measurement process. In this model, the phase distribution and the intensity profile recorded by the commercial sensor, as well as the spectrum of the fundamental beam are used as input data to simulate the spectral map according to Eq.(109). The simulated trace is then introduced in the proposed algorithm for phase retrieval. This will allow us to compare it with the experimental results and to analyze dependence with different parameters.

In the example below, we show the simulation and reconstruction of a defocused Gaussian beam (1.5λ PtV over a 1 mm pupil size, 0.5 mm FWHM). For simplicity, we will start with an example where the wavefront does not present chromatic aberrations. A 500 µm thick BBO Type-I crystal is used for detection purposes.

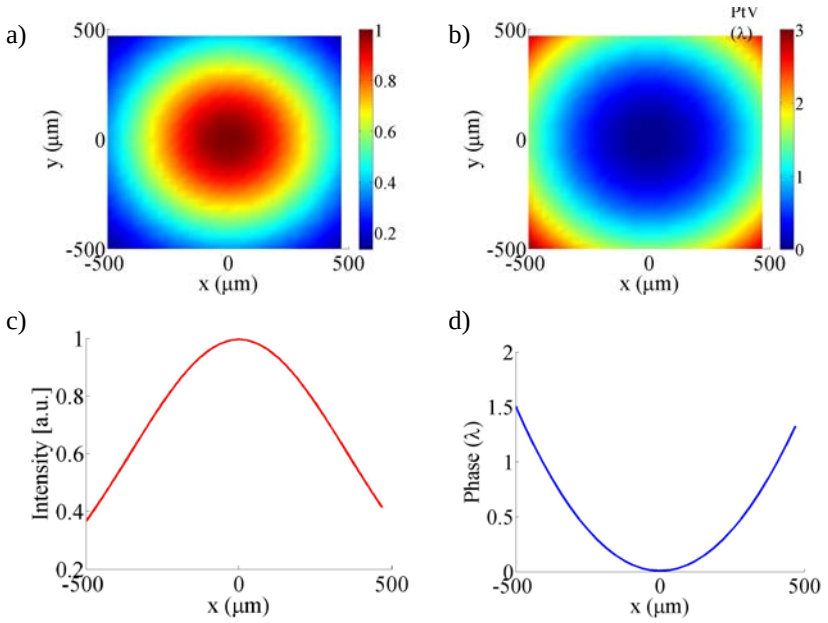

Fig 5. 8: Inputs for the simulation: a) Beam intensity (colour bar in arbitrary units), b) wavefront , c) intensity and d) wavefront along the scanning axis.

We first calculate the angles between the optical axis and the wave vectors perpendicular to the phase front surface. By using the Sellmeier equations for BBO, Eq.(112) and (113), the ordinary and extraordinary indices are computed as a function of the angle (position) and the wavelength. Then the phase mismatch is calculated according to Eq.(111) and substituted in Eq.(110) to obtain the phase matching curves. The spectrum of the fundamental beam, assumed to be a 9 nm FWHM Gaussian centred at 795 nm, is then used in Eq.(109) to obtain the spectra of the second-harmonic along the transverse axis.

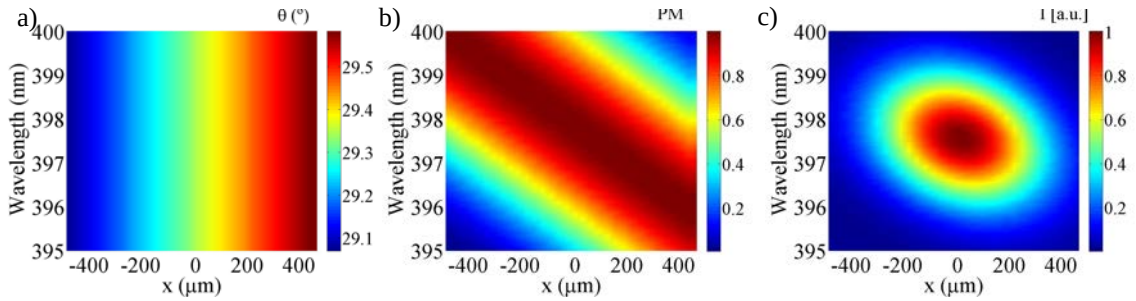

Fig 5. 9: a) Angles between the wave vectors and the optical axis, b) phase-matching curves along the scanning axis and c) simulated spectral trace.

The simulated spectral map is then inserted in the retrieval algorithm to test its accuracy. In Fig 5. 10 we present the comparison between the original and the retrieved phase. To quantitatively explore the deviation of the retrieved wavefront with respect to the original one, we performed a fitting in terms of Zernike polynomials. Values of 1.5779λ for defocus and 0.1765λ for astigmatism at 0º were obtained for the retrieved wavefront. These values imply a deviation of 4.9% and 5.8%, respectively, based on the data obtained for the original phase front.

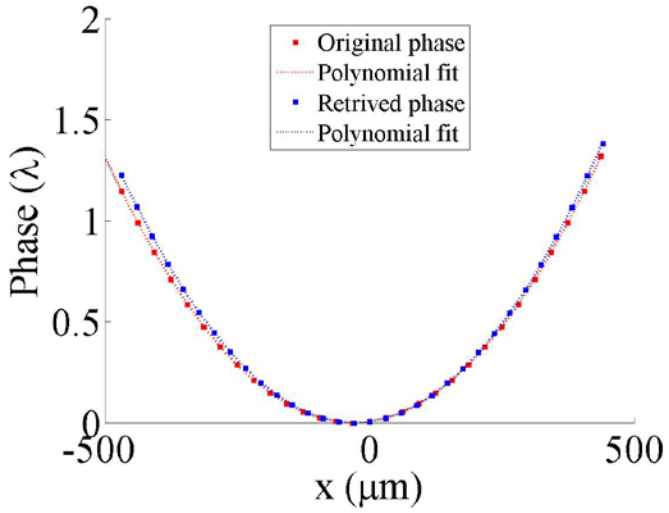

Fig 5. 10: Comparison between the original (red squares) and the retrieved (blue squares) wavefronts. The dashed line represents the fitting with Zernike polynomials.

A small deviation is observed at the extremes. This behaviour also appears in the retrieved phase matching curves. There are two reasons that can explain this effect. On the one hand, the signal from the spectrum of the fundamental beam and the spectral trace become very low at those points. On the other hand, we have worked under the assumption that for phase matching retrieval it was possible to approximate $n_e(\lambda,\theta)\approx n_o(\lambda_c)$. This last assumption starts to lose validity when it works for wavelengths that are far from the central one and when angles are too different from the perfect phase matching condition (i.e., very large wavefront aberrations).

5.4.2 Crystal thickness

As explained in Chapters 3 and 4, crystal thickness plays a crucial role in determining the spectral features of second-harmonic light. In particular, it limits the spectral bandwidth that can be frequency doubled.

Although we will return to this issue in the next section, where we will perform an experimental study of the phase retrieval for different aberrations and crystals, it is helpful to explore the effects of crystal thickness alone on the algorithm. In order to do this, we have performed the same simulation of the previous example under different sample lengths (300 and 1000 µm).

For the 1000 µm thick BBO, we obtained 1.5651λ defocus and 0.1875λ astigmatism, which set the deviation at 4.2% and 6.1% with respect to the original data. When the sample thickness is reduced to 300 µm, 1.6127λ and 0.1807λ for defocus and astigmatism are obtained (deviations of 7.0% and 2.6%, respectively).

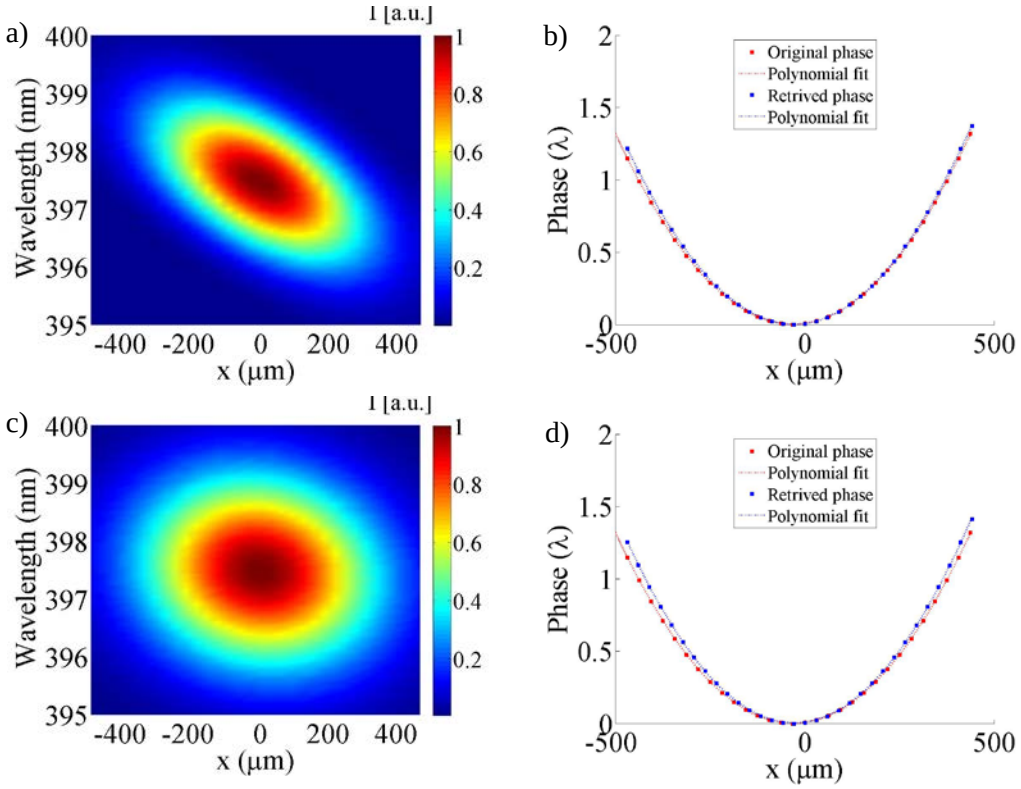

Fig 5. 11: Simulated spectral traces for wavefront measurements with a a) 1000 µm and c) 300 µm thick BBO crystal. b), d) Corresponding wavefronts (blue squares) and comparison to the original phase (red squares). The dashed lines represent the fitting with Zernike polynomials.

Although accuracy is slightly better in thicker crystals (especially as regards noisy traces, which will be further explained in the next section), one must also consider the bandwidth limitations imposed by crystal thickness.

On the basis of Eq.(109) it is possible to demonstrate that the degree of efficiency for the generated SH is over 50% for a range of angles around the perfect phase matching angle satisfying:

$$\delta\theta = \frac{2.78\lambda}{\pi L}\frac{1}{\sin\left(2\theta_{PM}\right)}\frac{1}{n_0\left(\lambda_{2\omega}\right)}\left[1-\frac{n_0^2\left(\lambda_{2\omega}\right)}{n_z^2\left(\lambda_{2\omega}\right)}\right]^{-1} \tag{118}$$

This value is usually termed as angular bandwidth [169] and can be regarded as the range of propagation angles around the perfect phase matching value for which an efficient SH signal will be generated. The angular bandwidth constrains the order of the aberrations that can be successfully measured with the proposed technique: if divergence between the wave vectors of a given wavefront exceeds this value, no appreciable SH signal will be produced and the accuracy of phase retrieval will decrease. In Table 1 we show the comparison among different crystal thickness values for both BBO, and KDP crystals.

	Crystal thickness		
	1000 µm	500 µm	300 µm
BBO	3.10 mrad	6.20 mrad	10.30 mrad
KDP	7.90 mrad	15.80 mrad	26.50 mrad

Table 5. 1 Angular bandwidth of BBO and KDP for different crystal thickness

5.4.3 Noise

All experimental measurement is affected by noise generated by laser fluctuations, errors in the apparatus... For this reason, it is important to test the algorithm under such conditions. To do so, we introduced random noise in the spectral trace of the previous example.

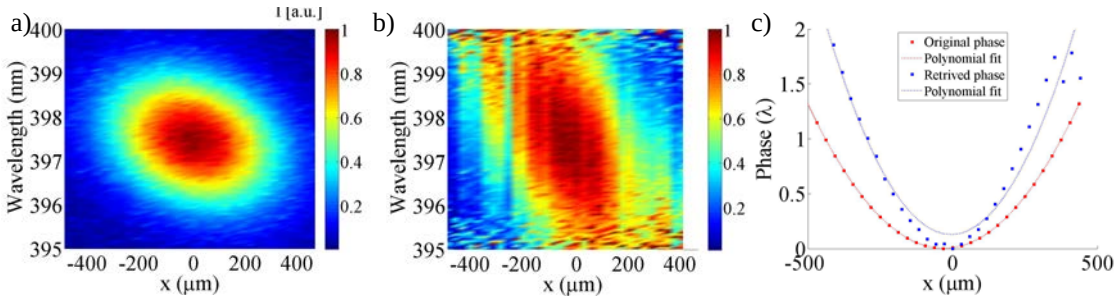

Fig 5. 12: a) Simulated noisy spectral trace for a 500 µm thick BBO, b) phase matching retrieval and c) comparison between the original and the reconstructed wavefronts.

As can be seen in Fig 5. 12, noise in the spectral map leads to difficulties in calculation at the extremes of the spectral bandwidth and the transverse axis, where the signal intensity is lower and the noise is amplified as it is divided by the spectrum for the estimation of phase matching.

It is therefore necessary to implement a code for noise treatment. To this end, one can resort to different strategies:

- *Averaging filter:* a first approach to noise treatment consists of averaging pixels by using a linear filter. In Matlab, where we have implemented the code, there are different functions for this purpose. In the example shown in Fig 5. 13, the "imfilter" was used.

- *Fourier transform:* in the frequency domain, the spectrum will consist of a main peak containing most of the information related to the trace, whereas the noise will yield high frequency terms. This makes it possible to isolate the central peak and obtain a noise-free trace by inverse Fourier transform. This method is generally more precise than the previous one.

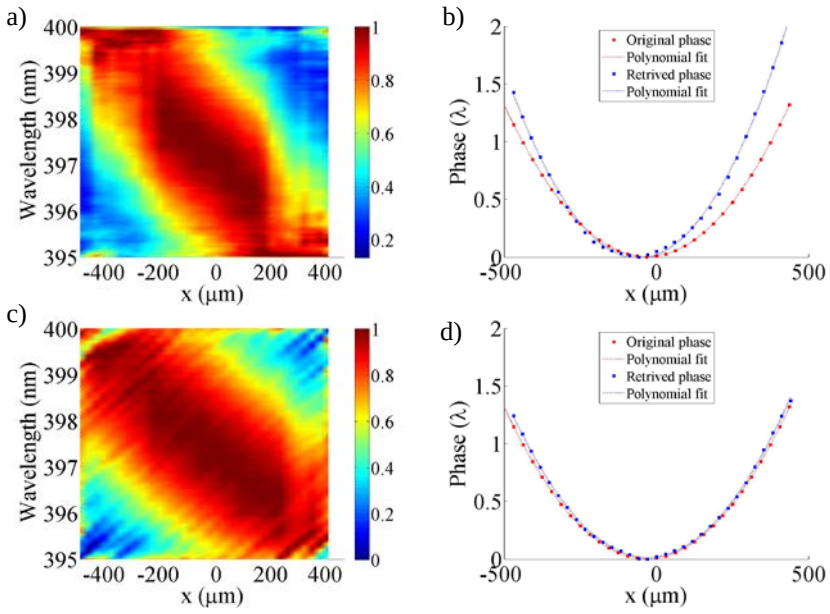

Fig 5. 13: Phase matching and comparison of phases for different noise treatment strategies: a) averaging filter and b) Fourier transform.

5.5. Experimental setup

The experimental setup used in this study is shown in Fig 5. 14. The laser source used was a Ti:Sapphire regenerative amplifier (Spitfire, Spectra Physics). This system delivers 120 fs pulses (9 nm full-width half-maximum –FWHM– in spectrum) at a 1 kHz repetition rate with a central wavelength of 795 nm and up to 1 mJ of energy.

The input beam was split into two replicas. One replica to be used as a reference for comparison purposes with the experimental results was directed towards a high-resolution multi-wave shearing interferometer (SID4-HR, Phasics) [138]. This type of wavefront sensors are particularly suitable for this application, since they are achromatic and provide a high-dynamic range. The other replica entered the measurement pathway for wavefront retrieval using the algorithm above reported. BBO crystals were used to frequency double the beam to be measured. All of them were cut for perfect phase matching at 795 nm working at normal incidence (α_s = 29.4º). Thickness values ranged between 300 and 1000 μm.

The pulse energy in all our measurements was carefully chosen (with the help of a half-wave plate and a linear polarizer) in order to maintain the BBO crystal's intensity around or below ~2

GW/cm^2. Working around this value, the intensity of the fundamental is low enough to prove that our theoretical approach is reasonably good, as discussed in the previous section, and at the same time we obtain enough SH signal to perform our measurements with very low noise levels.

With the crystal properly aligned, the SH signal was maximized for a non-aberrated beam. A band-pass filter (FGB37S, Thorlabs) was placed after the crystal in order to eliminate the non-converted fundamental wave. The SH beam emerging from the BBO crystal passed through a 4f-telescope composed of two achromatic lenses (AC254-175-A, Thorlabs) with a focal length of 175 mm. This telescope conjugated the SH signal at the exit of the crystal with the detection plane. On this detection plane, a fibre coupler (4 μm core, Thorlabs S630-HP) was mounted on a motorized linear actuator for accurate controlled movements. The choice of the fibre core and the motor resolution determined the maximum resolution achievable in the reconstruction procedure. In our case, precision in the positioning of the actuator was below 1 μm, which guarantees maximum resolution limited by the fibre core. The scanning direction was chosen to be along the x-axis (according to Fig 5. 6). The spectrum data were recorded with a high resolution spectrometer (Ocean Optics, HR4000).

Although large pulse energy could increase the SH signal thus facilitating detection, it cannot be arbitrarily large, since this would increase the risk of air breakdown in the intermediate focus of the optical system. To avoid this effect, we maintained the incident pulse energy within the 10 μJ range.

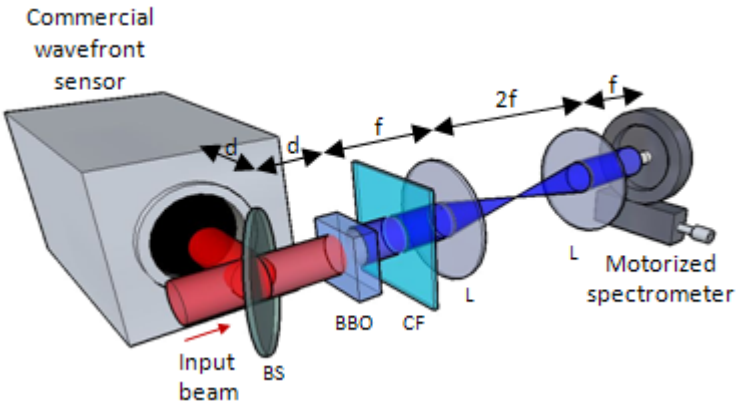

Fig 5. 14: Experimental setup. BS, beam-splitter; CF, band-pass filter; L, lenses; f, focal length of lenses; d, distance from BS to the BBO crystal and from BS to the wavefront sensor.

5.6. Results and discussion

5.6.1 Retrieved and measured wavefront aberration

The reliability and accuracy of the proposed phase retrieval method was tested on a femtosecond laser beam with different induced aberrations. As a first test, a convergent lens (400 mm focal length) was placed 354 mm away from the BBO crystal. The theoretical total aberration produced by this lens corresponded to a 2.60λ PtV phase distortion over a 0.86 mm pupil size. This aberrated beam passed through a 500 μm thick BBO crystal and reached the detection unit. At that plane the beam was scanned in 4 μm steps (to be consistent with the fibre core size) to record the spectrum for each position along the x direction. This spectral map is shown in Fig 5. 15a. The

corresponding wavefront was retrieved using both this map and the above described algorithm; this is shown in Fig 5. 15c (blue markers). This result can be compared with that of the wavefront measured with the commercial sensor (red symbols) in Fig 5. 15c. Both of them were fit with a second order polynomial (dashed lines in Fig 5. 15c), which allowed us to obtain the Zernike coefficients. Values of 2.53λ and 2.58λ for defocus, and of 0.28λ and 0.34λ for astigmatism (at 0º) were obtained from the retrieval algorithm and the commercial sensor respectively.

Moreover, the coefficient of determination R^2 was also computed. This is defined as:

$$R^2 = 1 - \frac{\sum_{i=1}^{N} (\psi_i - \varphi_i)^2}{\sum_{i=1}^{N} (\psi_i - \bar{\psi})^2} \tag{119}$$

ψ_i being the experimental wavefront values computed by the retrieval method, ϕ_i those measured with the commercial sensor, $\bar{\psi}$ the average and N the number of steps taken by the motor. In this case the measurement obtained for R^2 was 0.994, which indicates a very good agreement between both calculations of the wavefront. A reasonable agreement with the simulations was also found (see Fig 5. 15b and Fig 5. 15d).

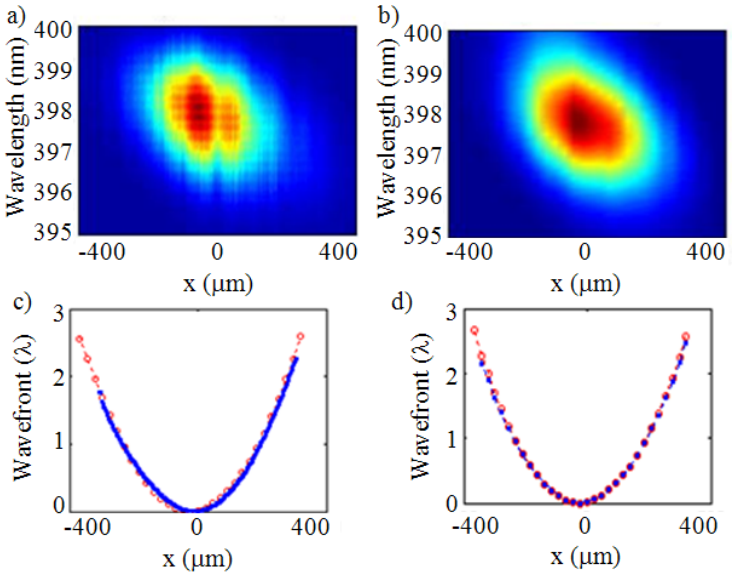

Fig 5. 15: Phase retrieval for an aberrated convergent beam (see details in the text). a) Measured spectral map. b) Simulated spectral map. Both experimental and simulated spectral maps are normalized. c) Wavefront retrieved from a) with the proposed algorithm (blue line). For comparsion, we show the wavefront measured with the commercial sensor (red open dots). d) Wavefront retrieved from b) with the proposed algorithm (blue line) and wavefront measured with the commercial sensor (red open dots, same as in c).

Under the same conditions as in the experiment, the results for the simulated wavefront retrieval (Fig 5. 15b) were 2.50λ for defocus and 0.32λ for astigmatism at 0º. These values show how close the experimental results are to those obtained with the wavefront retrieval algorithm: 3.2% and 6.5% for defocus and astigmatism respectively.

5.6.2 Effects of nonlinear crystal thickness

The influence of non-linear crystal thickness on wavefront retrieval was also experimentally tested using three BBO crystals (300, 500 and 1000 μm thickness). The incident beam was set at different amounts of defocus, while beam size was maintained.

As an example, the measured spectral maps for 300 and 1000 μm thick crystals for two different defocus values are shown in Fig. 6. Two main effects can be observed: on the one hand, the thicker the crystal, the stronger the spectral modulation of the maps due to the phase mismatch factor; on the other hand, a larger amount of defocus is associated with more tilted spectral maps, since a larger range of angles is involved.

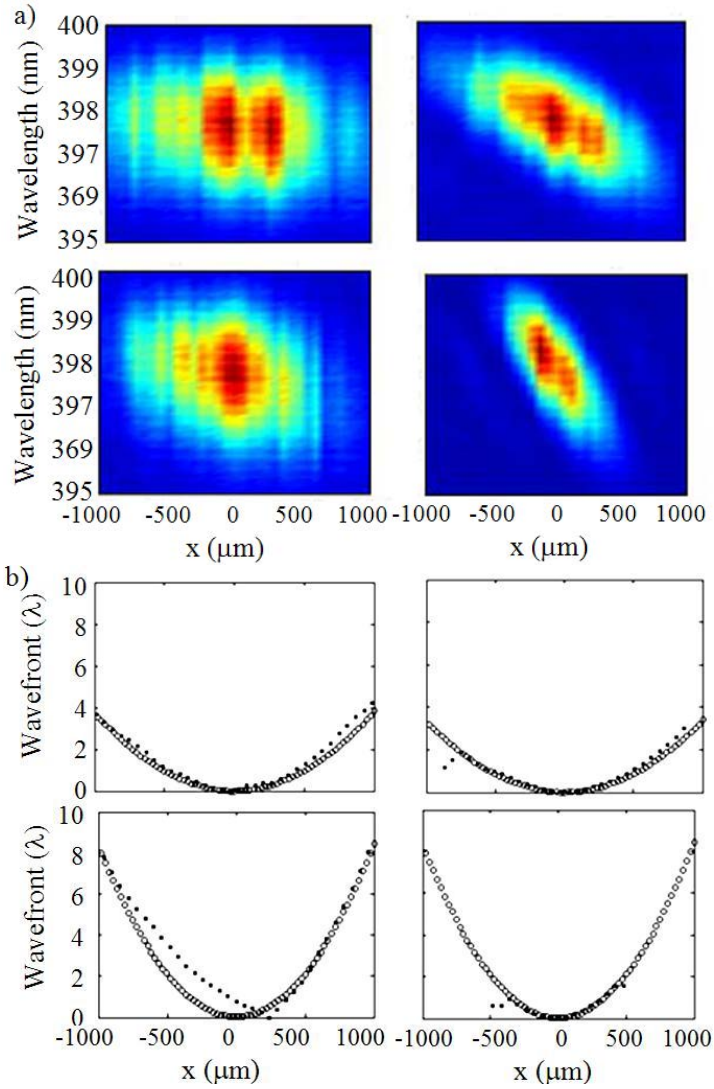

Fig 5. 16: a) Spectral traces for 300 μm (left panel) and 1000 μm (right panel) thick BBO for 0.95λ (upper panels) and 1.84 λ (lower panels) PtV defocus and a 1 mm pupil. All the traces are normalized. b) Experimentally retrieved wavefront (black symbols) and wavefront measured with the commercial sensor (white symbols).

Crystal thickness is therefore a constraint parameter when measuring aberrations. First, according to Eq.(118), the thicker the crystal is, the lower the phase distortion that can be analysed. Second, if the crystal is very thin, reconstruction can be noisy, since the phase-matching curve becomes too broad and therefore more difficult to be retrieved. The optimal solution would

be a crystal thickness with an angular bandwidth that exactly fits the aberration to measure. Obviously, this is meaningless in most cases provided that the aberration is unknown. Thus, the choice of a thin crystal will at least guarantee an adequate estimation of the magnitude of the aberration.

To take account of these effects, the coefficient of determination R^2 according to Eq.(119), for the measurements performed in the different crystals was calculated. Results are summarized in Table 5. 2. It can be observed that the largest value of R^2 corresponds to the crystal whose angular acceptance best fits PtV.

	Crystal thickness		
PtV	300 µm	500 µm	1000 µm
1.84λ	0.83	0.99	0.95
1.38λ	0.92	0.98	0.95
0.95λ	0.96	0.89	0.94

Table 5. 2: Experimental values for R^2 with different crystal (BBO) thickness values and amounts of defocus (PtV, over a 1 mm pupil).

5.6.3 Phase retrieval of wavefront with discontinuities

Finally, the robustness of the proposed technique when applied to sharpen beam profiles was tested. An example is shown in Fig 5. 17. In this case, discontinuity was generated by partially blocking the laser beam with a knife-edge. The beam was focused by means of a 200 mm focal length lens. A 500 µm thick BBO crystal was used for detection. This crystal was placed 110 mm away from the lens, which corresponds to 1.74λ PtV over a 1 mm pupil size. Since the phase is retrieved directly from the measurement and not from the derivatives, it is still possible to reconstruct the wavefront in spite of the discontinuities. Nevertheless, retrieval is more difficult when the R^2 value is of 0.92.

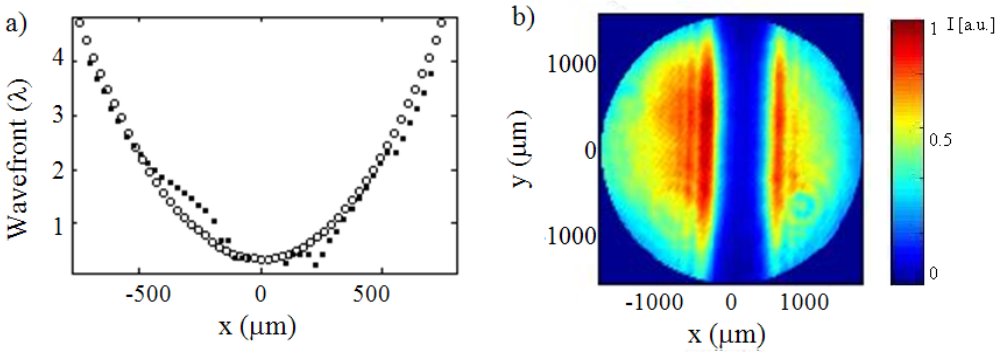

Fig 5. 17: a) Retrieved wavefront for a beam with discontinuity in the intensity profile (black squares) compared to the theoretically calculated wavefront (white dots). b) Beam intensity profile recorded with a CCD camera.

5.7. Summary and conclusions

We have developed and implemented a novel technique to retrieve the spatial phase of near transform-limited intense ultrashort pulses based on SHG in uniaxial nonlinear crystals. This technique is based on the measurement of the spectrum of the generated SH pulse along one axis and the application of a retrieval algorithm. The algorithm allows direct wavefront reconstruction

with a deviation from the real phase that can reach less that 3%. Robust reconstructions for sharpened intensity patterns, such as discontinuities, have also been proved.

Since our experimental setup is based on a fibre spectrometer, by choosing a tiny core fibre and a high-precision linear stage we can obtain very high spatial resolution (down to 4 microns for the experiments here reported). This makes the technique suitable for measuring small beam sizes under conditions where other sensing methods do not always show very accurate results. For instance, in the Hartman-Shack sensor, the size of each microlens (i.e. the pitch) limits spatial resolution in wavefront reconstruction. Since each lens acts as a spatial integrator, details smaller than its size cannot be captured. Limited degrees of spatial resolution would produce smoother wavefront aberrations, which might lead to an overestimation of the image quality of the system [230]. To our knowledge, the smaller commercially available pitch is 30 μm.

Moreover, a spectrometer is included in our experimental setup and therefore the presented procedure allows the measurement of the wavefront for the different spectral components of the incident beam. On the opposite, the spectral characterization of a broadband laser beam in terms of wavefront [6] with a Hartman-Shack sensor requires a set of narrow-band interference filters (as many as "wavelength slices" you want to measure). This advantage has not been explored in this work since with the current experimental conditions no dependence between the wavefront and the wavelength was found. However, this is particularly interesting for femtosecond pulses because chromatic aberration can be an issue, for example when using diffractive optics [231-233] or in the case of ultrahigh power lasers [234].

An important drawback is related to the choice of the crystal thickness, as it has been discussed. Thick crystals impose a limit to the range of aberrations to be measured. On the opposite, the thinner the crystal is, the larger the wavefront aberration that can be measured. However, the spectral maps will be noisier.

One of the disadvantages of the system as regards its present configuration is the time it takes to perform the measurements. This time depends on the resolution (i.e., number of steps performed by the motor) and the exposure time of the spectrometer. It could be reduced to a great extent if a slit-based imaging spectrograph was used instead of a fibre mounted on a motorized stage, since in such case the scanning would be replaced by a single shot measurement.

Additionally, there are certain issues to which special attention should be paid. First, for the crystal thicknesses we are using (around 1 mm), the intensity levels must be kept below 10 GW/cm^2 in order to avoid high-order nonlinear effects in the crystal (SPM, XPM…). Second, the technique cannot be applied in the case of strongly focusing beams, since non-collinear processes can become significant in the SHG process. Finally, a good alignment of the system is crucial to obtain a correct result. As in any imaging system, it is necessary to make sure that object and image planes are perfectly combined. Furthermore, the alignment of the crystal plays an essential role for obtaining a correct result.

To conclude, even though the method has been applied to the retrieval of the phase in relation to one axis (that is enough for defocus aberration), the procedure shown here is general and can be implemented in 2D. In this case, the use of a slit-based imaging spectrograph could enable an analogous procedure to that described in this work. The 1D wavefront retrieval demonstrated here might be very useful for beams providing cylindrical symmetry and in the analysis and optimization of telescopic systems and collimation devices.

6 Chromatic aberration for spectral shaping of pulses generated via nonlinear processes

6.1. Introduction

Most optical instruments use refractive or reflective elements (e.g. lenses, mirrors…) to control the distribution of light. In some cases it is possible to replace refractive or reflective elements with *diffractive optical elements* (DOEs), which can prove beneficial for certain applications [221]. DOEs can be used to perform functions that would be either difficult or impossible with refractive optics. Since they are based on diffraction, their operation presents a strong dependence on wavelength, or in other words, they present strong *chromatic aberration*. This enables the development of DOEs with more than one simultaneous focal point.

Chromatic aberration is present in most optical systems, and it is simply due to the dependence of the refractive index on wavelength. This dependence also induces a difference between phase and group velocities, which is responsible for a delay of the pulse front with respect to the wavefront [235]. In pulses that are not much shorter than 100 fs and allow to neglect GVD in thin lenses, this delay (known as propagation time difference) will be the dominant effect in the coupling among the temporal, spectral and spatial properties of a beam focused by a singlet lens. This will result in a spatiotemporal distortion of the pulse [236]: for instance, a temporal Gaussian pulse in the vicinity of the optical axis suffers temporal broadening, whereas spatial distribution

changes with time. Additionally, spherical aberration will also play an important role, favouring the shortening of pulses in the paraxial focus at the cost of a larger focal spot [237, 238].

In this chapter we will make use of the strong chromatic aberration produced by a diffractive lens to spectrally tailor nonlinear processes, such as second-harmonic [231] and supercontinuum generation [233], which will be further developed in the next chapter. To understand these applications we will first analyse the spatiotemporal characteristics of femtosecond pulses focused by means of diffractive optics [239].

The experiments presented in this chapter were developed in collaboration with the "Group de Recerca d'Optica" at the Universitat Jaume I in Castelló, although all the experimental setups were implemented at the laboratory for Intense Lasers of the University of Salamanca.

6.2. Diffractive lenses

Essentially, a *kinoform diffractive lens* (DL) [240] is an optical element that focuses light based on diffraction. In this sense, a DL has certain similarities with a Fresnel zone plane (FZP) [241], which consists of opaque and transparent symmetric rings. The constructive interference among the transmitted parts of the beam leads to the focusing of the same.

Unlike a FZP, a DL consists of a series of radial rings or *zones* of decreasing width composed of hyperboloid fragments (see Fig 6. 1). This type of transmission profile modifies the wavefront of the input beam so that a plane wave is transformed into a spherical wave. This is an important improvement with respect to the FZP, since an efficiency of nearly 100% can be achieved under illumination with a monochromatic light.

The operation principle of a DL [242] is schematically illustrated in Fig 6. 1. The structure focuses light because a 2π phase shift is impressed in each of the rings, which is achieved by changing the thickness T(r) in each section of the device as follows:

$$T(r) = \frac{\lambda_0}{(n-1)}\left(m - \frac{r^2}{2\lambda_0 f_0} \right) \tag{120}$$

where r refers to the radial coordinate, m is the zone number, λ_0 is the wavelength which the DL has been designed for, n is the refractive index of the DL and $f_0 = d / n^2$. The phase shift introduced by the lens is given by:

$$\varphi(r) = 2\pi\left(m - \frac{r^2}{2\lambda_0 f_0} \right) \tag{121}$$

This way, an original flat wavefront becomes a parabolic surface of the form:

$$\psi(r) = \frac{\pi}{\lambda}\frac{r^2}{f(\lambda)} \tag{122}$$

where λ is the wavelength and $f(\lambda)$ is the wavelength dependent focal length, which can be deduced by comparing expressions (121) and (122):

$$f(\lambda) = \frac{\lambda_0}{\lambda} f_0 \tag{123}$$

For monochromatic light (i.e., continuous waves) the behaviour of the beam focused by a DL or a refractive lens with the same numerical aperture (NA) is expected to be similar. However, for light with large spectral content (i.e., ultrashort pulses) Eq.(123) involves strong chromatic aberration and each wavelength will be focused at a different distance from the DL, as shown in Fig 6. 1.

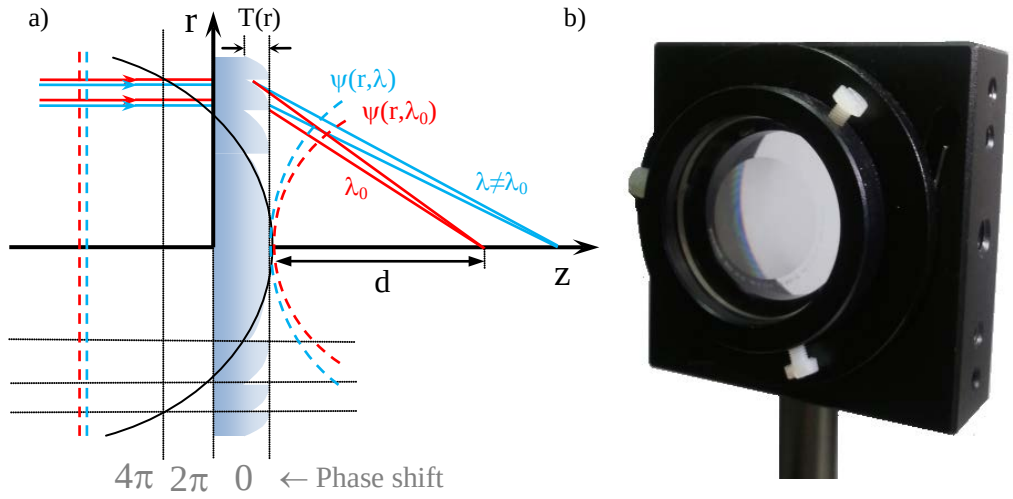

Fig 6. 1: a) Scheme of the operation principle of a DL. b) Image of a DL.

In particular, the DL that will be used throughout these experiments was designed with a focal length of f_0=150 mm for λ_0=565 nm. In Fig 6. 2 we have plotted the focal length as a function of the wavelength for the spectral content of our laser.

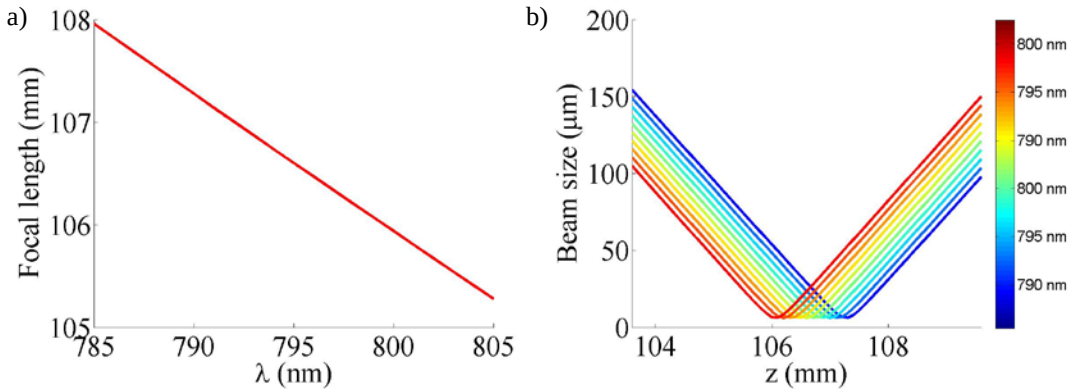

Fig 6. 2: a) Dependence of the focal length of the DL on the wavelength. b)Propagation of a Gaussian beam with large spectral content (see details in the text).

As a direct consequence, this distribution of the focal lengths will create a continuum of foci, instead of a single focal point. This has been illustrated in the right-side panel of Fig 6. 2, where the propagation of our laser pulses after going through the DL has been simulated. For this purpose we applied the propagation equation of Gaussian beams focused by a lens, substituting the focal length by Eq.(123):

$$\omega(z,\lambda)=\omega_0(\lambda)\left[\frac{z_R(\lambda)^2+\left[z-f(\lambda)\right]^2}{z_R(\lambda)^2+\left[f_0-f(\lambda)\right]^2}\right]^{1/2} \tag{124}$$

where z is the propagation axis, $\omega_0(\lambda)=\frac{f(\lambda)\lambda}{\pi\rho}$ is the beam radius in the focus, ρ being the beam radius at the entrance of the lens, and z_R is the Rayleigh length defined as:

$$z_R(\lambda)=\frac{\pi\omega_0^2(\lambda)}{\lambda} \tag{125}$$

As input for the simulation we used our laser parameters (9 nm spectral bandwidth at FWHM and 795 nm central wavelength). The intensity profile was approximated as a Gaussian distribution of 9 mm width at $1/e^2$.

Unlike refractive lenses, where the focal region coincides with the Rayleigh length, the region of a DL is defined as the area in the optical axis that contains the foci for all the wavelengths present in the laser bandwidth. Therefore, we can express the focal region of a DL as the difference between the focal lengths of the two wavelengths delimiting the spectral bandwidth of the laser:

$$\Delta f = f_0\frac{\Delta\lambda}{\lambda_0} \tag{126}$$

where Δλ is the laser bandwidth. Eq.(126) yields a focal region of Δf~1.3 mm for our laser pulses, which is several orders of magnitude larger than the focal region achieved with a singlet lens due to chromatic aberration:

$$\Delta f = -\frac{f_0\Delta\lambda\left(\frac{dn}{d\lambda}\right)_{\lambda=\lambda_0}}{n_0-1} \tag{127}$$

n_0 being the refractive index for λ_0.

As an example, let us consider BK7, one of the most common materials employed in lens manufacturing. A refractive lens made of BK7 (the dispersion formula for this glass can be found e.g. in Ref.[243]) with the same focal length for the central wavelength as the DL (i.e., f_0=106.6 mm for λ_0=795 nm) yields a focal region of Δf= 0.0377 mm for our laser pulses.

6.3. Femtosecond pulses focused by kinoform diffractive lenses

So far, we have reviewed the properties of a DL. To further understand the characteristics of the pulses focused by such a lens, it is necessary to perform a complete spatiotemporal and spatio-spectral characterization. In this section we will calculate the electric field in the focal region of our DL and obtain its experimental characterization [239] by means of the *Spatiotemporal amplitude-and-phase reconstruction by Fourier-transform of interference spectra of high-complex-beams* (STARFISH) technique [226, 244], as it will be explained in the following sections.

6.3.1 Theoretical model

Following Fresnel's diffraction theory, it is possible to obtain a numerical propagation of the pulses behind the DL. For an exact solution the lens should be modelled taking into account its kinoform profile as in (109), which demands a high degree of spatial resolution and therefore long computation time. Instead of an exact solution, it is possible to approach the effect of the DL by introducing a variable focal length of the type (123) in the phase.

Under the paraxial approximation, the electric field can be calculated using Fresnel's diffraction as [221]:

$$U(r_2,\lambda) = i\frac{2\pi}{\lambda z}\exp(-ikz)\exp\left(-\frac{ikr_2^2}{2z}\right)\int_0^\infty U_1(r_1,\lambda)\exp\left(-\frac{ikr_1^2}{2z}\right)J_0\left(\frac{kr_1r_2}{z}\right)r_1dr_1 \quad (128)$$

where r_2 and r_1 refer to the radial coordinates in the input and output planes respectively, U_1 is the input electric field distribution and J_0 is the Bessel function of the first kind of zero order. In our case U_1 can be approximated by:

$$U_1(r_1,\lambda) = U_0(r_1,\lambda)\exp\left[-i\psi(r_1,\lambda)\right] \quad (129)$$

U_0 being the electric field against the DL. In Eq.(129) we assume that the beam size is much smaller than the DL, so that diffraction due to the annular aperture can be neglected.

6.3.2 Experimental method

The experimental measurements were carried out applying the STARFISH technique [226, 244].

This method is based on *spectral interferometry*: a well-known pulse (called reference) interferes in the spectral domain with the pulse to be characterized (test pulse), which is delayed for a time τ with respect to the reference. The resulting spectrum is then:

$$S(\omega) = S_{test}(\omega) + S_{ref}(\omega) + 2\sqrt{S_{test}(\omega)S_{ref}(\omega)}\cos\left[\phi_{test}(\omega) - \phi_{ref}(\omega) - \omega\tau\right] \quad (130)$$

where $S_{test}(\omega)$ and $S_{ref}(\omega)$ are the spectra of the test and the reference, and $\phi_{test}(\omega)$ and $\phi_{ref}(\omega)$ stand for the phases of the test and reference pulses. If the spectrum (130) is Fourier transformed to the temporal domain, it presents three peaks: the central one at t=0 corresponds to the continuum (i.e., the sum of both spectra), while the two others peaks (at $t=\pm\tau$) correspond to the interference term. If one of the side peaks is filtered and a direct Fourier transform is applied, it is possible to obtain the spectral phase of the test pulse, ϕ_{test}. This information, together with the spectrum, $S_{test}(\omega)$, provides the complete characterization in the spectral domain.The temporal profile (intensity and phase) is obtained by simply applying an inverse Fourier transform. If this measurement is performed along different points in the transversal plane of the test beam, we will be able to retrieve their temporal profiles. In other words, we are correlating the spatial and temporal features, i.e., it is a *spatiotemporal characterization*.

The experimental setup is presented in Fig 6. 3. The laser pulses were split into two branches. The first one acted as reference and was fully characterized with a Grenouille (Swamp Optics) [245]. The second branch contained the DL (Institute of Automatics and Electrometry, Russia),

which was mounted on a delay stage (DS1). This configuration allowed us to change the distance between the DL and the end of the fibre coupler so that we could monitor the evolution along the propagation axis, z. The pulses behind the DL were our test pulses. The end of the fibre coupler was mounted on a motorized stage (Zaber, T-LA28), DS2, which allowed us to transversally scan the test beam. Since the problem presented rotational symmetry, we just performed the scan in the x-axis. A delay stage (DS3) served to properly adjust the delay to 2 ps between both pulses. Eventually, the test and reference pulses interfered through a fibre coupler, and the resulting spectrum (i.e., S(ω)) was resolved with a spectrometer (Avantes, AvaSpec 2048-USB1). The spatial resolution in this configuration was limited by the core mode fibre of the fibre coupler, which in our case was 4 μm.

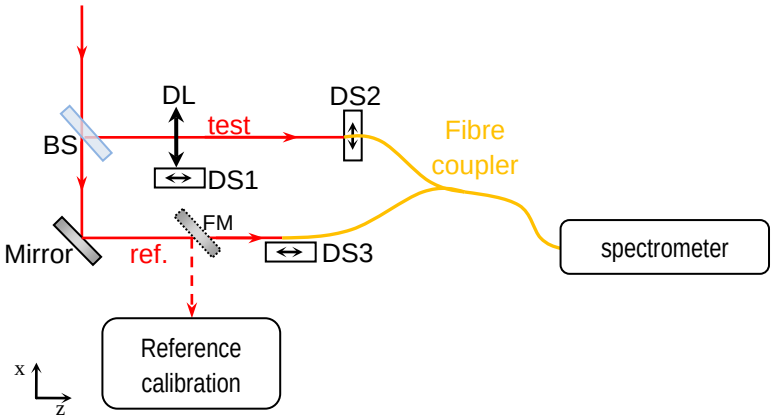

Fig 6. 3: Experimental setup for the characterization of the pulses focused by a DL. BS: beamsplitter; DS: delay stage; DL: diffractive lens; FM: flip mirror.

6.3.3 Wavefront characterization

The spatial resolution of most standard techniques (for example, Hartmann-Shack) prevents their use in measurements where high resolution is necessary, which is the case of the focal spot of a lens. Moreover, in the case of a DL we are interested in knowing the spectral dependence of the wavefront, which is only feasible if a spectrometer is involved in the setup.

These requirements are satisfied by several spatiotemporal characterization techniques. In [224], Rubino et al. implemented a grating that images the beam into a Hartmann-Shack sensor, retrieving the wavefront in one axis. In [225] the authors proposed the use of the iterative Gerchberg-Saxon algorithm to reduce the point-to-point phase drift introduced by the interferometer used in SEA TADPOLE [246] and to reconstruct the phase front.

Finally, high spatial resolution and frequency resolved measurements, along with the good stability of the interferometer, make STARFISH a suitable tool for direct phase retrieval [239, 244].

Fig 6. 4 shows the simulated and experimental wavefronts registered along the transverse coordinate, x, of the pulses delivered by our laser in the focal region of the DL at different planes along the propagation direction, z. As predicted by Eq.(123) we can observe that the bluer frequencies are focused at larger distances. This is clearly observed at z_0=106.6 mm, which coincides with the nominal focus for the central wavelength, $f(\lambda_0)$: while the redder wavelengths

present a divergent wavefront, the shorter ones are still focusing and thus present a converging phase front.

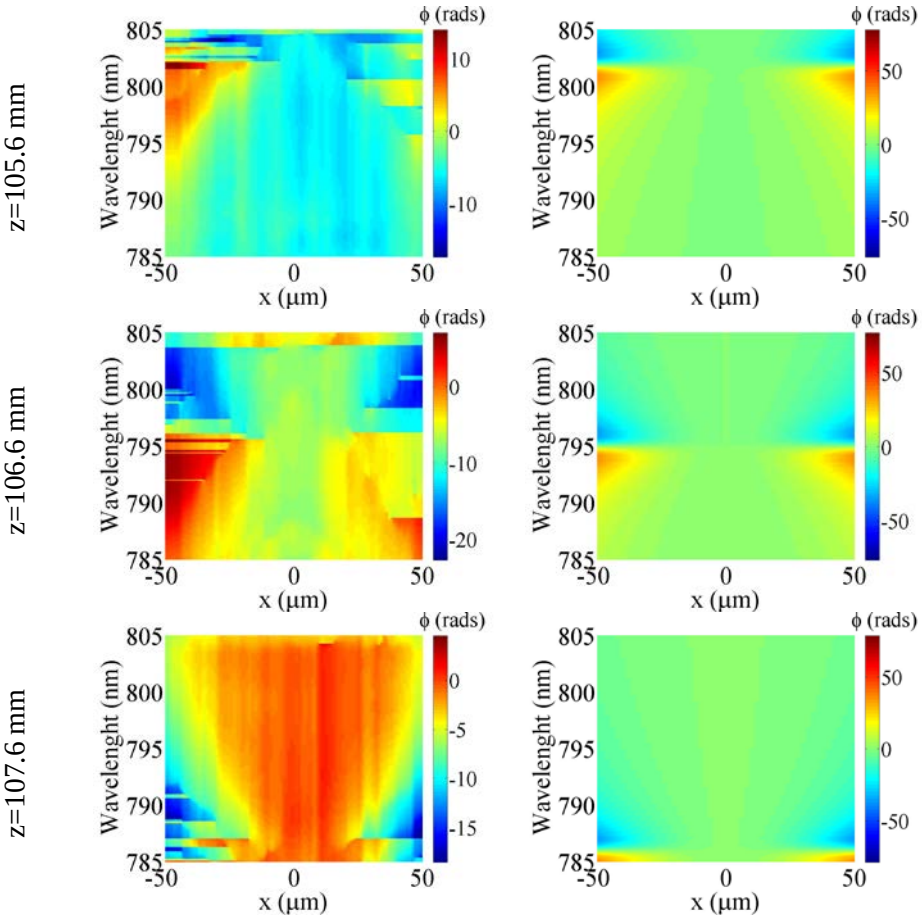

Fig 6. 4: Experimental (left column) and simulated (right column) wavefront characterization of pulses focused by the DL around the focal region.

6.3.4 Spatiotemporal dynamics

A complete spatiotemporal characterization is crucial to understand how the pulses are shaped when they undergo focusing by the DL.

The results for different propagation distances are presented in Fig 6. 5. The left column corresponds to the experimental measurements performed with STARFISH. In the right column we have depicted the simulations corresponding to the inverse Fourier transform of the spatio-spectral traces obtained with Eq.(128).

First, we observe that the pulse front curvature is the same at both sides of the focus, which is in agreement with previous studies for chromatic elements [235, 236]. At z_0=106.6 mm, spatiotemporal intensity consists of a main broadened central peak and a train of pulses in the wings. Additionally, spatial distribution changes with time, indicating the coupling of the temporal and spatial properties of the focused pulse.

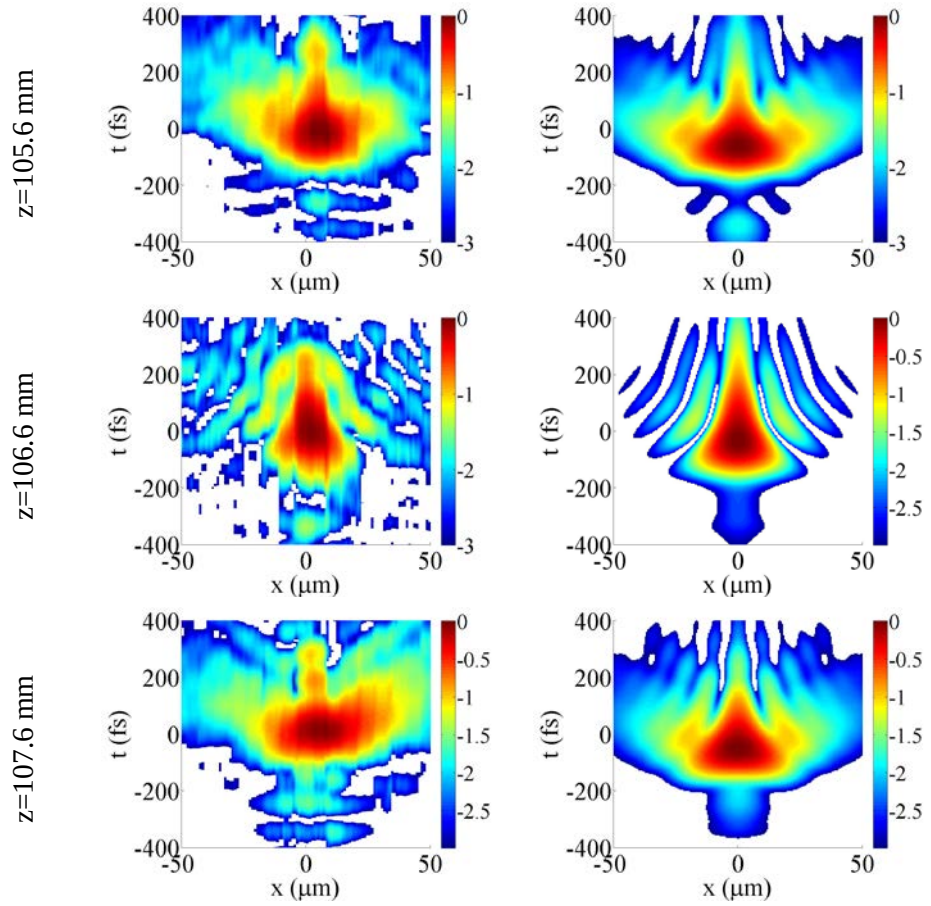

Fig 6. 5: Experimental (left) and simulated (right) spatiotemporal reconstruction for different distances

To further clarify these effects, it is interesting to plot the temporal and spectral profiles on axis (x=0), as in Fig 6. 7. In the first column, the instantaneous wavelength (i.e., the phase) has been represented with a dotted line and the intensity with a solid line. In the first panel (z=105.6 mm), the pulse is estimated to be 139 fs at FWHM. The longer wavelengths travel in the trailing part of the pulse, which corresponds to a negative chirp. In such case, the spectrum becomes flattened and the gravity centre is at 798.3 nm: since the longest wavelengths of the spectrum are focused, their spectral intensity increases, equalling that of the central wavelength and broadening the spectrum. For this reason, the pulse is compressed in time. The chirp can be easily explained by applying geometrical optics. The behaviour observed for the chirp can be explained as follows: if we refer back to Fig 6. 2b, we deduce that, for a distance z=105.5 mm, the redder wavelengths are in focus and the optical path is larger. In contrast, the blue wavelengths are out of focus. Since the core of the fibre used for the measurement was only 4 μm, only the on-axis rays are collected for the wavelengths. This situation is schematically illustrated in Fig 6. 6:

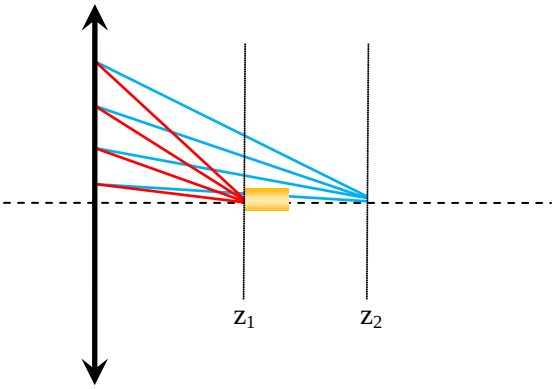

Fig 6. 6: Ray tracing of the diffractive lens for different wavelengths. The yellow block represents the fibre

At the nominal focus of the central wavelength, z=106.6 mm, the phase is almost flat and the pulse is broadened to 181 fs. The corresponding spectrum is narrower than that of the original pulse. This narrowing comes from the fact that the other wavelengths are now out of focus, yielding a higher ratio between the spectral intensity of the central wavelength and that of the remaining wavelengths. When the distance is increased with respect to the lens, the pulse is again shortened to 114 fs and the frequency distribution corresponds to positive chirp. The spectrum is again enlarged, in a situation similar to that of the first panel.

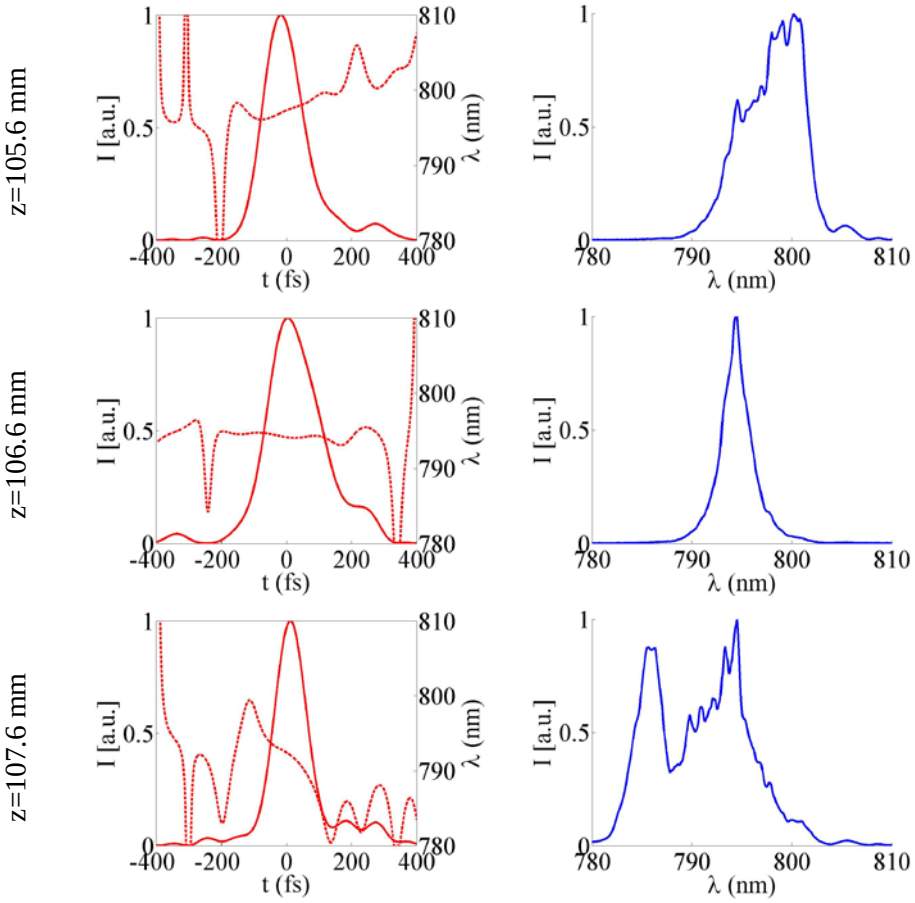

Fig 6. 7: On-axis temporal profile (left column) and spectrum (right column). The dotted line is the instantaneous wavelength (i.e., the phase), while the solid line corresponds to the intensity.

6.4. Application to parametric processes

6.4.1 Motivation

As mentioned in previous chapters, the possibility of extending the available femtosecond sources to new regions in the electromagnetic spectrum is one of the main concerns in the laser community. In this sense, second- and third- harmonic generation is probably one of the most extended methods to access shorter wavelengths. Therefore, there is great interest in generating such nonlinear effects with high efficiency and flexibility. In [247], for example, the conversion efficiency of second- and third harmonic generation was enhanced by means of Fresnel-lensing effects.

Our aim in this section is to present a summary of the results reported concerning the applicability of the DL in parametric processes to achieve wavelength tunability. This effect has been exploited, for example, to improve the scanning range in nonlinear microscopy [248]. For further reading, please refer to C. Romero's dissertation [249].

6.4.2 Second-harmonic generation

The DL was used to focus the laser pulses in a 0.5 mm type I BBO crystal (θ=29.1º, φ=0º), which was initially placed 104 mm away from the lens. The DL was mounted on a motorized stage that allowed its distance to be increased in steps of 75 µm. The spectrum was then captured with a spectrometer (HR4000, Ocean Optics). For comparison purposes, the same measurement was performed by replacing the DL with an achromat doublet with a focal length of 100 mm (Linos G063144525).

An example of the so-generated traces is shown in Fig 6. 8, where each column of the map corresponds to the second-harmonic (SH) spectra captured at different distances from the lens. On the left side of the picture, the results for the DL are presented. Unlike in the case of the achromat doublet (right panel of Fig 6. 8), a clear tunability of the central wavelength of the SH is observed, which is attributed to the strong chromatic aberration of the DL.

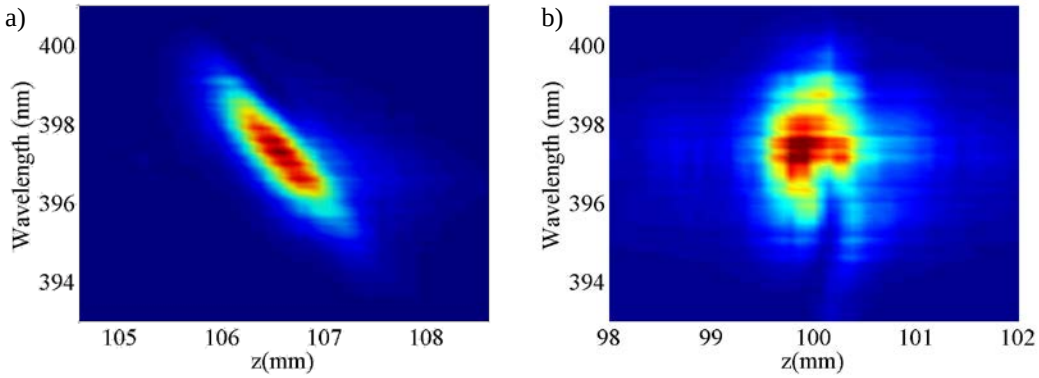

Fig 6. 8: SH spectrum as a function of the relative distance between the lens and the BBO for a) a diffractive and b) a refractive lens. See reference [231] for more details.

This confirms the possibility of tuning the central wavelength of the SH signal when changing the lens-crystal distance, provided that the thickness of the crystal is adequate (for samples thicker

than the focal region the effect is not observed, since all the wavelengths are focused inside the crystal).

Another effect can be observed when the maps for the diffractive and refractive lenses are compared: in the case of the DL, the bandwidth is reduced due to the combination of the strong chromatic aberration and the limited thickness of the crystal. The second consequence is a slight decrease in the conversion efficiency of pulses focused by a DL.

In order to assess the applicability of the so-generated SH pulses, a complete characterization is mandatory [232]. First, a correlation measurement was performed, yielding a pulse duration of 150 fs (near the Fourier transform limit for the corresponding spectrum).

Second, the spatial profile was analysed. As expected, the beams do not preserve the Gaussian shape due to the angular acceptance of the crystal. However, this effect is more significant in the case of the refractive lens, with an ellipticity of 0.32 in contrast to the 0.47 of the DL. Moreover, the beam exhibits good spatial quality and no diffraction patterns were observed. The spatial chirp was also measured by a spectral transversal scan and was found to be considerably larger in the case of the refractive lens.

6.4.3 Sum-frequency generation

The SH pulses described in Sect. 6.4.3 can be applied to achieve tunability in third-harmonic (TH) generation by means of sum-frequency with a sample of the fundamental beam. The process was performed in a BBO crystal (6x6x0.1 mm^3) cut for sum-frequency generation (θ=44.3º, φ=90º). The spectral maps for the TH signal are presented in Fig 6. 9, where we have plotted the spectrum of the TH pulses versus the distance from the first BBO crystal (employed for SHG) to the DL. In the right panel of the figure we show the results when the DL is replaced by the achromat doublet.

As it can be observed in the following figure, a certain degree of tunability is also achieved. Although this setup is not as easy to implement as that of the SHG, it could be practical in spectroscopy, since a tunable source in the near UV is useful in certain applications.

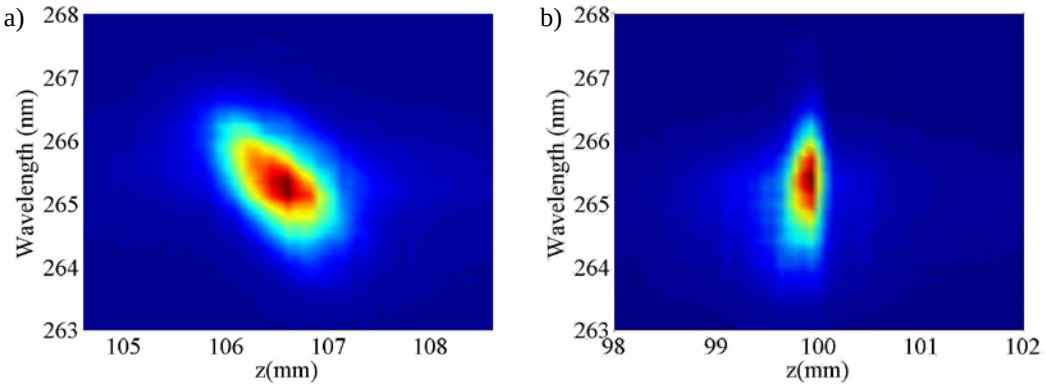

Fig 6. 9: TH spectrum as a function of the relative distance between the lens and the BBO for a) a diffractive and b) a refractive lens.

6.5. Application to supercontinuum generation

To conclude, let us introduce the last application of chromatic aberration induced by DLs, which will be the main concern of the next chapter: supercontinuum (SC) generation.

Although the parametric processes described in the previous section enable access to other wavelengths, in many experiments it is interesting to have a source that can deliver pulses in a wide range of frequencies. As mentioned in Chapter 3, optical parametric amplifiers (OPAs) are commonly used for this purpose. One of the key elements in certain ultrafast OPAs is SC generation.

A description of the SC process was already provided in Chapter 3: we referred to SC (or white light) generation as the interplay of processes that take place in a medium with third order susceptibility, giving rise to extreme spectral broadening when an intense pulse propagates through it.

The spectral properties of the generated pulses have been shown to depend on several factors that will be carefully described in the next chapter. In particular, the cut-off frequency is strongly related to the physical properties of the medium, such as the band-gap or its chromatic dispersion. It is also known that some experimental conditions have a significant influence on the spectral extension of the SC pulses. In particular, SC generation based on Fresnel diffraction effects was studied in [250] by using circular apertures.

The aim of this study was to take advantage of the focusing properties of the DL to obtain SC pulses in the visible with tailored spectra. As will be further explained in the next chapter, it was observed that, on the one hand, the anti-Stokes extension of the SC spectrum generated when using a DL was larger than that generated when using a refractive lens in analogous conditions. On the other hand, the spectra exhibited a certain degree of tunability when changing the lens-crystal distance.

6.6. Summary and conclusions

In this chapter we have introduced the fundamentals of diffractive optics and kinoform lenses. In particular, we have studied the focusing dynamics of a kinoform diffractive lens with a wavelength dependent focal length.

To this end, a numerical model based on Fresnel diffraction has been proposed and the experimental characterization by means of the spatiotemporal technique STARFISH has been presented, finding very good agreement between simulations and experimental results.

The capability of STARFISH to resolve the wavefront in the frequency domain has also been demonstrated. In addition, the high spatial resolution offered by this method allows the characterization of beams in the vicinity of the focus. Here we should remark that none of these two particular features can be obtained by traditional techniques. Therefore STARFISH can be considered a complete tool for the experimental description of pulse dynamics.

In the second block, we have briefly described the use of DLs to improve parametric processes (SHG, SFG) and SC generation. Unlike refractive lenses, DLs make it possible to tune the central wavelength of the generated signal by simply changing the relative distance between the sample and the lens. In the case of SHG and SFG, an alternative technique to produce a similar tunability

could be achieved by changing the orientation of a thick nonlinear crystal where the nonlinear process is taking place. However, the latter is not apt for ultrashort pulses because the shifting of the phase-matching curve in relation to the pulse spectrum will lead to the generation of a modulated spectrum in the SH pulse and, therefore, to a degraded temporal shape. In addition to the direct application of the generated tunable pulses to experiments in spectroscopy, the proposed technique can be extended to other processes like optical parametric amplification or even to high-order harmonic generation.

7

Supercontinuum generation in solids with diffractive lenses

7.1. Introduction.

As mentioned in previous chapters, the wavelength tunability of laser sources attracts a great deal of interest in many fields such as material processing, spectroscopy or biomedicine. To name some examples, in [251] second- and third- harmonic pulses from a femtosecond laser are used to remove tempera paints and in [252] they are used to induce periodic surface structures on thin polymers.

However second-order parametric processes make it possible to obtain frequency tunability in a discrete range. For this reason, in the last decade an effort in the ultrafast community has been made to improve optical parametric amplifiers (OPAs) [46, 249, 253].

In particular, there is currently a great amount of interest in their extension to the deep UV, since many biomolecules (e.g. DNA or proteins) undergo ultrafast processes in this range [254]. An example of such processes is the DNA photoprotection mechanism: when ultraviolet (UV) radiation is absorbed by DNA, the electronic energy acquired by the molecule is efficiently converted into vibrational energy (heat) on an ultrafast timescale (from a few tens to a few hundreds of femtoseconds) [255, 256] thus preventing DNA damage.

The tracking of ultrafast processes often requires the development of shaped UV pulses. To this end, several schemes have been proposed so far. For example, Tseng et al. [257] employed an acousto-optic modulator, whereas Krebs and co-workers [258] used an acousto-optic programmable dispersive filter to direct pulse shaping in the UV. In [259], Armstrong et al. used

adaptive optics in an OPA to produce optimized wavelength-tunable pulse shapes for the study of protein dynamics [260]. The aim of the work presented in this chapter is to improve the supercontinuum (SC) generation stage to later implement it in an OPA with special attention to the UV range. This will be achieved by exploiting the strong chromatic aberration of the diffractive lens (DL) for the spectral control of the supercontinuum (SC) generation process [233], as was mentioned at the end of Chapter 6.

This chapter is organized as follows: first, we will review the physical factors and experimental conditions that determine the spectral characteristics of the SC. Then the experimental setup will be presented and the main results will be reported. Finally, a complete characterization is performed to assess the usefulness of the so generated pulses.

7.2. Spectral characteristics of the supercontinuum

Back in Chapter 3, we defined supercontinuum generation as the spectral broadening suffered by an intense pulse when it propagates in a medium in which the dominant lowest order of nonlinear susceptibility is $\chi^{(3)}$. In that chapter, a brief review of the main processes (self-focusing, self-phase modulation, self-steepening, Raman response, ionization and filamentation) responsible for SC generation was also presented.

A typical SC spectrum is shown in Fig 7. 1: the signal extends from the near infrared to the UV-visible region. There are modulations near the central wavelength and a strong Stokes/anti-Stokes asymmetry is observed: the extent of the anti-Stokes pedestal typically reaches frequencies of 10000 – 20000 cm^{-1}, while the Stokes side remains within 1000 – 2000 cm^{-1}. More recently, it was observed that a continuous spectrum with simultaneous broadening to low and high frequencies could be developed for ultraintense lasers ($P \sim 30 P_{cr}$) [199].

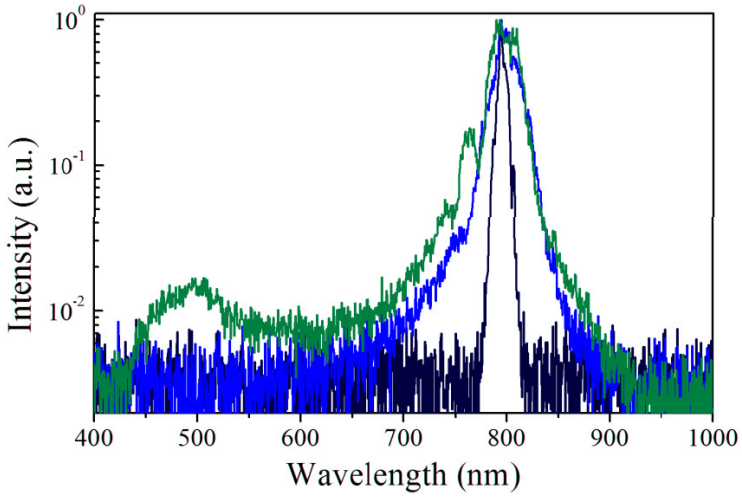

Fig 7. 1: SC spectrum generated in a 3 mm sapphire plate (green line). The dark blue line represents the spectrum of the initial laser pulse, whereas the blue line corresponds to a self-phase modulated spectrum.

In spite of its widespread use, SC generation remains far from being well understood. In particular, the mechanisms determining the spectral properties of the SC pulses (such as the spectral width and the cut-off frequency) are still under discussion. In this section, we will review

the main physical factors and experimental conditions that have so far been demonstrated to play a role in determining the spectral features of SC pulses.

7.2.1 Band-gap dependence

Provided that multiphoton ionization (MPI) is an important mechanism of free-electron generation with femtosecond pulses, Brodeur and Chin proposed the band-gap of a material as a parameter to predict the width of the SC in condensed media [261]. In their study, they analysed the SC spectra for different condensed media and carefully determined the threshold power for SC generation.

They reported a band-gap E_{gap} below which no continuum generation was observed. This threshold value corresponded to $E_{gap}^{th} \simeq 4.7\,eV$. Additionally, a trend that increased anti-Stokes spectral broadening with the band-gap was described.

These observations can be explained as follows. It is well known that a sharp peak intensity, which is limited by MPE up to a certain electron density N_e, develops during self-focusing (which can be regarded as the primary mechanism triggering the process). According to the authors, the appearance of free electrons by MPE during the intensity spike causes a sudden negative index change and thus a drop in nonlinear phase that translate into a large anti-Stokes broadening by SPM.

The threshold band-gap for SC generation is attributed to the dependence of the intensity necessary to generate N_e electrons on the band-gap energy of the medium [190], which presents a jump at E_{gap}^{th} due to the passage from 3-photon to 4-photon MPI. Therefore, the intensity achieved in media with $E_{gap} > E_{gap}^{th}$ is sufficient to accumulate enough nonlinear phase shifts for SC generation.

7.2.2 Chromatic dispersion

Based on computer simulations, Kolesik et al. elucidated that chromatic dispersion plays an important role in determining the spectral broadening of the SC [183, 262]. These authors proposed a model that included chromatic dispersion. In this scenario, the SC spectra for two identical media with different chromatic dispersion under the same experimental conditions were computed. It was found that the change in the SC spectrum follows that of the linear chromatic dispersion.

The band-gap dependence described in Sect. 7.2.1 is interpreted under this assertion as a result of the stronger dispersion at shorter wavelengths.

7.2.3 Input chirp

Since the chirp yields a decrease in the peak power of a pulse, one should expect that the more positively (negatively) chirped the pulse is, the higher the threshold energy to generate SC will be in a positive (negative) dispersive medium. This assertion was confirmed by Yang et al in [263]. Their results also shed some light into the dynamics of the SC generation process in ZK7 glass. Unlike transform limited pulses, where refocusing of filaments takes place, in negatively chirped pulses a single beam collapse can persist for relatively long distances (i.e., the energy required for multi-collapse is increased and the number of collapse events becomes reduced). It was also found

that conversion efficiency reduces with the chirp and the cut-off wavelength moves towards longer values. These properties were attributed to an ionization-free regime of filamentation, where the arrest of collapse is performed by other mechanisms such as GVD.

Kandidov and co-workers also addressed this issue in relation to air in [182]. Besides the negative chirp, they provide simulations for positive chirp. They concluded that the filament is always spread out for positive chirp, but the dynamics for negatively chirped pulses depend on the ratio between the compression and self-focusing distances. The largest filament is obtained when both distances are similar.

7.2.4 Pump energy

Many studies have concluded that the anti-Stokes side remains constant with the pump energy, while relative intensities change in different parts of the spectrum [264].

In reference [265], for example, the SC spectra was studied as a function of the input energy for water, chloroform and glass. In all cases, a limit attributed to a clamp in the intensity due to multiple filamentation was observed in the cut-off frequency: above a certain degree of input energy, the emergence of multiple filaments would allow a distribution of the pulse energy into many nearly identical plasma channels, preventing increases in peak intensity and also more broadening towards shorter wavelengths.

Yang and Mu tracked the evolution of the filaments created in a 7 mm long ZK7 sample as the energy was increased [266]. The pulses (50 fs, 800 nm central wavelength) were focused by means of a concave gold-mirror (1m radius). A 6 mm iris was placed before the mirror, thus having a diffraction pattern with the axial maximum intensity at the focal position. At low power (4 mW), a short single filament (0.8 mm) was observed, connected to a spectrum symmetrically broadened towards the shorter and longer wavelength regions. At 5 mW a second filament, identical to the first one, develops. When the laser power is higher (up to 8 mW), more refocusing filaments are created and the spacing between focusing filaments becomes shorter. This behaviour is connected to an enhancement of the anti-Stokes region in the SC spectrum. Finally, when the laser power is as high as 9mW, separated longitudinal filaments are no longer observed and instead a spatial fusion of multiple refocusing events takes place.

In reference [181] the dependence of the SC spectrum with the pump energy is investigated for a 4 mm long YAG crystal. At high energies the spectrum presents pronounced spectral wiggles. One possible explanation, which fits well with the filament characterization performed in other studies (e.g. [267]) is a refocusing of filament and continuum generation at two positions within the crystal. Both filaments could temporally interfere resulting in a modulated spectrum. At very high energies, a colourful pattern, which is thought to be the result of single filamentation break-up, is described.

7.2.5 Pump wavelength

In [264] the authors reported that the spectral width of the anti-Stokes of the spectrum is approximately doubled when the pump wavelength is increased from 400 nm to 800 nm for calcium fluoride and fused silica. In contrast, the chirp of the SC was found to be smaller for shorter wavelengths.

In [181] the wavelength was tuned in the mid-infrared, from 1100 to 1600 nm, showing the same trend: as the pump is moved towards longer wavelengths, spectral broadening is extended to the Stokes side, although it maintains the same cut-off frequency.

7.2.6 Pulse duration

As to pulse duration, experiments with 45 fs and 300 fs pulses under similar conditions suggest that the shorter the pulse, the broader the white light spectrum [268]. This difference has been explained in terms of SPM and free electron generation: since SPM is inversely proportional to pulse duration, shorter pulses are expected to yield broader spectra.

7.2.7 Polarization

It has been proved that polarization affects the conversion efficiency of the process of SC generation. Under the same conditions, the signal intensity of SC obtained with linear polarization was found to be higher than with circular polarization [268]. This is rationalized on the basis of MPI and SPM. On the one hand, the ionization rate depends on the state of polarization of the incident field. On the other hand, when the material exhibiting third order susceptibility is exposed to an intense field, cross-phase modulation (XPM) may occur besides SPM. XPM gives rise to a change in the nonlinear index that depends not only on intensity, but also on polarization.

7.2.8 Crystal thickness

As reported in [181], for increasing crystal length the spectrum shows largely increasing energy density in the Stokes side, and the required pump energy to optimize the SC spectrum decreases for longer crystals. Moreover, minimum crystal thicknesses are found to yield a plateau-like spectrum, but above this value, cut-off frequency does not vary with sample thickness.

7.2.9 Focus position

Geometrical conditions also play an important role in the spectral shaping of SC pulses.

In [264] Ziolek et al. focused 800 nm, 100 fs pulses with a 100 mm focal length lens in a 10 mm long cuvette filled with water. They concluded that the anti-Stokes edge is constant and that spectral width does not depend on the focus position, even if the distance between the lens and the cuvette is short. However, the spectral density of the anti-Stokes side increases as the focus approaches the front of the cuvette.

This scenario arises some controversy as regards the observations of Dharmadhikari et al. [268] for 45 fs pulses focused by a 300 mm focal length lens in a 7.5 cm long BaF_2 crystal. Unlike the previous case, very high power levels were employed for this study (~3000 P_{cr}). It was concluded that when the focus is moved towards the rear face of the crystal, the spectral content of the redder wavelengths is increased with respect to the blue ones. In contrast, when the focus is situated near the front face, the broadest white light spectrum is achieved. The authors explain this behaviour on the grounds that crystal dispersion broadens the pulse and therefore reduces its peak intensity.

However, there are certain relevant differences to be taken into account regarding the experimental conditions and which could partly explain the aforementioned disagreement. First, in the latter experiment, the sample (75 mm of BaF_2) and focusing conditions (30 cm focal length

lens) were different. Most importantly, short pulses (45 fs) and very high powers ($P\sim3000P_{cr}$) were applied.

It is very interesting to have a look at the results by Fang and Kobayashi for the evolution of the spectrum of the SC pulses generated in fused silica [269], since, as we shall see later, their experimental conditions are similar to ours. In their experiment, 795 nm, 50 fs pulses where focused with a concave mirror (yielding a numerical aperture of approximately 0.033) in a 2 mm sample, with the energy set at 1.5times the threshold energy. The spectrum was monitored for different positions of the plate around the focus, and they concluded that the blue broadening becomes more pronounced as the focus reaches the front face of the glass.

7.2.10 Numerical aperture

In [267] the filamentation of focused 120 fs pulses in fused silica is studied under different focusing conditions. When the energy was set to 2.1 μJ a single filament was observed for all the numerical apertures (NA) studied. However, when the energy was increased to 3.3 μJ three regimes were observed. For small numerical apertures (NA~0.01) a single long filament was observed. For medium apertures (NA~0.04) the induced plasma filament exhibits a two-focus structure, whereas for larger apertures (NA~0.09) it shows a short filament. These observations are closely connected with the process dynamics in each case. In the first case, self-focusing and GVD play a significant role in propagation, whereas for larger aperture the dynamics is governed by multiphoton ionization.

These results agree with those obtained by Ashcom et al [270]. In their experiment, these authors reported a larger range of NA, reaching NAs of 0.65. For NAs above 0.25, no SC was observed. This fact is attributed to the short propagation distance at high intensity, which prevents the proper accumulation of the nonlinear effects that produce SC. For NAs smaller than 0.25, the confocal parameter becomes smaller as the NA increases, yielding a shorter interaction length and therefore less blue broadening.

The dependence of the conversion efficiency on the NA has also been studied in [268] and [181] using different focal lengths, the conclusion being that high NAs lead to higher efficiencies. Additionally, as reported in [181], there is an optimum NA that significantly improves the stability and spectral extension of the SC pulses.

In reference [267], Wu et al reported the role of NA for various input powers. They concluded that for all NAs (ranging from 0.15 to 0.85) at low energies there is only one focus. As the energy is increased, a second focus appears for NAs below 0.65. However, for a 0.85 NA there are no multiple foci, but a long filament.

7.3. Supercontinuum generation with diffractive lenses

7.3.1 Experimental setup

The experimental setup (Fig 7. 2) for the experiments described in this chapter is relatively simple and does not differ too much from commonly used schemes for SC generation in solids.

The energy of the input pulses is measured with an analogue power meter (Spectra Physics, model 407-A) and the required adjustments are made by using a polarizer and a half-wave plate. An iris is placed before the focusing element to control the NA. A diffractive lens (Institute of

Automatics and Electrometry, Russia) with a focal length of f_0=106.6 nm for the central wavelength is used as the focusing element (a complete description of this was provided in Chapter 6). For comparison purposes, it is sometimes replaced by a 100 mm focal length achromat (Linos, G063144525).

As targets, we used sapphire plates (Eksma Optics) with different degrees of thickness, all of them with the optical axis set parallel to the laser polarization. The samples are mounted on a translational stage in order to precisely control lens-plate distance. Finally, a band-pass filter (Thorlabs, FG37S) allows us to remove the non-converted fundamental beam. The spectral analysis is carried out with a spectrometer (Avantes, AvaSpec-2048) coupled to the beam through a 50 μm core fibre (Ocean Optics, P50-2-UV/VIS). In order to concentrate the light into the fibre, a second lens is placed after the band-pass filter.

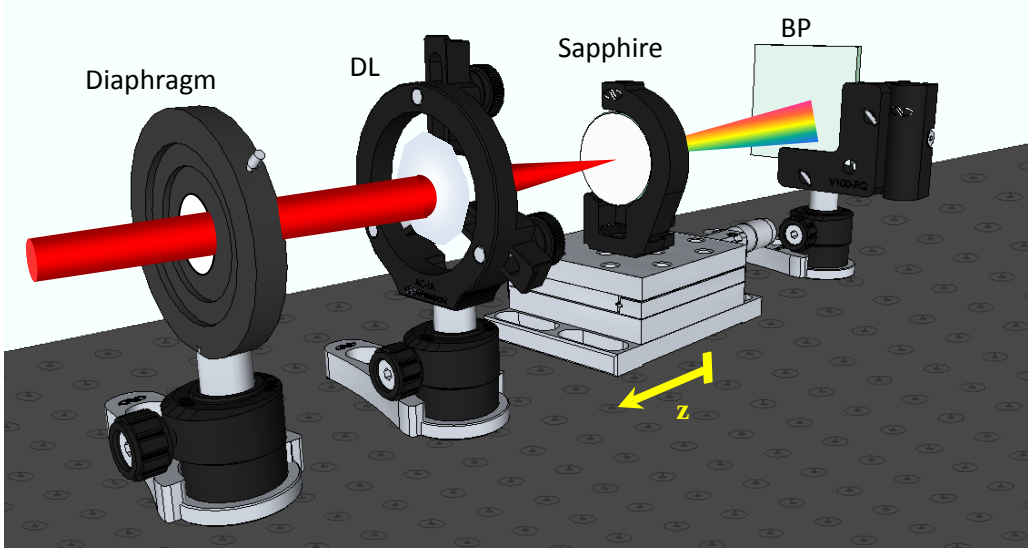

Fig 7. 2: Experimental setup for SC generation: a diaphragm is used to control the NA; the DL (replaced with an achromat for comparison purposes) focuses the pulses in a 3 mm sapphire plate. A band-pass filter (BP) is used to remove the non-converted fundamental light. The yellow arrow indicates larger values of z.

7.3.2 Results

Before going on to the experiments, the threshold energy for SC generation (i.e., the minimum energy to appreciate visible light projected onto a screen) with the iris fully open was determined for the different samples. In all cases, a filament is observed inside the sample. The results are shown in Table 7. 1, where the losses caused by the efficiency of the DL (~69%) have been taken into account.

		Sapphire			Fused silica
Thickness		1 mm	2 mm	3 mm	3 mm
Pulse energy	DL	1.66 μJ	0.97 μJ	0.97 μJ	1.24 μJ
	RL	-	-	0.46 μJ	0.50 μJ

Table 7. 1: Energy thresholds for SC generation for the samples employed in this study with either a diffractive lens (DL) or a refractive lens (RL). The efficiency of the DL has been taken into account to calculate these results.

We attribute the discrepancy between the threshold energies found for the DL and the refractive lens (RL) to the longer focal volume of the DL. This can also rationalize the difference between

the threshold energy of the 1 mm plate and the others, since in the former case the difference between the foci of the DL (~1.2 mm) is larger than the crystal thickness. Once the threshold energy (E_{th}) was determined, we set the pulse energy in all cases at $1.4E_{th}$, which allowed us to perform the experiments under equivalent conditions in terms of energy. Under these conditions, we obtained a single filament and we observed no significant damage to the sample.

We then recorded the spectra for both the DL and the RL, as the sample was moved towards the lens (increasing values of z indicate decreasing lens-sample distances). For this study, we used the 3 mm sapphire plate, since it is the most stable one. The respective spectral maps for the DL and the RL are shown on the first and second panel of Fig 7. 4. Differences between the two traces are evident. On the one hand, in the first panel we observe a larger region where the SC is generated, which is explained due to the larger focal volume of the DL (1.3 mm as opposed to the 0.5 mm of the RL). On the other hand, a large degree of wavelength tunability is observed for the DL. To better explain these effects, in Fig 7. 4c we have plotted the spectra extracted from the spectral map of the DL for different distances.

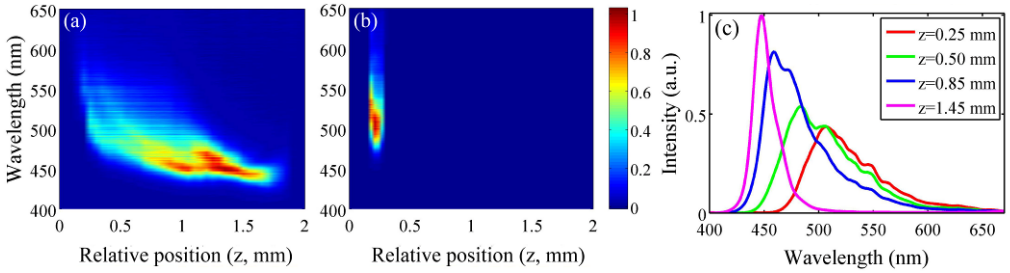

Fig 7. 4: Spectral maps for a) the DL and b) the RL as the distance between the lens and the crystal becomes reduced (corresponding to larger values of z). c) Spectra extracted from the first panel for different z.

Taking a closer look at Fig 7. 4 to examine the tunability exhibited by the DL, one finds that as the crystal is moved towards the lens (i.e., the focus position for the central wavelength is nearer to the rear face) the spectrum shifts towards shorter wavelengths. In particular, for the highest value of z, a strongly peaked structured centred at 450 nm is observed, extending the anti-Stokes cut-off wavelength to 420 nm (note that this value is sensitively shorter than the minimum achieved with the RL, 460 nm). This is opposed to what is observed in the case of achromatic elements, where the content of red wavelengths increased with respect to the blue ones as the focus was moved towards the rear face (see Sect. 7.2.9).

In Fig 7. 3 we show a large exposure photography of the experimental setup as the crystal was moved towards the DL. One can clearly see how the SC light is tuned towards shorter wavelengths.

A spectral stability measurement was also performed [249]. An acquisition was done each 5 s during 500 s. Spectral stability is found to be quite good, but it deteriorates as the peak shifts to

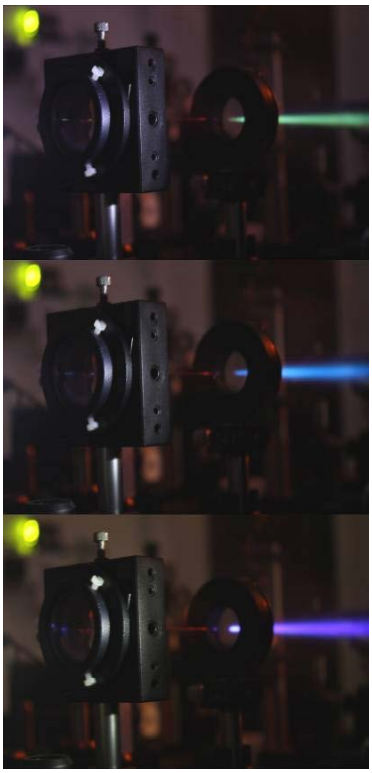

Fig 7. 3: Photography of the SC generated with a DL for different DL-sample distances.

the extreme blue border. This is reflected in the standard deviation: 0.97 nm for 463.4 nm and 3.02 nm for 444.5 nm.

In the following sections we will examine the role of different parameters in the so generated SC pulses and discuss the possible mechanisms behind the observed effects based on a study of filament development inside the crystal.

7.4. Parameters dependence

7.4.1 Pump energy

We first investigated the role of pump energy in the spectral content of the SC. For this purpose, the 3 mm sapphire plate was fixed at z=1.4 mm and the spectra were recorded for input energies of $1.28E_{th}$ (1.24 μJ), $1.57E_{th}$ (1.52 μJ), $1.71E_{th}$ (1.66 μJ), and $2E_{th}$ (1.93 μJ), as shown in Fig 7. 5.

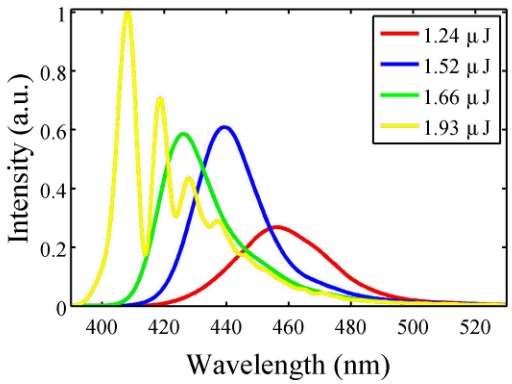

Fig 7. 5: Spectra recorded for different input energy when the 3 mm sapphire plate is fixed at z=1.4 mm.

Unlike white light generation with achromatic lenses, energy seems to play a role in shaping the spectrum. From Fig 7. 5 one deduces that the anti-Stokes side is enhanced as energy increases. When the energy doubles the threshold, the cut-off wavelength is extended below 400 nm. In such case, however, the stability is poor and the spectrum becomes highly modulated, which could be attributed to degradation of the sample.

7.4.2 Numerical aperture

The NA was controlled by changing the aperture of the iris placed just before the DL. First, we determined the energy threshold for SC generation for different apertures (from 1 to 12 mm) [249]. It must be mentioned that a previous calibration had been made to determine the transmission through the different iris diameters so that we could accurately calculate the amount of energy that was focused into the sample.

The highest energy required for SC generation is found for the closer diaphragm (approximately 1 μJ for 1mm iris). The threshold power decreases as the iris diameter becomes larger. However, the minimum value is reached in an iris of 4 mm; for larger apertures, threshold energy grows continuously. A similar behaviour was observed for the RL, although in this case threshold energy is constant for apertures of 6 mm and larger. Similar results were reported for fused silica [270]. This may suggest that diffraction plays an important role in the development of the filament for white light generation.

We have selected two iris sizes, 5.5 mm and 7.0 mm, to illustrate the effect of NA on continuum generation with a DL. These diaphragms correspond to a NA of 0.026 and of 0.034 respectively. Note that the iris that is fully open (Sect. 7.3.2) corresponds to NA~0.04. For comparison with the previous measurements, we decided to set the energy at $1.4E_{th}$ for all the experiments reported in this section. This yields energies of 0.98 μJ and 1.10 μJ for irises of 5.5 and 7.0 mm, respectively.

The spectra for both situations are presented in Fig 7. 6. The spectrum is centred in bluer wavelengths as the focus is nearer to the rear face, as was the case when the diaphragm was fully open. However, some differences are found with respect to the spectra in Fig 7. 4. First, the extension of the region where SC is generated is larger. This is easily explained in terms of an extension of the focal volume (for comparison, note that the Rayleigh length of an achromatic lens with a focal length of 106.6 mm is 0.380 mm for NA=0.026, 0.235 mm for NA=0.034 and 0.142 mm for NA=0.04).

Second, the spectral extension of the SC is broader and presents a flatter shape, but tunability is partially lost. As to the extension of the anti-Stokes side, by observing these maps and comparing them to those in Fig 7. 4, we can conclude that cut-off wavelength decreases as NA increases. This behavior is the opposite of that described for refractive lenses (Sect. 7.2.10). In Sect. 7.5.1, filament formation will be connected to the spectra reported here.

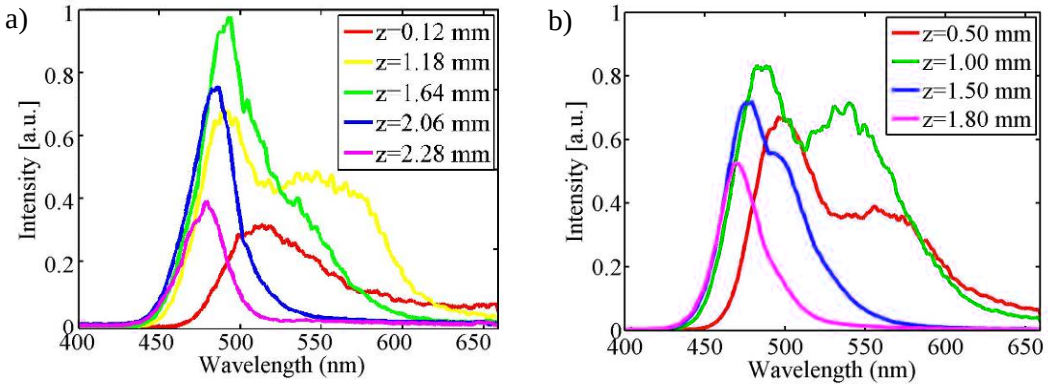

Fig 7. 6: Spectra taken for a) NA=0.026 and pulse energy of 0.98 μJ and b) NA=0.034 and pulse energy of 1.10 μJ.

7.4.3 Crystal thickness

Two other sapphire samples of thicknesses 1 and 2 mm were tested. The corresponding spectral maps are shown in the figure below (both of them with the iris fully open and the energy set at $1.4E_{th}$, E_{th} being the corresponding threshold dated in Table 7. 1). The effect of tunability is also observed, but it becomes less pronounced as thickness decreases. Note also that the extension of the spatial region where SC is generated is half the one in the case of the 3 mm crystal. In the 1 mm sapphire, stability is remarkably poorer than in the other two cases, due to the fact that this thickness is smaller than the focal region of the DL, which is detrimental to the proper formation and propagation of the filament.

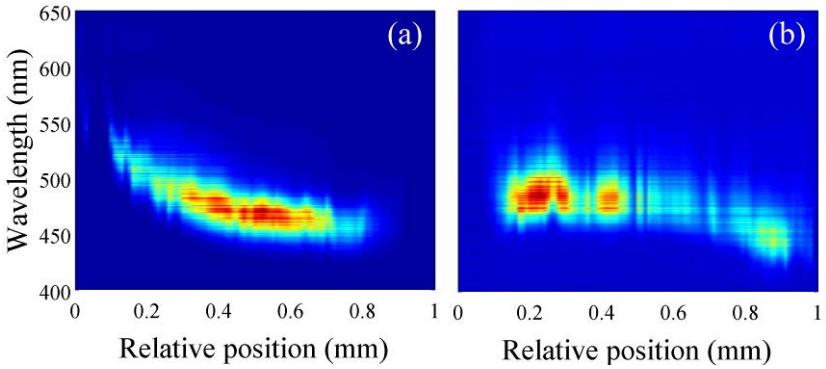

Fig 7. 7: Spectral maps for sapphire plates with two different thicknesses: a) 2 mm and b) 1mm.

7.4.4 Material

To test the reported effects on other material, we chose another commonly used medium for white light generation: fused silica. As in previous experiments, the measurement was performed with an input energy of $1.4E_{th}$ and the iris fully open. Tunability is also present, as can be seen in Fig 7. 8, but the length of the region where SC is generated is significantly smaller than that of the 3 mm sapphire.

One can also perceive poorer stability – shown as the lack of the spectrum in certain positions – when compared to the 3 mm sapphire plate. This can be associated with long term degradation of the material [46].

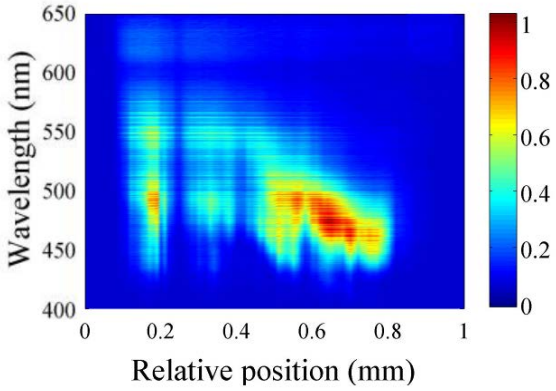

Fig 7. 8: Spectral map for a 3 mm fused silica plate.

7.5. Phenomenology

7.5.1 Supercontinuum dynamics with diffractive lenses

For a better understanding of the mechanisms behind the reported experiments, we studied the evolution of the filament inside the sample under the focusing conditions reported in the previous section.

For the present characterization, the experimental setup of Fig 7. 2 was employed. For this set of experiments, the circular border of the sample was partially polished to optical grade. A 45 mm focal length lens (Thorlabs, AC254-045-B) was used to image the filament onto a CCD sensor

(UEye1480-SE-C). The integration time was set at several milliseconds, thus the images are the average of several laser pulses. The calibration of the image dimensions (pixel/mm) was obtained by moving the sample over a specific distance along the z-axis with the translational stage. The displacement was then measured in terms of pixels with the software provided with the CCD sensor, and the equivalence in length units (mm) was then established. The image of the filament and the corresponding SC spectra are captured, since the distance between the DL (replaced at some points with a 100 mm focal length RL for comparison) and the 3 mm sapphire plate is varied. We have chosen z as the distance from the rear face of the crystal when SC generation is first observed. Increasing absolute values of z are associated with the approach of the sample towards the DL.

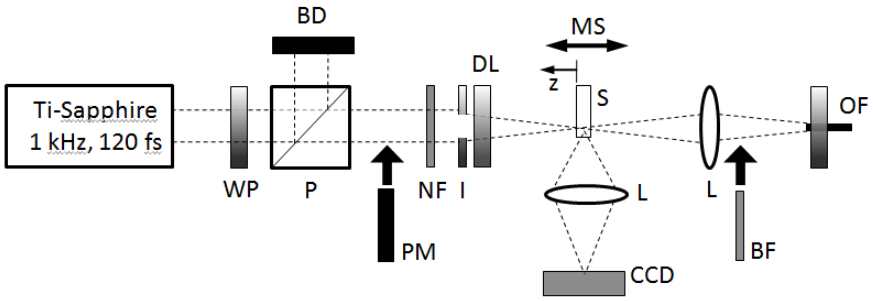

Fig 7. 9: Experimental setup for measuring the evolution of white-light filaments. WP, half-wave plate; P, linear polarizer; PM, power meter; BD, beam dumper; NF, neutral-density filter; I, iris; DL, kinoform diffractive lens; MS, motorized linear stage; S, sample (sapphire); L, lens; OF, optical fibre.

Let us start with the evolution of the filament that takes place when focusing with the DL if the iris is fully open (NA~0.04). The energy threshold to generate SC was found to be in the order of 0.85 μJ, slightly below that reported in Table 7. 1. This discrepancy has two possible explanations. First, small adjustments of the laser can slightly compress or stretch the pulses, thus changing peak intensity. Second, the sensitivity of the power meter, placed before a neutral density filter, highly affects the estimation of the input energy. For these reasons we decided to set the energy at $1.4E_{th}$, E_{th} equalling 0.85μJ.

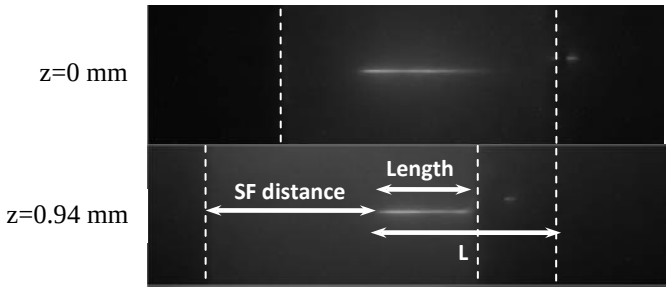

Fig 7. 10: Definition of the distances used in Table 7. 2.

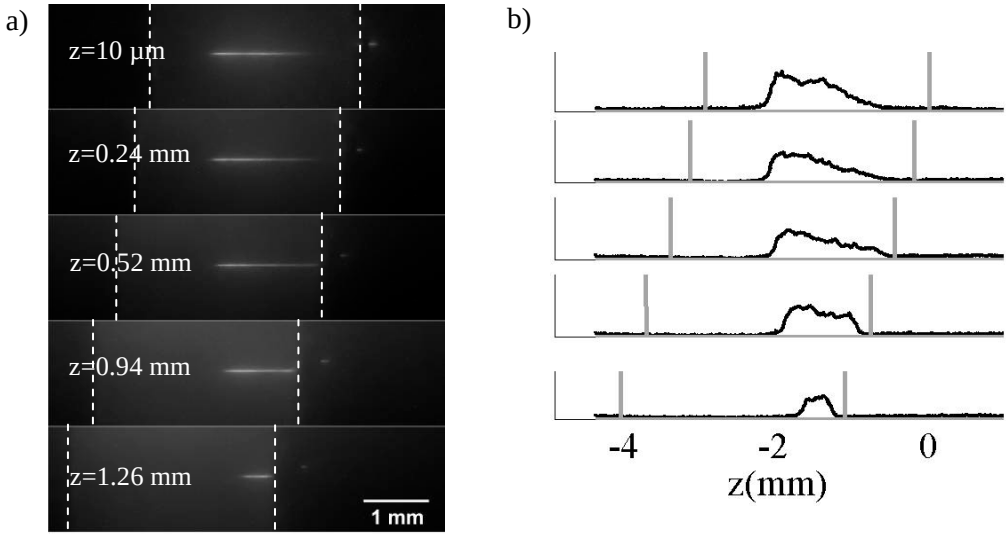

Fig 7. 11: a)Plasma luminescence as the sample approaches the DL and b) corresponding profiles. The iris was fully open and the input energy was 1.20 µJ. The vertical gray lines indicate the limits of the crystal.

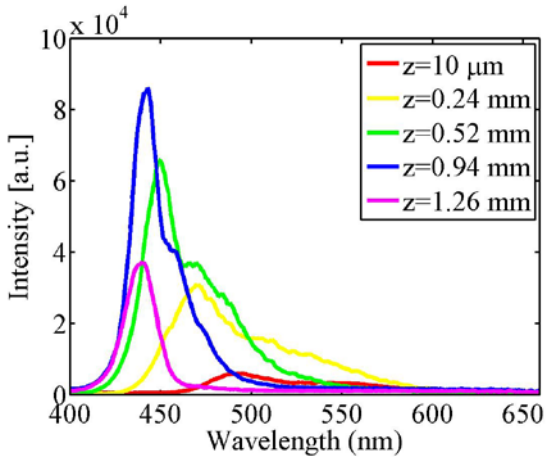

Fig 7. 12: Spectra corresponding to the filaments shown in the previous figure.

z	Filament length	SF distance	L	λ_{peak}
10 µm	2000 µm	530 µm	2.30 mm	492.7 nm
0.24 mm	2000 µm	775 µm	2.30 mm	472.4 nm
0.52 mm	1750 µm	1230 µm	2.30 mm	449.7 nm
0.94 mm	1360 µm	1600 µm	2.07 mm	442.7 nm
1.26 mm	700 µm	2240 µm	1.80 mm	440.4 nm

Table 7. 2: Filament length, SF distance, starting point (L) and SC peak wavelength as a function of z for the DL when the iris is fully open.

In Fig 7. 11 we can see the pictures of the plasma luminescence in the sapphire as the sample moves towards the DL (situated on the left side). In the right-side panel we have plotted the on-axis intensities of the plasma luminescence. In these plots, the background (taken as the image average in those parts where there was no filament) has been subtracted. Additionally, to connect the spectral properties of the SC with the filament inside the sapphire, the corresponding spectra have been depicted in Fig 7. 12.

In Table 7. 2 we report the values obtained from an estimation of the filament length, the self-focusing (SF) distance (measured from the front face of the crystal) and L, which is the distance from z=0 to the starting point of the filament (see description in Fig 7. 10). In the right-hand column we show the wavelength for which the maximal degree of SC spectral density is reached, namely λ_{peak}.

Although the on-axis plasma intensity always presents an abrupt increase, typical of mutiphoton ionization processes, certain differences appear as z is changed.

When the IR femtosecond pulse is focused on the sample slightly behind the first interface, a filament that extends around 2 mm develops. A careful inspection of the intensity profile along this filament suggests the existence of a refocusing process: the profile does not exhibit monotonically decreasing intensity after the main peak; on the contrary, intensity slightly increases again before entering into a smooth decrease. The spectrum of the SC generated under these conditions shows a peaked structure whose maximum is around 500 nm, abruptly dropping towards shorter wavelengths.

As the crystal approaches the DL, the input pulse propagates along a larger distance before self-focusing and the filament becomes shorter. We observe that the starting point of the plasma intensity increase is moved towards the back side of the crystal (i.e., shorter values of L). This is correlated with a more pronounced content of blue frequencies in the spectrum, together with an extension of the anti-Stokes side and spectral narrowing. Contrary to the first three cases, where the decay in plasma intensity is smooth and takes place within the sample, for the largest values of z this decay is clamped by the rear face of the crystal. In other words, the filament does not develop properly because its extension is clipped due to the presence of the end face of the sapphire. This fact is directly related with the narrowing in the spectrum, since the new frequencies are generated as the filament develops [83].

Similar studies have been previously conducted [269] using a concave mirror to focus the femtosecond pulse into a fused silica sample. The sample was moved around the focal point and the spectra of the output pulses were analysed. It was clearly demonstrated, both for experimental measurements and for numerical simulations, that the extension of the spectrum towards the shorter wavelengths increases with the filament extension. When the filament length was not clipped by the output face of the sample, the spectra showed the largest extension. Similar results were reported for water by Ziolek et al [264].

The results obtained with the DL seem to be contradictory to the aforementioned observations: we obtained the shorter wavelengths when the filament extension was strongly clipped by the output face of the sapphire plate, although total spectral content in this case was smaller because the spectrum exhibits only a narrow peak structure in the blue.

Although we have no clear evidence, we think that in such particular dynamics of the pulse focused by a DL[271], the dispersion introduced by the material prior to filament formation could, to some extent, lead to an intensity increase that pushes the spectral components of the SC further towards the blue as the crystal is moved towards the lens. Numerical simulations including the nonlinear propagation features would be necessary to confirm this hypothesis.

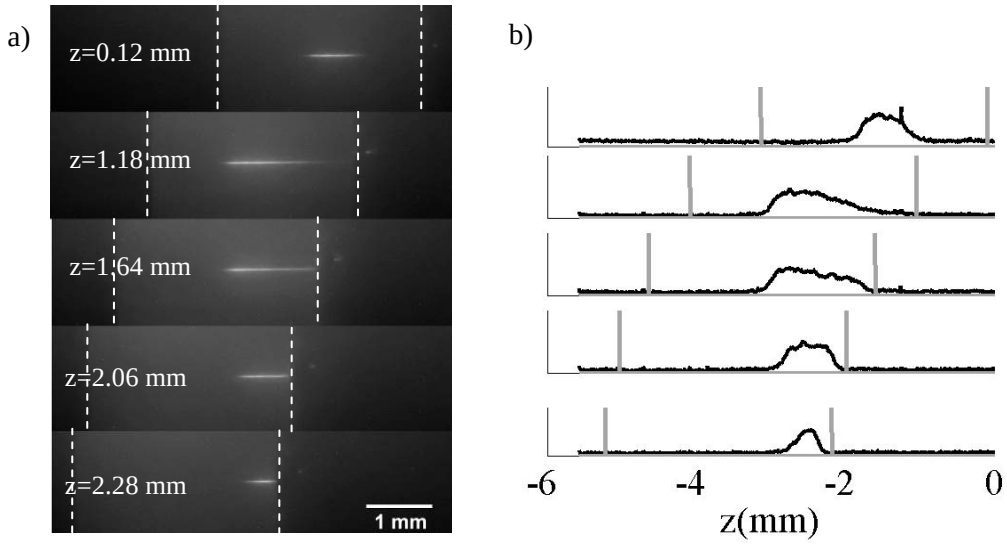

Fig 7. 13: a) Plasma luminescence as the sample approaches the DL and b) corresponding profiles. The iris diameter was 5.5 mm (NA=0.026) and the input energy was 0.72 µJ. The vertical gray lines indicate the limits of the crystal.

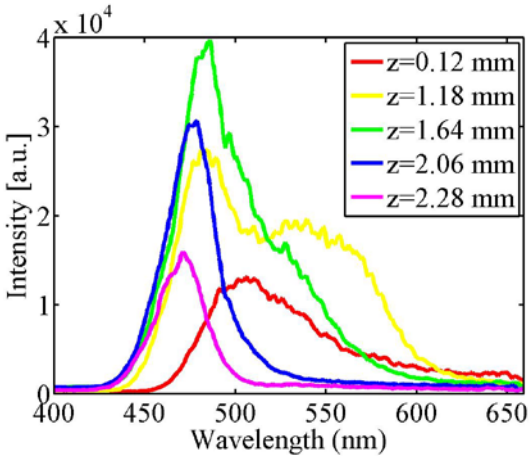

Fig 7. 14: Spectra corresponding to the filaments shown in the previous figure.

z	Filament length	SF distance	L	λ_{peak}
0.12 mm	1053 µm	1130 µm	1.975 mm	505.6 nm
1.18 mm	2015 µm	906 µm	3.015 mm	483.5 nm
1.64 mm	1453 µm	1460 µm	3.164 mm	485.8 nm
2.06 mm	980 µm	1930 µm	3.026 mm	478.3 nm
2.28 mm	640 µm	2300 µm	2.890 mm	471.3 nm

Table 7. 3: Filament length, SF distance, starting point and SC peak wavelength as a function of z for the DL when the iris is closed to 5.5 mm (NA=0.026).

We now proceed to examine filament formation when the diaphragm aperture is set to 5.5 mm (NA~0.026). The threshold energy was E_{th}= 0.54 µJ (the iris transmittance and losses due to the DL have been taken into account). This is again slightly lower than the values previously reported under similar conditions [249]. The input energy was then set at 0.76 µJ, so that the experimental conditions could be compared with the previous case. Similarly, in Fig 7. 13 we have included the photography of the plasma luminescence and in Fig 7. 14 the corresponding spectra.

As discussed in the preceding section, the extension of the region where the SC is generated is larger when the NA is reduced, due to broadening of the focusing region. The trend for the SF distance and filament length is the same as in the case of a full iris aperture: SF takes place at points further from the front face and filament length decreases as the sample approaches the DL (Fig 7. 13). However, there are some noticeable differences. First, we observe that the on-axis plasma intensity presents a smoother profile than in the previous case. Second, the pulse travels longer propagation distances prior to self-focusing (notice that the shortest SF distance is 906 µm, in contrast to 530 µm when the iris was fully open). These two facts are compatible with the enlargement of the depth of focus associated with a smaller NA [270] (at low NA, SF increases the pulse intensity as it propagates through the sample).

As in the preceding experiments, shorter filaments and larger propagation before self-focusing are associated with a blue shift in the spectrum. However, as mentioned in Sect. 7.4.2, the cut-off wavelength is remarkably larger when the NA is reduced. Even when filament lengths and SF distances are comparable (for example, at z=1.26 mm for NA=0.04 and z=2.28 mm for NA=0.026) the central wavelength of the blue peak remains significantly larger for the lowest NA (479 nm in contrast to 447 nm when the iris was fully open). Additionally, the effect of tunability is not as pronounced as in the previous case, which is shown in the values reached by the peak wavelength as z becomes increased.

To further explore the dynamics of the DL when the iris aperture is reduced, we performed a spatiotemporal simulation following the same procedure as in Chapter 6. Results at the focus position of the DL for the central wavelength are shown in Fig 7. 15.

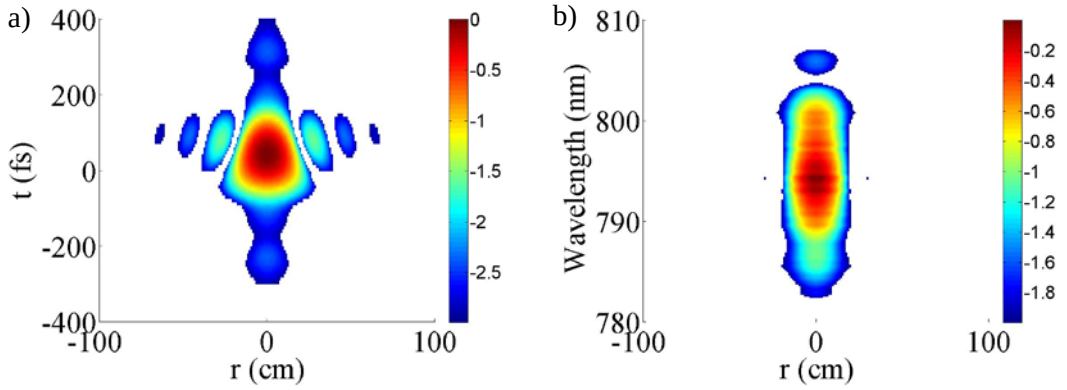

Fig 7. 15: Simulation of the a) spatiotemporal and b) spatio-spectral features at the focus of the DL for the central wavelength when the iris aperture is reduced to 5.5 mm (NA=0.026). The graphs are plotted in logarithmic scale.

Two effects become evident when compared to the simulations for a fully open diaphragm (Chapter 6). On the one hand, the central peak of the spatiotemporal profile is enlarged and the wings are broadened. This is explained by the larger focus size due to the smaller input beam diameter. On the other hand, the spectrum shape is kept nearly constant along the radial coordinate, unlike in the case where the iris was fully open. Therefore, we can expect this to have an impact on the temporal profile. To clarify this point, we have plotted the on-axis intensity and phase in the following picture for three positions along the propagation axis, f_0-1, f_0 and f_0+1 mm, f_0=106.6 mm being the focus position for the central wavelength.

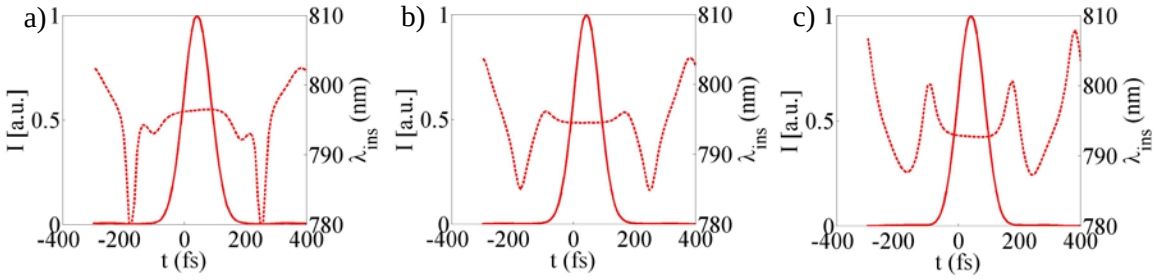

Fig 7. 16: Intensity (solid line) and instantaneous wavelength (dotted line) for a) z=105.5 mm, b) z=106.6 mm and c) z=107.6 mm for the DL when the iris is closed to 5.5 mm (NA=0.026).

Two main differences are observed with respect to the previous case. First, the pulses are shortened, which has to do with a flatter distribution of the spectrum. Moreover, pulse duration remains similar in all cases (~100 fs). Second, the phase is almost flat (contrary to what happened when the iris was fully open). These observations can be attributed to a decrease in chromatic aberration when the diaphragm is closed: in such situation, focusing is smoother and beam size variation for different wavelengths at a fixed position in the focal plane is not as pronounced as in the previous case.

7.5.2 Role of diffraction versus Rayleigh length

To discern the role played by the Rayleigh length versus chromatic aberration, we will test white light generation with achromatic lenses. In the first set of experiments this will be done by closing the iris mm and focusing with a refractive lens (RL). In a second test, the lens will be replaced by a longer focal length achromat and the iris will remain fully open. With this study we will be able to discriminate not only the effect of NA, but also the effect of diffraction induced by the iris (if any).

Previously, we need to choose a criterion to find similar focusing regions to that of the DL. The Rayleigh lengths are usually compared for this purpose. However, this approach cannot be used in this study. On the one hand, the Rayleigh length depends on the wavelength for the DL, and on the other, it is not well-defined for diffracting beams (i.e., when the iris is not fully open). In reference [272] Urey proposed semi-analytical formulas to calculate the FWHM of the diffraction spot of a Gaussian beam as a function of the truncation ratio and a system f-number.

To obtain an accurate propagation we monitored the beam profile of the pulses focused by the DL along the propagation direction (Fig 7. 17a). For this purpose we used a high resolution CMOS-based camera (uEye, UI-1460-C) mounted on a motorized stage (Zaber, T-LA28). The minimum beam size at $1/e^2$ is estimated to be 22.4 µm. The track of the corresponding maxima registered by the camera (i.e., relative peak intensity) is plotted in Fig 7. 17c. The distance between the points where intensity drops to half the maximum is Δz=1.9 mm. This distance is the criterion we have chosen to perform a quantitative comparison with the RL.

The RL with the closest NA (iris fully open) to the DL was a 100 mm focal length achromat (Thorlabs, AC254-100-B). When the iris is closed to 5.5 mm (Fig 7. 17b), we find a similar focal region to that of the DL (Δz=2.0 mm). At the focal plane, the spot presents an Airy diffraction pattern with a width of 25.6 µm at $1/e^2$.

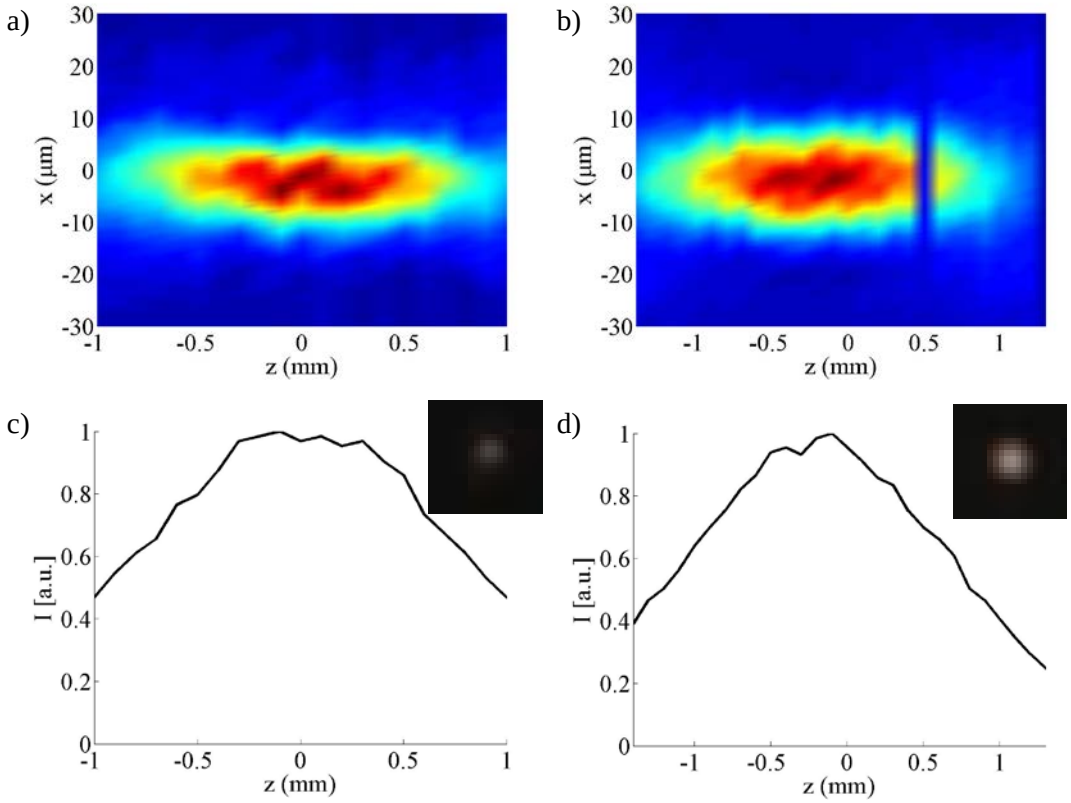

Fig 7. 17: Beam profile in the focusing region of a) the DL and b) 100 mm focal length LR when the iris is closed to 5.5 mm. Corresponding relative peak intensity along the propagation direction in the vicinity of the focus of a) the DL and b) the RL. Inset: image of the focal spot.

Before introducing the results, let us briefly examine the SC generation with the achromatic lens (f=100 mm) and the diaphragm open (NA~0.04). Under these conditions, the focal spot is calculated to be 11.24 μm at $1/e^2$ criterion. The Rayleigh length is estimated to be 0.150 mm (the M^2 factor was experimentally found to be 1.2 [117] and has been included in this estimation). Since for Gaussian beams the distance Δz equals the double of the Rayleigh length, we can deduce that Δz~0.3 mm.

The energy threshold was found to be E_{th}=0.65 μJ, so the input energy for the experiments was set at 0.90 μJ (1.4 E_{th}). The results are summarized in the panels of Fig 7. 18. Two important differences with respect to the DL become evident by simply looking at the filament graphs. First, the filament is generated at the front face of the crystal which translates into very short SF distances, as opposed to what is observed for the DL. For larger values of z there is no filament generation. Second, for the longest distances a two peak structure is observed in the on-axis intensity distribution, thus suggesting a weak refocusing filament. At these positions (where the sample is nearer to the lens) the corresponding spectrum is displaced to the redder wavelengths, as opposed to the trend observed in the case of the DL. In this case the temporal and spectral intensity shapes stay similar along the radial coordinate (Fig 7. 19), although the maximum varies across the axis as a consequence of the Gaussian profile at the focus. Pulse width is around 100 fs and is found to be constant for different propagation lengths.

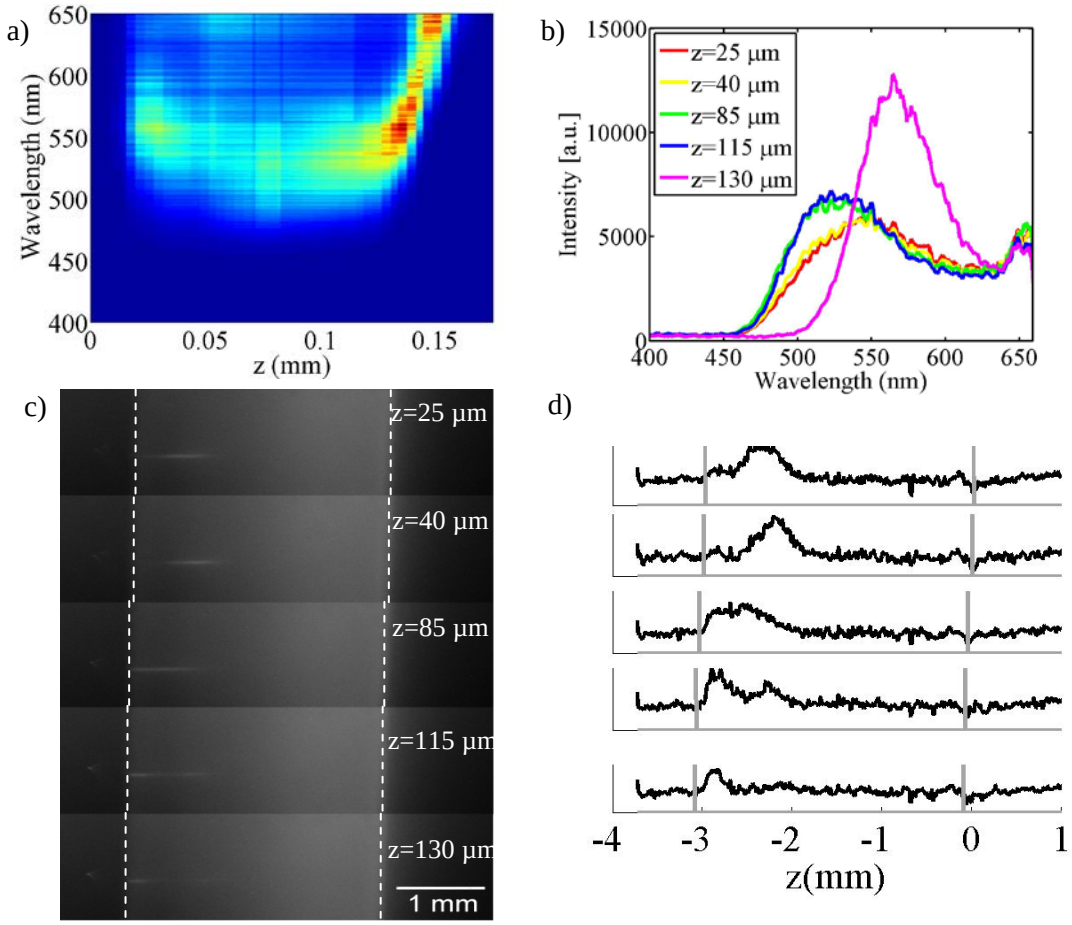

Fig 7. 18: a) Normalized spectral map of the SC generated when the 3 mm sapphire is approaching the RL (f=100 mm, NA=0.04). b) Spectra for the distances shown in the legend. c) Photography of plasma luminescence corresponding to the spectra of panel c) and d) the on-axis intensity.

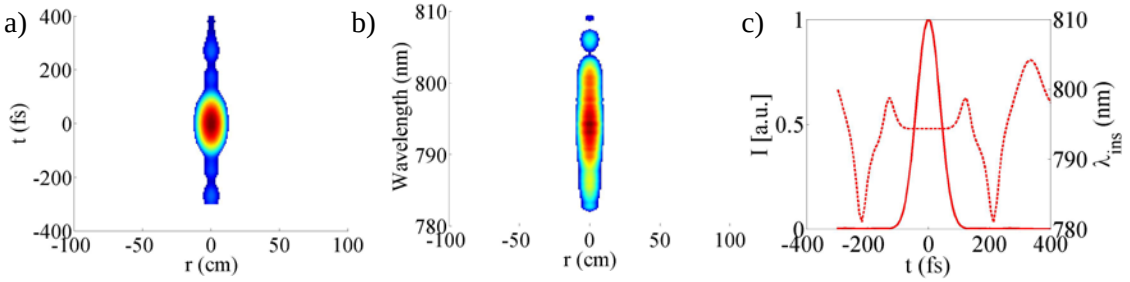

Fig 7. 19: a) Spatiotemporal, b) spatio-spectral and c) intensity (solid line) and phase (dotted line) characterization at the focus of a 100 mm focal length lens when the iris is fully open (NA=0.04). The same color scale from Fig 7. 15 applies to these graphs.

z	Filament length	SF distance	L	λ_{peak}
0.025 mm	1.208 mm	0.020 mm	2.966 mm	549.6 nm
0.040 mm	1.352 mm	0.023 mm	2.963 mm	549.6 nm
0.085 mm	1.282 mm	0.049 mm	2.989 mm	523.0 nm
0.115 mm	1.192 mm	0.039 mm	3.025 mm	522.5 nm
0.130 mm	0.417 nm	0.052 nm	3.035 mm	564.1 nm

Table 7. 4: Filament length, SF distance, starting point and SC peak wavelength as a function of z for an achromatic lens (f=100 mm, NA=0.04).

When the iris is closed to 5.5 mm we achieve NA~0.027 and Δz~2 mm. Note that the NA is similar to that obtained for DL when the iris diameter was set at 5.5 mm. Under these conditions, the energy threshold is 0.7 μJ (the iris and filter transmissions were taken into account) so the input energy was set at 1.4 times this value (0.98 μJ).

The spectral map (Fig 7. 20a) presents some similarities with that of the DL (Fig 7. 4a): as the crystal approaches the lens, the content of longer wavelengths becomes reduced, yielding a peaked structure centred in the shortest wavelengths. However, unlike in the case of the DL, the anti-Stokes cut-off wavelength remains constant throughout the whole range. Additionally, in the former case the spectral width (Fig 7. 4c) is fairly the same (except for z>1.5 mm, where the spectrum is narrowed and peak intensity increases). In contrast, in this case there is an optimum value of z for that leads to enhancement of the spectral broadening (z~1.20 mm), as shown in Fig 7. 20b. This trend is a close reproduction of the behavior of the SC generated with the DL when the NA was reduced to 0.026 (Fig 7. 14).

The plasma luminescence photography (Fig 7. 20c and d) also reveals certain similarities with the latter. For the first three distances, z, the electron density from the plasma is very similar. However, unlike the DL, the filaments move upstream together with the crystal. In other words, as z increases L maintains similar values for the DL, but changes for the RL. In consequence, the SF distances are larger for the DL than for the RL.

Since the diaphragm limits the input beam, the focal spot presents diffraction rings which are reflected along the spatial coordinate in the spatiotemporal and spatio-spectral maps (Fig 7. 21). Nevertheless, no changes in the spectrum or in the temporal profile are observed with respect to the case in which the iris was fully open.

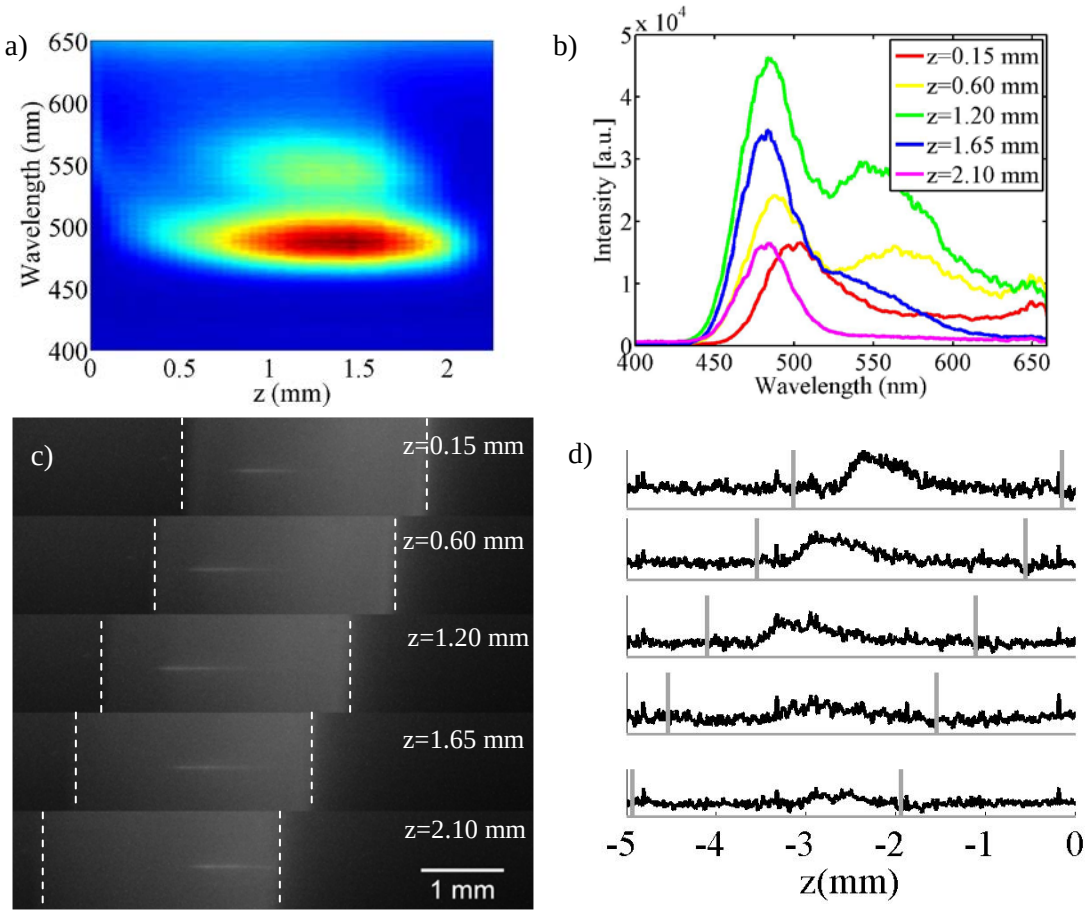

Fig 7. 20: a) Spectral map of the SC generated when the 3 mm sapphire is approaching the RL (f=100 mm) and the iris is closed to 5.5 mm (NA=0.027). b) Spectra for the distances shown in the legend. c) Photography of plasma luminescence corresponding to the spectra of panel b) and d) the on- axis intensity.

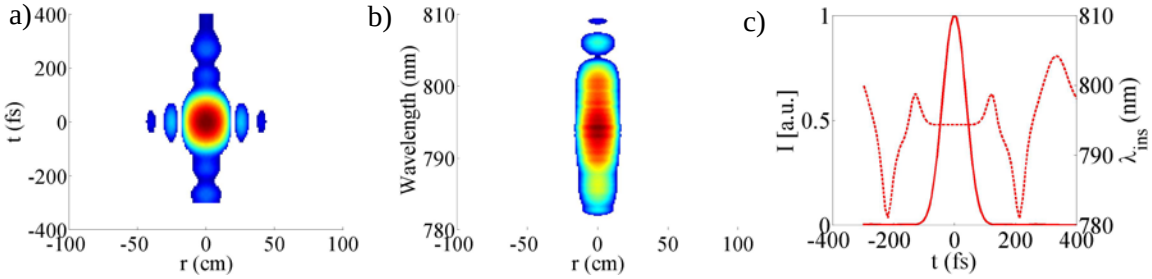

Fig 7. 21: a) Spatiotemporal, b) spatio-spectral and c) intensity (solid line) and phase (dotted line) characterization at the focus of a 100 mm focal length lens when the iris aperture is reduced to 5.5 mm (NA=0.027).

z	Filament length	SF distance	L	λ_{peak}
0.15 mm	1.283 mm	0.420 mm	2.720 mm	502.8 nm
0.60 mm	1.368 mm	0.342 mm	3.212 mm	488.3 nm
1.20 mm	1.263 mm	0.526 mm	3.573 mm	484.8 nm
1.65 mm	1.671 mm	1.037 mm	3.505 mm	483.0 nm
2.10 mm	1.119 mm	1.828 mm	3.107 mm	484.8 nm

Table 7. 5: Filament length, SF distance, starting point and SC peak wavelength as a function of z for an achromatic lens (f=100 mm, NA=0.027).

Finally, we replaced the 100 mm lens with a 200 mm focal length achromatic doublet and kept the iris fully open. With this configuration a similar NA is achieved (NA~0.022), but the input Gaussian beam is not truncated. Therefore, this test will be helpful to discriminate effects due to diffraction by the iris aperture (if any).

The focusing region in this case is estimated to be Δz~1.2 mm and the focal spot width 22.5 μm at $1/e^2$. The energy threshold for SC generation is in the same order as in the previous test, E_{th}=0.50 μJ. In order to work under analogous conditions, we set the energy at $1.4E_{th}$ (0.7 μJ) again. Results are presented in Fig 7. 22.

First, it is remarkable that in spite of having a shorter Δz, the extension of the region where SC is generated is analogous to the previous case. Although the spectral extension and behavior of the white light are similar to the previous case, the spectral density of the shorter wavelengths with respect to the redder ones is enhanced in this latter case (similarly to what happened with the DL with the iris fully open). Again, the variation of the cut-off frequency is not observed under these conditions. No significant variations were found in filament formation (Fig 7. 22c and d), suggesting that the diffraction pattern present in the previous case did not play a relevant role in the SC generation process under these conditions.

The absence of diffraction provides a smaller spot (the width of the focal spot from the simulation is 22 μm at $1/e^2$, which agrees well with the expected value) and a lack of diffraction rings in the spatial profile. In spite of these differences, no variations in the spatiotemporal and spatio-spectral maps (Fig 7. 23) were observed.

z	Filament length	SF distance	L	λ_{peak}
0.15 mm	1.038 mm	1.952 mm	1.193 mm	536.3 nm
0.30 mm	1.161 mm	0.553 mm	2.740 mm	488.7 nm
0.70 mm	1.200 mm	0.284 mm	3.392 mm	481.1 nm
1.50 mm	1.400 mm	1.300 mm	3.200 mm	482.3 nm
1.80 mm	1.590 mm	1.421 mm	3.386 mm	481.1 nm
2.00 mm	1.017 mm	1.990 mm	3.007 mm	480.6 nm

Table 7. 6: Filament length, SF distance, starting point and SC peak wavelength as a function of z for a refractive lens (f=200 mm, NA=0.022).

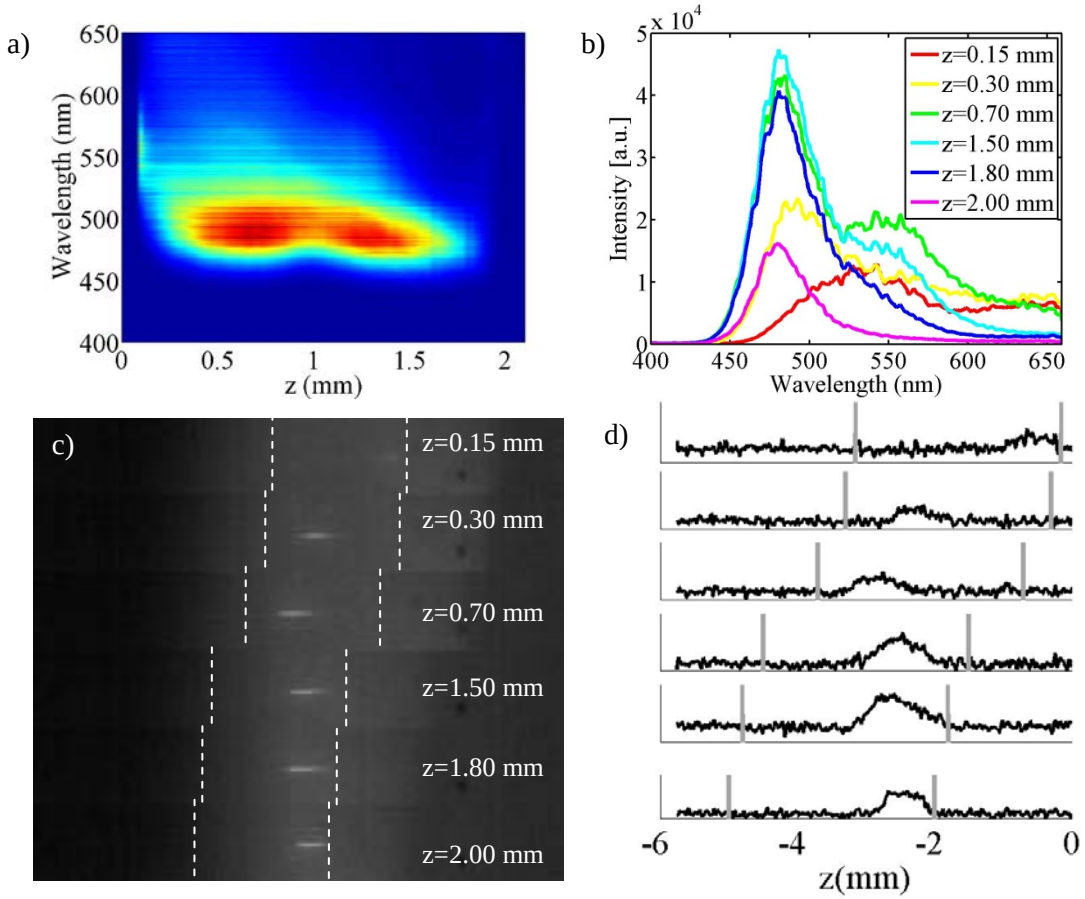

Fig 7. 22: a) Spectral map of the SC generated when the 3 mm sapphire is approaching the refractive lens (f=200 mm, NA=0.022). b) Spectra for the distances shown in the legend. c) Photography of plasma luminescence corresponding to the spectra of panel c) and d) the on-axis intensity.

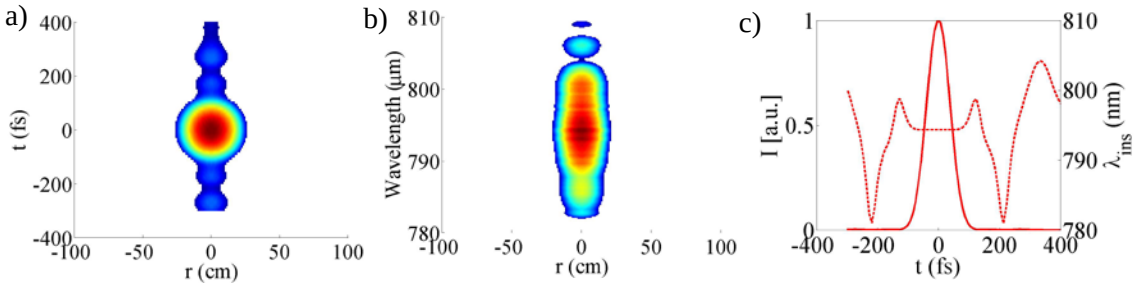

Fig 7. 23: a) Spatiotemporal, b) spatio-spectral and c) intensity (solid line) and phase (dotted line) characterization at the focus of a 200 mm focal length lens when the iris is fully open (NA=0.022). Same color scale from Fig 7. 15 applies to these graphs.

7.5.3 Conclusions

In this analysis, no significant differences were found between the SC generated with diffracted and refractive lenses with the same NA. This suggests that the role of diffraction in shaping the spectrum of the generated SC is negligible compared to the sustainable nonlinear effect resulting from the enlargement of the Rayleigh length, at least under the experimental conditions described in this study.

The effects of a pure enlargement of the Rayleigh length can be deduced by comparing the SC spectra given by the two achromatic lenses, with focal lengths of 100 and 200 mm, taking into account that the latter gives a Rayleigh length approximately four times larger than the first one. The first effect is a more extended region of beam focusing where white-light can be generated. Second, the pulse takes longer to self-focus and refocusing filaments are not as pronounced as for larger NAs. As to the spectrum, the central wavelength is observed to be frequency shifted to the bluer part of the spectrum, but unlike the SC generated with a DL, no tunability was found. Another feature is a slight decrease in the cut-off frequency, but in any case comparable with that described for the DL. The decrease of the spectral density of the longer wavelengths is also observed when the NA is reduced with an achromatic lens. However, the spectral width of the observed SC with the DL under similar conditions is narrower. Additionally, filament formation inside the sample also presented some dissimilarities with that of the DL, where refocusing filaments were observed.

All these observations suggest that, in spite of playing a crucial role, an enlargement of the focusing region is not sufficient to describe the SC behaviour observed with the DL and some other mechanisms must become involved in the process. In this sense, the spatiotemporal and spatio-spectral unique features of the pulses focused with a DL that have been described could be partly responsible for some of the observations. However, a complete numerical model - including nonlinear effects and the complex structure of the input pulses - for intense short pulses propagating in sapphire would be necessary to find a full explanation.

7.6. Spatial characterization

7.6.1 Beam profile

In order to assess the usefulness of the so generated SC pulses, we have performed a complete spatial characterization. One of the main concerns attaining white light generation with diffractive elements is the possible appearance of diffraction patterns, conical emission rings... in the beam profile which would drastically reduce spatial quality.

To ensure that this is not our case, we registered the beam profile for different z with a CMOS-based digital camera (Canon, Powershot G10) after projecting the light onto a white screen (with no filter).

We started with pulses focused with the DL when the iris was fully open (Fig 7. 24). In this snapshot sequence, the energy was set at 1.38 μJ, corresponding to 1.4 E_{th}. The movement of the sample along the propagation axis was larger than in previous experiments (in Fig 7. 24 negative values of z correspond to positions further from the point where SC generation was first observed in previous measurements). Three regimes are clearly differentiated. The first one corresponds to the behaviour described before. When the lens-crystal relative distance is increased no SC generation is observed, although we used the spectrometer to check that SPM was taking place. 1.5 mm further, white light generation is again observed, presenting similar features to those typically observed with an achromatic lens. In our opinion, this situation arises when the sample is distant from the lens and the focal region is completely out of it, the beam being thus divergent at the entrance of the sample.

Beam quality is reasonably good (the annular pattern corresponds to non-converted IR light).

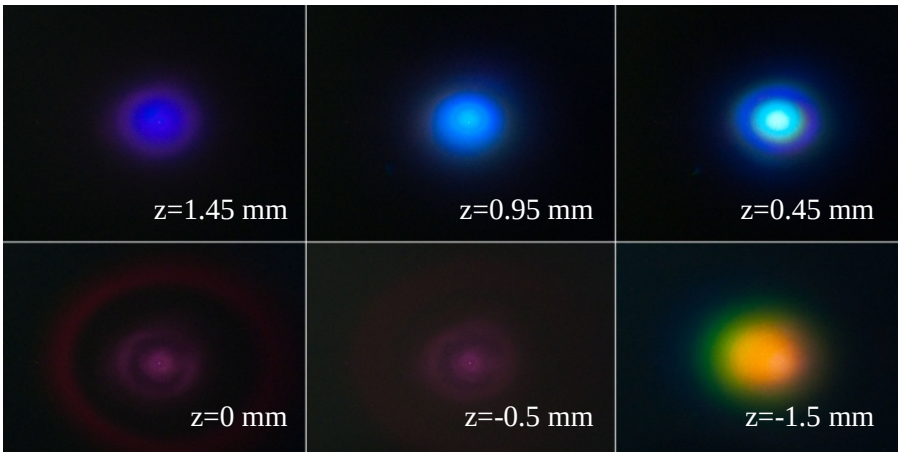

Fig 7. 24: Pictures of the SC pulses after being projected on a screen with the iris fully open.

In the subsequent set of photographs the iris diameter was closed to 4 mm and the energy was set at 3 μJ (1.1 E_{th}). In this case, the effect of the absence of continuum disappeared, so it may be assumed that this effect is related to the strong focusing of the previous case. As expected, the effect of tunability is also present in the spatial profile, presenting different colors as z is changed.

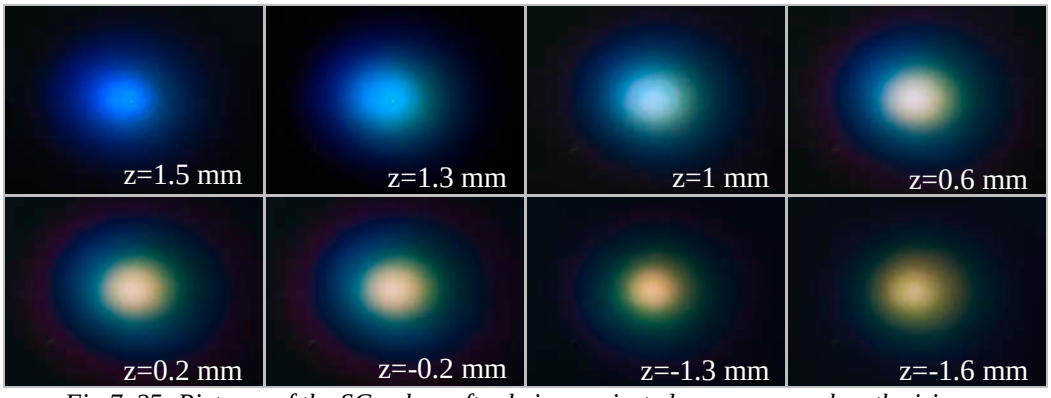

Fig 7. 25: Pictures of the SC pulses after being projected on a screen when the iris diameter is 4 mm.

Following the discussion of the previous section, we checked the beam profile for pulses focused with an achromatic doublet under different focusing conditions. To this end, a high-resolution CMOS based camera (UEye, SE-1450-C) was employed to register the SC beam profile. To remove the unconverted infrared light, a band-pass filter was used (FG37S, Thorlabs). The transmission of the filter has been taken into account to properly adjust the colors of the images.

The sequences of photographs for the same cases presented in the previous section are shown in Fig 7. 26 (100 mm focal length, iris fully open, E=0.90 μJ, NA~0.04), Fig 7. 27 (100 mm focal length, iris fully closed to 4.8 mm, E=0.65 μJ, NA~0.024) and Fig 7. 28 (200 mm focal length, iris fully open, E=0.70 μJ, NA~0.022).

In the first case we observe a higher content of redder wavelengths, which is in good agreement with the results obtained for the spectra. The beam profile is nearly Gaussian and its size does not change as the sample is moved along the propagation axis.

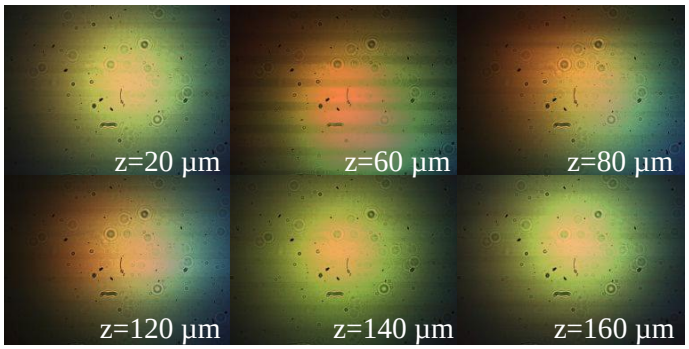

Fig 7. 26: SC beam profile registered with a CMOS camera. The pulses were focused with the 100 mm achromatic doublet and the iris fully open.

However, when the iris aperture is reduced to 4.8 mm, apart from a more prominent content of shorter wavelengths (as expected from spectral analysis), one observes that beam divergence depends on the lens-crystal's relative position. The beam quality is fairly good and no diffraction patterns are observed in this sequence.

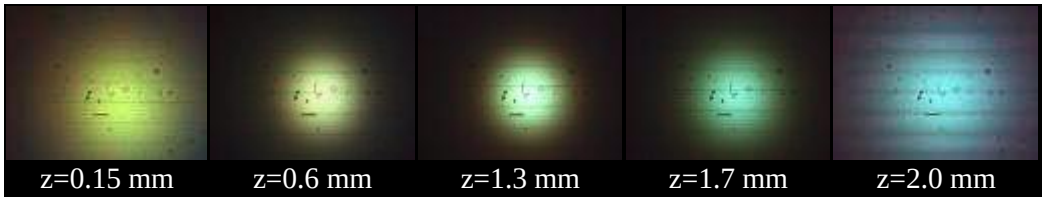

Fig 7. 27: SC beam profile registered with a CMOS camera. The pulses were focused with the 100 mm achromatic doublet and the iris aperture closed to 4.8 mm.

Similarly to the prior measurements, the beam size varies as the sample is moved with respect to the 200 mm focal length lens keeping the diaphragm open.

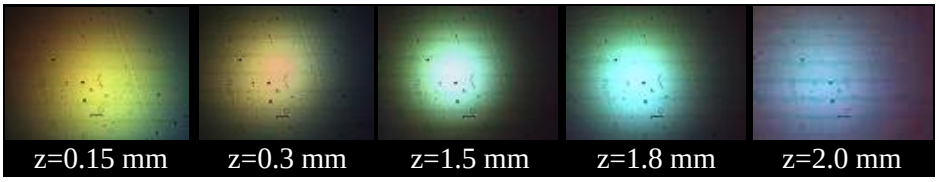

Fig 7. 28: SC beam profile registered with a CMOS camera. The pulses were focused with the 200 mm achromatic doublet and the iris fully open.

We attribute this change in beam size simply to beam divergence along the focal region in which we are moving the sample. Due to the short length travelled in the first case, this effect could not be observed.

It is important to remark that no diffraction patterns were described when the iris was closed, which suggests that the nonlinear effects taking place in the sapphire prevent spatial distortions in the SC pulses. This also agrees well with the spatial features of the white-light generated with the DL, where no remarkable diffraction outlines were perceived.

7.6.2 Focusability

Many of the SC applications require focusing beams to increase intensity, for example when seeding an OPA. Although the continua show smooth and circular beam profiles, the processes giving rise to SC are highly nonlinear. It is therefore crucial to investigate the spatio-spectral beam features when focusing the continuum towards an experiment.

To this end, we built the setup sketched in Fig 7. 29: the infrared pulses are focused by the DL in a 3 mm sapphire plate which is mounted on a motorized stage. A band-pass filter (FG37S, Thorlabs) removes the unconverted IR beam. A 45 mm focal length lens (AC254-045-A1, Thorlabs) collimates the beam to be further focused by a second lens (f= 200 mm, AC245-200-A1, Thorlabs). With this configuration it is possible to achieve a large Rayleigh length and a beam magnification that allows us to monitor the spatial quality of the beam around the focus. For this purpose a CMOS camera (uEye 1450-SE-C) is placed in the focal plane of the latter lens and mounted on a translational stage. L=0 corresponds to the focus of L2 and the sign criteria assign positive values as the distance from L2 decreases (see Fig 7. 29).

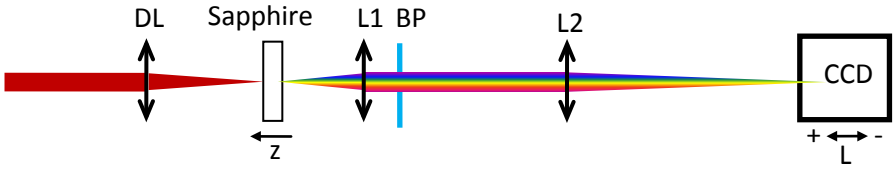

Fig 7. 29: Setup for SC focusability characterization. DL: diffractive lens; BP: band-pass filter; L1: 45 mm focal length lens; L2: 20 mm focal length lens.

The beam profile was monitored along 60 mm in steps of 2 mm. This allows us to accurately describe the focal region of the SC pulses. Additionally, the camera used in this setup records three channel (RGB) files. Although it is not very precise (the three channels partially overlap), we can examine beam divergence for the red, green and blue frequencies or, in other words, find out if the beam presents chromatic aberration.

We will first analyze the results for the DL when the iris is fully open. The sample employed for the study was a 3 mm sapphire. The measured energy threshold was E_{th}=0.96 μJ and the energy was set at E=1.30 μJ. The study was performed for five lens-sample distances (z=0.15, z=0.45, z=0.8, z=0.9 and z=1.20 mm), but for the sake of readability here we will just present the analysis for z=0.45 mm and z=1.20 mm. The first one corresponds to a representative case where the spectrum still contains redder frequencies, whereas the latter is an example of the blue peaked structure.

In Fig 7. 30 we show the images together with the intensity profile for different positions around the focal region of a 200 mm focal length lens. At positive values of L (corresponding to positions before the focus) the beam presents diffraction rings. After the focus this pattern disappears, giving rise to a smooth Gaussian profile.

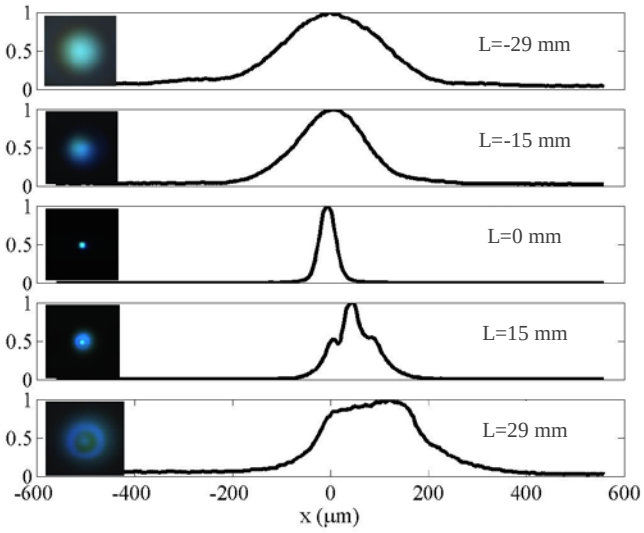

Fig 7. 30: Intensity profile around the focus of a 200 mm focal length achromatic doublet. The sample is placed at z=0.45 mm and the iris is fully open.

In order to quantify beam quality, we estimated the M^2 factor. To this end we used the propagation equation for perfect Gaussian beams (see Fig 7. 31 for the geometric description of the parameters involved in the formulas):

$$\omega(z) = \omega_0 \sqrt{1 + \left(\frac{z}{z_R}\right)^2} \tag{131}$$

where $2z_R = 2\frac{\omega_0^2 \pi}{\lambda}$ is the Rayleigh length and ω_0 is the beam radius at the focus given by:

$$\omega_0 = \frac{2\lambda f}{D\pi} \tag{132}$$

D being the beam size at the entrance of the lens.

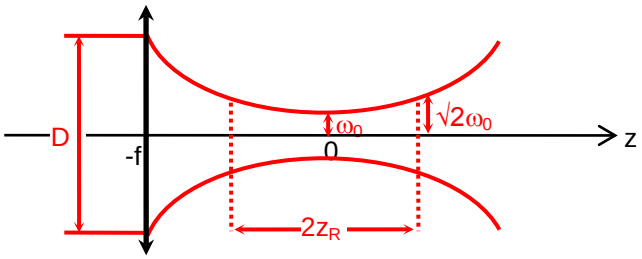

Fig 7. 31: Scheme illustrating the propagation of Gaussian beams.

For real beams, Eq.(131) is rewritten as:

$$\omega(z) = \omega_0 \sqrt{1 + \left(\frac{z}{\overline{z}_R} \right)^2} \tag{133}$$

The Rayleigh length is now redefined including the beam quality factor M^2:

$$\overline{z}_R = \frac{\omega_0^2 \pi}{M^2 \lambda} \tag{134}$$

For a diffraction limited beam $M^2=1$. Smaller values are not possible.

In Fig 7. 32a we have plotted the beam waist at FWHM [i.e., 1.18ω(z)] extracted from the image profiles in the focal region and fit to Gaussian propagation. At this point it is useful to remember the relationship between the beam waist (diameter) at FWHM, namely D_{FWHM}, and the beam radius at $1/e^2$, ω:

$$D_{FWHM} = 1.18\omega \tag{135}$$

Taking $\omega^2(z)$ and z^2 as dependent and independent variables respectively, we can perform a linear adjustment of the experimental data to Eq.(133) to estimate M^2. This way the slope will be given by $\frac{\omega_0^2}{\overline{z}_R^2}$, whereas the interception at the ordinate will be the square of the beam radius, ω_0^2. Very recently, Schulze et al proposed an alternative easy method to measure the M^2 factor by means of a spatial light modulator [273].

In this case, we obtained a focal spot of 44.24 μm (diameter at FWHM) and a Rayleigh range of $2z_R$=10.21 mm and M^2=1.84, which indicates that the quality of the so generated SC pulses is fairly good.

We have depicted a similar plot for the RGB channels of the camera that corresponds roughly to λ_R=645 nm, λ_G=510 nm and λ_B=440 nm. The focus in all three channels is in the same position, which allows us to conclude that chromatic aberration is negligible. Beam divergence is similar in all three cases, although slightly larger in that of the red channel. This feature of the SC has been also observed under achromatic focusing [181].

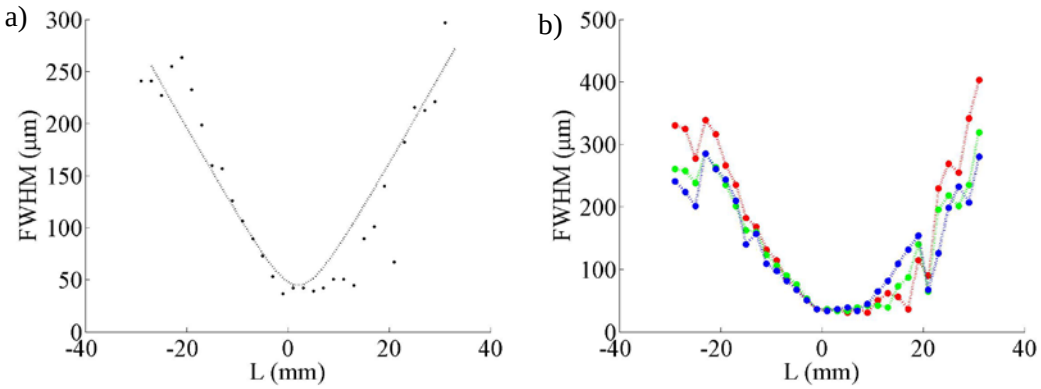

Fig 7. 32: a) Beam waist at FWHM in the focal region: experimental (black circles) and theoretical Gaussian fit (dotted line). b) Beam waist at FWHM for each RGB channel. The sample is placed at z=0.45 mm and the iris is fully open.

As the sample is brought close to the DL (z=1.20 mm) the diffraction pattern disappears, presenting a smooth Gaussian profile throughout the whole range. The focal spot size is 35 µm (diameter at FWHM) intensity and the Rayleigh length 8.63 mm. This yields an M^2 factor of 1.48.

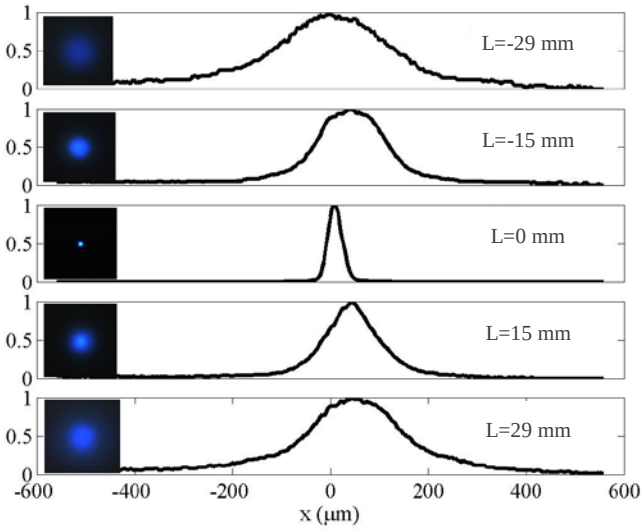

Fig 7. 33: Intensity profile around the focus of a 200 mm focal length achromatic doublet. The sample is placed at z=1.20 mm and the iris is fully open.

The chromatic aberration is again negligible, but the divergence of the redder wavelengths is larger than the other. However, one has to be careful with these data, since the spectral density of the long wavelengths is very low.

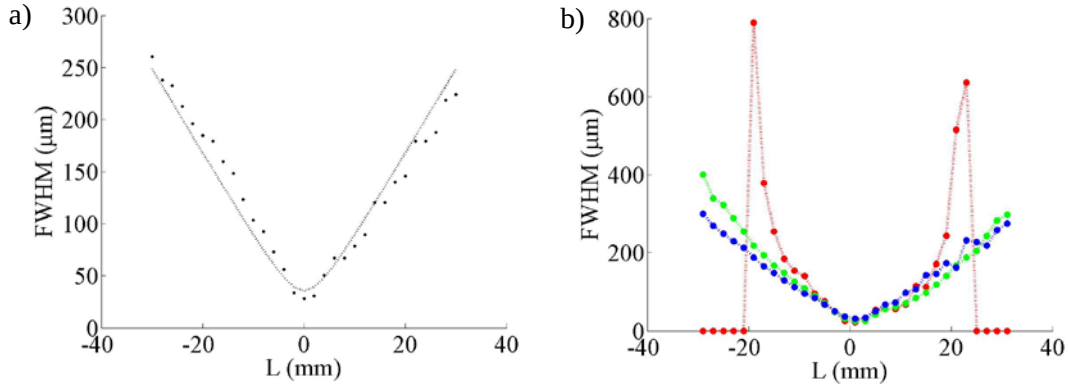

Fig 7. 34: a) Beam waist at FWHM in the focal region: experimental (black circles) and theoretical Gaussian fit (dotted line). b) Beam waist at FWHM for each RGB channel. The sample is placed at z=1.20 mm and the iris is fully open.

We will now proceed to examine the results when the iris aperture is closed to 5.5 mm. The measured energy threshold was E_{th}=0.60 µJ and the energy was set at E=0.85 µJ. The study was performed for five lens-sample distances (z=0.15, z=0.90, z=0.14, z=0.9 and z=1.20 mm), but we will limit our analysis to z=0.90 mm and z=2.15 mm.

The diffraction rings are not observed in this sequence. However, chromatic aberration is worse than in the previous case: as can be seen in Fig 7. 36, long wavelengths are focused before short ones. This is also observed in Fig 7. 35: at L=-14 mm the spot presents a different color than at L=14 mm.

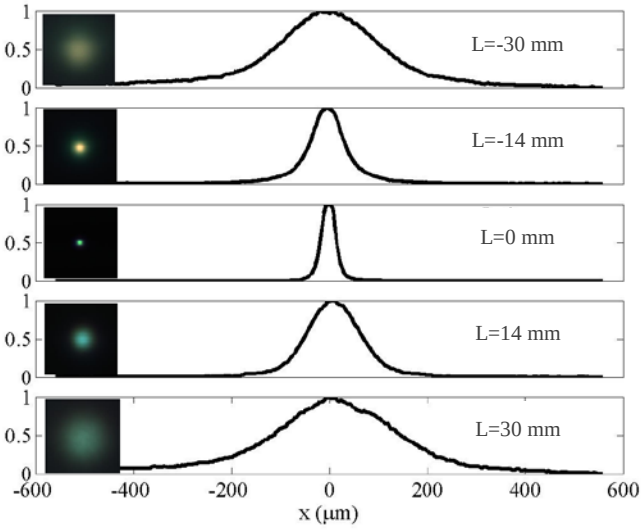

Fig 7. 35: Intensity profile around the focus of a 200 mm focal length achromatic doublet. The sample is placed at z=0.90 mm and the iris aperture is 5.5 mm.

The beam diameter at the focus is 40 µm and the Rayleigh range 9.95 mm. With these parameters one obtains M^2=1.65.

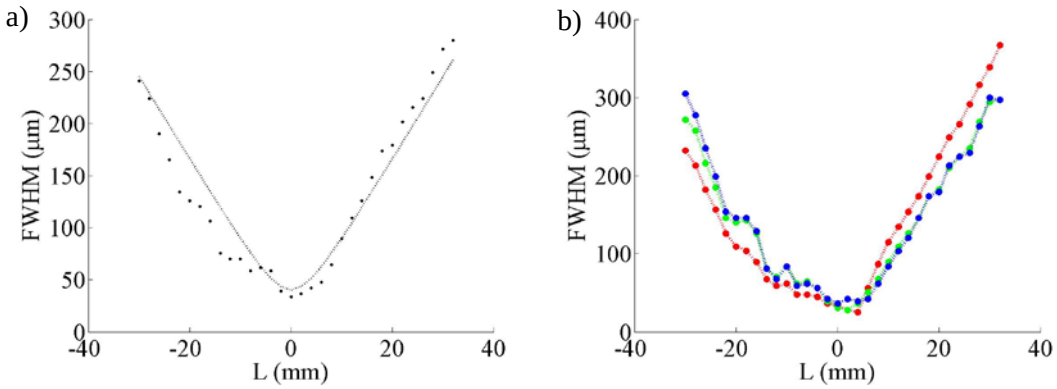

Fig 7. 36: a) Beam waist at FWHM in the focal region: experimental (black circles) and theoretical Gaussian fit (dotted line). b) Beam waist at FWHM for each RGB channel. The sample is placed at z=0.90 mm and the iris aperture is 5.5 mm.

To conclude, we will characterize the focus under the same conditions as when the sample was approached to the DL (z=2.15 mm). The sequence is shown in Fig 7. 37. The beam exhibits a very nice Gaussian profile. At the focus position, the spot size is 20 µm (diameter at FWHM). The Rayleigh range is estimated to be 2.72mm, which for the central wavelength of 440 nm yields an M^2 factor of 1.44.

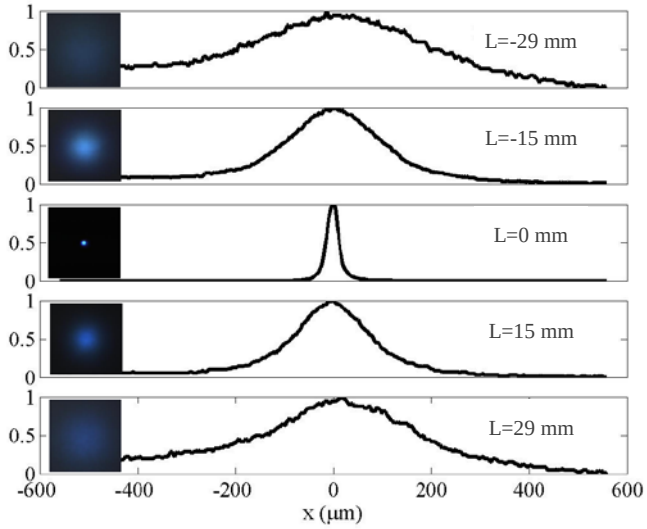

Fig 7. 37: Intensity profile around the focus of a 200 mm focal length achromatic doublet. The sample is placed at z=2.15 mm and the iris aperture is 5.5 mm.

As to divergence, the behaviour is quite similar to that observed when the diaphragm was fully open: redder wavelengths are more divergent than shorter ones.

For purposes of comparison with Fig 7. 33 and Fig 7. 34, we might think that the beam is more divergent when the iris aperture is reduced to 5.5 mm. However, we must remark that the lens used for collimating the SC beam was adjusted for the case when the iris was fully open. Since SC divergence depends not only on the focal length of the DL, but also on the point where the filament is formed, it may occur that the second lens is not collimating the SC pulses when the relative distance DL-sample is changed.

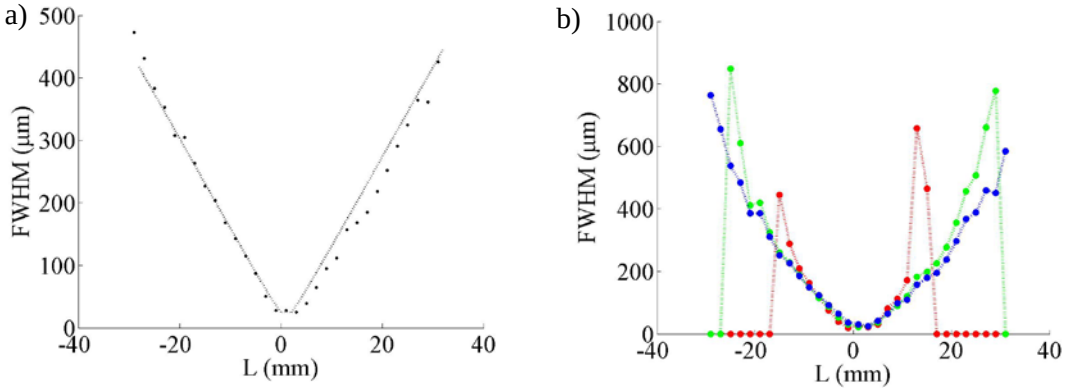

Fig 7. 38: a) Beam waist at FWHM in the focal region: experimental (black circles) and theoretical Gaussian fit (dotted line). b) Beam waist at FWHM for each RGB channel. The sample is placed at z=2.15 mm and the iris aperture is 5.5 mm.

7.6.3 Spatial chirp

To finish with spatial characterization, we explored whether the SC pulses were spatially chirped. For this purpose, we employed a fibre coupled spectrometer (Avantes, AvaSpect-2048) mounted

on a motorized stage to record the spectrum along a transversal scan of the beam. The distance between the sapphire and the fibre was 200 mm. Since rotational symmetry can be assumed, we scanned the beam just along one axis.

For the fully open iris, we found an energy threshold of E_{th}=0.76 μJ so the energy was set at 1.06 μJ. In Fig 7. 39 we show the results for z=0.60 mm and z=1.30 mm: the spectrum has been depicted as a function of the divergence angle θ. In the first case stability is slightly worse, which is reflected in the form of missing spectra in the spectral map. In the first figure, no spatial chirp is observed, and the map is just modulated by the Gaussian spatial profile. The second case agrees well with the conclusions obtained in the previous section: the longer wavelengths diverge more than the bluer ones. For this reason, the spectral content of shorter wavelengths is negligible at larger values of θ.

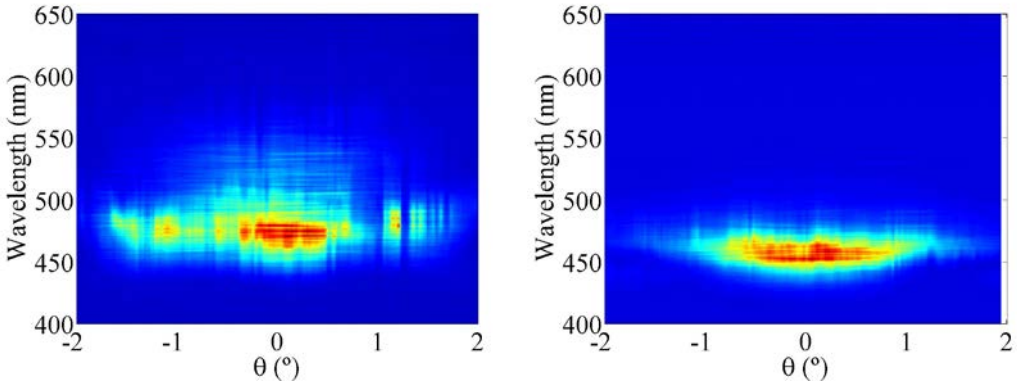

Fig 7. 39: Transverse spectral scans when the iris is fully open for a) z=0.60 mm and b) z=1.30 mm.

When the iris aperture is set at 5.5 mm, the energy threshold decreases to 0.50 μJ. Therefore, we set the energy at 0.70 μJ. In Fig 7. 40 we present the spectral maps for z=0.90 mm and z=1.90 mm, as examples of the two SC regimes. In both cases, no spatial chirp is observed and the divergence can be considered similar for all the wavelengths.

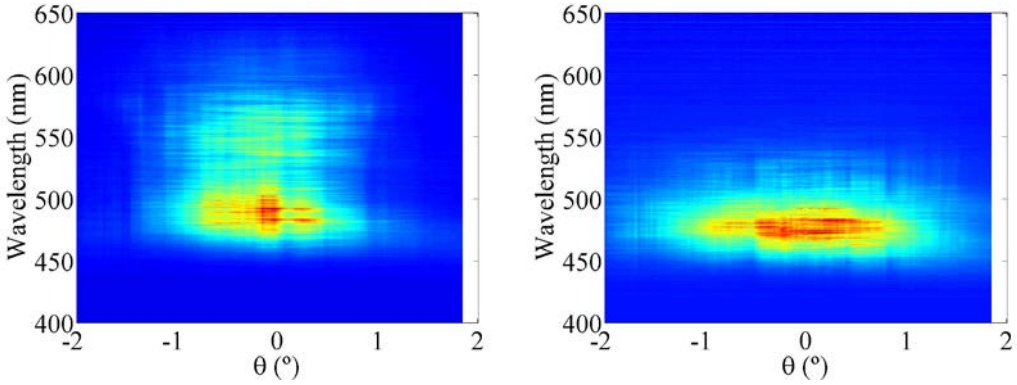

Fig 7. 40: Transverse spectral scans when the iris is 5.5 mm for a) z=0.90 mm and b) z=1.90 mm.

7.7. Extension to the UV

In order to extend the tunability of the pulses to the UV, we performed a setup for sum-frequency generation with the fundamental IR pulses. To this end, a sample of the 795 nm, 120 fs pulses was taken before the setup for SC generation. A length-variable motorized delay line was mounted for this beam to equalize both optical paths, and it was focused in a type-I BBO (θ= 44.3º, ϕ= 90º, 100 µm thick) through a f= 75 mm lens. The SC pulses were also directed towards the BBO and were focused by a concave mirror (f= 50 mm) into the crystal, forming an angle of ~20º with the fundamental. Once the spatial and temporal overlap was achieved, UV radiation was generated at the output of the crystals between both beams. When we tuned the central wavelength of the SC pulses by changing the position Z of the sapphire crystal, the generated UV signal was tuned accordingly. However, small adjustments of the delay line were required to optimize the temporal overlap between the two pulses and maximize the generated signal. In Fig 7. 41 we can see the spectra measured for different positions of the sapphire crystal.

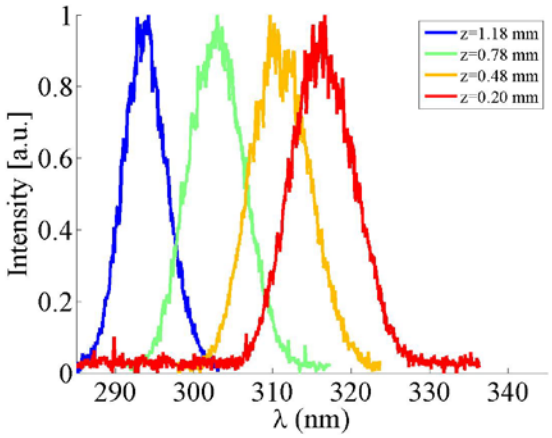

Fig 7. 41: Spectra obtained by sum-frequency generation of the SC pulses with a fundamental pulse. The position of the sapphire crystal was scanned thus obtaining tunability of the sum-frequency in the range 290 – 320 nm.

7.8. Temporal characterization

The most widely used techniques [106], such as frequency-resolved optical gating (FROG) and spectral phase interferometry for direct electric field reconstruction (SPIDER), are based on SHG. This involves certain drawbacks when the pulses are too weak to yield efficient signals or when absorption and phase-matching constraints of nonlinear crystals limit the useful nonlinear processes. In the past decade, an effort has been made to overcome these difficulties. For example, O'Shea et al. demonstrated an increased bandwidth using an angle-dithered nonlinear crystal for FROG measurements [274] .

These difficulties can be substantially reduced by employing XFROG [275, 276], which is based on spectrally resolved cross correlation (SFG, DFG) of the weak unknown pulse with a fully characterized strong reference pulse as a function of the time delay.

Stibenz and Steinmeyer demonstrated an improved SPIDER setup that was particularly suitable for measuring compressed white-light continuum pulses [277]; and more recently, Liu et al.

proposed cross correlation frequency-resolved optical gating with molecular alignment induced birefringence functioned as a gate to characterize SC pulses [278].

In this case, we used the setup described in Section 7.7 to measure the temporal duration of the SC pulses by generating the cross-correlation trace. The sapphire crystal was placed at z=1.18 mm thus obtaining the spectral peak centred at the shortest wavelength (462 nm). Relative delay between the interacting pulses was controlled with the motorized stage that was continuously moved in steps of 2 μm while the power of the generated UV was registered. As a result, the cross-correlation trace (Fig 7. 42) is obtained. An estimation of temporal duration of the SC pulses can be achieved by applying the expression [279]:

$$\tau_{SC} = \left(\tau_{XC}^{p} - \tau_{IR}^{p}\right)^{1/p} \tag{136}$$

where τ_{XC} is the FWHM of the cross-correlation trace, τ_{IR} is the temporal duration of the fundamental pulses (120 fs) and p=2 if we assume Gaussian envelopes. Then, we obtain τ_{SC}~160 fs, but we must take into account that there is a significant time smearing in the crystal between the IR and the blue pulses that amounts to ~20 fs, thus we expect the pulse duration of the IR pulses to be a few tens of fs shorter.

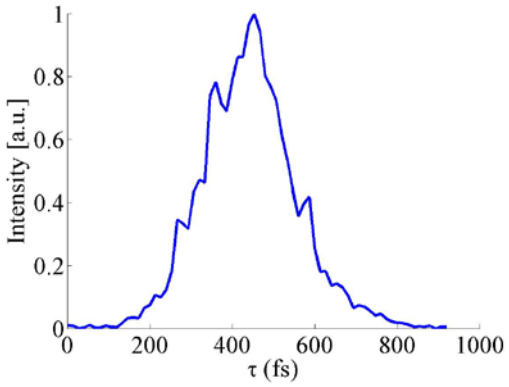

Fig 7. 42: Cross-correlation traces of the SC pulses generated at z=1.18 mm and E=1.25 μJ with the fundamental pulses.

7.9. Summary and conclusions

We have experimentally studied the visible SC generated by focusing near infrared femtosecond pulses with a kinoform DL in sapphire. The spectra of the so-generated SC pulses exhibit a strongly peaked structure at the blue border, with residual content of red wavelengths. For a given energy, the central wavelength of this peak can be accurately shifted over a range larger than 50 nm by simply changing the relative distance between the DL and the crystal. Moreover, when comparing the results with those obtained using an achromatic RL in analogous conditions (NA and pulse energy) we found that the maximum extension (blue border) of the spectral power is significantly larger with the DL.

To further explore the dynamics of the process, side-view pictures of the filament formed in the crystal have been taken with a CMOS camera. We showed that the clipping of the filament in the exit face of the crystal is directly connected with the reported behavior.

The spatial properties of the generated SC pulses have been analyzed for different situations. For the strongest clipping of the filament, the generated blue beam exhibited fairly good spatial properties with nearly Gaussian mode. As filament clipping is reduced, the spatial structure becomes worse and a ring-like structure appears. The spatial chirp and chromatic aberration were also studied, finding that both of them are negligible.

The tunability of the SC pulses has been extended to the UV by sum-frequency generation with the fundamental infrared beam in a BBO crystal. The setup was also used to measure the temporal duration of the SC pulses by cross-correlation, and pulse lengths in the range of 150 fs are obtained.

From our results the use of a DL for SC generation in bulk exhibits very interesting features for the spectral control of the generated light. We believe that the SC pulses obtained in this way could have many applications, e.g., for seeding ultrafast optical parametric amplifiers.

A Appendix

Laser parameters

In this appendix we present a summary of the parameters of the laser beam used in the experiments (Spitfire, Spectra Physics). In the table below we present the characteristics of the laser as provided by the manufacturer:

Pulse duration	120 fs
Central wavelength	795 nm
Pulse bandwidth (FWHM)	9 nm
Pulse energy	1 mJ
Repetition rate	1 kHz
Beam diameter ($1/e^2$)	9 mm
Pre-pulse contrast ratio	> 1000:1
Post-pulse contrast ratio	>100:1
Energy stability	<0.5% rms over 24 hours
Beam pointing stability	<20 µrad/ºC
Spatial mode	TEM_{00} (M^2>1.3 on both axes)
Polarization	Linear, horizontal

Table A. 1: Laser specifications as provided by the manufacturer

We have also performed some measurements of the laser parameters relevant to our experiments. The spatial characteristics (beam profile and wavefront) are given in Chapter 2. In

this appendix we present the characterization of the pulse in the temporal domain and of its corresponding spectrum:

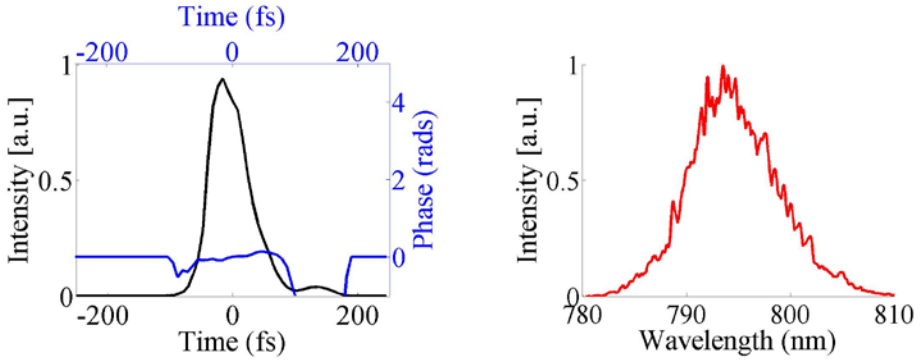

Fig A. 1: a) Pulse in the temporal domain. b) Corresponding spectrum

The laser parameters obtained are close to those provided by the manufacturer. The spectral bandwidth at FWHM was found to be 8.9 nm. The phase in the temporal domain is nearly flat, yielding a pulse duration of approximately 110 fs.

B Appendix

Wavefront sensor stability

In this appendix we provide a calibration of the commercial sensor SID4-HR (Phasics). We experimentally observed that the phase retrieved by the sensor presented some fluctuations. To test whether these distortions were compatible with the sensor error or whether they were due to instabilities, we performed a stabilization measurement. For this purpose, the wavefront of a collimated HeNe laser was registered each 6 seconds for a period of 120 minutes. The results are summarized in Fig B. 1.

From this figure we conclude that the sensor requires at least 80 minutes to operate in a stabilized regime. As it was discussed with the company, this response time is attributed to the warming of the camera.

Together with the stabilization regime in Table B.1 we present the sensor features as provided by the manufacturer.

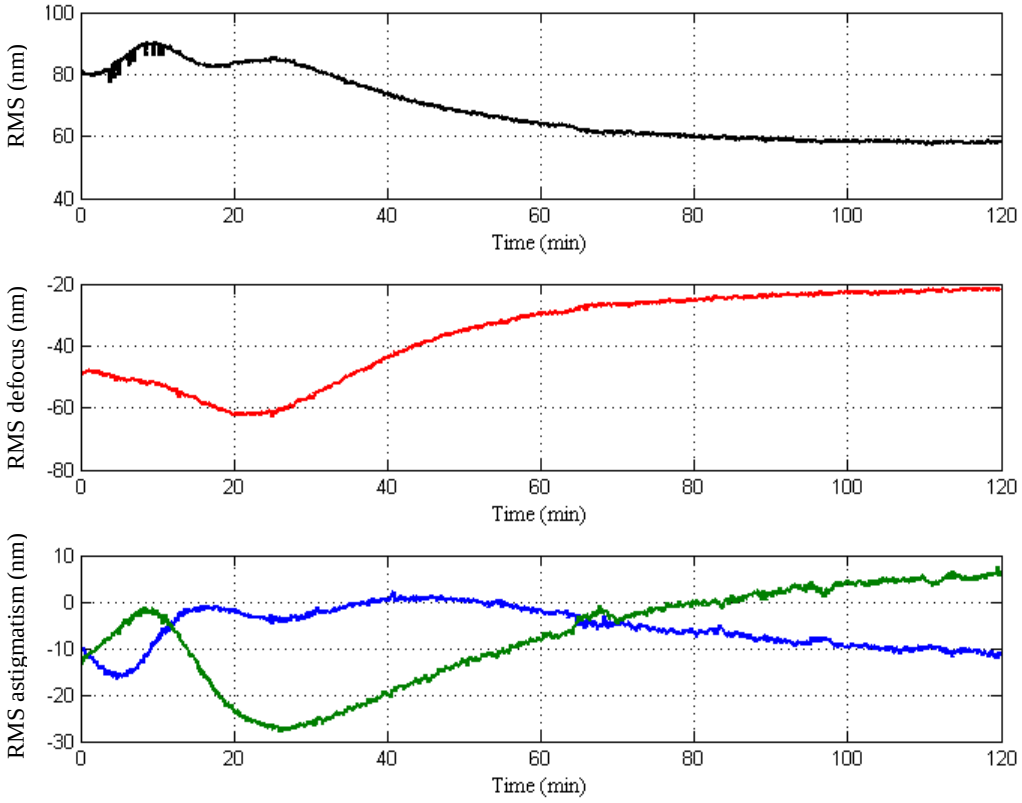

Fig B. 1: Experimental stabilization curve of the SID4-HR

Aperture dimension	8.9 x 11.8 mm^2
Spatial resolution	29.6 µm
Sampling	300 x 400 (>120 000 points)
Wavelength range	350 nm to 1100 nm
Precision (absolute/relative)	10 nm RMS / 2 nm RMS
Repeatability	2 nm RMS
Dynamic	> 500 µm
Acquisition frequency	10 fps
Real-time processing frequency	> 3 fps (full resolution)
Dimensions (l x H x L)	76 x 63 x 132 mm
Weight	620 g

Table B. 1: SID4-HR specifications (as provided by the manufacturer)

C Appendix

Zernike polynomials

The *Zernike polynomials* are a set of orthogonal polynomials on the unit disk that constitute a proper basis to express the wavefront.

Since Zernike polynomial are orthogonal, the phase projection is unique and can be expressed as follows:

$$\psi(\rho,\theta) = \sum_{n,m} {}^{e}c_n^m \, {}^{e}Z_n^m(\rho,\theta) + {}^{o}c_n^m \, {}^{o}Z_n^m(\rho,\theta)$$

where

$${}^{e}Z_n^m = \sqrt{2(n+1)}R_n^m(\rho)\cos(m\theta)$$
$${}^{o}Z_n^m = \sqrt{2(n+1)}R_n^m(\rho)\sin(m\theta)$$

In Table C. 1 we show the Zernike polynomials (up to the fourth order) in the RMS mode and the conversion factor to PtV. Fig C. 1 is the corresponding graphical representation.

#	n	m	Name	PtV/RMS factor	Cartesian form (RMS)	Polar form (RMS)
1	0	0	Piston	1	1	1
2	1	1	Tilt X	2	$\sqrt{4}x$	$\sqrt{4}\rho\cos(\theta)$
3	1	-1	Tilt Y	2	$\sqrt{4}y$	$\sqrt{4}\rho\sin(\theta)$
4	2	0	Defocus	$\sqrt{3}$	$\sqrt{3}\left(2x^2+2y^2-1\right)$	$\sqrt{3}(2\rho^2-1)$
5	2	2	0º Astigmatism	$\sqrt{6}$	$\sqrt{6}\left(x^2-y^2\right)$	$\sqrt{6}\rho^2\cos(2\theta)$
6	2	-2	45º Astigmatism	$\sqrt{6}$	$\sqrt{6}2xy$	$\sqrt{6}\rho^2\sin(2\theta)$
7	3	1	Coma X	$\sqrt{8}$	$\sqrt{8}\left(3x^3+3xy^2-2x\right)$	$\sqrt{8}(3\rho^3-2\rho)\cos(\theta)$
8	3	-1	Coma Y	$\sqrt{8}$	$\sqrt{8}\left(3x^2y+3y^3-2y\right)$	$\sqrt{8}(3\rho^3-2\rho)\sin(\theta)$
9	3	3	30º Trefoil	$\sqrt{8}$	$\sqrt{8}\left(x^3y-3xy^2\right)$	$\sqrt{8}\rho^3\cos(3\theta)$
10	3	-3	0º Trefoil	$\sqrt{8}$	$\sqrt{8}\left(3x^2y-y^3\right)$	$\sqrt{8}\rho^3\sin(3\theta)$
11	4	0	Spherical aberration	$\sqrt{5}$	$\sqrt{5}\left(6x^4+12x^2y^2+6y^4-6x^2-6\right)$	$\sqrt{5}(6\rho^4-6\rho^2+1)$
12	4	2	0º Secondary astigmatism	$\sqrt{10}$	$\sqrt{10}\left(4x^4-4y^4-3x^2+3y^2\right)$	$\sqrt{10}(4\rho^4-3\rho^2)\cos(2\theta)$
13	4	-2	45º Secondary astigmatism	$\sqrt{10}$	$\sqrt{10}\left(8x^3y+8xy^3-6xy\right)$	$\sqrt{10}(4\rho^4-3\rho^2)\sin(2\theta)$
14	4	4	0º Tetrafoil	$\sqrt{10}$	$\sqrt{10}\left(x^4-6x^2y^2+y^4\right)$	$\sqrt{10}\rho^4\cos(4\theta)$
15	4	-4	22.5º Tetrafoil	$\sqrt{10}$	$\sqrt{10}\left(4x^3y-4xy^3\right)$	$\sqrt{10}\rho^4\sin(4\theta)$

Table C. 1: Orthonormalized Zernike polynomials in RMS mode

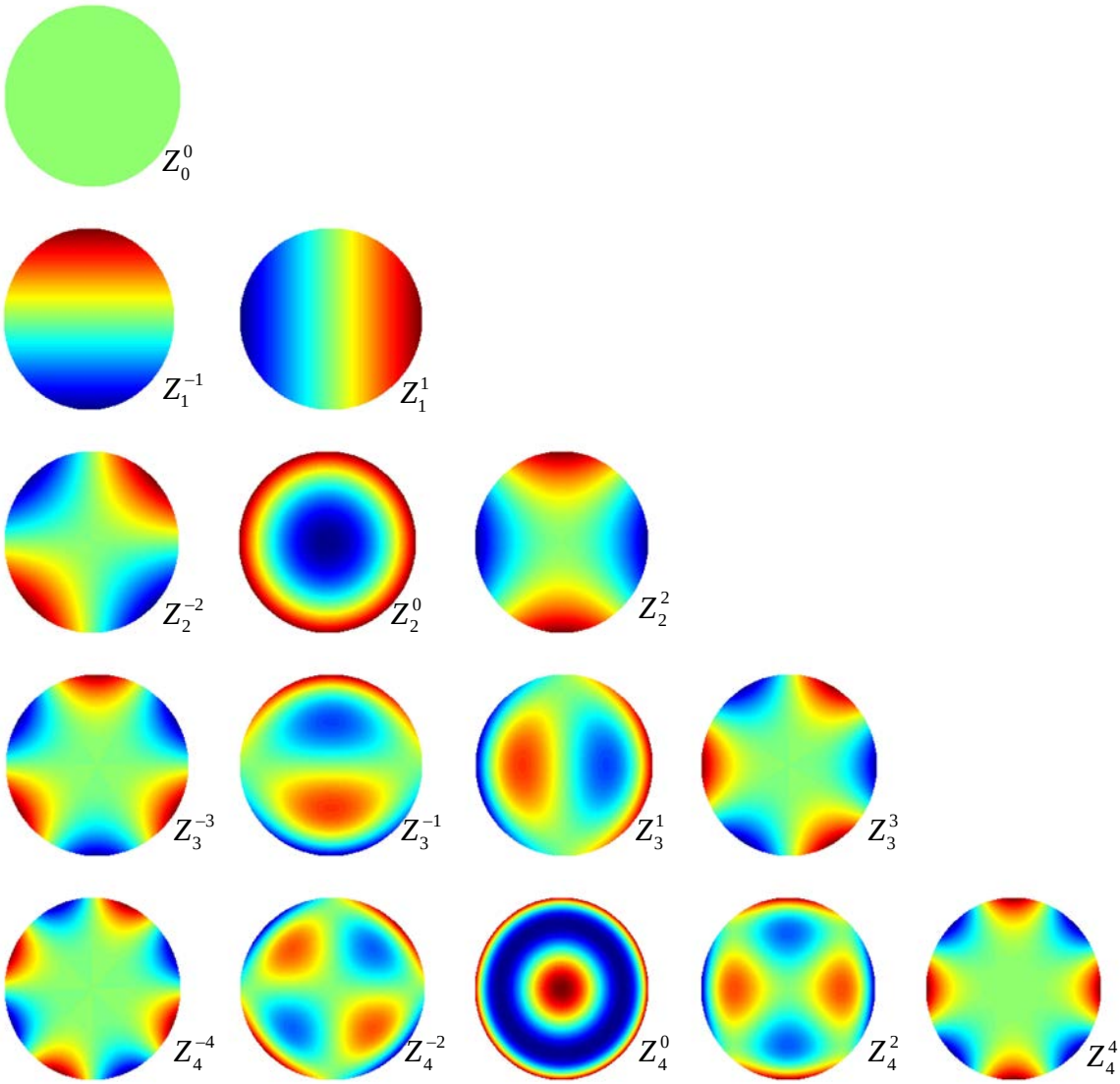

Fig C. 1: Zernike polynomials

Bibliography

1. T. H. Maiman, "Stimulated optical radiation in ruby," Nature **187**, 493-494 (1960).

2. B. Alonso, R. Borrego-Varillas, C. Hernández-García, J. A. Pérez-Hernández, and C. Romero, *El láser, la luz de nuestro tiempo* (Globalia Ediciones Anthema, 2012).

3. G. Mourou, and T. Tajima, "More Intense, Shorter Pulses," Science **331**, 41-42 (2011).

4. G. A. Mourou, N. J. Fisch, V. M. Malkin, Z. Toroker, E. A. Khazanov, A. M. Sergeev, T. Tajima, and B. Le Garrec, "Exawatt-Zettawatt pulse generation and applications," Optics Communications **285**, 720-724 (2012).

5. T. Tajima, and G. Mourou, "Zettawatt-exawatt lasers and their applications in ultrastrong-field physics," Physical Review Special Topics-Accelerators and Beams **5**, 031301 (2002).

6. G. A. Mourou, C. P. J. Barty, and M. D. Perry, "Ultrahigh-intensity lasers: Physics of the extreme on a tabletop," Physics Today **51** (1998).

7. A. V. Korzhimanov, A. A. Gonoskov, E. A. Khazanov, and A. M. Sergeev, "Horizons of petawatt laser technology," Physics-Uspekhi **54** (2011).

8. T. Brabec, and F. Krausz, "Intense few-cycle laser fields: Frontiers of nonlinear optics," Reviews of Modern Physics **72**, 545-591 (2000).

9. F. J. McClung, and R. W. Hellwarth, "Giant optical pulsations from ruby," Journal of Applied Physics **33**, 828-830 (1962).

10. L. E. Hargrove, R. L. Fork, and M. A. Pollack, "Locking of He-Ne modes induced by synchronous intracavity modulation " Applied Physics Letters **5**, 4-5 (1964).

11. C. V. Shank, and E. P. Ippen, "Subpicosecond kilowatt pulses from a mode-locked CW dye laser," Applied Physics Letters **24**, 722-725 (1974).

12. P. F. Moulton, "Spectroscopic and laser characteristics of $TiAl_2O_3$," Journal of the Optical Society of America B-Optical Physics **3**, 125-133 (1986).

13. D. Strickland, and G. Mourou, "Compression of amplified chirped optical pulses," Optics Communications **56**, 219-221 (1985).

14. J. Squier, F. Salin, G. Mourou, and D. Harter, "100 fs pulse generation and amplification in $TiAl_3$," Optics Letters **16**, 324-326 (1991).

15. W. H. Lowdermilk, and J. E. Murray, "The multipass amplifier: theory and numerical analysis," Journal of Applied Physics **51**, 2436-2445 (1980).

16. B. N. Chichkov, C. Momma, S. Nolte, F. vonAlvensleben, and A. Tunnermann, "Femtosecond, picosecond and nanosecond laser ablation of solids," Applied Physics A-Materials Science & Processing **63**, 109-115 (1996).

17. R. Osellana, G. Cerullo, and R. Ramponi, *Femtosecond laser micromachining* (Springer Berlin, 2012).

18. H. Lubatschowski, A. Heisterkamp, F. Will, A. I. Singh, J. Serbin, A. Ostendorf, O. Kermani, R. Heermann, H. Welling, and W. Ertmer, "Medical and biological applications for ultrafast laser pulses," in *3rd International Symposium on Laser Precision Microfabrication*(Osaka, Japan, 2003).

19. E. Esarey, P. Sprangle, J. Krall, and A. Ting, "Overview of plasma-based accelerator concepts," IEEE Transactions on Plasma Science **24**, 252-288 (1996).

20. T. Tajima, and J. M. Dawson, "Laser electron accelerator," Physical Review Letters **43**, 267-270 (1979).

21. V. Malka, S. Fritzler, E. Lefebvre, M. M. Aleonard, F. Burgy, J. P. Chambaret, J. F. Chemin, K. Krushelnick, G. Malka, S. P. D. Mangles, Z. Najmudin, M. Pittman, J. P. Rousseau, J. N. Scheurer, B. Walton, and A. E. Dangor, "Electron acceleration by a wake field forced by an intense ultrashort laser pulse," Science **298**, 1596-1600 (2002).

22. C. G. R. Geddes, C. Toth, J. van Tilborg, E. Esarey, C. B. Schroeder, D. Bruhwiler, C. Nieter, J. Cary, and W. P. Leemans, "High-quality electron beams from a laser wakefield accelerator using plasma-channel guiding," Nature **431**, 538-541 (2004).

23. C. Gahn, G. D. Tsakiris, A. Pukhov, J. Meyer-ter-Vehn, G. Pretzler, P. Thirolf, D. Habs, and K. J. Witte, "Multi-MeV electron beam generation by direct laser acceleration in high-density plasma channels," Physical Review Letters **83**, 4772-4775 (1999).

24. J. Faure, Y. Glinec, A. Pukhov, S. Kiselev, S. Gordienko, E. Lefebvre, J. P. Rousseau, F. Burgy, and V. Malka, "A laser-plasma accelerator producing monoenergetic electron beams," Nature **431**, 541-544 (2004).

25. A. Buck, M. Nicolai, K. Schmid, C. M. S. Sears, A. Saevert, J. M. Mikhailova, F. Krausz, M. C. Kaluza, and L. Veisz, "Real-time observation of laser-driven electron acceleration," Nature Physics **7**, 543-548 (2011).

26. W. P. Leemans, B. Nagler, A. J. Gonsalves, C. Toth, K. Nakamura, C. G. R. Geddes, E. Esarey, C. B. Schroeder, and S. M. Hooker, "GeV electron beams from a centimetre-scale accelerator," Nature Physics **2**, 696-699 (2006).

27. R. A. Snavely, M. H. Key, S. P. Hatchett, T. E. Cowan, M. Roth, T. W. Phillips, M. A. Stoyer, E. A. Henry, T. C. Sangster, M. S. Singh, S. C. Wilks, A. MacKinnon, A. Offenberger, D. M. Pennington, K. Yasuike, A. B. Langdon, B. F. Lasinski, J. Johnson, M. D. Perry, and E. M. Campbell, "Intense high-energy proton beams from petawatt-laser irradiation of solids," Physical Review Letters **85**, 2945-2948 (2000).

28. V. Malka, S. Fritzler, E. Lefebvre, E. d'Humieres, R. Ferrand, G. Grillon, C. Albaret, S. Meyroneinc, J. P. Chambaret, A. Antonetti, and D. Hulin, "Practicability of protontherapy using compact laser systems," Medical Physics **31**, 1587-1592 (2004).

29. F. Krausz, and M. Ivanov, "Attosecond physics," Reviews of Modern Physics **81**, 163-234 (2009).

30. G. Korn, S. V. Bulanov, J.-P. Chambaret, D. Charambilidis, J. Collier, M. Dunne, K. Ertel, J. Hein, S. Karsch, F. Krausz, G. Mourou, P. Nickles, K. Osvay, B. Rus, W. Sandner, G. Tsakiris,

T. Tajima, and Ieee, *Extreme Light Infrastructure (ELI): Physics and Lasers at the ultra-intense frontier* (2010).

31. T. Tajima, B. C. Barish, C. P. Barty, S. Bulanov, P. Chen, J. Feldhaus, J. Hajdu, C. H. Keitel, J.-C. Kieffer, D.-K. Ko, W. Leemans, D. Normand, L. Palumbo, K. Rzazewski, A. Sergeev, Z.-M. Sheng, F. Takasaki, M. Teshima, and E. L. I. S. A. Comm, "Science of Extreme Light Infrastructure," in *1st International Conference on Light at Extreme Intensities (LEI 2009)*(Brasov, ROMANIA, 2010).

32. G. V. Dunne, "New strong-field QED effects at extreme light infrastructure," European Physical Journal D **55**, 327-340 (2009).

33. S. W. Hawking, "Black-hole explosions," Nature **248**, 30-31 (1974).

34. W. G. Unruh, "Notes on black-hole evaporation," Physical Review D **14**, 870-892 (1976).

35. "Extreme Light Infrastructure (ELI) www.eli-laser.eu."

36. L. Roso, "Salamanca Pulsed Laser Center: the Spanish Petawatt," in *International Conference on Applications of Optics and Photonics*(Braga, PORTUGAL, 2011).

37. "Centro de Láseres Pulsados, CLPU www.clpu.es."

38. P. A. Franken, G. Weinreich, C. W. Peters, and A. E. Hill, "Generation of optical harmonics," Physical Review Letters **7**, 118-119 (1961).

39. B. Sheehy, J. D. D. Martin, L. F. DiMauro, P. Agostini, K. J. Schafer, M. B. Gaarde, and K. C. Kulander, "High harmonic generation at long wavelengths," Physical Review Letters **83**, 5270-5273 (1999).

40. T. Popmintchev, M.-C. Chen, O. Cohen, M. E. Grisham, J. J. Rocca, M. M. Murnane, and H. C. Kapteyn, "Extended phase matching of high harmonics driven by mid-infrared light," Optics Letters **33**, 2128-2131 (2008).

41. B. E. Schmidt, A. D. Shiner, M. Giguere, P. Lassonde, C. A. Trallero-Herrero, J. C. Kieffer, P. B. Corkum, D. M. Villeneuve, and F. Legare, "High harmonic generation with long-wavelength few-cycle laser pulses," Journal of Physics B-Atomic Molecular and Optical Physics **45**, 074008 (2012).

42. C. Vozzi, G. Cirmi, C. Manzoni, E. Benedetti, F. Calegari, G. Sansone, S. Stagira, O. Svelto, S. De Silvestri, M. Nisoli, and G. Cerullo, "High-energy, few-optical-cycle pulses at 1.5 mu m with passive carrier-envelope phase stabilization," Optics Express **14**, 10109-10116 (2006).

43. F. Rotermund, V. Petrov, and F. Noack, "Femtosecond noncollinear parametric amplification in the mid-infrared," Optics Communications **169**, 183-188 (1999).

44. O. Chalus, P. K. Bates, M. Smolarski, and J. Biegert, "Mid-IR short-pulse OPCPA with micro-Joule energy at 100 kHz," Optics Express **17**, 3587-3594 (2009).

45. C. Erny, C. Heese, M. Haag, L. Gallmann, and U. Keller, "High-repetition-rate optical parametric chirped-pulse amplifier producing 1-mu J, sub-100-fs pulses in the mid-infrared," Optics Express **17**, 1340-1345 (2009).

46. G. Cerullo, and S. De Silvestri, "Ultrafast optical parametric amplifiers," Review of Scientific Instruments **74**, 1-18 (2003).

47. C. C. Wang, and G. W. Racette, "Measurement of parametric gain accompanying optical difference frequency generation," Applied Physics Letters **6**, 169-171 (1965).

48. Giordmai.Ja, and R. C. Miller, "Tunable coherent parametric oscillation in $LiNbO_3$ at opical frequencies," Physical Review Letters **14**, 973-976 (1965).

49. R. R. Alfano, and S. L. Saphiro, "Emission in the Region 4000 to 7000 Å Via Four-Photon Coupling in Glass," Physical Review Letters **24**, 584-587 (1970).

50. E. Pontecorvo, S. M. Kapetanaki, M. Badioli, D. Brida, M. Marangoni, G. Cerullo, and T. Scopigno, "Femtosecond stimulated Raman spectrometer in the 320-520nm range," Optics Express **19**, 1107-1112 (2011).

51. A. Kummrow, M. Wittmann, F. Tschirschwitz, G. Korn, and E. T. J. Nibbering, "Femtosecond ultraviolet pulses generated using noncollinear optical parametric amplification and sum frequency mixing," Applied Physics B-Lasers and Optics **71**, 885-887 (2000).

52. D. Brida, C. Manzoni, G. Cirmi, M. Marangoni, S. Bonora, P. Villoresi, S. De Silvestri, and G. Cerullo, "Few-optical-cycle pulses tunable from the visible to the mid-infrared by optical parametric amplifiers," Journal of Optics **12**, 013001 (2010).

53. A. Dubietis, G. Jonusauskas, and A. Piskarskas, "Powerful femtosecond pulse generation by chirped and stretched pulse parametric amplification in BBO crystal," Optics Communications **88**, 437-440 (1992).

54. I. N. Ross, P. Matousek, M. Towrie, A. J. Langley, and J. L. Collier, "The prospects for ultrashort pulse duration and ultrahigh intensity using optical parametric chirped pulse amplifiers," Optics Communications **144**, 125-133 (1997).

55. S. Witte, R. T. Zinkstok, W. Hogervorst, and K. S. E. Eikema, "Generation of few-cycle terawatt light pulses using optical parametric chirped pulse amplification," Optics Express **13**, 4903-4908 (2005).

56. D. Herrmann, L. Veisz, R. Tautz, F. Tavella, K. Schmid, V. Pervak, and F. Krausz, "Generation of sub-three-cycle, 16 TW light pulses by using noncollinear optical parametric chirped-pulse amplification," Optics Letters **34**, 2459-2461 (2009).

57. V. V. Lozhkarev, G. I. Freidman, V. N. Ginzburg, E. V. Katin, E. A. Khazanov, A. V. Kirsanov, G. A. Luchinin, A. N. Mal'shakov, M. A. Martyanov, O. V. Palashov, A. K. Poteomkin, A. M. Sergeev, A. A. Shaykin, and I. V. Yakovlev, "Compact 0.56 Petawatt laser system based on optical parametric chirped pulse amplification in KD*P crystals," Laser Physics Letters **4**, 421-427 (2007).

58. O. Chekhlov, E. J. Divall, K. Ertel, S. J. Hawkes, C. J. Hooker, I. N. Ross, P. Matousek, C. Hernandez-Gomez, Y. Tang, T. Winstone, D. Neely, R. Clarke, P. Foster, S. J. Hancock, B. E. Wyborn, and J. L. Collier, "Development of Petawatt laser amplification systems at the central laser facility - art. no. 67350J," in *International Conference on Lasers, Applications, and Technologies*(Minsk, BYELARUS, 2007).

59. N. Ishii, L. Turi, V. S. Yakovlev, T. Fuji, F. Krausz, A. Baltuska, R. Butkus, G. Veitas, V. Smilgevicius, R. Danielius, and A. Piskarskas, "Multimillijoule chirped parametric amplification of few-cycle pulses," Optics Letters **30**, 567-569 (2005).

60. S. Witte, R. T. Zinkstok, A. L. Wolf, W. Hogervorst, W. Ubachs, and K. S. E. Eikema, "A source of 2 terawatt, 2.7 cycle laser pulses based on noncollinear optical parametric chirped pulse amplification," Optics Express **14**, 8168-8177 (2006).

61. E. A. Khazanov, and A. M. Sergeev, "Petawatt lasers based on optical parametric amplifiers: their state and prospects," Physics-Uspekhi **51** (2008).

62. C. Skrobol, I. Ahmad, S. Klingebiel, C. Wandt, S. A. Trushin, Z. Major, F. Krausz, and S. Karsch, "Broadband amplification by picosecond OPCPA in DKDP pumped at 515 nm," Optics Express **20**, 4619-4629 (2012).

63. Z. Major, S. A. Trushin, I. Ahmad, M. Siebold, C. Wandt, S. Klingebiel, T.-J. Wang, J. A. Fulöp, A. Henig, S. Krube, R. Weingartner, A. Popp, J. Osterhoff, R. Hörlein, J. Hein, V. Pervak, A. Apolonski, F. Krausz, and S. Karsch, "Basic concepts and current status of the Petawatt Field Synthesizer - a new approach to ultrahigh filed generation," (Rev. Laser Eng., 2009), pp. 431-436.

64. A. McPherson, G. Gibson, H. Jara, U. Johann, T. S. Luk, I. A. McIntyre, K. Boyer, and C. K. Rhodes, "Studies of multiphoton production of vacuum ultraviolet-radiation in the rare-gases," Journal of the Optical Society of America B-Optical Physics **4**, 595-601 (1987).

65. N. H. Burnett, H. A. Baldis, M. C. Richardson, and G. D. Enright, "Harmonic generation in CO_2 laser target interaction," Applied Physics Letters **31**, 172-174 (1977).

66. P. B. Corkum, "Plasma perspective on strong-field multiphoton ionization," Physical Review Letters **71**, 1994-1997 (1993).

67. A. Rundquist, C. G. Durfee, Z. H. Chang, C. Herne, S. Backus, M. M. Murnane, and H. C. Kapteyn, "Phase-matched generation of coherent soft X-rays," Science **280**, 1412-1415 (1998).

68. T. Popmintchev, M.-C. Chen, P. Arpin, M. M. Murnane, and H. C. Kapteyn, "The attosecond nonlinear optics of bright coherent X-ray generation," Nature Photonics **4**, 822-832 (2010).

69. T. Popmintchev, M.-C. Chen, D. Popmintchev, P. Arpin, S. Brown, S. Alisauskas, G. Andriukaitis, T. Balciunas, O. D. Muecke, A. Pugzlys, A. Baltuska, B. Shim, S. E. Schrauth, A. Gaeta, C. Hernandez-Garcia, L. Plaja, A. Becker, A. Jaron-Becker, M. M. Murnane, and H. C. Kapteyn, "Bright Coherent Ultrahigh Harmonics in the keV X-ray Regime from Mid-Infrared Femtosecond Lasers," Science **336**, 1287-1291 (2012).

70. P. M. Paul, E. S. Toma, P. Breger, G. Mullot, F. Auge, P. Balcou, H. G. Muller, and P. Agostini, "Observation of a train of attosecond pulses from high harmonic generation," Science **292**, 1689-1692 (2001).

71. M. Hentschel, R. Kienberger, C. Spielmann, G. A. Reider, N. Milosevic, T. Brabec, P. Corkum, U. Heinzmann, M. Drescher, and F. Krausz, "Attosecond metrology," Nature **414**, 509-513 (2001).

72. N. Milosevic, P. B. Corkum, and T. Brabec, "How to use lasers for imaging attosecond dynamics of nuclear processes," Physical Review Letters **92**, 013002-013006 (2004).

73. M. Drescher, M. Hentschel, R. Kienberger, M. Uiberacker, T. Westerwalbesloh, U. Kleineberg, U. Heinzmann, and F. Krausz, "Time-resolved electron spectroscopy of atomic inner-shell dynamics," Journal of Electron Spectroscopy and Related Phenomena **137**, 259-264 (2004).

74. A. Baltuska, T. Udem, M. Uiberacker, M. Hentschel, E. Goulielmakis, C. Gohle, R. Holzwarth, V. S. Yakoviev, A. Scrinzi, T. W. Hansch, and F. Krausz, "Attosecond control of electronic processes by intense light fields," Nature **421**, 611-615 (2003).

75. M. Uiberacker, T. Uphues, M. Schultze, A. J. Verhoef, V. Yakovlev, M. F. Kling, J. Rauschenberger, N. M. Kabachnik, H. Schroeder, M. Lezius, K. L. Kompa, H. G. Muller, M. J. J. Vrakking, S. Hendel, U. Kleineberg, U. Heinzmann, M. Drescher, and F. Krausz, "Attosecond real-time observation of electron tunnelling in atoms," Nature **446**, 627-632 (2007).

76. R. Kienberger, M. Hentschel, M. Uiberacker, C. Spielmann, M. Kitzler, A. Scrinzi, M. Wieland, T. Westerwalbesloh, U. Kleineberg, U. Heinzmann, M. Drescher, and F. Krausz, "Steering attosecond electron wave packets with light," Science **297**, 1144-1148 (2002).

77. P. B. Corkum, and F. Krausz, "Attosecond science," Nature Physics **3**, 381-387 (2007).

78. H. Niikura, F. Legare, R. Hasbani, M. Y. Ivanov, D. M. Villeneuve, and P. B. Corkum, "Probing molecular dynamics with attosecond resolution using correlated wave packet pairs," Nature **421**, 826-829 (2003).

79. S. Baker, J. S. Robinson, C. A. Haworth, H. Teng, R. A. Smith, C. C. Chirila, M. Lein, J. W. G. Tisch, and J. P. Marangos, "Probing proton dynamics in molecules on an attosecond time scale," Science **312**, 424-427 (2006).

80. E. Gagnon, P. Ranitovic, X.-M. Tong, C. L. Cocke, M. M. Murnane, H. C. Kapteyn, and A. S. Sandhu, "Soft X-ray-driven femtosecond molecular dynamics," Science **317**, 1374-1378 (2007).

81. P. Agostini, and L. F. DiMauro, "The physics of attosecond light pulses," Reports on Progress in Physics **67**, 813-855 (2004).

82. A. Braun, G. Korn, X. Liu, D. Du, J. Squier, and G. Mourou, "Self-channeling of high-peak-power femtosecond laser-pulses in air," Optics Letters **20**, 73-75 (1995).

83. A. Couairon, and A. Mysyrowicz, "Femtosecond filamentation in transparent media," Physics Reports-Review Section of Physics Letters **441**, 47-189 (2007).

84. C. P. Hauri, W. Kornelis, F. W. Helbing, A. Heinrich, A. Couairon, A. Mysyrowicz, J. Biegert, and U. Keller, "Generation of intense, carrier-envelope phase-locked few-cycle laser pulses through filamentation," Applied Physics B-Lasers and Optics **79**, 673-677 (2004).

85. J. Kasparian, R. Sauerbrey, and S. L. Chin, "The critical laser intensity of self-guided light filaments in air," Applied Physics B-Lasers and Optics **71**, 877-879 (2000).

86. J. Kasparian, M. Rodriguez, G. Mejean, J. Yu, E. Salmon, H. Wille, R. Bourayou, S. Frey, Y. B. Andre, A. Mysyrowicz, R. Sauerbrey, J. P. Wolf, and L. Woste, "White-light filaments for atmospheric analysis," Science **301**, 61-64 (2003).

87. J. C. Diels, R. Bernstein, K. E. Stahlkopf, and X. M. Zhao, "Lightning control with lasers," Scientific American **277** (1997).

88. S. Tzortzakis, D. Anglos, and D. Gray, "Ultraviolet laser filaments for remote laser-induced breakdown spectroscopy (LIBS) analysis: applications in cultural heritage monitoring," Optics Letters **31**, 1139-1141 (2006).

89. S. W. Bahk, P. Rousseau, T. A. Planchon, V. Chvykov, G. Kalintchenko, A. Maksimchuk, G. A. Mourou, and V. Yanovsky, "Generation and characterization of the highest laser intensities (10(22) W/cm(2))," Optics Letters **29**, 2837-2839 (2004).

90. V. Yanovsky, V. Chvykov, G. Kalinchenko, P. Rousseau, T. Planchon, T. Matsuoka, A. Maksimchuk, J. Nees, G. Cheriaux, G. Mourou, and K. Krushelnick, "Ultra-high intensity-300-TW laser at 0.1 Hz repetition rate," Optics Express **16**, 2109-2114 (2008).

91. A. Baltuska, T. Fuji, and T. Kobayashi, "Visible pulse compression to 4 fs by optical parametric amplification and programmable dispersion control," Optics Letters **27**, 306-308 (2002).

92. J. Queneuille, F. Druon, A. Maksimchuk, G. Cheriaux, G. Mourou, and K. Nemoto, "Second-harmonic generation and wave-front correction of a terawatt laser system," Optics Letters **25**, 508-510 (2000).

93. Q. Sun, H. Liu, N. Huang, and W. Zhao, "Influence of the wavefront mismatch, spatial chirp and multimode pump on the beam quality of OPCPA," Journal of Modern Optics **59**, 628-635 (2012).

94. A. H. Zewail, "Femtochemistry: Atomic-scale dynamics of the chemical bond," Journal of Physical Chemistry A **104**, 5660-5694 (2000).

95. C. Manzoni, D. Polli, and G. Cerullo, "Two-color pump-probe system broadly tunable over the visible and the near infrared with sub-30 fs temporal resolution," Review of Scientific Instruments **77**, 023103 (2006).

96. D. Brida, C. Manzoni, G. Cirmi, D. Polli, and G. Cerullo, "Tracking Ultrafast Energy Flow in Molecules Using Broadly Tunable Few-Optical-Cycle Pulses," IEEE Journal of Selected Topics in Quantum Electronics **18**, 329-339 (2012).

97. B. Alonso, O. Varela, I. J. Sola, J. San Roman, A. Zair, C. Mendez, and L. Roso, "Energy scaling-up of stable single filament," Applied Physics B-Lasers and Optics **101**, 15-22 (2010).

98. O. Varela, A. Zair, J. San Roman, B. Alonso, I. Juan Sola, C. Prieto, and L. Roso, "Above-millijoule super-continuum generation using polarisation dependent filamentation in atoms and molecules," Optics Express **17**, 3630-3639 (2009).

99. C. P. Hauri, J. Biegert, U. Keller, B. Schaefer, K. Mann, and G. Marowski, "Validity of wave-front reconstruction and propagation of ultrabroadband pulses measured with a Hartmann-Shack sensor," Optics Letters **30**, 1563-1565 (2005).

100. C. Peth, S. Kranzusch, K. Mann, and W. Viol, "Characterization of gas targets for laser produced extreme ultraviolet plasmas with a Hartmann-Shack sensor," Review of Scientific Instruments **75**, 3288-3293 (2004).

101. F. Tavella, K. Schmid, N. Ishii, A. Marcinkevicius, L. Veisz, and F. Krausz, "High-dynamic range pulse-contrast measurements of a broadband optical parametric chirped-pulse amplifier," Applied Physics B-Lasers and Optics **81**, 753-756 (2005).

102. C. Thaury, F. Quere, J. P. Geindre, A. Levy, T. Ceccotti, P. Monot, M. Bougeard, F. Reau, P. D'Oliveira, P. Audebert, R. Marjoribanks, and P. H. Martin, "Plasma mirrors for ultrahigh-intensity optics," Nature Physics **3**, 424-429 (2007).

103. A. Jullien, O. Albert, F. Burgy, G. Hamoniaux, L. P. Rousseau, J. P. Chambaret, F. Auge-Rochereau, G. Cheriaux, J. Etchepare, N. Minkovski, and S. M. Saltiel, "10(-10) temporal contrast for femtosecond ultraintense lasers by cross-polarized wave generation," Optics Letters **30**, 920-922 (2005).

104. E. J. Divall, and I. N. Ross, "High dynamic range contrast measurements by use of an optical parametric amplifier correlator," Optics Letters **29**, 2273-2275 (2004).

105. D. Meshulach, Y. Barad, and Y. Silberberg, "Measurement of ultrashort optical pulses by third-harmonic generation," Journal of the Optical Society of America B-Optical Physics **14**, 2122-2125 (1997).

106. I. A. Walmsey, and C. Dorrer, *Characterization of ultrashort electromagnetic pulses* (2009).

107. R. Trebino, and D. J. Kane, "Using phase retrieval to measure the intensity and phase of ultrashort pulses - frequency-resolved optical gating," Journal of the Optical Society of America a-Optics Image Science and Vision **10**, 1101-1111 (1993).

108. C. Iaconis, and I. A. Walmsley, "Spectral phase interferometry for direct electric-field reconstruction of ultrashort optical pulses," Optics Letters **23**, 792-794 (1998).

109. M. Nisoli, S. DeSilvestri, and O. Svelto, "Generation of high energy 10 fs pulses by a new pulse compression technique," Applied Physics Letters **68**, 2793-2795 (1996).

110. S. Kane, and J. Squier, "Grism-pair stretcher-compressor system for simultaneous second- and third-order dispersion compensation in chirped-pulse amplification," Journal of the Optical Society of America B-Optical Physics **14**, 661-665 (1997).

111. F. X. Kartner, N. Matuschek, T. Schibli, U. Keller, H. A. Haus, C. Heine, R. Morf, V. Scheuer, M. Tilsch, and T. Tschudi, "Design and fabrication of double-chirped mirrors," Optics Letters **22**, 831-833 (1997).

112. R. Szipocs, and A. KohaziKis, "Theory and design of chirped dielectric laser mirrors," Applied Physics B-Lasers and Optics **65**, 115-135 (1997).

113. S. Ranc, G. Cheriaux, S. Ferre, J. P. Rousseau, and J. P. Chambaret, "Importance of spatial quality of intense femtosecond pulses," Applied Physics B-Lasers and Optics **70**, S181-S187 (2000).

114. M. Born, and E. Wolf, *Principles of Optics* (Cambridge University Press, 2003).

115. A. E. Siegman, "New developments in laser resonators," in *Proc. SPIE Confernce on Optical Resonators*(Los Angeles, Ca, 1990), pp. 2-14.

116. J. Alda, J. Alonso, and E. Bernabeu, "Characterization of aberrated laser beams," Journal of the Optical Society of America a-Optics Image Science and Vision **14**, 2737-2747 (1997).

117. I. Gallardo, "Diseño y construcción de un medidor de factor de propagación M^2," in *MSc thesis*(Universidad de Salamanca, 2011).

118. J. C. Wyant, and K. Creath, "Basic wavefront aberration theory for optical metrology," (Applied optics and optical engineering, 1992).

119. J. Y. Wang, and D. E. Silva, "Wave-front interpretation with Zernike polynomials," Applied Optics **19**, 1510-1518 (1980).

120. "SID4 3.1 User handbook," (Phasics, 2006).

121. J. Hartmann, "Objektivuntersuchungen," (Z. Instrumentenkd, 1904), pp. 1-21.

122. M. P. Rimmer, and J. C. Wyant, "Evaluation of large aberrations using a lateral shearing interferometer having variable shear," Applied Optics **14**, 142-150 (1975).

123. E. Gaviola, "On the quantitative use of the Foucault knife-edge test," Journal of the Optical Society of America **26**, 163-163 (1936).

124. M. Mansuripur, "The Ronchi test," (Optics and Photonics News, 1997), pp. 42-46.

125. S. R. Chamot, C. Dainty, and S. Esposito, "Adaptive optics for ophthalmic applications using a pyramid wavefront sensor," Optics Express **14**, 518-526 (2006).

126. B. Vohnsen, S. Castillo, and D. Rativa, "Wavefront sensing with an axicon," Optics Letters **36**, 846-848 (2011).

127. L. Changhai, X. Fengjie, H. Shengyang, and J. Zongfu, "Performance analysis of multiplexed phase computer-generated hologram for modal wavefront sensing," Applied optics **50**, 1631-1639 (2011).

128. C. Schulze, D. Naidoo, D. Flamm, O. A. Schmidt, A. Forbes, and M. Duparre, "Wavefront reconstruction by modal decomposition," Optics express **20**, 19714-19725 (2012).

129. I. A. Litvin, A. Dudley, F. S. Roux, and A. Forbes, "Azimuthal decomposition with digital holograms," Optics Express **20**, 10996-11004 (2012).

130. R. V. Shack, and B. C. Platt, "Production and use of a lenticular Harmann screen," Journal of the Optical Society of America **61**, 656 (1971).

131. B. C. Platt, and R. Shack, "History and principles of Shack-Hartmann wavefront sensing," Journal of Refractive Surgery **17**, S573-S577 (2001).

132. J. Primot, "Theoretical description of Shack-Hartmann wave-front sensor," Optics Communications **222**, 81-92 (2003).

133. A. G. Aleksandrov, V. E. Zavalova, A. V. Kudryashov, A. L. Rukosuev, P. N. Romanov, V. V. Samarkin, and Y. V. Sheldakova, "Shack-Hartmann wavefront sensor for measuring the parameters of high-power pulsed solid-state lasers," Quantum Electronics **40**, 321-326 (2010).

134. J. Primot, "Three-wave lateral shearing interferometer," Applied Optics **32**, 6242-6249 (1993).

135. J. Primot, and L. Sogno, "Achromatic three-wave (or more) lateral shearing interferometer," Journal of the Optical Society of America a-Optics Image Science and Vision **12**, 2679-2685 (1995).

136. J. C. Chanteloup, F. Druon, M. Nantel, A. Maksimchuk, and G. Mourou, "Single-shot wave-front measurements of high-intensity ultrashort laser pulses with a three-wave interferometer," Optics Letters **23**, 621-623 (1998).

137. J. C. Chanteloup, "Multiple-wave lateral shearing interferometry for wave-front sensing," Applied Optics **44**, 1559-1571 (2005).

138. S. Velghe, J. Primot, N. Guerineau, M. Cohen, and B. Wattellier, "Wave-front reconstruction from multidirectional phase derivatives generated by multilateral shearing interferometers," Optics Letters **30**, 245-247 (2005).

139. R. Borrego-Varillas, C. Méndez, I. Arias, and L. Roso, "Medida del frente de onda de un láser mediante interferometría a tres y cuatroondas," in *IX Reunión Nacional de Óptica*(Ourense, 2009).

140. A. M. Nugumanov, R. V. Smirnov, and V. I. Sokolov, "A method for measuring the radiation wave front by using a three-wave lateral shearing interferometer," Quantum Electronics **30**, 435-440 (2000).

141. C. G. Durfee, S. Backus, M. M. Murnane, and H. C. Kapteyn, "Design and implementation of a TW-class high-average power laser system," Ieee Journal of Selected Topics in Quantum Electronics **4**, 395-406 (1998).

142. U. J. Greiner, and H. H. Klingenberg, "Thermal lens correction of a diode-pumped NdYAG laser of high TEM00 power by an adjustable-curvature mirror," Optics Letters **19**, 1207-1209 (1994).

143. C. Hernandez-Gomez, J. L. Collier, S. J. Hawkes, C. N. Danson, C. B. Edwards, D. A. Pepler, I. N. Ross, and T. B. Winstone, "Wave-front control of a large-aperture laser system by use of a static phase corrector," Applied Optics **39**, 1954-1961 (2000).

144. J. M. Bueno, B. Vohnsen, L. Roso, and P. Artal, "Temporal wavefront stability of an ultrafast high-power laser beam," Applied Optics **48**, 770-777 (2009).

145. F. Druon, G. Cheriaux, J. Faure, J. Nees, M. Nantel, A. Maksimchuk, J. C. Chanteloup, and G. Vdovin, "Wave-front correction of femtosecond terawatt lasers by deformable mirrors," Optics Letters **23**, 1043-1045 (1998).

146. S.-W. Bahk, E. Fess, B. E. Kruschwitz, and J. D. Zuegel, "A high-resolution, adaptive beam-shaping system for high-power lasers," Optics Express **18**, 9151-9163 (2010).

147. Y. Akahane, J. L. Ma, Y. Fukuda, M. Aoyoma, H. Kiriyama, J. V. Sheldakova, A. V. Kudryashov, and K. Yamakawa, "Characterization of wave-front corrected 100 TW, 10 Hz laser pulses with peak intensities greater than 10(20) W/cm(2)," Review of Scientific Instruments **77**, 023102 (2006).

148. S. Fourmaux, S. Payeur, A. Alexandrov, C. Serbanescu, F. Martin, T. Ozaki, A. Kudryashov, and J. C. Kieffer, "Laser beam wavefront correction for ultra high intensities with the 200 TW laser system at the Advanced Laser Light Source," Optics Express **16**, 11987-11994 (2008).

149. V. Samarkin, A. Aleksandrov, and A. Kudryashov, "Bimorph mirrors for powerful laser beam correction and formation," in *High-Resolution Wavefront Control: Methods, Devices, and Applications Iii*, J. D. V. M. A. G. M. T. Gonglewski, ed. (2002), pp. 269-276.

150. M. Aoyama, K. Yamakawa, Y. Akahane, J. Ma, N. Inoue, H. Ueda, and H. Kiriyama, "0.85-PW, 33-fs Ti : sapphire laser," Optics Letters **28**, 1594-1596 (2003).

151. H. Baumhacker, G. Pretzler, K. J. Witte, M. Hegelich, M. Kaluza, S. Karsch, A. Kudryashov, V. Samarkin, and A. Roukossouev, "Correction of strong phase and amplitude modulations by two deformable mirrors in a multistaged Ti : sapphire laser," Optics Letters **27**, 1570-1572 (2002).

152. C. P. J. Barty, M. Key, J. Britten, R. Beach, G. Beer, C. Brown, S. Bryan, J. Caird, T. Carlson, J. Crane, J. Dawson, A. C. Erlandson, D. Fittinghoff, M. Hermann, C. Hoaglan, A. Iyer, L. Jones, I. Jovanovic, A. Komashko, O. Landen, Z. Liao, W. Molander, S. Mitchell, E. Moses, N. Nielsen, H. H. Nguyen, J. Nissen, S. Payne, D. Pennington, L. Risinger, M. Rushford, K. Skulina, M. Spaeth, B. Stuart, G. Tietbohl, and B. Wattellier, "An overview of LLNL high-energy short-pulse technology for advanced radiography of laser fusion experiments," Nuclear Fusion **44**, S266-S275 (2004).

153. B. Wattellier, J. Fuchs, J. P. Zou, K. Abdeli, C. Haefner, and H. Pepin, "High-power short-pulse laser repetition rate improvement by adaptive wave front correction," Review of Scientific Instruments **75**, 5186-5192 (2004).

154. B. Wattellier, J. Fuchs, J. P. Zou, K. Abdeli, H. Pepin, and C. Haefner, "Repetition rate increase and diffraction-limited focal spots for a nonthermal-equilibrium 100-TW Nd : glass laser chain by use of adaptive optics," Optics Letters **29**, 2494-2496 (2004).

155. J. P. Zou, B. Wattellier, J. Fuchs, K. Abdeli, J. C. Chanteloup, and C. Haefner, "High focusability performance obtained on the LULI 100TW laser facility by use of a dielectric coated deformable mirror," in *Conference on Laser Resonators and Beam Control VII*(San Jose, CA, 2004), pp. 37-44.

156. J.-P. Zou, A.-M. Sautivet, J. Fils, L. Martin, K. Abdeli, C. Sauteret, and B. Wattellier, "Optimization of the dynamic wavefront control of a pulsed kilojoule/nanosecond-petawatt laser facility," Applied Optics **47**, 704-710 (2008).

157. "www.phasics.fr."

158. R. Paschotta, *Encyclopedia of laser physics and tecnhology* (Wiley, 2008).

159. F. Valle, "Caracterización y optimización de un jet de gas para aceleración de electrones con láser," in *MSc thesis*(Universidad de Salamanca, 2012).

160. P. Gibbon, "Short pulse lasers interactions with matter," (Imperial College Press, 2005).

161. J. L. Henares, and C. Ruiz, "Ultrashort electron beam and X ray generation with a GW laser in air," (International workshop in laser-plasma interaction at ultra-high intensity, 2012).

162. "http://code.google.com/p/balas."

163. B. Alonso, R. Borrego-Varillas, I. J. Sola, O. Varela, A. Villamarin, M. V. Collados, J. San Roman, J. M. Bueno, and L. Roso, "Enhancement of filamentation postcompression by astigmatic focusing," Optics Letters **36**, 3867-3869 (2011).

164. Q. Sun, H. B. Jiang, Y. Liu, Y. H. Zhou, H. Yang, and Q. H. Gong, "Effect of spherical aberration on the propagation of a tightly focused femtosecond laser pulse inside fused silica," Journal of Optics a-Pure and Applied Optics **7**, 655-659 (2005).

165. C. R. Giuliano, A. Yariv, and Marburge.Jh, "Enhancement of self-focusing threshold in sapphire with elliptical beams," Applied Physics Letters **21**, 58-60 (1972).

166. K. L. Baker, "Curvature wave-front sensors for electron density characterization in plasmas," Review of Scientific Instruments **74** (2003).

167. K. L. Baker, J. Brase, M. Kartz, S. S. Olivier, B. Sawvel, and J. Tucker, "The use of a Shack-Hartmann wave front sensor for electron density characterization of high density plasmas," Review of Scientific Instruments **73** (2002).

168. G. R. Plateau, N. H. Matlis, C. G. R. Geddes, A. J. Gonsalves, S. Shiraishi, C. Lin, R. A. van Mourik, and W. P. Leemans, "Wavefront-sensor-based electron density measurements for laser-plasma accelerators," Review of Scientific Instruments **81** (2010).

169. R. W. Boyd, *Nonlinear optics (third edition)* (Academic Press, San Diego, 2008).

170. V. G. Dmitriev, G. G. Gurzadyan, and D. N. Nikogosgan, *Handbook of nonlinear optical crystals* (Springer, 1999).

171. P. A. Franken, G. Weinreich, C. W. Peters, and A. E. Hill, "Generation of optical harmonics," Physical Review Letters **7**, 118-& (1961).

172. M. Sheik-Bahae, and M. P. Hasselbeck, "Third-order optical nonlinearities," in *Handbook of Optics IV*(McGraw-Hill).

173. M. Sheikbahae, A. A. Said, and E. W. Vanstryland, "High-sensitivity, single-beam n_2 measurements," Optics Letters **14**, 955-957 (1989).

174. R. Desalvo, D. J. Hagan, M. Sheikbahae, G. Stegeman, E. W. Vanstryland, and H. Vanherzeele, "Self-focusing and self-defocusing by cascaded second order effects in KTP," Optics Letters **17**, 28-30 (1992).

175. J. P. Caumes, L. Videau, C. Rouyer, and E. Freysz, "Direct measurement of wave-front distortion induced during second-harmonic generation: application to breakup-integral compensation," Optics Letters **29**, 899-901 (2004).

176. G. I. Stegeman, M. Sheikbahae, E. Vanstryland, and G. Assanto, "Large nonlinear phase-shifts in second-order nonlinear optical processes," Optics Letters **18**, 13-15 (1993).

177. C. Kolleck, "Cascaded second-order contribution to the third-order nonlinear susceptibility," Physical Review A **69**, 812-817 (2004).

178. S. S. Mao, F. Quere, S. Guizard, X. Mao, R. E. Russo, G. Petite, and P. Martin, "Dynamics of femtosecond laser interactions with dielectrics," Applied Physics a-Materials Science & Processing **79**, 1695-1709 (2004).

179. R. R. Alfano, *The Supercontinuum Laser Source* (Springer, 2006).

180. R. R. Alfano, and S. L. Saphiro, "Emission in the Region 4000 to 7000 Å Via Four-Photon Coupling in Glass," Phy. Rev. Lett. **24**, 584-587 (1970).

181. M. Bradler, P. Baum, and E. Riedle, "Femtosecond continuum generation in bulk laser host materials with sub-mu J pump pulses," Applied Physics B-Lasers and Optics **97**, 561-574 (2009).

182. V. P. Kandidov, O. G. Kosareva, I. S. Golubtsov, W. Liu, A. Becker, N. Akozbek, C. M. Bowden, and S. L. Chin, "Self-transformation of a powerful femtosecond laser pulse into a white-light laser pulse in bulk optical media (or supercontinuum generation)," Applied Physics B-Lasers and Optics **77**, 149-165 (2003).

183. M. Kolesik, G. Katona, J. V. Moloney, and E. M. Wright, "Theory and simulation of supercontinuum generation in transparent bulk media," Applied Physics B-Lasers and Optics **77**, 185-195 (2003).

184. J. L. Tate, "Intense laser propagation in sapphire," in *Graduate School*(Ohio State University, 2004).

185. V. I. Klimov, and D. W. McBranch, "Femtosecond high-sensitivity, chirp-free transient absorption spectroscopy using kilohertz lasers," Optics Letters **23**, 277-279 (1998).

186. Z. W. Wilkes, S. Varma, Y. H. Chen, H. M. Milchberg, T. G. Jones, and A. Ting, "Direct measurements of the nonlinear index of refraction of water at 815 and 407 nm using single-shot supercontinuum spectral interferometry," Applied Physics Letters **94**, 211102-211103 (2009).

187. J. K. Ranka, R. W. Schirmer, and A. L. Gaeta, "Observation of pulse splitting in nonlinear dispersive media," Physical Review Letters **77**, 3783-3786 (1996).

188. G. G. Luther, J. V. Moloney, A. C. Newell, and E. M. Wright, "Self-focusing threshold in normally dispersive media," Optics Letters **19**, 862-864 (1994).

189. G. G. Luther, A. C. Newell, J. V. Moloney, and E. M. Wright, "Short-pulse conical emission and spectral broadening in normally dispersive media," Optics Letters **19**, 789-791 (1994).

190. A. Brodeur, and S. L. Chin, "Ultrafast white-light continuum generation and self-focusing in transparent condensed media," Journal of the Optical Society of America B-Optical Physics **16**, 637-650 (1999).

191. J. H. Marburger, "Self-focusing: theory," Prog. Quantum Elec. **4**, 35-110 (1975).

192. J. E. Rothenberg, "Pulse splitting during self-focusing in normally dispersive media," Optics Letters **17**, 583-585 (1992).

193. J. E. Rothenberg, "Space-time focusing: breakdown of the slowly varying envelope approximation in the self-focusing of femtosecond pulses," Optics Letters **17**, 1340-1342 (1992).

194. G. Z. Yang, and Y. R. Shen, "Spectral broadening of ultrashort pulses in a nonlinear medium," Optics Letters **9**, 510-512 (1984).

195. A. L. Gaeta, "Catastrophic collapse of ultrashort pulses," Physical Review Letters **84**, 3582-3585 (2000).

196. G. Eckhardt, S. E. Schwarz, F. J. McClung, R. W. Hellwarth, E. J. Woodbury, and D. Weiner, "Stimulated Raman scattering from organic liquids," Physical Review Letters **9**, 455-457 (1962).

197. N. Bloembergen, "The influence of electron plasma formation in superbroadening in light filaments," Optics Communications **8**, 285-288 (1973).

198. Q. R. Xing, K. M. Yoo, and R. R. Alfano, "Conical emission by four photon parametric generation by using femtosecond laser pulses," Applied Optics **32**, 2087-2089 (1993).

199. N. Y. Vislobokov, and A. P. Sukhorukov, "Supercontinuum generation by ultra-high power femtosecond laser pulses in dielectrics," Physics of Wave Phenomena **17**, 11-14 (2009).

200. J. Queneuille, F. Druon, A. Maksimchuk, G. Cheriaux, G. Mourou, and K. Nemoto, "Second-harmonic generation and wave-front correction of a terawatt laser system," Optics Letters **25** (2000).

201. F. L. Zhang, Y. H. Wang, M. Z. Sun, Q. Y. Bi, X. L. Xie, and Z. Q. Lin, "Numerical simulations of the impact of wavefront phase distortions of pump on the beam quality of OPA," Chinese Optics Letters **8**, 217-220 (2010).

202. Q. Sun, H. Liu, N. Huang, and W. Zhao, "Influence of the wavefront mismatch, spatial chirp and multimode pump on the beam quality of OPCPA," Journal of Modern Optics **59** (2012).

203. D. Eimerl, J. M. Auerbach, and P. W. Milonni, "Paraxial wave theory of second harmonic and third harmonic generation in uniaxial crystals 1 Narrow-band pump fieldsFIELDS," Journal of Modern Optics **42**, 1037-1067 (1995).

204. D. A. Kleinman, A. Ashkin, and G. D. Boyd, "Second harmonic generation of light by focused laser beams," Physical Review **145**, 338-379 (1966).

205. D. A. Kleinman, and R. C. Miller, "Dependence of second-harmonic generation on position of focus," Physical Review **148**, 302-312 (1966).

206. P. Pliszka, and P. P. Banerjee, "Nonlinear transverse effects in second harmonic generation," Journal of the Optical Society of America B-Optical Physics **10**, 1810-1819 (1993).

207. T. Harimoto, M. Aoyama, K. Yamakawa, and M. Yonemura, "Suppression of cubic nonlinearity in second-harmonic generation of ultrahigh-intensity laser pulses by initial frequency chirp," Japanese Journal of Applied Physics Part 1-Regular Papers Short Notes & Review Papers **41**, 139-144 (2002).

208. J. Hou, Y. D. Zhang, W. H. Jiang, and N. Ling, "Second-harmonic generation of beams with aberrations," Journal of the Optical Society of America B-Optical Physics **19**, 1380-1390 (2002).

209. R. W. Boyd, "Nonlinear optics (third edition)," (Academic Press, San Diego, 2008).

210. A. Marcinkevicius, R. Tommasini, G. D. Tsakiris, K. J. Witte, E. Gaizauskas, and U. Teubner, "Frequency doubling of multi-terawatt femtosecond pulses," Applied Physics B-Lasers and Optics **79**, 547-554 (2004).

211. J. Y. Zhang, J. Y. Huang, H. Wang, K. S. Wong, and G. K. Wong, "Second-harmonic generation from regeneratively amplified femtosecond laser pulses in BBO and LBO crystals," Journal of the Optical Society of America B-Optical Physics **15**, 200-209 (1998).

212. E. Sidick, A. Knoesen, and A. Dienes, "Ultrashort pulse second harmonic generation 1 Transformed-limited fundamental pulses," Journal of the Optical Society of America B-Optical Physics **12**, 1704-1712 (1995).

213. E. Sidick, A. Dienes, and A. Knoesen, "Ultrashort pulse second harmonic generation 2 Non-transformed-limited fundamental pulses," Journal of the Optical Society of America B-Optical Physics **12**, 1713-1722 (1995).

214. V. Krylov, A. Rebane, A. G. Kalintsev, H. Schwoerer, and U. P. Wild, "Second harmonic generation of amplified femtosecond Ti:sapphire laser pulses," Optics Letters **20**, 198-200 (1995).

215. E. Sidick, A. Dienes, and A. Knoesen, "Ultrashort pulse second-harmonic generation. II Non-transform-limited fundamental pulses," Journal of the Optical Society of America B-Optical Physics **12**, 1713-1722 (1995).

216. E. Sidick, A. Knoesen, and A. Dienes, "Ultrashort-pulse second-harmonic generation. I Transform-limited fundamental pulses," Journal of the Optical Society of America B-Optical Physics **12**, 1704-1712 (1995).

217. V. Krylov, A. Rebane, A. G. Kalintsev, H. Schwoerer, and U. P. Wild, "Second-harmonic generation of amplified femtoseconed Ti:Sapphire laser pulses," Optics Letters **20**, 198-200 (1995).

218. A. V. Smith, "SNLO (http://www.as-photonics.com/SNLO.html)."

219. A. V. Smith, "How to select nonlinear crystals and model their performance using SNLO software," in *Conference on Nonlinear Materials, Devices, and Applications*(Spie-Int Soc Optical Engineering, San Jose, Ca, 2000), pp. 62-69.

220. A. V. Smith, and M. S. Bowers, "Phase distortions in sum-frequency and difference-frequency mixing in crystals," Journal of the Optical Society of America B-Optical Physics **12**, 49-57 (1995).

221. J. W. Goodman, *Introduction to Fourier Optics* (McGraw Hill, 1996).

222. F. Hache, A. Zeboulon, G. Gallot, and G. M. Gale, "Cascaded second-order effects in the femtosecond regime in beta barium borate: self-compression in a visible femtosecond optical parametric oscillator," Optics Letters **20**, 1556-1558 (1995).

223. R. Grunwald, U. Neumann, U. Griebner, K. Reimann, G. Steinmeyer, and V. Kebbel, "Ultrashort-pulse wave-front autocorrelation," Optics Letters **28**, 2399-2401 (2003).

224. E. Rubino, D. Faccio, L. Tartara, P. K. Bates, O. Chalus, M. Clerici, F. Bonaretti, J. Biegert, and P. Di Trapani, "Spatiotemporal amplitude and phase retrieval of space-time coupled ultrashort pulses using the Shackled-FROG technique," Optics Letters **34**, 3854-3856 (2009).

225. P. Bowlan, and R. Trebino, "Using phase diversity for the measurement of the complete spatiotemporal electric field of ultrashort laser pulses," Journal of the Optical Society of America B-Optical Physics **29**, 244-248 (2012).

226. B. Alonso, I. J. Sola, O. Varela, J. Hernandez-Toro, C. Mendez, J. San Roman, A. Zair, and L. Roso, "Spatiotemporal amplitude-and-phase reconstruction by Fourier-transform of interference spectra of high-complex-beams," Journal of the Optical Society of America B-Optical Physics **27**, 933-940 (2010).

227. B. Alonso, R. Borrego-Varillas, O. Mendoza-Yero, Í. J. Sola, J. San Román, G. Mínguez-Vega, and L. Roso, "Frequency resolved wavefront retrieval dynamics of diffractive focused

ultrashort pulses," Journal of the Optical Society of America B-Optical Physics **29**, 1993-2000 (2012).

228. R. Borrego-Varillas, C. Romero, J. R. V. de Aldana, J. M. Bueno, and L. Roso, "Wavefront retrieval of amplified femtosecond beams by second-harmonic generation," Optics Express **19**, 22851-22862 (2011).

229. J. C. Diels, and W. Rudolph, *Ultrashort laser pulse phenomena* (Academic Press, 2006).

230. P. M. Prieto, F. Vargas-Martin, S. Goelz, and P. Artal, "Analysis of the performance of the Hartmann-Shack sensor in the human eye," Journal of the Optical Society of America a-Optics Image Science and Vision **17**, 1388-1398 (2000).

231. G. Minguez-Vega, C. Romero, O. Mendoza-Yero, J. R. V. de Aldana, R. Borrego-Varillas, C. Mendez, P. Andres, J. Lancis, V. Climent, and L. Roso, "Wavelength tuning of femtosecond pulses generated in nonlinear crystals by using diffractive lenses," Optics Letters **35**, 3694-3696 (2010).

232. C. Romero, R. Borrego-Varillas, O. Mendoza-Yero, G. Mínguez-Vega, C. Méndez, and J. R. Vázquez de Aldana, "Second-harmonic generation of femtosecond pulses focused on BBO with a diffractive lens," (submitted, 2012).

233. C. Romero, R. Borrego-Varillas, A. Camino, G. Minguez-Vega, O. Mendoza-Yero, J. Hernandez-Toro, and J. R. V. de Aldana, "Diffractive optics for spectral control of the supercontinuum generated in sapphire with femtosecond pulses," Optics Express **19**, 4977-4984 (2011).

234. H. M. Heuck, P. Neumayer, T. Kuehl, and U. Wittrock, "Chromatic aberration in petawatt-class lasers," Applied Physics B-Lasers and Optics **84**, 421-428 (2006).

235. Z. Bor, "Distortion of femtosecond laser-pulses in lenses," Optics Letters **14**, 119-121 (1989).

236. M. Kempe, U. Stamm, B. Wilhelmi, and W. Rudolph, "Spatial and temporal transformation of femtosecond laser-pulses by lenses and lens systems," Journal of the Optical Society of America B-Optical Physics **9**, 1158-1165 (1992).

237. M. Kempe, and W. Rudolph, "Impact of chromatic and spherical aberration on the focusing of ultrashort light-pulses by lenses," Optics Letters **18**, 137-139 (1993).

238. M. Kempe, and W. Rudolph, "Femtosecond pulses in the focal region of lenses," Physical Review A **48**, 4721-4729 (1993).

239. B. Alonso, R. Borrego-Varillas, O. Mendoza-Yero, Í. J. Sola, J. San Román, G. Mínguez-Vega, and L. Roso, "Frequency resolved wavefront retrieval dynamics of diffractive focused ultrashort pulses," (submitted, 2012).

240. J. A. Jordan, P. M. Hirsch, L. B. Lesem, and D. L. Vanrooy, "Kinoform lenses," Applied Optics **9**, 1883-1887 (1970).

241. E. Hetch, *Optics* (Addison Welsey, 1998).

242. V. Moreno, J. F. Roman, and J. R. Salgueiro, "High efficiency diffractive lenses: Deduction of kinoform profile," American Journal of Physics **65**, 556-562 (1997).

243. "Optical glass datasheet catalog," (SCHOTT, 2012).

244. B. Alonso, "Complete characterization of ultrashort laser pulses," in *PhD thesis*(Universidad de Salamanca, 2012).

245. P. O'Shea, M. Kimmel, X. Gu, and R. Trebino, "Highly simplified device for ultrashort-pulse measurement," Optics Letters **26**, 932-934 (2001).

246. P. Bowlan, P. Gabolde, A. Shreenath, K. McGresham, R. Trebino, and S. Akturk, "Crossed-beam spectral interferometry: a simple, high-spectral-resolution method for completely characterizing complex ultrashort pulses in real time," Optics Express **14**, 11892-11900 (2006).

247. S. Cavalieri, L. Fini, E. Sali, and R. Buffa, "Enhancement of harmonic generation by Fresnel-lensing effects," Optics Letters **31**, 1298-1300 (2006).

248. C. Yang, K. Shi, H. Li, Q. Xu, V. Gopalan, and Z. Liu, "Chromatic second harmonic imaging," Optics Express **18**, 23837-23843 (2010).

249. C. Romero, "Optical parametric processes with femtosecond pulses in nonlinear crystals. Novel schemes and applications.," in *PhD thesis*(Universidad de Salamanca, 2012).

250. X. H. Ni, C. Wang, X. C. Liang, M. Al-Rubaiee, and R. R. Alfano, "Fresnel diffraction supercontinuum generation," Ieee Journal of Selected Topics in Quantum Electronics **10**, 1229-1232 (2004).

251. M. Oujja, A. Garcia, C. Romero, J. R. Vazquez de Aldana, P. Moreno, and M. Castillejo, "UV laser removal of varnish on tempera paints with nanosecond and femtosecond pulses," Physical Chemistry Chemical Physics **13**, 4625-4631 (2011).

252. E. Rebollar, J. R. Vazquez de Aldana, J. A. Perez-Hernandez, T. A. Ezquerra, P. Moreno, and M. Castillejo, "Ultraviolet and infrared femtosecond laser induced periodic surface structures on thin polymer films," Applied Physics Letters **100**, 041106 (2012).

253. D. Brida, C. Manzoni, G. Cirmi, M. Marangoni, S. Bonora, P. Villoresi, S. De Silvestri, and G. Cerullo, "Few-optical-cycle pulses tunable from the visible to the mid-infrared by optical parametric amplifiers," Journal of Optics **12** (2010).

254. D. Brida, C. Manzoni, G. Cirmi, D. Polli, and G. Cerullo, "Tracking Ultrafast Energy Flow in Molecules Using Broadly Tunable Few-Optical-Cycle Pulses," Ieee Journal of Selected Topics in Quantum Electronics **18** (2012).

255. C. T. Middleton, K. de La Harpe, C. Su, Y. K. Law, C. E. Crespo-Hernandez, and B. Kohler, "DNA Excited-State Dynamics: From Single Bases to the Double Helix," Annual Review of Physical Chemistry **60**, 217-239 (2009).

256. C. E. Crespo-Hernandez, B. Cohen, P. M. Hare, and B. Kohler, "Ultrafast excited-state dynamics in nucleic acids," Chemical Reviews **104**, 1977-2019 (2004).

257. C.-h. Tseng, S. Matsika, and T. C. Weinacht, "Two-Dimensional Ultrafast Fourier Transform Spectroscopy in the Deep Ultraviolet," Optics Express **17**, 18788-18793 (2009).

258. N. Krebs, R. A. Probst, and E. Riedle, "Sub-20 fs pulses shaped directly in the UV by an acousto-optic programmable dispersive filter," Optics Express **18**, 6164-6171 (2010).

259. M. R. Armstrong, P. Plachta, E. A. Ponomarev, and R. J. D. Miller, "Versatile 7-fs optical parametric pulse generation and compression by use of adaptive optics," Optics Letters **26**, 1152-1154 (2001).

260. M. Armstrong, P. Plachta, E. A. Ponomarev, J. P. Ogilvie, A. M. Nagy, and R. J. D. Miller, "Versatile seven-femtosecond pulse compressor of parametrically amplified pulses using adaptive optics: studies of the primary events in protein dynamics," Applied Physics B-Lasers and Optics **74**, S127-S132 (2002).

261. A. Brodeur, and S. L. Chin, "Band-gap dependence of the ultrafast white-light continuum," Physical Review Letters **80**, 4406-4409 (1998).

262. M. Kolesik, G. Katona, J. V. Moloney, and E. M. Wright, "Physical factors limiting the spectral extent and band gap dependence of supercontinuum generation," Physical Review Letters **91**, 043905-043909 (2003).

263. J. Yang, Y. Yang, R. Wang, and W. Han, "Characteristics of filamentation in ZK7 glass by negatively chirped femtosecond laser pulses," Science in China Series E-Technological Sciences **51**, 849-856 (2008).

264. M. Ziolek, R. Naskrecki, and J. Karolczak, "Some temporal and spectral properties of femtosecond supercontinuum important in pump-probe spectroscopy," Optics Communications **241**, 221-229 (2004).

265. W. Liu, S. Petit, A. Becker, N. Akozbek, C. M. Bowden, and S. L. Chin, "Intensity clamping of a femtosecond laser pulse in condensed matter," Optics Communications **202**, 189-197 (2002).

266. J. Yang, and G. Mu, "Multi-dimensional observation of white-light filaments by femtosecond laser pulses in condensed medium," Optics Express **15**, 4943-4952 (2007).

267. Z. X. Wu, H. B. Jiang, Q. Sun, H. Yang, and Q. H. Gong, "Filamentation and temporal reshaping of a femtosecond pulse in fused silica," Physical Review A **68** (2003).

268. A. K. Dharmadhikari, F. A. Rajgara, and D. Mathur, "Systematic study of highly efficient white light generation in transparent materials using intense femtosecond laser pulses," Applied Physics B-Lasers and Optics **80**, 61-66 (2005).

269. X. J. Fang, and T. Kobayashi, "Evolution of a super-broadened spectrum in a filament generated by an ultrashort intense laser pulse in fused silica," Applied Physics B-Lasers and Optics **77**, 167-170 (2003).

270. J. B. Ashcom, R. R. Gattass, C. B. Schaffer, and E. Mazur, "Numerical aperture dependence of damage and supercontinuum generation from femtosecond laser pulses in bulk fused silica," Journal of the Optical Society of America B-Optical Physics **23**, 2317-2322 (2006).

271. B. Alonso, R. Borrego-Varillas, O. Mendoza-Yero, Í. J. Sola, J. San Román, G. Mínguez-Vega, and L. Roso, "Frequency resolved wavefront retrieval dynamics of diffractive focused ultrashort pulses," J. Opt. Soc. Am. B **29**, 1993-2000 (2012).

272. H. Urey, "Spot size, depth-of-focus, and diffraction ring intensity formulas for truncated Gaussian beams," Applied Optics **43**, 620-625 (2004).

273. C. Schulze, D. Flamm, M. Duparre, and A. Forbes, "Beam-quality measurements using a spatial light modulator," Optics Letters **37**, 4687-4689 (2012).

274. P. O'Shea, M. Kimmel, X. Gu, and R. Trebino, "Increased-bandwidth in ultrashort-pulse measurement using an angle-dithered nonlinear-optical crystal," Optics Express **7**, 342-349 (2000).

275. S. Linden, H. Giessen, and J. Kuhl, "XFROG - A new method for amplitude and phase characterization of weak ultrashort pulses," Physica Status Solidi B-Basic Research **206**, 119-124 (1998).

276. B. Tsermaa, B. K. Yang, K. Myung-Whun, and J. S. Kim, "Characterization of Supercontinuum and Ultraviolet Pulses by Using XFROG," Journal of the Optical Society of Korea **13**, 158-165 (2009).

277. G. Stibenz, and G. Steinmeyer, "High dynamic range characterization of ultrabroadband white-light continuum pulses," Optics Express **12**, 6319-6325 (2004).

278. J. Liu, Y. Feng, H. Li, P. Lu, H. Pan, J. Wu, and H. Zeng, "Supercontinuum pulse measurement by molecular alignment based cross-correlation frequency resolved optical gating," Optics Express **19**, 40-46 (2011).

279. A. P. Baronavski, H. D. Ladouceur, and J. K. Shaw, "Analysis of cross-correlation, phase-velocity mismatch and group-velocity mismatches in sum-frequency generation," IEEE Journal of Quantum Electronics **29**, 580-589 (1993).